



HAL
open science

Development of hybrid photoelectrodes via assemblage of a ruthenium based photosensitizer and a metal-metal oxide nanocatalyst for the solar O₂ generation

Quyen Nguyen Thi

► **To cite this version:**

Quyen Nguyen Thi. Development of hybrid photoelectrodes via assemblage of a ruthenium based photosensitizer and a metal-metal oxide nanocatalyst for the solar O₂ generation. Coordination chemistry. Université Paul Sabatier - Toulouse III, 2021. English. NNT : 2021TOU30046 . tel-03343059

HAL Id: tel-03343059

<https://theses.hal.science/tel-03343059v1>

Submitted on 13 Sep 2021

HAL is a multi-disciplinary open access archive for the deposit and dissemination of scientific research documents, whether they are published or not. The documents may come from teaching and research institutions in France or abroad, or from public or private research centers.

L'archive ouverte pluridisciplinaire **HAL**, est destinée au dépôt et à la diffusion de documents scientifiques de niveau recherche, publiés ou non, émanant des établissements d'enseignement et de recherche français ou étrangers, des laboratoires publics ou privés.



THÈSE

**En vue de l'obtention du
DOCTORAT DE L'UNIVERSITÉ DE TOULOUSE**

Délivré par l'Université Toulouse 3 - Paul Sabatier

Présentée et soutenue par

Quyên NGUYEN THI

Le 26 mai 2021

**Développement de photoélectrodes hybrides via l'assemblage
d'un photosensibilisateur à base de ruthénium et d'un
nanocatalyseur métal / oxyde métallique pour la génération d'O₂
solaire**

Ecole doctorale : **SDM - SCIENCES DE LA MATIÈRE - Toulouse**

Spécialité : **Chimie Organométallique et de Coordination**

Unité de recherche :

LCC - Laboratoire de Chimie de Coordination

Thèse dirigée par

Catherine AMIENS et Phong TRAN DINH

Jury

M. Vincent ARTERO, Rapporteur

M. Xavier SALA, Rapporteur

Mme Valérie KELLER, Examinatrice

M. Fabien DELPECH, Examineur

Mme Catherine AMIENS, Directrice de thèse

M. Phong TRAN DINH, Co-directeur de thèse



THÈSE

**En vue de l'obtention du
DOCTORAT DE L'UNIVERSITÉ DE TOULOUSE**

Délivré par l'Université Toulouse 3 - Paul Sabatier

Présentée et soutenue par

Quyên NGUYEN THI

Le 26 mai 2021

**Développement de photoélectrodes hybrides via l'assemblage
d'un photosensibilisateur à base de ruthénium et d'un
nanocatalyseur métal / oxyde métallique pour la génération d'O₂
solaire**

Ecole doctorale : **SDM - SCIENCES DE LA MATIÈRE - Toulouse**

Spécialité : **Chimie Organométallique et de Coordination**

Unité de recherche :

LCC - Laboratoire de Chimie de Coordination

Thèse dirigée par

Catherine AMIENS et Phong TRAN DINH

Jury

M. Vincent ARTERO, Rapporteur

M. Xavier SALA, Rapporteur

Mme Valérie KELLER, Examinatrice

M. Fabien DELPECH, Examineur

Mme Catherine AMIENS, Directrice de thèse

M. Phong TRAN DINH, Co-directeur de thèse

Acknowledgments

I greatly thank French Embassy for having awarded me the doctoral grant under the program Bourse d'Excellence 2018-2021. I am grateful for the funding sources that allowed me to pursue my dream.

I would like to thank Dr. Vincent Artero, Dr. Xavier SaLa, Dr. Valérie Keller and Dr. Fabien Delpech for accepting being the jury members of my Ph.D. thesis.

I am extremely grateful to my supervisor, Prof. Tran Dinh Phong and Prof. Catherine Amiens, for giving me the possibility to work on this topic and for their invaluable advice, continuous support and patience during my Ph.D. study. Your immense knowledge and plentiful experience have encouraged me in my academic research and daily life. You were and remained my best role model for a scientist, mentor, and teacher. Without your help and support, this Ph.D. thesis would have been completed. A simple world could not express all my thanks to both of you.

This Ph.D. thesis could not have been completed without the support of collaborators, technicians and researchers, providing ideas and tools for me understanding all samples. I spent most of my time in LCC, where I completed most of the work in this thesis; therefore, I would like to thank all the people in LCC for their help and support during the past three years. Especially Dr. Vincent Collière for performing HR-TEM and teaching me how not to destroy TEM microscopy. I want to thank Alix Saquet, Alain Moreau for providing access to electrochemical service and ICP-AES analysis, Dr. JF Meunier for recording the Mössbauer spectrum, and Dr. Yanick for NMR.

I sincerely thank Dr. Karine Philippot and Dr. Rosa Axet for their help and discussion about chemistry and life.

I would like to thank all current and former members of team L "Engineering of metal nanoparticles," at LCC, for all their valuable time that we shared together in this adventure. Special thanks will be sent to Lorraine and Francois for all their help on my PhD work and their efforts to teach me French during more than three years in LCC. I thank Laurent Peres, Miquel Cardona

Farreny, Roberto Gonzalez Gomez, Laura Mallon Pernia, Lea Godard, Elena Martin Morales, Paul Mathieu for their friendship.

Additionally, this Ph.D. thesis has involved collaborations with many different people/labs. I would like to express my special thanks to Prof. Gilles Lemerrier and Dr. Elodie Rousset for their help in synthesizing and characterizing the ruthenium complex and many fruitful scientific discussions. Many thanks for their valuable advice and efforts in order to make my thesis completed.

I would like to express my gratitude to Dr. Pierre Lecante from CEMES for X-ray analysis, scientific discussion and all his kind support when we have a chance to work in synchrotron Thailand. I also extend my gratitude to Dr. Wantana Klysubun and team beamline BL8 for setting up the Fe K-edge EXAFS experiment in Synchrotron Thailand. This is the first time for me working in a synchrotron, and I had lots of good memories there. I thank Dr. Jerome Esvan for the XPS analysis as well as his results analysis. I also thank Dr. Marc Respaud for Mössbauer fitting and his scientific discussion.

I am also thankful for all current and former CECS lab members who have contributed to my work and living via different manners. A special thanks to Mrs. Nguyen Thi Chuc, Mr. Le Van Hoang, and Mr. Tran Duc Tien for their kindness in helping me perform the photoelectrochemical assessment in Vietnam.

I would like to thank my family for giving me their love and unconditional support me all the way long. Words cannot express how grateful that, after all, I still have a family where I can come back whenever I have trouble out there.

And to you, my darling who has a talent for making me smile, happy and feel better in any situation. I always felt lucky that you have come and been my side. The past three years have not been easy for me in both academically and personally. I truly thank you for always being by my side during my good and bad times. Your unconditional supports had helped me a lot on the way I found myself again. I hope that I can support and make you happy as you do for me.

Abbreviations

APA	3-aminopropyl phosphonic acid
APTES	3-aminopropyl triethoxysilane
AP	Acidification potential
ATMPA	Aminotris(methylenephosphonic acid
ATR-IR	Attenuated total reflection- infrared spectroscopy
B.E.	Binding energy
bcc	Body-centered cubic
BET	Brunauer-emmett-teller
<i>b</i> -Fe@FeOx@Ru	<i>Biphasic</i> -iron@iron oxide@ruthenium
BIP	benzimidazole-phenol
bpy	biphenylpyridine
Cat	Catalyst
CB	Conduction band
CC	Carbon cloth
CEPA	2-carboxyethyl phosphonic acid
CNTs	Carbon nano tubes
CoPi	Cobalt phosphate
CP	Chronopotentialmetric
CVD	Chemical vapor deposition
dppf	1,1'-Bis(diphenylphosphino)ferrocene
E.q	Equation
ECSA	Electrochemistry active surface area
EDTMPA	Ethylenediamine tetra(methylene phosphonic acid)

EISA	Evaporation -induced self-assembly
EtOH	Ethanol
EXAFS	Extended X-ray absorption fine structure
FFT	Fast fourier transformation
FM Fe	Ferromagnetic iron
FTO	Fluorine-doped tin oxide
FWHM	Full width at half maximum
GWP	Global warming potential
HAADF-STEM	High angle annular dark field- scanning transmission electron spectroscopy
HDA	Hexadecylamine
HDA.HCl	Hexadecylammonium chloride
HER	Hydrogen evolution reaction
HMDS	Hexamethyldisilazane
HR-TEM	High resolution - transmission electron microscopy
ICP-OES	Inductively coupled plasma - optical emission spectroscopy
IEA	International energy agency
IMPA	Iminodi (methylphosphonic acid)
<i>IS</i>	Isomeric shift
ITO	Indium tin oxide
LC	Ligand center
LDH	Layered double hydroxide
LSV	Linear sweep voltammetry
<i>m</i> -Fe@FeOx@Ru	<i>Monophasic</i> -iron@iron oxide@ruthenium
MLCT	Metal to ligand charge transfer

NF	Nickel foam
<i>n</i> -Fe@FeOx	<i>Native</i> iron-iron oxide
NMR	Nuclear magnetic resonance
NPs	Nanoparticles
<i>NS</i>	<i>nanosheets</i>
ODE	Octadecene
OER	Oxygen evolution reaction
pba	Pyridine benzoic acid
PECs	Photoelectrochemical cells
phen	1,10-phenanthroline
PM Fe	Paramagnetic iron
PMOD	Photochemical metal organic deposition
PS	Photosensitizer
RDE	Rotating disk electrode
RDF	Radical distribution function
<i>r</i> -Fe@FeOx	<i>Reconstructed</i> iron-iron oxide
rGO	Reduced graphene oxide
RHE	Reversible hydrogen electrode
SAED	Selected area electron diffraction
SCC	Social cost of carbon
SEM	Scanning Electron Microscopy
SPM Fe	Superparamagnetic Iron
TEM	Transmission electron microscopy
THF	Tetrahydrofuran
TOF	Turn over frequency

TON	Turn over number
tpy	Terpyridine
TWy	Terawatt-years
WAXS	Wide angle X-ray scattering
WOCs	Water oxidation catalysts
WTES	World total energy supply
XPS	X-ray photoelectron spectroscopy

General introduction

Nowadays, with the increase in population, urbanization, and living standards the energy demand is rapidly increasing. However, as a result of this growth in energy consumption, and as 85 % of the energy consumed comes from fossil fuels, we are now facing more and more serious environmental and health issues. Consequently, the replacement of fossil fuels by a clean and renewable energy source is today one of the most urgent challenges for humanity. In this context, it is predicted that hydrogen will play an important role in the development of sustainable energy and clean environment. As water splitting is one of the best-known methodologies for the mass production of hydrogen, solar driven water splitting processes represent promising technological solutions to the energy consumption and environmental issues that we are currently facing. However, the process of water splitting is normally slow and energetically uphill so it requires both energy and a catalyst to be effective. This can be done in a photoelectrochemical cell which mimics the function of natural photosynthesis. However, the cost of the catalysts developed so far is too high to enable the large scale implementation of this technology.

In this PhD, our objective is to investigate the potential of abundant and cheap nanomaterials for the development of new photoelectrodes that could be used in photoelectrochemical cells, focusing on the more challenging water oxidation half-reaction. To do so, we envisaged the covalent grafting of a molecular light harvester, based on a Ru complex, on metal/metal oxide catalysts of cheap and abundant metals such as Fe@FeOx, and NiFe oxide NPs.

The organization of the thesis is the following:

Chapter I- Introduction

A general introduction on the energy shortage and related environmental issues that human beings are faced with today is given. Thereafter the significance of using hydrogen as future energy carrier, and of producing it in photoelectrochemical cells, is presented. Then some basic information on the water splitting process, and water oxidation catalysts are introduced. Finally,

the state of the art related to the development of solar water splitting and photoelectrochemical cells is given.

Chapter II – Synthesis and functionalization of Fe@FeOx NPs with different aminophosphonic acids for water oxidation catalysis

In this chapter, the state of the art on the use of Fe oxide NPs as water oxidation catalysts are first reported. Then the synthesis and characterization of Fe@FeOx core-shell nanoparticles are described, followed by the results from the surface modification of these nanoparticles by different aminophosphonic acids. Finally, the performance of these nanomaterials in water oxidation catalysis is reported and discussed in comparison with literature data.

Chapter III- Fe@FeOx grafted with a Ru complex for photocatalysed water splitting

It is the heart of this PhD dissertation. The main goal was to assemble a photosensitizer and a metal oxide nanocatalyst by a covalent linkage to afford a hybrid nanocatalyst which could be integrated later on as a photoanode in a photoelectrochemical cell. A brief literature review on preceding examples of such hybrid nanocatalysts is first given. Then the synthesis and characterization of a Ru based photosensitizer is reported, as well as its successful covalent grafting on Fe@FeOx nanoparticles through a phosphonic acid pending group. Finally, the catalytic activity of this hybrid Ru based photosensitizer-Fe@FeOx in solar driven water oxidation is discussed in comparison with a simple mixture of photosensitizer and catalyst, and with literature data, to evidence the benefit of the covalent linkage.

Chapter IV – Investigation of the catalytic activity of NiFeOx NPs

Chapter IV is devoted to the study the synergistic effect of Ni and Fe in bimetallic oxide nanocatalysts for water oxidation reaction. First, some key information such as: the advantages of using bimetallic systems, the role of Fe in the enhancement of the electrocatalytic activity in mixed Ni-Fe compound, the optimum Fe to Ni ratio, and the different methods developed to synthesized NiFe oxide thin films and NPs as water oxidation catalysts in alkaline solution are given. Then the different NiFe oxide NPs investigated in this work are described, as well as their surface

modification with 3-aminopropyl phosphonic acid. Finally, their activity as water oxidation catalysts is discussed in comparison to literature data.

Chapter V- General conclusions and perspectives

In chapter V, the key points of this thesis are highlighted, and the perspectives opened by this work are discussed.

This doctoral thesis was supported by a grant of excellence delivered by the French Government. It was co-supervised by Professor Dr. Catherine Amiens from the Laboratoire de Chimie de Coordination (LCC-CNRS, Toulouse, France) and Professor Dr. Phong Tran Dinh from the University of Science and Technology of Hanoi (USTH, Hanoi, Viet Nam). The experimental work has been conducted in three laboratories: at LCC where the metal/metal oxide nanocatalysts were developed, at CECS (Laboratory of Chemistry for Energy Conversion and Storage, in Hanoi) for the evaluation of the electro and photocatalytic activity of the nanomaterials, and at ICMR (Institut de Chimie Moleculaire de Reims) for the synthesis of the Ru based photosensitizers in collaboration with Pr. Gilles Lemercier and Dr. Elodie Rousset. This work also benefited from collaborations with Dr. Pierre Lecante (CEMES, Toulouse) and Pr. Marc Respaud (CEMES, Toulouse) for the study of the structural and magnetic properties of the nanomaterials, respectively, and from Dr. Jérôme Esvan (CIRIMAT, Toulouse) for the study of their electronic properties, and of Vincent Collière for the HR-TEM and ARM studies.

Table of contents

Chapter I - Introduction

1. World energy outlook and environmental problem	13
2. Hydrogen as energy carrier in the future	16
3. Water splitting:	18
4. Water oxidation catalysts	19
4.1 Parameters used to evaluate water oxidation catalysts	21
4.1.1 Overpotential (η , η_{10})	21
4.1.2 Electrocatalytic stability	22
4.1.3. Tafel slope	23
4.1.4. TOF and TON	25
5. Solar driven water splitting.....	25
5.1 Photoelectrochemical cell	28
6. References	31

Chapter II - Synthesis and functionalization of Fe@FeO_x NPs with different aminophosphonic acids for water oxidation catalysis

1. Introduction.....	36
2. Results and discussion	55
2.1. Synthesis and characterization of nanomaterials.....	55
2.1.1. Synthesis and characterization of Fe@FeO _x NPs	55
2.1.2. Reconstruction of the iron oxide layer.....	63
2.1.3. Water transfer of Fe@FeO _x NPs.....	74
2.2. Electrocatalytic activity of <i>r</i> -Fe@FeO _x NPs and <i>r</i> -Fe@FeO _x @APAs NPs in OER..	83
3. Conclusions.....	89
4. References	90

Chapter III- Fe@FeO_x NPs grafted with a Ru complex for photocatalysed water splitting

1. Introduction.....	93
2. Synthesis and characterization of the [Ru-PO(OH) ₂]-Cl ₂ ·7H ₂ O.....	106

3. Synthesis and characterization of hybrid nanomaterials PS-Fe@FeO _x NPs.....	114
4. Photo-electrochemical water oxidation catalysis	127
5. Conclusion	133
6. References	137

Chapter IV-Investigation of the catalytic activity of NiFeO_x NPs

1. Introduction.....	142
1.1 Some hypothesis on the origin of activity enhancement	145
1.2 Optimal composition	147
1.3 Synthesis methods for NiFe-based thin films and main results in electrocatalysis thereof.....	148
1.4 Synthesis of NiFe based NPs and main results in electrocatalysis thereof.....	154
2. Description of the nanomaterials used in this work.....	160
2.1 Ni and Fe oxide reference samples	161
2.2 Synthesis and characterization of the Fe-rich sample (1Ni/9Fe oxide NPs).....	166
2.3 Synthesis and characterization of NiFeO _x NPs with compositions 1Ni/1Fe and 2Ni/1Fe.....	169
2.4 Water transfer of NiFeO _x NPs using 3-amino propyl phosphonic acid:.....	175
3. Evaluation of the nanomaterials in WOC.....	180
3.1 Electrocatalytic activity in OER	180
3.2 Electrocatalytic Stability.....	182
3.3. Cyclic Voltametry studies.....	183
4. Conclusions.....	188
5. References	191

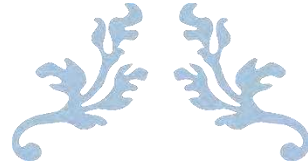
Chapter V - General conclusions and perspectives

General conclusions and perspectives.....	194
---	-----

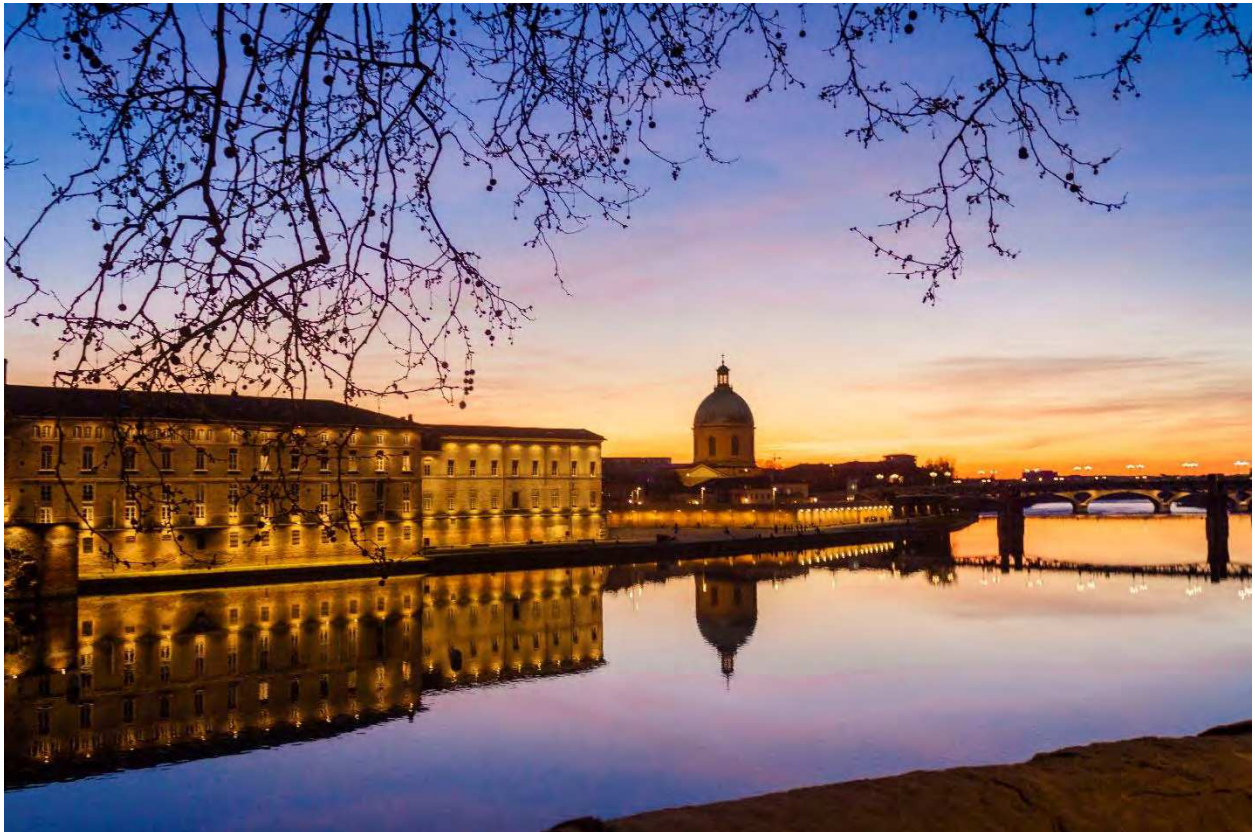
Experimental section

1. Materials	197
2. Synthesis.....	197
2.1. Synthesis of the [Ru(phen) ₂ (phen-PO(OH) ₂](Cl) ₂ complex.....	197
2.2. Synthesis of Fe nanoparticles	198
2.2.1. <i>n</i> -Fe@FeO _x NPs.	198
2.2.2. <i>a</i> -Fe@FeO _x NPs.....	199

2.2.3. <i>r</i> -Fe@FeO _x NPs	199
2.2.4. Grafting of aminophosphonic acids	199
2.2.5. PS-Fe@FeO _x @Ru hybrid nanomaterial.....	200
2.2.6. NiO _x -PVP NPs reference sample	201
2.2.7. FeO _x , 2Ni/1Fe oxide, 1Ni/1Fe oxide and 1Ni/9Fe oxide NPs	201
2.2.8. 2Ni/1Fe oxide-APA, 1Ni/1Fe oxide-APA NPs	201
3. Electrochemical measurement of <i>r</i> -Fe@FeO _x NPs and <i>r</i> -Fe@FeO _x @APAs NPs.....	201
4. Photoelectrochemical measurements	202
4.1 Preparation of photoanodes	202
4.2 Photocatalytic activity of as-prepared photoanodes	202
5. Electrochemical measurements for sample 2Ni/1Fe oxide-APA, 1Ni/1Fe oxide-APA, 1Ni/9Fe oxide-HMDS, FeO _x -HMDS, and NiO _x -PVP NPs.....	203
6. Characterization techniques	204
6.1. TEM and HR-TEM.....	204
6.2. XPS	204
6.3. ICP-OES.....	205
6.4. WAXS.....	205
6.5. EXAFS.....	205
6.6. Mössbauer spectroscopy	205
6.7. ATR-FTIR.....	206
7. General calculations.....	206
7.1. Estimation of the atomic % of Fe metal in a NP from sample <i>r</i> -Fe@FeO _x NPs based on HR-TEM results.....	206
7.2. Determination of the average shell thickness of the oxide layer in a NP from <i>r</i> -Fe@FeO _x NPs based on Mossbauer data.	207
7.3 Estimation of the number of Ru complexes grafted per Fe@FeO _x NP	208
7.4. Calculation of Turnover number (TON) and Turnover frequency (TOF) of the catalyst:	211
7.4.1 Calculation the TON per PS and TOF per PS on sample <i>m</i> -Fe@FeO _x @Ru NP:	211
7.4.2. Calculation the TON per PS and TOF per PS on sample <i>b</i> -Fe@FeO _x @Ru NP:	212
8. References	213



CHAPTER I - INTRODUCTION



Sunset – Garonne river – Toulouse – France 2019

Table of contents – Chapter I

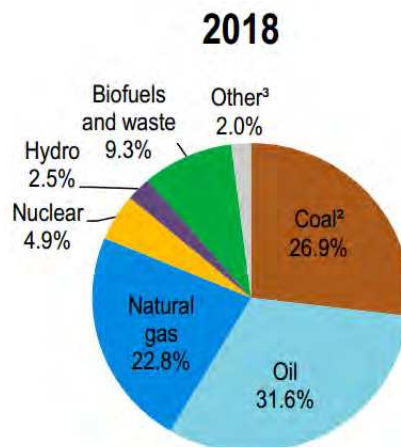
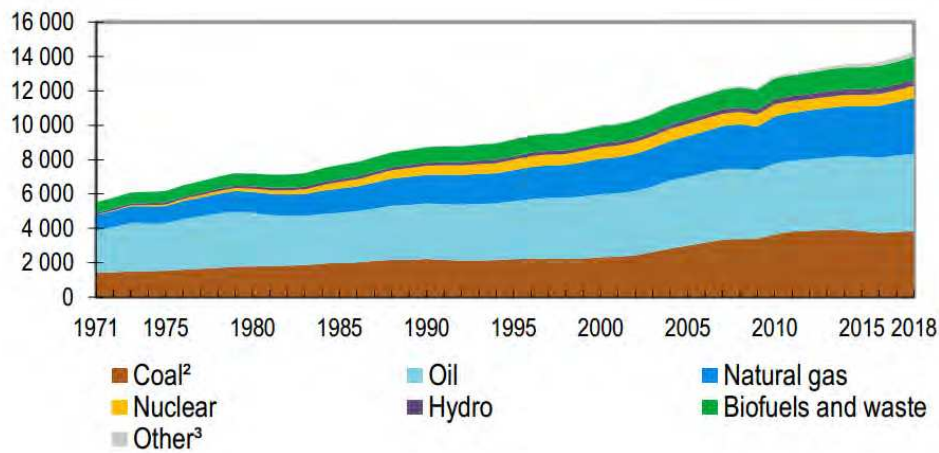
1. World energy outlook and environmental problem.....	13
2. Hydrogen as energy carrier in the future	16
3. Water splitting:.....	18
4. Water oxidation catalysts	19
4.1 Parameters used to evaluate water oxidation catalysts	21
4.1.1 Overpotential (η, η_{10}).....	21
4.1.2 Electrocatalytic stability.....	22
4.1.3. Tafel slope.....	23
4.1.4. TOF and TON.....	25
5. Solar driven water splitting.....	25
5.1 Photoelectrochemical cell.....	28
6. References	31

Chapter I - Introduction

Chapter I - Introduction

1. World energy outlook and environmental problem

Today the world population is 7.8 billion and is expected to grow up to 9 billion by 2050, and about 10 billion by 2100[1]. This population growth is accompanied by a rapid rise in the economic growth thus placing additional demands on energy supply (Figure 1-top)[2]. The world energy consumption (~ 13.5 TW by 2001) is expected to double by 2050 and triple by 2100[3]. Nowadays, the major source of energy (~80%) is still the combustion of fossil fuel such as coal, oil and natural gas (Figure 1-bottom)[2].



14 282 Mtoe

Figure 1. World total energy supply (WTES) by source (Mtoe) from 1971 to 2018[2] (²: in these graphs, peat and oil shale are aggregated with coal. ³: includes geothermal, solar, wind, tide/wave/ocean, heat, and other sources.

As fossil fuels have high energy density, humanity has become dependent on them for most of its needs. However, combustion of fossil fuels has detrimental effects on climate and health. An overwhelming scientific consensus maintains that climate change is primarily caused by the combustion of fossil fuels, which releases CO₂ and other greenhouse gases into the atmosphere (Figure 2)[4]. It has been recorded that the greenhouse gases emission has drastically increased since the pre-industrial era (1850-1900), largely driven by the economic development and population growth (Figure 3). Before the industrial revolution (1750-1850) CO₂ emission from burning fossil fuels was very low. The increase of CO₂ emissions remained low until the middle of the 20th century. For example, in 1950 the total CO₂ emission all over the world was 5 billion tones. But after 1950 it started to increase rapidly: for example, in 2000 it was 25 billion tones and now it is over 35 billion tons. CO₂ emissions are expected to increase from 29 billion tons per year to 43 billion tons per year in the very near future if the present trend is maintained, with disastrous consequences for our planet's ecosystem[5].

Atmospheric carbon dioxide and Earth's surface temperature (1880-2019)

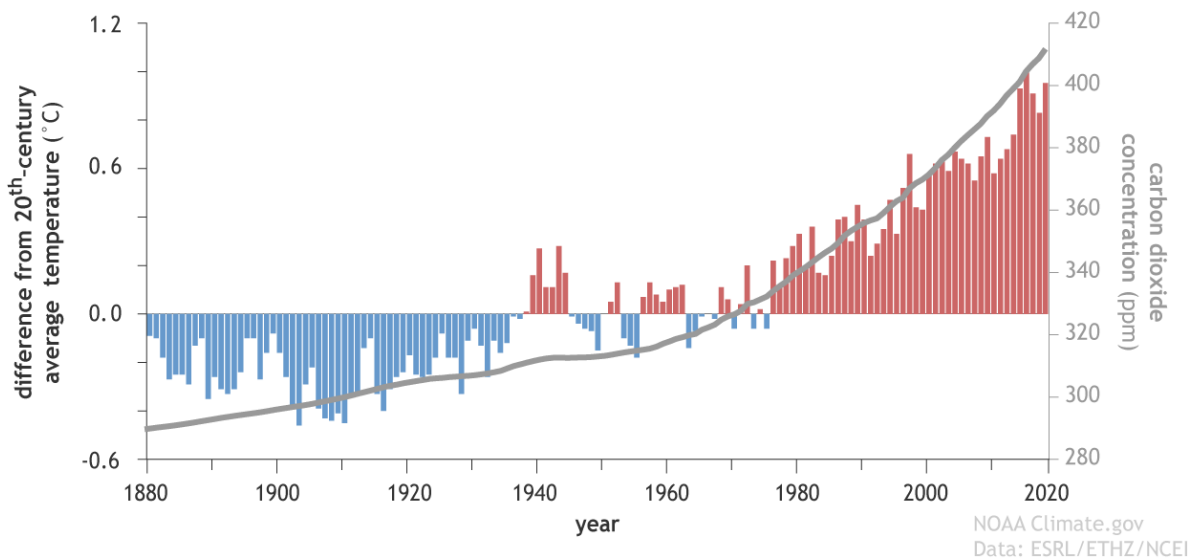


Figure 2. Atmospheric carbon dioxide and Earth's surface temperature from 1880 to 2019[4]. Yearly temperature compared to the twentieth-century average (red and blue bars) from 1880–2019, based on data from NOAA NCEI, plus atmospheric carbon dioxide concentrations (gray line): 1880-1958 from IAC, 1959-2019 from NOAA ESRL. Original graph by Dr. Howard Diamond (NOAA ARL), and adapted by NOAA Climate.gov.

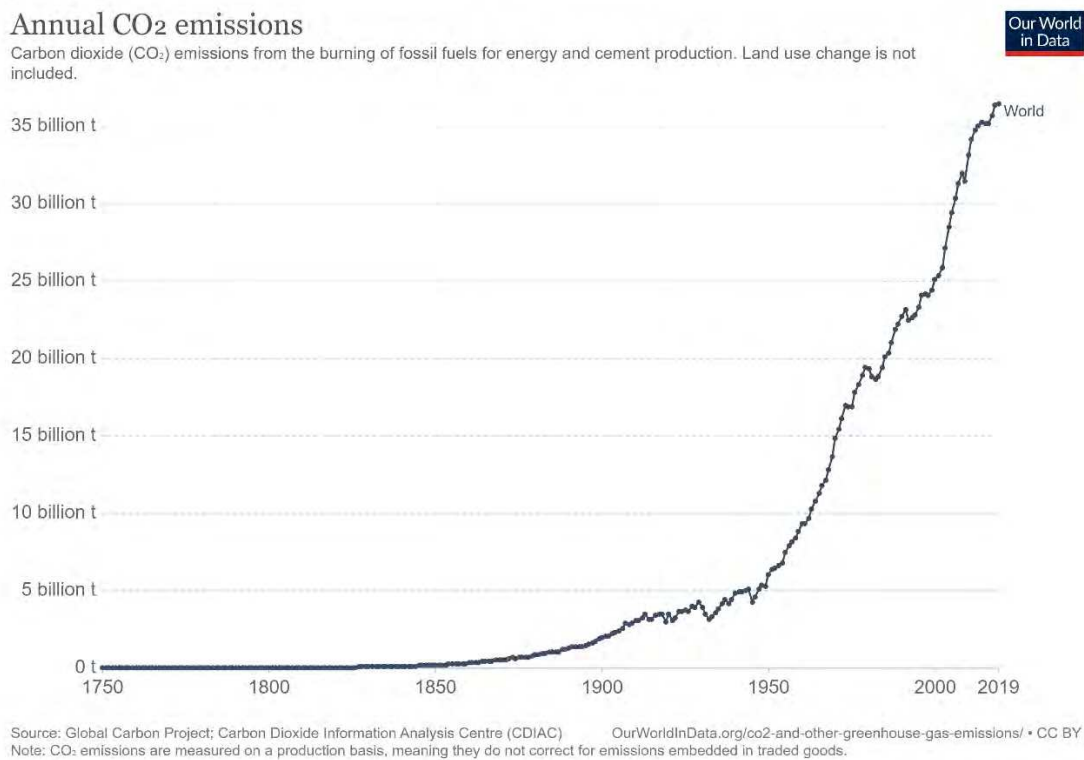


Figure 3. Annual CO₂ emissions from the burning of fossil fuels for energy and cement production[5].

In order to avert some of the worst effects of climate change we need to prevent the global temperature from rising more than 1.5 °C above the average temperature recorded during the pre-industrial era. To do that, global carbon emissions should have dropped to zero by 2050 [6]. It will take a variety solutions to achieve this goal and so the development of renewable energy sources, and usage thereof, is the greatest challenge for humanity in the 21st century[7, 8]. Renewable energy sources like wind, geothermal, hydropower and solar energy are nearly unlimited and environmental friendly, when they do not imply any emission of CO₂. They can be thus good alternatives to the combustion of fossil fuels. Among all the renewable energy sources listed above, solar power is by far the largest source of renewable energy ($\sim 1.2 \times 10^{14}$ kJ are received at the Earth’s surface every second[9]), which means that all the energy needed for human activities in 1 year is obtained in less than 1.5 h)[10]. Conversion of solar energy into chemical fuels is an attractive strategy as it provides energy storage in the smallest possible configuration which is chemical bonds, like Nature has been using sunlight as the primary energy source to oxidize water and generate carbohydrates for over a billion years. Among all chemical fuels, hydrogen has the highest gravimetric energy density (143 MJ/kg) which is 6 times the energy density of coal and at least 3 times that of other chemical fuels such as liquid

hydrocarbon (47 MJ/kg)[11]. More importantly, it is also a green fuel, as it releases only energy and water upon combustion. It is thus expected to have a key role in the near future[12].

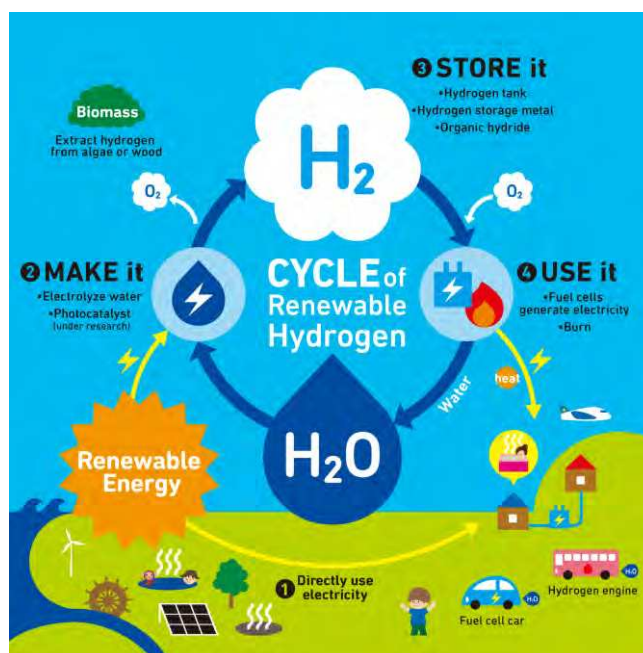
2. Hydrogen as energy carrier in the future

Hydrogen is the most abundant element on Earth but it is not found freely in nature as it is very reactive. Hydrogen always exists combined with other elements for example in the water molecule H₂O. Hydrogen can be produced in a number of different ways such as natural gas reformation, coal gasification, nuclear power, electrolysis of water,...*etc*[13]. The diversity of potential supply energy sources and technologies used to produce hydrogen is an important reason for hydrogen to become a promising energy carrier in the future. Presently, hydrogen is mainly produced by steam methane reforming using natural gas as the feed stock. However, this process releases a huge amount of CO₂, a by-product of the reaction, into the atmosphere (eq. 1). Globally hydrogen production is responsible for the release of 843 tons of CO₂ every year[14]. In view of the above, production of hydrogen from steam reforming of natural gas is obviously not a sustainable process.



Eq. 1. global scheme for methane reforming

Production of hydrogen from water is at first sight more sustainable, hence an attractive alternative process. However, hydrogen can only be considered as a clean form of energy at a global scale if the primary energy used to split water doesn't in itself impact our environment. Scheme 1 shows the practical use of renewable hydrogen cycles as source of energy. At the beginning of this cycle, hydrogen can be produced by electrolysis of water using one of the renewable energy sources such as solar, wind, bio-mass, hydro-electricity. Production of hydrogen from solar-water splitting would be the best sustainable process as it only requires water and sunlight to operate, both largely abundant on earth. Once hydrogen produced, it can be stored before its use (*e.g.* in fuel cells[15] or as reducing agent to transform biomaterials and CO₂ into fuels[16]). Thus, at the end of the cycle, hydrogen only reacts with oxygen releasing water into the atmosphere, and therefore this hydrogen cycle is fully sustainable. Hydrogen obtained by this way would be a versatile carbon neutral energy carrier.



Scheme 1. The renewable hydrogen cycle (source: <https://en.rh2.org/what-is-rh2/basic/>).

Table 1 presents the overall comparisons of selected hydrogen production methods based on hydrogen production costs in correlation with environmental impact, energy efficiency and exergy efficiency[17]. The ranking is between 0 and 10, where 0 refers to a poor performance and 10 refers to the ideal case. Among the different technologies for hydrogen production, the solar energy based hydrogen production (e.g., photoelectrochemical method (entry M10), photocatalysis (entry M9), PV electrolysis (entry M8) and artificial photosynthesis (entry M18)) are promising ways as they both have the potential for up-scaling and a good balance on environmental issues (column SCC, GWP and AP in Table 1). However, the high cost of hydrogen produced by those techniques and the low efficiency is a strong limiting factor for practical application (Figure 4 and Table 1). Therefore, a lot of improvements are needed on the different aspects of hydrogen production from solar energy in order to make it a cost-effective alternative to carbon fuels.

Table 1. Overall comparisons of selected hydrogen production methods (Normalized)[17].

Method		Energy efficiency	Exergy efficiency	Cost	SCC	GWP	AP
M1	Electrolysis	5.30	2.50	7.34	3.33	3.33	8.86
M2	Plasma arc decomposition	7.00	3.20	9.18	0.83	0.83	5.14
M3	Thermolysis	5.00	4.00	6.12	7.50	7.50	7.43
M4	Thermochemical water splitting	4.20	3.00	8.06	9.17	9.17	9.43
M5	Biomass conversion	5.60	4.50	8.10	6.67	6.67	2.00
M6	Biomass gasification	6.50	6.00	8.25	5.83	5.83	0.00
M7	Biomass reforming	3.90	2.80	7.93	6.25	6.25	0.86
M8	PV electrolysis	1.24	0.70	4.50	7.50	7.50	7.71
M9	Photocatalysis	0.20	0.10	5.19	9.58	9.58	9.71
M10	Photoelectrochemical method	0.70	0.15	0.00	9.58	9.58	9.71
M11	Dark fermentation	1.30	1.10	7.52	9.58	9.58	9.71
M12	High temperature electrolysis	2.90	2.60	5.54	7.92	7.92	8.57
M13	Hybrid thermochemical cycles	5.30	4.80	7.41	9.43	9.43	9.02
M14	Coal gasification	6.30	4.60	9.11	0.00	0.00	1.31
M15	Fossil fuel reforming	8.30	4.60	9.28	2.50	2.50	5.71
M16	Biophotolysis	1.40	1.30	7.27	7.50	7.50	9.71
M17	Photofermentation	1.50	1.40	7.61	9.58	9.58	9.71
M18	Artificial photosynthesis	0.90	0.80	7.54	9.58	9.58	9.71
M19	Photoelectrolysis	0.78	0.34	7.09	8.33	8.33	9.71
Ideal	(zero-emissions and cost, 100% efficiency)	10.00	10.00	10.00	10.00	10.00	10.00

SCC: social cost of carbon: the marginal external cost of a unit of CO₂ emission (\$/kg H₂ produced)

GWP: global warming potential (g CO₂ eq./kg H₂ produced)

AP: acidification potential (g SO₂ eq./kg H₂ produced)

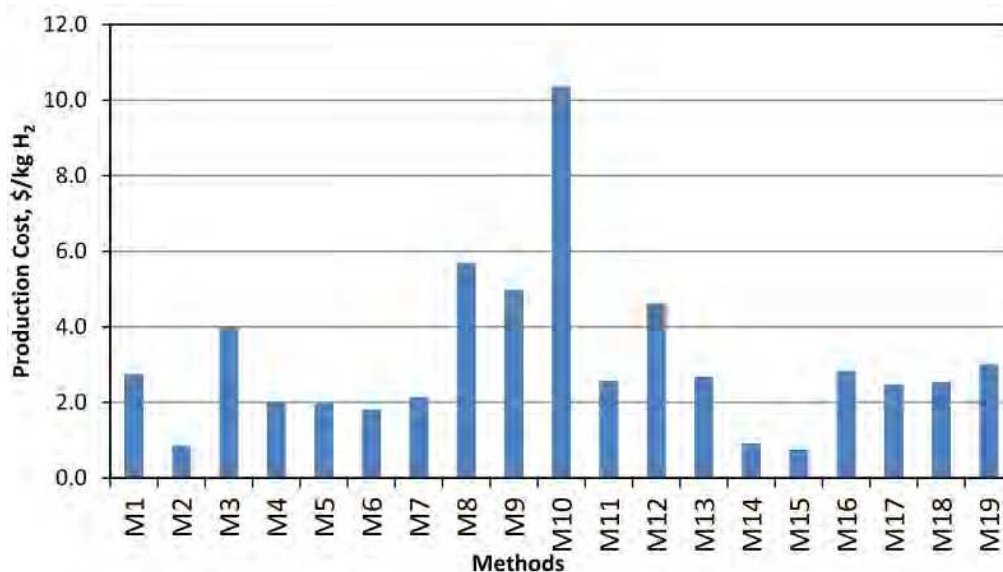
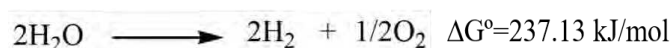


Figure 4. Production cost of selected hydrogen production methods (per kg of hydrogen)[17].

3. Water splitting:

The splitting of water into hydrogen and oxygen is a thermodynamically unfavorable chemical reaction that requires an energy input to overcome the energy barrier, as shown in scheme 2.



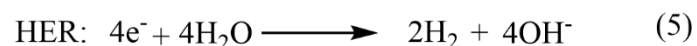
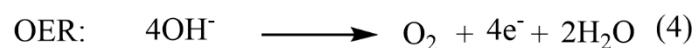
Scheme 2. water splitting reaction.

This thermodynamically up-hill process comprises two sluggish half reactions: the oxygen evolution reaction (OER) and the hydrogen evolution reaction (HER), described as equations (2) and (3), or (4) and (5) in acidic and basic conditions, respectively (scheme 3). Both of them are critical for the overall efficiency of water splitting, but OER is considered as the critical step because of the complex proton-coupled multi electron transfer process and dioxygen bond formation which limit its kinetics[18]. It is the slow kinetics of OER that limits the efficiency of hydrogen production from water splitting.

Acidic conditions



Basic conditions



Scheme 3. OER and HER in acidic and basic conditions

In practice neither HER nor OER can occur at the standard potential (*i.e.* at 0 V *vs.* RHE for HER and at 1.23 V *vs.* RHE for OER): a lower (for HER) or higher (for OER) potential value is needed to induce these reactions. The difference between this value and the thermodynamic potential value of the half-reaction considered is defined as the overpotential (η) [19, 20]. The corresponding additional energy, needed for the reaction to proceed at an appreciable rate (measured as the number of charges exchanged per unit area of electrode and per unit time, *i.e.* the current density), is defined as the activation energy. It compensates the activation energy barrier of the reaction and some other resistances in the device. The higher is the rate of water splitting targeted, the greater is the activation energy (hence η) required. Therefore, the role of an electrocatalyst is to increase the rate of the reaction at low overpotential value.

4. Water oxidation catalysts

During water splitting the slow four electrons transfer process of OER accounts for the large energy loss. Extensive efforts have thus been made recently in identifying molecular complexes

and solid materials that are highly active catalysts for OER, hereafter called WOC (for water oxidation catalyst) [21, 22].

An efficient WOC should: i) be conductive as it will speed up the electron transfers between the reactant, the catalyst and the electrode, therefore reducing the Ohmic drop in the water oxidation process; ii) allow the incoming reactant molecule to adsorb easily on its surface; iii) provide efficient electron transfer to form reaction intermediates and mediate the recombination between the reactive intermediate species into the final products; iv) allow the products to easily desorb from its surface to engage in a new reaction cycle. The majority of the homogeneous water oxidation catalysts are based on the second-and third-row transition metals Ru and Ir, the molecular complexes of which are robust and highly active for OER[21, 23].

In the case of solid catalysts, nanostructuring, which maximizes the surface area and the exposure of catalytically active sites, is an effective tool for lowering the OER overpotential. For example, nanoparticles (NPs) are known to have a high surface per mass ratio and a high density of catalytically active sites[24-26], and their active surface area can be controlled by controlling their size and morphology. For example, Esswein and co-workers have elucidated the dependence of the crystalline Co_3O_4 NPs electrocatalytic activity in OER on the size of these NPs: increasing the catalyst surface area by decreasing the size of the Co_3O_4 NPs by an order of magnitude decreased the overpotential required to achieve a specific current density (~ 50 mV)[27]. Also NPs are easier to characterize than electrodeposited thin films, electrodeposition being a technique broadly used at present to fabricate electrocatalysts. Third NPs scatter-light which also has a positive impact in case of solar driven processes, as shown in solar-fuel devices[28]. Given the above, developing electrocatalysts at the nanoscale is an attractive path to accelerate the water oxidation reaction.

To the best of our knowledge, Ir/Ru-based [18, 29, 30] nanostructured catalysts are considered as the best WOC in alkaline solutions as they can easily generate a current density of $10\text{mA}/\text{cm}^2$, the approximate current density expected for a 10% efficient solar-to-fuels conversion device under 1 sun illumination, at an overpotential $\sim 200\text{-}350$ mV. However, the high cost and scarcity of these noble metals severely hinder their large scale application for sustainable energy technologies. In addition, their stability in either acidic or basic conditions is not optimum. For example, the highly active RuO_2 oxidizes into soluble RuO_4 species under the anodic potential applied for OER, leading to a poor stability in acidic as well as in alkaline conditions. IrO_2 also

oxidizes, into IrO_3 , under anodic bias leading to the slow dissolution of IrO_2 under working conditions[31, 32]. Thus considering the high cost and low stability of those WOC, it is mandatory to develop highly efficient, and robust alternative WOC from non-noble metals which are low-cost. In this context, metal oxides [22, 33], hydroxides [34, 35], and oxyhydroxides [36-38] of earth-abundant elements are the most promising candidates. Therefore, various WOC based on low-cost and earth-abundant transition metals (mainly Mn, Fe, Co, Ni, Cu...) have been studied for visible light-driven OER in the recent years[33, 39]. Among them, Fe is the 4th most common element in the earth's crust, and the less toxic [40]. Furthermore, this compound has been reported to be an active and stable electrocatalyst for OER in alkaline solution, providing promising alternatives to the Ir/Ru-based catalysts[41, 42]. We will discuss more on the current development of Fe oxide-based OER catalysts in the next chapter.

4.1 Parameters used to evaluate water oxidation catalysts

The catalytic activity of a given OER electrocatalyst is often discussed based on some key parameters such as overpotential, Tafel slope, stability, turnover number (TON) and turnover frequency (TOF). These parameters are not only crucial for comparing the catalytic performance of various catalysts but they also offer insightful information regarding the mechanism of the electrochemical reaction. With these considerations, we provide hereafter a brief introduction to these key parameters.

4.1.1 Overpotential (η , η_{10})

It is worth noting that the catalytic current recorded during OER is often normalized with respect to the geometric surface area of the electrode. Besides, the catalytic current can also be normalized with respect to other parameters like the mass of catalyst, its specific surface area, or the electrochemically active surface area.

In many cases, two different values of overpotential are reported namely the onset overpotential η that marks the beginning of the OER current and the overpotential η_{10} corresponding to the overpotential value at which the current density reaches 10 mA/cm^2 (which relates to the current density of a solar water splitting device operating at 12.3% efficiency). These values are determined from linear sweep voltammetry (LSV) curves (see a typical LSV curve on Figure 5) which represent the relation between the generated current density (mA/cm^2) (in Y axis) and

the potential applied (in X axis). For example, in Figure 5 the onset overpotential η and overpotential at 10 mA/cm^2 η_{10} of sample $\text{Ni}_2\text{Fe}_1\text{-O}$ (black curve) are $\eta = 190 \text{ mV}$ and $\eta_{10} = 240 \text{ mV}$, respectively[43].

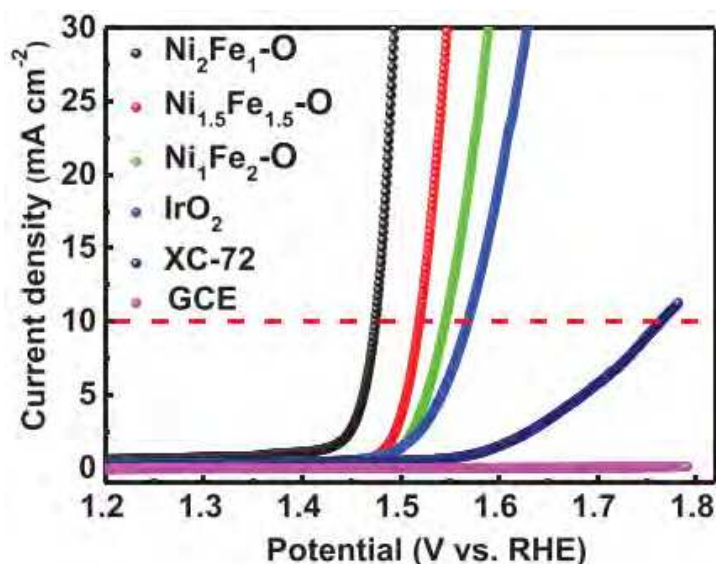


Figure 5. LSV curves of $\text{Ni}_2\text{Fe}_1\text{-O}$, $\text{Ni}_{1.5}\text{Fe}_{1.5}\text{-O}$, $\text{Ni}_1\text{Fe}_2\text{-O}$, IrO_2 , XC-72, and glassy carbon electrode (GCE) in 1M KOH solution at scan rate 5 mV/s [43].

Significant efforts have been performed to achieve low η values with earth-abundant WOC in alkaline solution. For example, in 1 M KOH, to achieve 10 mA/cm^2 , NiFeS (65 mV)[44], NiFeS-Fe (101.6 mV)[44], Ni(OH)₂ nano sheets (NS) on Nickel foam (NF) (170 mV)[45], Ni-P NS (190 mV)[46], ...,etc exhibit remarkably low η values. Especially, NiFeS which consists in binary Ni-Fe sulfides with crystalline NiS and Ni₃S₂ phases displays a low η_{10} value of 65 mV in 1 M KOH, this value is even 315 mV lower than the one recorded for IrO₂ in 1M NaOH ($\eta_{10} = 380 \text{ mV}$) [47]. However, after 1000 CV cycles, the NiFeS activity decays which clearly indicates the limited durability of this material. Hollow $\alpha\text{-Fe}_2\text{O}_3$ nanorod/CNT composite is another good example. This composite reached 10 mA/cm^2 at $\eta_{10} = 383 \text{ mV}$ but displayed a poor durability as it lost 90 % of its catalytic activity after 20 h[25]. So the study of the stability of the electrocatalysts is also of prime importance.

4.1.2 Electrocatalytic stability

The stability of a metal oxide catalyst is commonly studied by chronoamperometric (CA) or chronopotentiometric (CP) experiments during a few hours. The variation (or not) of the catalytic activity during such experiments will be used as an indication of the stability of the catalyst. For example, the electrocatalytic stability of a catalyst under catalytic conditions can

be determined using controlled-current electrolysis. In practice, the catalyst is held at a constant current density of 10 mA/cm² for a given time meanwhile the operating potential is measured as a function of time. If the $\eta_{t=0}$ and $\eta_{t=x \text{ h}}$ values are identical, we can conclude that the catalyst is stable under working conditions for at least x h. McCrory and co-workers used a protocol based on electrolysis at 10 mA/cm² during 2 h. to evaluated the short-term stability of OER catalysts in alkaline solution as shown in Table 2[48].

Table 2. Benchmarking parameters for each catalyst investigated in 1M NaOH [48]

catalyst	ECSA/cm ²	RF	$\eta_{t=0}/V$	$\eta_{t=2h}/V$	$j_{0.7}/\text{mA cm}^{-2}$	$j_{0.35}/\text{mA cm}^{-2}$	ϵ	reported $\eta_{t=0}/V$
CoO _x (a)	1.9 ± 0.6	10 ± 3	0.39 ± 0.04	0.42 ± 0.04	0.9 ± 0.3	0.09 ± 0.04	0.94 ± 0.08	0.38 ^a
CoO _x (b) ("CoPi")	5.1 ± 1.7	26 ± 9	0.42 ± 0.02	0.44 ± 0.02	0.4 ± 0.1	0.015 ± 0.006	1.00 ± 0.10	0.43 ^b 0.41 ^c
CoFeO _x	3.6 ± 0.9	19 ± 5	0.37 ± 0.02	0.43 ± 0.03	7 ± 3	0.4 ± 0.2	0.98 ± 0.08	0.34 ^a 0.32 ^d
IrO _x	21 ± 10	105 ± 53	0.32 ± 0.04	1.05 ± 0.20	42 ± 13	0.4 ± 0.2	0.92 ± 0.07	0.30 ^e
NiO _x	1.8 ± 0.5	9 ± 3	0.42 ± 0.02	0.41 ± 0.05	1.1 ± 0.4	0.12 ± 0.05	0.93 ± 0.08	0.42 ^f
NiCeO _x	3.3 ± 1.2	17 ± 6	0.43 ± 0.03	0.44 ± 0.02	1.6 ± 0.7	0.11 ± 0.07	0.90 ± 0.08	0.28 ^f
NiCoO _x	5.2 ± 2.1	27 ± 11	0.38 ± 0.03	0.36 ± 0.01	6 ± 3	0.2 ± 0.1	0.92 ± 0.08	0.40 ^g
NiCuO _x	1.8 ± 0.3	9 ± 2	0.41 ± 0.01	0.44 ± 0.03	1.4 ± 0.6	0.15 ± 0.07	0.95 ± 0.13	0.42 ^h
NiFeO _x	1.1 ± 0.5	6 ± 3	0.35 ± 0.01	0.38 ± 0.02	15 ± 6	3 ± 2	1.00 ± 0.04	0.29 ^a
NiLaO _x	1.2 ± 0.3	6 ± 1	0.41 ± 0.03	0.46 ± 0.05	2.5 ± 0.9	0.4 ± 0.2	0.96 ± 0.09	0.36 ^f
GC background	1.9 ± 0.9	10 ± 5	1.19 ± 0.03	1.29 ± 0.02	<0.05	<0.005	0.76 ± 0.07	–

The lack in stability and durability of WOCs increase the operation and maintenance costs of the water electrolysis [49]. Recently, significant efforts have been performed to achieve remarkably high long term stability on earth-abundant WOCs in alkaline medium. For example, Ni-P nanosheets are still stable after 180 h at η_{10} in 1 M KOH[50].

4.1.3. Tafel slope

The Tafel slope is an important kinetics parameter which can be derived from Tafel plots. Tafel plots drawn using the electrochemical polarization method give valuable insight into the mechanism of OER. The Tafel equation is described in eq. 6.

$$\eta = a + b \times \log j$$

Eq. 6. Tafel equation

Following this eq., when the overpotential (η) is plotted against the logarithm of the current density ($\log [j \text{ (mA/cm}^2\text{)}]$) a straight line with slope b (the so-called Tafel slope) and intercept a can be obtained. Furthermore, the value of this intercept a can be used to determine the exchange current density i_0 and thus standard heterogeneous rate constant. However, due to the extreme irreversibility of OER, the steady state polarization data is mostly used to understand

the rate determining step[51]. Figure 6b shows the Tafel plots of $\text{Ni}_2\text{Fe}_1\text{-O}$, $\text{Ni}_{1.5}\text{Fe}_{1.5}\text{-O}$, $\text{Ni}_1\text{Fe}_2\text{-O}$, IrO_2 , XC-72, GCE samples deduced from the corresponding LSV curves (Figure 6a).

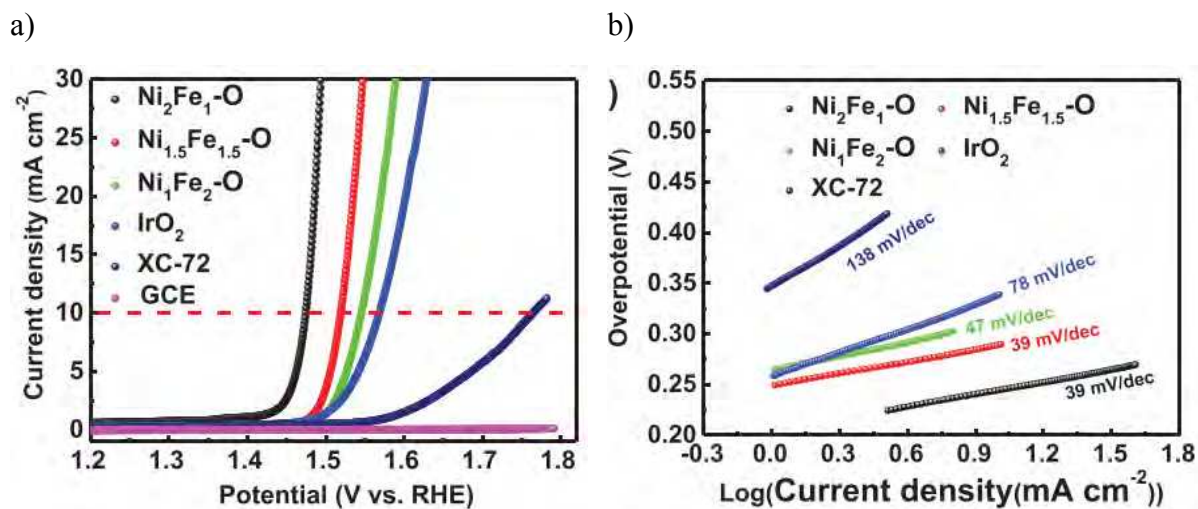
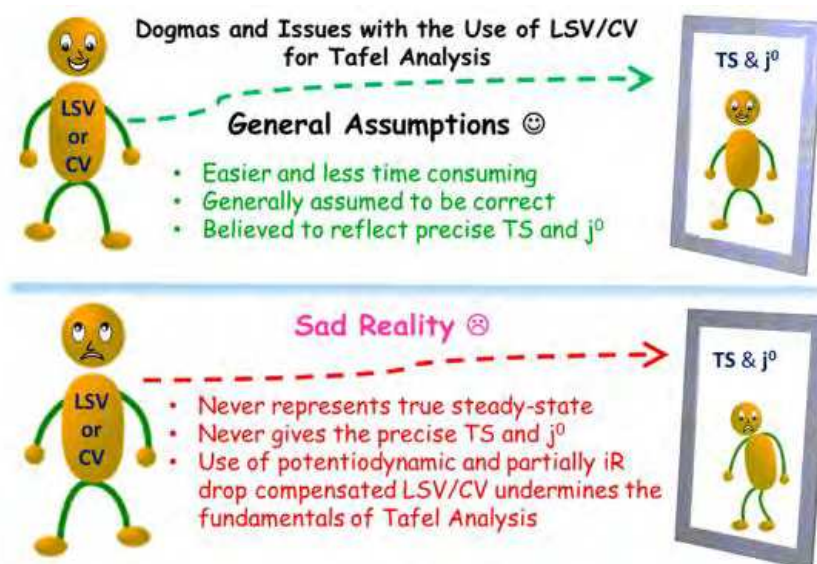


Figure 6. a) LSV curves and b) corresponding Tafel plots of $\text{Ni}_2\text{Fe}_1\text{-O}$, $\text{Ni}_{1.5}\text{Fe}_{1.5}\text{-O}$, $\text{Ni}_1\text{Fe}_2\text{-O}$, IrO_2 , XC-72, and glassy carbon electrode (GCE) in 1M KOH solution at scan rate 5 mV/s[43].

However, as pointed out recently by Menezes and coworkers, the steady state is seldom reached when recording potentiodynamic polarization curves such as CV and LSV, even if they are recorded at very low scan rate (Scheme 4). It is thus dangerous to draw conclusion on mechanistic aspects of the reaction from the Tafel plots issued from such measurements. Especially if iR drop uncompensated potentiodynamic polarization curves are used (as the fundamental basic in Tafel analysis relies on data acquired in a steady state regime and absence of iR drop[52]).



Scheme 4. Graphical sketch advocating against the use of dynamic LSV/CV responses for deriving Tafel plots. TS and j^0 denote Tafel slope and exchange current density, respectively[52].

4.1.4. TOF and TON

The TOF (turn over frequency) of a heterogeneous catalyst can be defined as the mole of product obtained per catalytically active site and per unit time. The TOF thus represents the intrinsic catalytic activity of the catalyst. In practice, as the number of catalytically active sites is seldom known, the TOF is calculated from the number of surface atoms, or the total number of atoms in the nanocatalyst when its size and morphology are not well determined (as it is not possible to calculate the percentage of atoms that occupies the surface in this case).

The TON (turn over number) of a catalyst describes how many cycles it is able to perform before becoming inactive.

Another parameter that can be used to describe and compare one catalyst to the others is the Electrochemically Active Surface Area (ECSA). This value can be estimated from the electrochemical double-layer capacitance of the catalytic surface[53], or Faradic efficiency.

5. Solar driven water splitting

In order to split water into hydrogen and oxygen using solar energy different strategies have been applied[54-57]. Three of which are shown in Figure 7 [57].

i) Photovoltaics (PV) – electrolysis combination: it could be the easiest method as it is simple to wire a p-n junction PV device (or multiple PEV cells to provide higher voltage) with a commercial electrolyzer. This kind of device is the most mature technologically but the high-cost of this technique for broad commercialization is a critical issue (Figure 7, left).

ii) Photocatalytic colloidal solutions: here the light-harvesting materials are NPs dispersed in solution where both the OER and HER occur, leading to a possible explosive H_2 and O_2 mixture (Figure 7, right).

iii) Photoelectrochemical devices (PEC): wireless, thus avoiding Ohmic drop and where oxygen and hydrogen are generated in different compartments, from OER and HER respectively. PECs represent a compromise between technological maturity, and cost, but rely on the development of individual photoanode and photocathode. In PEC, solar energy is collected by light-harvesting components that enable light-induced charge separation after excitation, water serves as an electron and proton donor at the photoanode and protons are converted into hydrogen at the cathode (or photocathode) (Figure 7, middle).

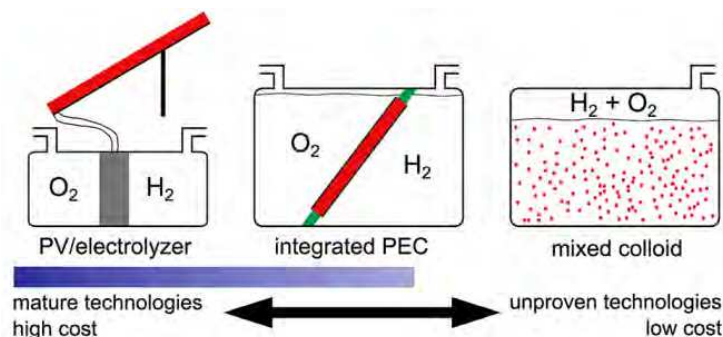


Figure 7. Schematic diagrams of three device architectures available for solar-driven water splitting: (left) a photovoltaic (PV) cell wired to an electrolyte; (center) an integrated photoelectrochemical cell (PEC) where the water splitting reaction occurs at the surface of a semiconductor panel in solution; (right) a suspended colloid (photocatalytic) system wherein water splitting reactions occur at the surface of semiconductor particles immersed in solution. The order according to their relative technological maturity and projected costs to manufacture[57].

In the development of PEC devices, the conventional liquid-junction PEC was intensively studied for the last four decades. Basically, in this design the single semiconductor (SC) carry out light absorption, charger separation and catalysis (Figure 8, left). Because the SC here plays both the roles of light absorber and catalyst for water splitting therefore, the ideal SC should

have a balanced in number of defects. Indeed, a good light absorber is a SC that forms electron/hole pairs efficiently and thus present few defects. Meanwhile, as a good catalyst it operates four-electron/four-proton exchange, break and forms bonds and therefore, often has many defects. Finding a SC that can play both roles (a good catalyst and a good light absorber) in the same time is thus difficult so the present liquid-junction PEC displayed very low efficiency for solar-driven water splitting[56].

In contrary to the liquid-junction PEC, PEC with wireless buried junction PEC configuration comprises a multi-jn SC coated with a HER catalyst on one side and an OER catalyst on the other side (Figure 8, right). In this case, the SC and catalyst are different materials that can be optimized independently and consequently the efficiency for water splitting from buried junction PEC is rapidly increasing[58, 59]. One typical example for the buried junction PEC device is the artificial leaf developed by Daniel G. Nocera's group as shown in Figure 9[60]. This artificial leaf is a wireless buried junction comprising a Si junction coated by NiMoZn and Co-OEC as HER and OER catalysts, respectively.

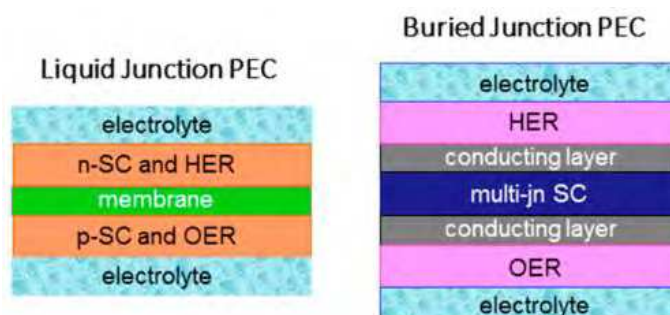


Figure 8. Simplified liquid-junction PEC (left) and buried junction PEC (right)[61].

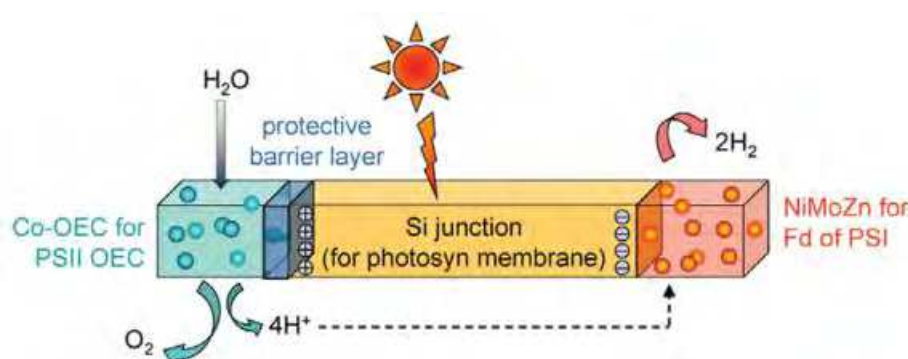


Figure 9. Construction of an artificial leaf[60].

5.1 Photoelectrochemical cell

As described above, water splitting is a thermodynamically uphill reaction, requiring at least a potential of 1.23 V at pH 0 to proceed (Scheme 2). The energy required (1.23 eV) can be provided by any electromagnetic radiation with a wavelength shorter than $\sim 1000\text{nm}$. The entire visible spectrum and near-infrared, which covers $\sim 80\%$ solar irradiance, can thus be used for this purpose [62]. The water splitting process can be accomplished in a photoelectrochemical cell comprising a photoanode where the OER takes place with solar energy input, and a photocathode (or a simple cathode) where the HER occurs. The photoanode and photocathode are separated by a proton exchange membrane (Figure 10) [21].

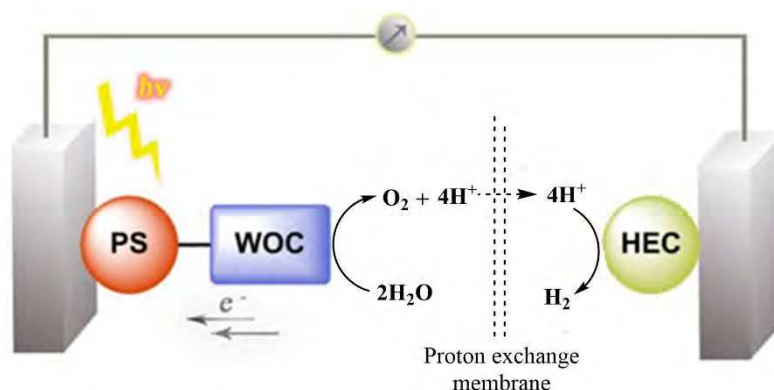


Figure 10. Schematic picture of a molecular assembly for overall H_2O splitting consisting of a photosensitizer (PS), a water oxidation catalyst (WOC), and a hydrogen evolving catalyst (HEC), for the production of solar fuels, adapt from ref.[21].

The first example of PEC was reported by Fujishima and Honda in 1972[63]. It involved TiO_2 as a photoanode (band gap: 3.2 eV), which limited the range of radiations that could induce charge separation to the UV part of the solar spectrum. Since then, the construction of photoelectrochemical cells to perform light-driven water splitting has been extensively explored in order to enable the reaction to be driven by visible light[64].

Let's focus on the OER compartment. A simple PEC description is shown in Figure 10[21]. Basically it has three components: a photosensitizer (PS) for light absorption, a water oxidation catalyst (WOC) which oxidized water to oxygen and a reduction catalyst for proton reduction. For the light absorbing component: it can be n-type semiconductors like TiO_2 [63], BiVO_4 [65-68], $\alpha\text{-Fe}_2\text{O}_3$ [69, 70], WO_3 [71-74], or molecular dyes like ruthenium trisbipyridine complexes[75-77], perylene[78-81], polyheptazine[82-84], metal-free porphyrins[85] and π -

conjugated naphthalene benzimidazole polymers[86]. Molecular dyes present the advantage of efficiently absorbing light in the visible region, contrarily to semiconductors. When the light-absorbing component is a molecular chromophore, it can be simply deposited on a transparent semiconductor electrode such as Fluorine doped tin oxide (FTO) or Indium tin oxide (ITO) or coordinated to the surface of a semiconductor such as TiO₂, which is itself deposited on the photoanode. The initial step in this system involves light absorption by the PS to generate a long - lived charge – separated state by transferring an electron to the conduction band (CB) of the semiconductor. Then the oxidized PS receives an electron from the covalently bound WOC or from the functionalized semiconductor surface to come back to ground state PS. After four successive electron transfers, the highly oxidized WOC is reduced by two water molecules releasing oxygen, and protons in the process. The protons generated at the photoanode will then go through the proton exchange membrane to the photocathode, combine with electrons and produce hydrogen.

The performance of these systems strongly depends on the light absorption properties and electron transfer events between the semiconductor catalyst and the light absorber[87]. Under operating conditions, light absorption leading to the charge separation occurs both in the molecular photosensitizer and in the semiconductor catalyst. However, the charge recombination processes are much faster (time scale for back electron transfer typically in microseconds to milliseconds) than the multi electron processes required by the water splitting reaction. More precisely, it has been evidenced that the insufficient rate of electron transfers from the WOCs to the PS together with the undesired back-electron transfer phenomenon from the PS to the WOCs are the main reasons for the low efficiency of the hybrid systems in light-driven water splitting[88, 89]. One of the promising ways to solve this problem is to link the PS to the WOC by a covalent grafting. Covalent grafting between these two components results in faster charge transfers, therefore improving the catalytic activity of these systems. In this regard, several research groups have investigated the photocatalytic activity of hybrid PS-WOCs systems for light-driven water splitting. We will describe in more details the development of hybrid PS-WOCs systems in chapter III.

With this idea in mind, our work has focused first on the development of new Fe-based nanomaterials and on the evaluation of their efficiency in OER, as a function of their surface

Chapter I - Introduction

state. The main results will be reported in chapter II. In the third chapter, we describe our approach to solve the problem of charge transfer between PS and WOCs by designing a new hybrid system for light-driven water splitting. It consists in the covalent grafting of a Ru(II) tris(1,10-phenanthroline) derivative with a pendant phosphonic acid functional group, at the surface of Fe oxide nanoparticles used as WOC. Finally, we will report the results obtained on nanostructured NiFe nanocatalysts and show that they represent a more promising system in chapter IV.

6. References

1. Lee, R., *The Outlook for Population Growth*. Science, 2011. **333**(6042): p. 569-573.
2. IEA. *Key World Energy Statistics 2020*. 2020 [cited 2021 25th March]; Available from: <https://www.iea.org/reports/key-world-energy-statistics-2020>
3. Lewis, N.S. and D.G. Nocera, *Powering the planet: Chemical challenges in solar energy utilization*. Proceedings of the National Academy of Sciences, 2006. **103**(43): p. 15729-15735.
4. Lindsey, R. *If carbon dioxide hits a new high every year, why isn't every year hotter than the last?* 2020 [cited 2021 25th March]; Available from: <https://www.climate.gov/news-features/climate-qa/if-carbon-dioxide-hits-new-high-every-year-why-isn%E2%80%99t-every-year-hotter-last>.
5. Roser, H.R.a.M. *CO₂ emissions*. 2019 [cited 2021 25th March]; Available from: <https://ourworldindata.org/co2-emissions>.
6. Saint-Geniès, G.d.L. *The IPCC Report Will Have Profound Effects on Climate Governance*. 2018 [cited 2021 25th March]; Available from: https://www.cigionline.org/articles/ipcc-report-will-have-profound-effects-climate-governance?utm_source=google_ads&utm_medium=grant&gclid=CjwKCAjwxuuCBhATEiwAIIIz0X5UIB_R7STtPEIHx-F8HLP2pX6QFzfuzu64pK40GKnjVKeg5qujyx0CcIEQAvD_BwE.
7. Gray, H.B., *Powering the planet with solar fuel*. Nature Chemistry, 2009. **1**(1): p. 7-7.
8. Salameh, Z., *Chapter 1 - Factors Promoting Renewable Energy Applications*, in *Renewable Energy System Design*, Z. Salameh, Editor. 2014, Academic Press: Boston. p. 1-32.
9. Blankenship, R.E., et al., *Comparing Photosynthetic and Photovoltaic Efficiencies and Recognizing the Potential for Improvement*. Science, 2011. **332**(6031): p. 805-809.
10. Lewis, N.S., Crabtree, G, Nozik, A J, Wasielewski, M R, Alivisatos, P, Kung, H, Tsao, J, Chandler, E, Walukiewicz, W, Spitler, M, Ellingson, R, Overend, R, Mazer, J, Gress, M, Horwitz, J, Ashton, C, Herndon, B, Shapard, L, and Nault, R M. *Basic Research Needs for Solar Energy Utilization. Report of the Basic Energy Sciences Workshop on Solar Energy Utilization*. 2005; Available from: <https://www.osti.gov/biblio/899136-basic-research-needs-solar-energy-utilization-report-basic-energy-sciences-workshop-solar-energy-utilization-april>.
11. Schlappbach, L. and A. Züttel, *Hydrogen-storage materials for mobile applications*. Nature, 2001. **414**(6861): p. 353-358.
12. Grimes, C.A., O.K. Varghese, and S. Ranjan, *Hydrogen Generation by Water Splitting*, in *Light, Water, Hydrogen: The Solar Generation of Hydrogen by Water Photoelectrolysis*, C.A. Grimes, O.K. Varghese, and S. Ranjan, Editors. 2008, Springer US: Boston, MA. p. 35-113.
13. Acar, C. and I. Dincer, *3.1 Hydrogen Production*, in *Comprehensive Energy Systems*, I. Dincer, Editor. 2018, Elsevier: Oxford. p. 1-40.
14. IEA. *The Future of Hydrogen*. 2019 [cited 2021 25th March]; Available from: <https://www.iea.org/reports/the-future-of-hydrogen>
15. Jacobson, M.Z., W.G. Colella, and D.M. Golden, *Cleaning the Air and Improving Health with Hydrogen Fuel-Cell Vehicles*. Science, 2005. **308**(5730): p. 1901-1905.
16. Fang, R., et al., *Efficient and selective hydrogenation of biomass-derived furfural to cyclopentanone using Ru catalysts*. Green Chemistry, 2015. **17**(8): p. 4183-4188.

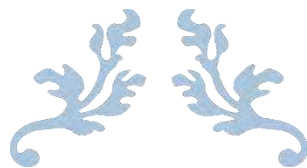
17. Dincer, I. and C. Acar, *Review and evaluation of hydrogen production methods for better sustainability*. International Journal of Hydrogen Energy, 2015. **40**(34): p. 11094-11111.
18. Chen, Z., et al., *Iridium-based nanomaterials for electrochemical water splitting*. Nano Energy, 2020. **78**: p. 105270.
19. Jiao, Y., et al., *Design of electrocatalysts for oxygen- and hydrogen-involving energy conversion reactions*. Chemical Society Reviews, 2015. **44**(8): p. 2060-2086.
20. Anantharaj, S., et al., *Recent Trends and Perspectives in Electrochemical Water Splitting with an Emphasis on Sulfide, Selenide, and Phosphide Catalysts of Fe, Co, and Ni: A Review*. ACS Catalysis, 2016. **6**(12): p. 8069-8097.
21. Kärkäs, M.D., et al., *Artificial Photosynthesis: Molecular Systems for Catalytic Water Oxidation*. Chemical Reviews, 2014. **114**(24): p. 11863-12001.
22. Song, F., et al., *Transition Metal Oxides as Electrocatalysts for the Oxygen Evolution Reaction in Alkaline Solutions: An Application-Inspired Renaissance*. Journal of the American Chemical Society, 2018. **140**(25): p. 7748-7759.
23. Matheu, R., et al., *The development of molecular water oxidation catalysts*. Nature Reviews Chemistry, 2019. **3**(5): p. 331-341.
24. Zhang, Y.-X., et al., *Diethylenetriamine (DETA)-assisted anchoring of Co₃O₄ nanorods on carbon nanotubes as efficient electrocatalysts for the oxygen evolution reaction*. Journal of Materials Chemistry A, 2015. **3**(4): p. 1761-1768.
25. Bandal, H.A., et al., *Fe₂O₃ hollow nanorods/CNT composites as an efficient electrocatalyst for oxygen evolution reaction*. Electrochimica Acta, 2016. **222**: p. 1316-1325.
26. Liu, Q., A.M. Asiri, and X. Sun, *Hematite nanorods array on carbon cloth as an efficient 3D oxygen evolution anode*. Electrochemistry Communications, 2014. **49**: p. 21-24.
27. Esswein, A.J., et al., *Size-Dependent Activity of Co₃O₄ Nanoparticle Anodes for Alkaline Water Electrolysis*. The Journal of Physical Chemistry C, 2009. **113**(33): p. 15068-15072.
28. McKone, J. and N. Lewis, *CHAPTER 3 Structured Materials for Photoelectrochemical Water Splitting*, in *Photoelectrochemical Water Splitting: Materials, Processes and Architectures*. 2013, The Royal Society of Chemistry. p. 52-82.
29. Yu, J., et al., *Recent Advances and Prospective in Ruthenium-Based Materials for Electrochemical Water Splitting*. ACS Catalysis, 2019. **9**(11): p. 9973-10011.
30. McCrory, C.C.L., et al., *Benchmarking Hydrogen Evolving Reaction and Oxygen Evolving Reaction Electrocatalysts for Solar Water Splitting Devices*. Journal of the American Chemical Society, 2015. **137**(13): p. 4347-4357.
31. Wohlfahrt-Mehrens, M. and J. Heitbaum, *Oxygen evolution on Ru and RuO₂ electrodes studied using isotope labelling and on-line mass spectrometry*. Journal of Electroanalytical Chemistry and Interfacial Electrochemistry, 1987. **237**(2): p. 251-260.
32. Kötz, R., et al., *In-situ identification of RuO₄ as the corrosion product during oxygen evolution on ruthenium in acid media*. Journal of Electroanalytical Chemistry and Interfacial Electrochemistry, 1984. **172**(1): p. 211-219.
33. Miller, A.M. *Earth-Abundant Heterogeneous Water Oxidation Catalysts*. Chem. Rev, 2016. **116**: p. 14120-14136.
34. Gong, M., et al., *An Advanced Ni-Fe Layered Double Hydroxide Electrocatalyst for Water Oxidation*. Journal of the American Chemical Society, 2013. **135**(23): p. 8452-8455.
35. Lu, Z., et al., *Three-dimensional NiFe layered double hydroxide film for high-efficiency oxygen evolution reaction*. Chemical Communications, 2014. **50**(49): p. 6479-6482.

36. Lei, L., et al., *Demystifying the active roles of NiFe-based oxides/(oxy)hydroxides for electrochemical water splitting under alkaline conditions*. Coordination Chemistry Reviews, 2020. **408**: p. 213177.
37. Burke, M.S., et al., *Oxygen Evolution Reaction Electrocatalysis on Transition Metal Oxides and (Oxy)hydroxides: Activity Trends and Design Principles*. Chemistry of Materials, 2015. **27**(22): p. 7549-7558.
38. Dionigi, F. and P. Strasser, *NiFe-Based (Oxy)hydroxide Catalysts for Oxygen Evolution Reaction in Non-Acidic Electrolytes*. Advanced Energy Materials, 2016. **6**(23): p. 1600621.
39. Kärkäs, M.D. and B. Åkermark, *Water oxidation using earth-abundant transition metal catalysts: opportunities and challenges*. Dalton Transactions, 2016. **45**(37): p. 14421-14461.
40. Yaroshevsky, A.A., *Abundances of chemical elements in the Earth's crust*. Geochemistry International, 2006. **44**(1): p. 48-55.
41. Bora, D.K., A. Braun, and E.C. Constable, "In rust we trust". *Hematite – the prospective inorganic backbone for artificial photosynthesis*. Energy & Environmental Science, 2013. **6**(2): p. 407-425.
42. Feng, C., et al., *Fe-Based Electrocatalysts for Oxygen Evolution Reaction: Progress and Perspectives*. ACS Catalysis, 2020. **10**(7): p. 4019-4047.
43. Dong, C., et al., *Eutectic-Derived Mesoporous Ni-Fe-O Nanowire Network Catalyzing Oxygen Evolution and Overall Water Splitting*. Advanced Energy Materials, 2018. **8**(5): p. 1701347.
44. Dong, B., et al., *Two-step synthesis of binary Ni-Fe sulfides supported on nickel foam as highly efficient electrocatalysts for the oxygen evolution reaction*. Journal of Materials Chemistry A, 2016. **4**(35): p. 13499-13508.
45. Rao, Y., et al., *Hydrotalcite-like Ni(OH)₂ Nanosheets in Situ Grown on Nickel Foam for Overall Water Splitting*. ACS Applied Materials & Interfaces, 2016. **8**(49): p. 33601-33607.
46. Wang, X., et al., *Bifunctional Nickel Phosphide Nanocatalysts Supported on Carbon Fiber Paper for Highly Efficient and Stable Overall Water Splitting*. Advanced Functional Materials, 2016. **26**(23): p. 4067-4077.
47. Jung, S., et al., *Benchmarking nanoparticulate metal oxide electrocatalysts for the alkaline water oxidation reaction*. Journal of Materials Chemistry A, 2016. **4**(8): p. 3068-3076.
48. McCrory, C.C.L., et al., *Benchmarking Heterogeneous Electrocatalysts for the Oxygen Evolution Reaction*. Journal of the American Chemical Society, 2013. **135**(45): p. 16977-16987.
49. Zeng, K. and D. Zhang, *Recent progress in alkaline water electrolysis for hydrogen production and applications*. Progress in Energy and Combustion Science, 2010. **36**(3): p. 307-326.
50. Ping, J., et al., *Self-Assembly of Single-Layer CoAl-Layered Double Hydroxide Nanosheets on 3D Graphene Network Used as Highly Efficient Electrocatalyst for Oxygen Evolution Reaction*. Advanced Materials, 2016. **28**(35): p. 7640-7645.
51. Doyle, R.L., et al., *Redox and electrochemical water splitting catalytic properties of hydrated metal oxide modified electrodes*. Physical Chemistry Chemical Physics, 2013. **15**(33): p. 13737-13783.
52. Anantharaj, S., et al., *The Pitfalls of Using Potentiodynamic Polarization Curves for Tafel Analysis in Electrocatalytic Water Splitting*. ACS Energy Letters, 2021. **6**(4): p. 1607-1611.

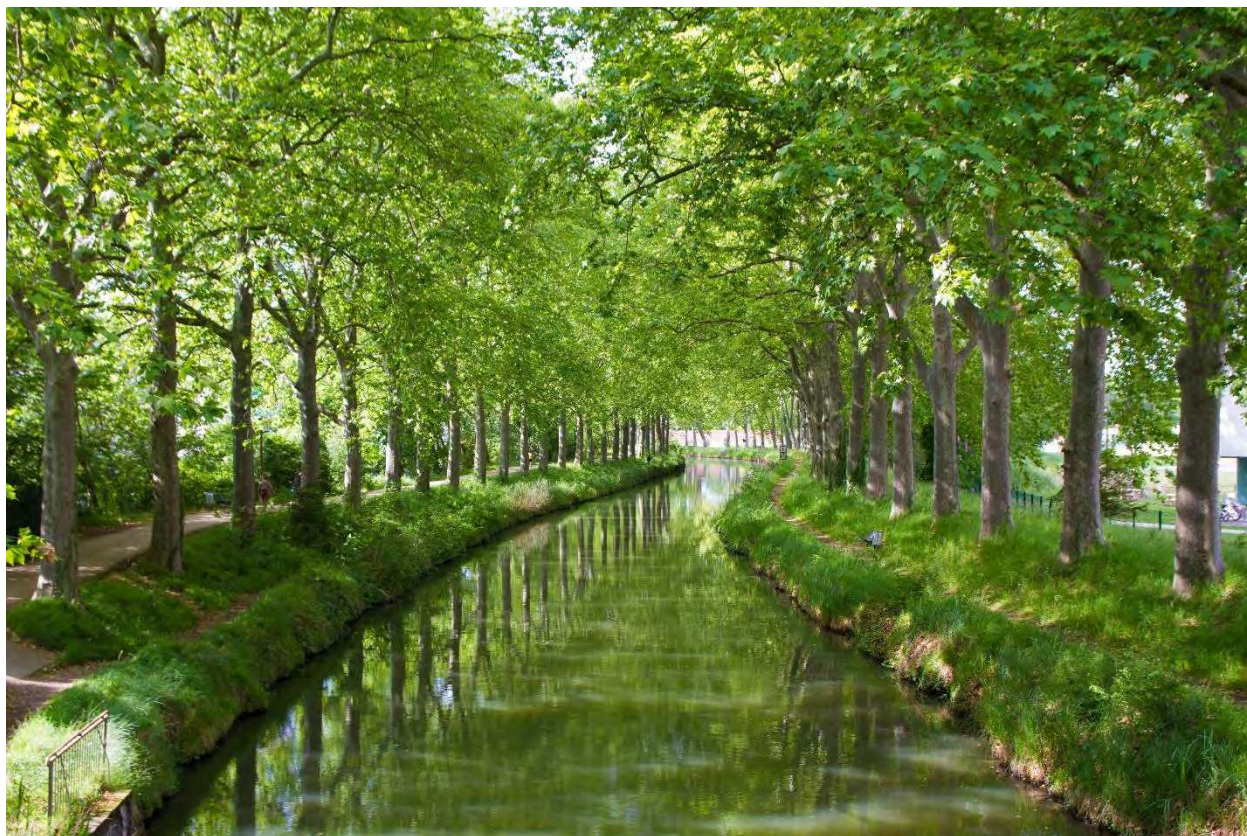
53. Trasatti, S. and O.A. Petrii, *Real surface area measurements in electrochemistry*. Pure and Applied Chemistry, 1991. **63**(5): p. 711-734.
54. Nozik, A.J., *Photoelectrochemistry: Applications to Solar Energy Conversion*. Annual Review of Physical Chemistry, 1978. **29**(1): p. 189-222.
55. Bard, A.J. and M.A. Fox, *Artificial Photosynthesis: Solar Splitting of Water to Hydrogen and Oxygen*. Accounts of Chemical Research, 1995. **28**(3): p. 141-145.
56. Walter, M.G., et al., *Solar Water Splitting Cells*. Chemical Reviews, 2010. **110**(11): p. 6446-6473.
57. McKone, J.R., N.S. Lewis, and H.B. Gray, *Will Solar-Driven Water-Splitting Devices See the Light of Day?* Chemistry of Materials, 2014. **26**(1): p. 407-414.
58. Cheng, W.-H., et al., *Monolithic Photoelectrochemical Device for Direct Water Splitting with 19% Efficiency*. ACS Energy Letters, 2018. **3**(8): p. 1795-1800.
59. Kim, J.H., et al., *Toward practical solar hydrogen production – an artificial photosynthetic leaf-to-farm challenge*. Chemical Society Reviews, 2019. **48**(7): p. 1908-1971.
60. Nocera, D.G., *The Artificial Leaf*. Accounts of Chemical Research, 2012. **45**(5): p. 767-776.
61. Nocera, D.G., *Solar Fuels and Solar Chemicals Industry*. Accounts of Chemical Research, 2017. **50**(3): p. 616-619.
62. McDaniel, N.D. and S. Bernhard, *Solar fuels: thermodynamics, candidates, tactics, and figures of merit*. Dalton Transactions, 2010. **39**(42): p. 10021-10030.
63. Fujishima, A. and K. Honda, *Electrochemical Photolysis of Water at a Semiconductor Electrode*. Nature, 1972. **238**(5358): p. 37-38.
64. Kirner, J.T. and R.G. Finke, *Water-oxidation photoanodes using organic light-harvesting materials: a review*. Journal of Materials Chemistry A, 2017. **5**(37): p. 19560-19592.
65. Kim, T.W., et al., *Simultaneous enhancements in photon absorption and charge transport of bismuth vanadate photoanodes for solar water splitting*. Nature Communications, 2015. **6**(1): p. 8769.
66. Tayebi, M. and B.-K. Lee, *Recent advances in BiVO₄ semiconductor materials for hydrogen production using photoelectrochemical water splitting*. Renewable and Sustainable Energy Reviews, 2019. **111**: p. 332-343.
67. Kim, T.W. and K.-S. Choi, *Nanoporous BiVO₄ Photoanodes with Dual-Layer Oxygen Evolution Catalysts for Solar Water Splitting*. Science, 2014. **343**(6174): p. 990-994.
68. Seabold, J.A. and K.-S. Choi, *Efficient and Stable Photo-Oxidation of Water by a Bismuth Vanadate Photoanode Coupled with an Iron Oxyhydroxide Oxygen Evolution Catalyst*. Journal of the American Chemical Society, 2012. **134**(4): p. 2186-2192.
69. Sivula, K., *Nanostructured α -Fe₂O₃ Photoanodes*, in *Photoelectrochemical Hydrogen Production*, R. van de Krol and M. Grätzel, Editors. 2012, Springer US: Boston, MA. p. 121-156.
70. Shen, S., et al., *Hematite heterostructures for photoelectrochemical water splitting: rational materials design and charge carrier dynamics*. Energy & Environmental Science, 2016. **9**(9): p. 2744-2775.
71. Swierk, J.R. and T.E. Mallouk, *Design and development of photoanodes for water-splitting dye-sensitized photoelectrochemical cells*. Chemical Society Reviews, 2013. **42**(6): p. 2357-2387.
72. Prévot, M.S. and K. Sivula, *Photoelectrochemical Tandem Cells for Solar Water Splitting*. The Journal of Physical Chemistry C, 2013. **117**(35): p. 17879-17893.

73. Tofanello, A., et al., *Strategies to improve the photoelectrochemical performance of hematite nanorod-based photoanodes*. APL Materials, 2020. **8**(4): p. 040905.
74. Liu, X., F. Wang, and Q. Wang, *Nanostructure-based WO₃ photoanodes for photoelectrochemical water splitting*. Physical Chemistry Chemical Physics, 2012. **14**(22): p. 7894-7911.
75. Berardi, S., et al., *Molecular artificial photosynthesis*. Chemical Society Reviews, 2014. **43**(22): p. 7501-7519.
76. Sherman, B.D., et al., *Light-Driven Water Splitting by a Covalently Linked Ruthenium-Based Chromophore–Catalyst Assembly*. ACS Energy Letters, 2017. **2**(1): p. 124-128.
77. He, J., et al., *Ruthenium-Based Photosensitizers for Dye-Sensitized Solar Cells*, in *Organometallics and Related Molecules for Energy Conversion*, W.-Y. Wong, Editor. 2015, Springer Berlin Heidelberg: Berlin, Heidelberg. p. 91-114.
78. Kirner, J.T., et al., *Visible-Light-Assisted Photoelectrochemical Water Oxidation by Thin Films of a Phosphonate-Functionalized Perylene Diimide Plus CoOx Cocatalyst*. ACS Applied Materials & Interfaces, 2014. **6**(16): p. 13367-13377.
79. Ronconi, F., et al., *Modification of Nanocrystalline WO₃ with a Dicationic Perylene Bisimide: Applications to Molecular Level Solar Water Splitting*. Journal of the American Chemical Society, 2015. **137**(14): p. 4630-4633.
80. Kamire, R.J., et al., *Photodriven Oxidation of Surface-Bound Iridium-Based Molecular Water-Oxidation Catalysts on Perylene-3,4-dicarboximide-Sensitized TiO₂ Electrodes Protected by an Al₂O₃ Layer*. The Journal of Physical Chemistry C, 2017. **121**(7): p. 3752-3764.
81. Kirner, J.T. and R.G. Finke, *Sensitization of Nanocrystalline Metal Oxides with a Phosphonate-Functionalized Perylene Diimide for Photoelectrochemical Water Oxidation with a CoOx Catalyst*. ACS Applied Materials & Interfaces, 2017. **9**(33): p. 27625-27637.
82. Bledowski, M., et al., *Visible-light photocurrent response of TiO₂–polyheptazine hybrids: evidence for interfacial charge-transfer absorption*. Physical Chemistry Chemical Physics, 2011. **13**(48): p. 21511-21519.
83. Wang, L., et al., *Dynamics of Photogenerated Holes in TiO₂-Polyheptazine Hybrid Photoanodes for Visible Light-Driven Water Splitting*. Journal of The Electrochemical Society, 2012. **159**(7): p. H616-H622.
84. Wang, L., et al., *Ultrasmall CoO(OH)_x Nanoparticles As a Highly Efficient “True” Cocatalyst in Porous Photoanodes for Water Splitting*. ACS Catalysis, 2017. **7**(7): p. 4759-4767.
85. Swierk, J.R., et al., *Metal-free organic sensitizers for use in water-splitting dye-sensitized photoelectrochemical cells*. Proceedings of the National Academy of Sciences, 2015. **112**(6): p. 1681-1686.
86. Bornoz, P., et al., *Direct Light-Driven Water Oxidation by a Ladder-Type Conjugated Polymer Photoanode*. Journal of the American Chemical Society, 2015. **137**(49): p. 15338-15341.
87. Yu, Z., F. Li, and L. Sun, *Recent advances in dye-sensitized photoelectrochemical cells for solar hydrogen production based on molecular components*. Energy & Environmental Science, 2015. **8**(3): p. 760-775.
88. Youngblood, W.J., et al., *Visible Light Water Splitting Using Dye-Sensitized Oxide Semiconductors*. Accounts of Chemical Research, 2009. **42**(12): p. 1966-1973.
89. De Tovar, J., et al., *Light-driven water oxidation using hybrid photosensitizer-decorated Co₃O₄ nanoparticles*. Materials Today Energy, 2018. **9**: p. 506-515.

Chapter I - Introduction



Chapter II – Synthesis and functionalization of Fe@FeO_x NPs with different aminophosphonic acids for water oxidation catalysis



Canal du midi – Toulouse – France 2019

Table of contents – Chapter II

1. Introduction.....	36
2. Results and discussion	55
2.1. Synthesis and characterization of nanomaterials.....	55
2.1.1. Synthesis and characterization of Fe@FeO _x NPs	55
2.1.2. Reconstruction of the iron oxide layer.....	63
2.1.3. Water transfer of Fe@FeO _x NPs.....	74
2.2. Electrocatalytic activity of <i>r</i> -Fe@FeO _x NPs and <i>r</i> -Fe@FeO _x @APAs NPs in OER..	83
3. Conclusions.....	89
4. References	90

Chapter II – Fe@FeOx@APAs

Chapter II - Synthesis and functionalization of Fe@FeOx NPs with different aminophosphonic acids for water oxidation catalysis

1. Introduction

Transition metal oxides have been known for many years as good catalysts for OER[1, 2]. Among them Fe has emerged as an attractive non-precious metal for its potential catalytic activity for water splitting in the past few decades as Fe is more abundant and less toxic than other transition metals like Co or Ni. In view of this, Fe related nanomaterials including Fe complexes, Fe alloys, and Fe oxides have recently been studied for OER[3].

In this section we outline the historical development in the use of Fe-oxide based electrocatalysts, and summarize the view points on the catalytically active sites. The synthesis techniques and the major challenges in improving the intrinsic catalytic activity and stability of these oxides are also discussed.

As an OER catalyst, Fe has not been as broadly investigated as other transition metals like Ni and Co due to the low conductivity of iron oxide and high overpotential required to drive OER on Fe₂O₃. In the past decade, only few publications on the investigation of Fe oxide-based catalysts for OER have been published. For example, in 2010, Lyons *et al.*, investigated the kinetics of the OER proceeding on passive Fe oxide anodes in 1M NaOH electrolyte using steady state polarization to determine the Tafel slopes and reaction order vs. OH⁻. Tafel slope values in the range 45-48 mV/decade were recorded for pre-reduced Fe anodes (Figure 1)[4]. In this study, the passive Fe oxide formed directly on the surface of Fe metal foil electrodes during OER.

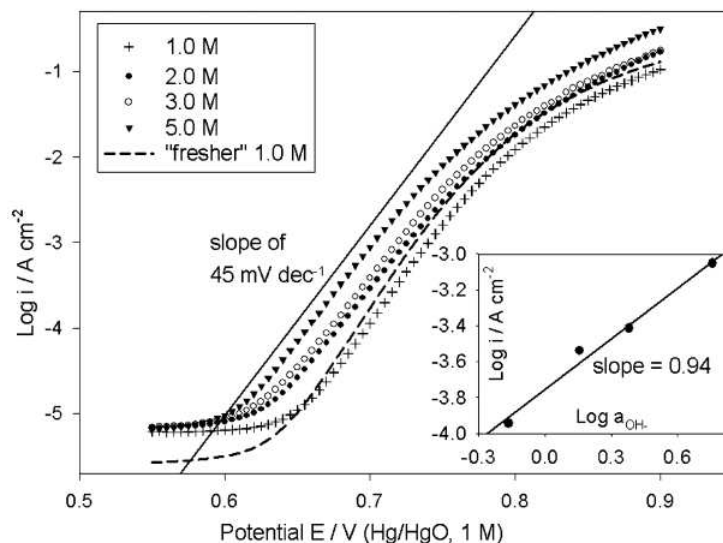


Figure 1. OER steady state polarization curves for a pre-reduced Fe electrode in various NaOH solutions. The trace denoted as ‘fresher 1.0 M’ was recorded for the same electrode in an earlier experiment, before satisfactory reproducibility with respect to Tafel slope had become established. Inset–reaction order plots constructed from the reproducible polarization data at a potential of $E = 0.7\text{ V}$ [4].

Although most of metal oxide-based OER catalysts were studied in the crystalline form, high activities were also reported with amorphous phases. For example, in 2013, Smith *et al.*, have demonstrated that at low-temperature, the photochemical metal-organic deposition (PMOD) could produce amorphous iron oxide film (a-Fe₂O₃) with a thickness of ~100 -200 nm onto FTO electrodes and studied their catalytic activity for OER (Figure 2). This as-prepared amorphous Fe₂O₃ afforded a current density of 0.5 mA/cm² at an overpotential of 400mV and exhibited a Tafel slope as small as 40 mV/decade in 0.1 M KOH. The catalytic properties of this amorphous iron oxide are superior to those of hematite in identical conditions (Figure 3)[5].

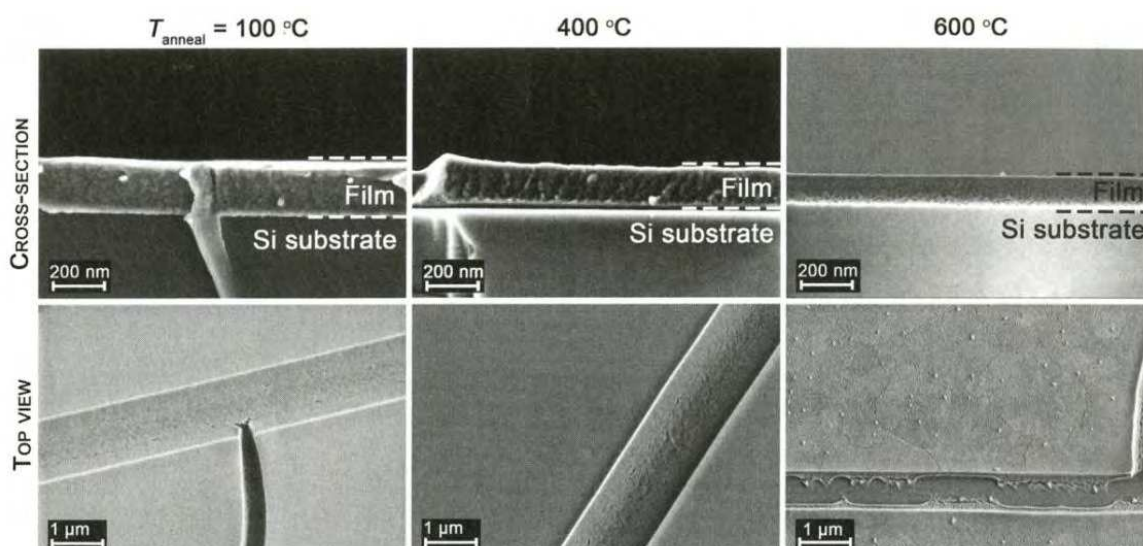


Figure 2. SEM cross-section and top-down surface images of amorphous Fe₂O₃ films prepared by PMOD, followed by a 1-hour annealing step in air at $T = 100^\circ, 400^\circ$ and 600° [5].

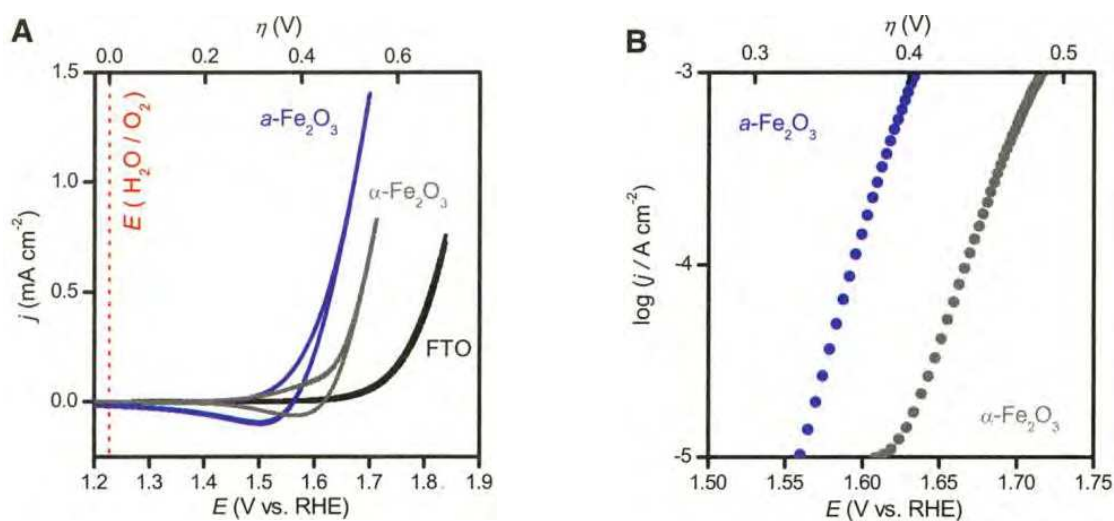


Figure 3. A) cyclic voltammograms for films of α -Fe₂O₃ (blue) and hematite (gray), and a blank fluorine-doped tin oxide (FTO) substrate. B) Tafel plot showing the higher catalytic activity of α -Fe₂O₃ relative to hematite in 0.1 M KOH[5].

In 2016 Jung and co-workers studied the activity and stability of commercial Fe₂O₃ NPs with a size $< 5 \mu\text{m}$ as OER catalyst in alkaline solution (1 M NaOH). To do so the NPs were simply drop-casted on a glassy carbon working electrode using Nafion as a binder to form a thin catalyst film. The results showed that these NPs required first an over potential as high as 1.24 V vs. RHE to

reach a current density of 10 mA/cm², while after 2 h. the overpotential reach 10 mA/cm² even increased up to 1.28 V vs. RHE. In addition, a strong degradation of the catalyst in the steady state was observed, therefore the Tafel plot could not be recorded [2]. However, although the NPs in this study are indicated as crystalline, their crystalline phase (hematite or maghemite) was not reported.

In 2016, Hu *et al.*, used an anodic electrodeposition method to investigate the relationship between catalyst loading and catalytic activity of various deposited catalysts such as FeOx, CoOx, NiOx, CoNiOx, CoFeOx, CoFeNiOx...on Au-coated 10 MHz quartz crystal substrates in 1M KOH solution by consecutive anodic linear sweeps. In this study the FeOx thin film of 2-5 nm thickness was the least active in comparison with the other metal oxide thin films (Figure 4)[6].

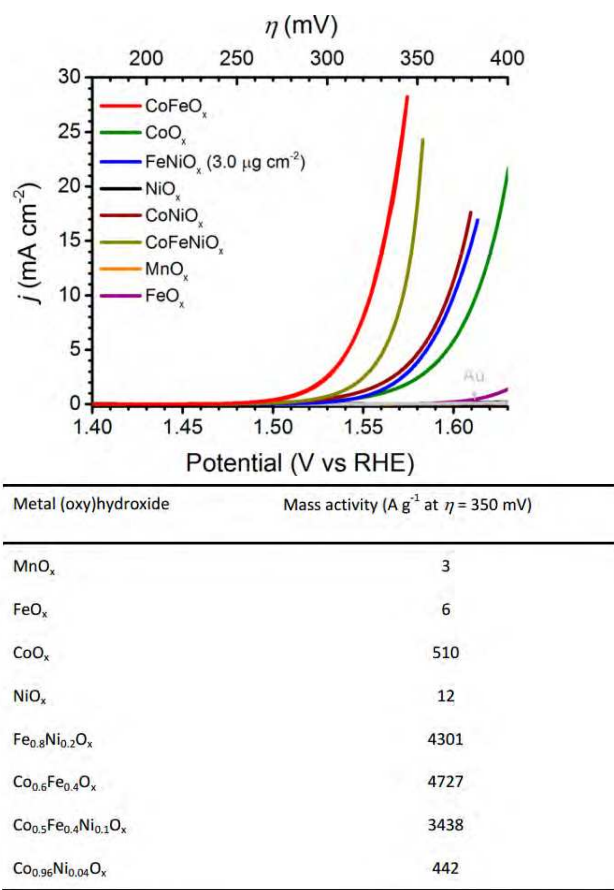


Figure 4. Current study – potential curves of different metal oxide thin films deposited on Au substrates in 1M KOH (top) and summary of intrinsic mass activity of various thin film metal oxide/(oxy)hydroxide for OER in 1M KOH at $\eta=350$ mV (bottom) [6].

In 2018, Kwong and co-workers have demonstrated that a crystalline iron oxide film consisting of mixed polymorphs of maghemite and hematite denoted as (c-Fe₂O₃) was a highly active OER catalyst in H₂SO₄ 0.5M. It produced a current density of 10 mA/cm² at an overpotential of 650 mV for 24h (Figure 5a), a Tafel slope of only 56mV/decade (Figure 5b), whereas the maghemite (γ-Fe₂O₃) film was also equally active but corroded after ~6 hours and the hematite (α-Fe₂O₃) film was OER-inactive. The crystalline Fe₂O₃ films were prepared onto Ti foil substrates by a spray pyrolysis deposition method followed by low-temperature annealing in Ar resulting in nanometer-size individual grains, coalesced into irregularly shaped, micron-size (<1.5 μm) agglomerates as characterized through scanning electron microscopy (SEM) (Figure 6)[7]. By using X-ray photoelectron spectroscopy and electrochemical impedance spectroscopy, these studies also showed that the differences in the surface interaction with the water molecules and protons, and in the electrical conductivity displayed by the polymorphs were responsible for the differences in catalytic activity of the films in comparison with maghemite and hematite films. Indeed, in the mixed- polymorph film, hematite acted as non-catalytic scaffold that stabilized maghemite against acidic corrosion during OER. On the other hand, the Fe vacancy sites associated with the maghemite structure facilitated the surface adsorption of water molecules, and gave a high electrical conductivity, which enhanced the charge transport across the film. They are thus pointed out as the sites responsible for the high catalytic activity of crystalline mixed iron oxide film.

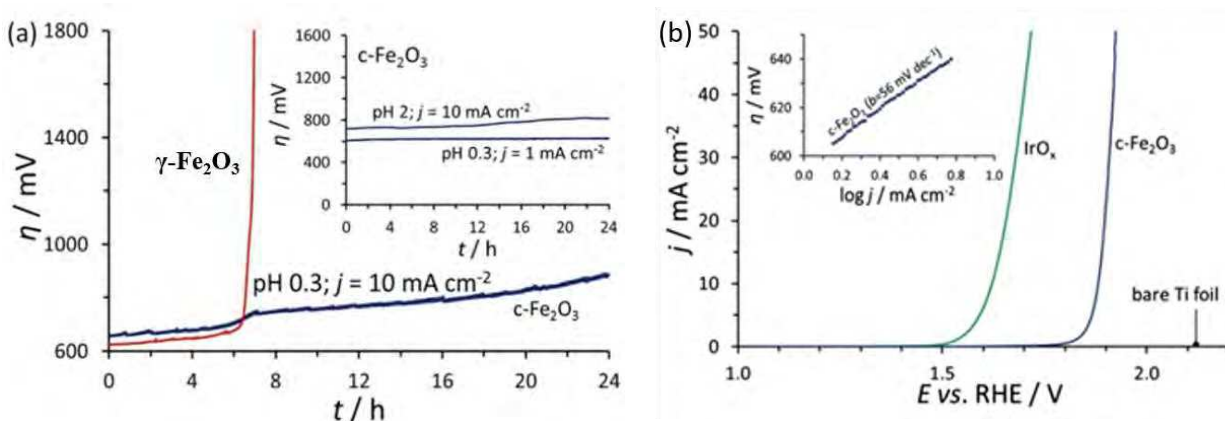


Figure 5. a) Chronopotentiometric (CP) measurement of $\gamma\text{-Fe}_2\text{O}_3$ and $c\text{-Fe}_2\text{O}_3$ (mass loading $1\text{mg}\cdot\text{cm}^{-2}$) at $\text{pH } 0.3, j=10\text{mAcm}^{-2}$. The insert shows the CP tests for $c\text{-Fe}_2\text{O}_3$ at $\text{pH } 0.3, j=1\text{mA}\cdot\text{cm}^{-2}$ and at $\text{pH } 2, j=10\text{mAcm}^{-2}$ b) Polarization curves of $c\text{-Fe}_2\text{O}_3$ and IrO_x (used as a reference) measured in $0.5\text{M H}_2\text{SO}_4$ ($\text{pH } 0.3$), the insert shows the corresponding Tafel plot of $c\text{-Fe}_2\text{O}_3$, adapted from reference [7].

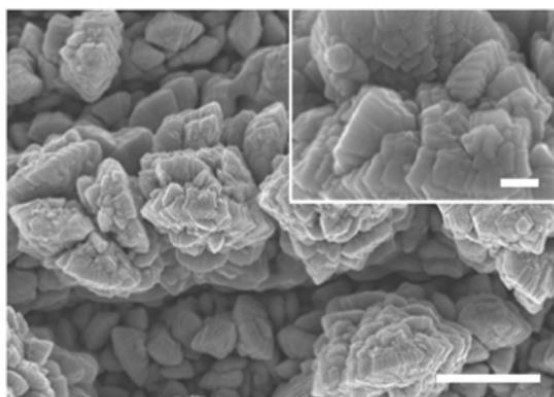


Figure 6. SEM images of as-prepared $c\text{-Fe}_2\text{O}_3$. The insert shows the surface morphology at higher magnification. Scale bar: $1\mu\text{m}$, insert 100nm [7].

In 2019, Kauffman and co-workers deposited Fe_2O_3 islands of *ca.* 5-6 nm large and maximum thickness 0.5 nm on a Au (111) substrate as shown in STM (scanning tunneling microscopy) images in Figure 10. This 2L- $\text{Fe}_2\text{O}_3/\text{Au}$ electrode was studied as OER catalyst in $\text{KOH } 0.1\text{M}$. A direct correlation between the number of Fe edge-sites, and more precisely the formation of hydroxylated iron species, and the catalytic activity of the 2L- $\text{Fe}_2\text{O}_3/\text{Au}$ electrode in alkaline solution could be made. This was supported by DFT calculations which further pointed out that

the hydroxylated Fe atoms at the edge-sites along the catalyst/support interface (Figure 7) were probably the active reaction sites. This 2L-Fe₂O₃/Au nanostructured electrode also demonstrated higher OER activity than an ultrathin IrO_x/Au catalyst at moderate overpotential with nearly similar metal loading (Figure 8), and an average Tafel slope of 77.6 mV/decade was determined [8].

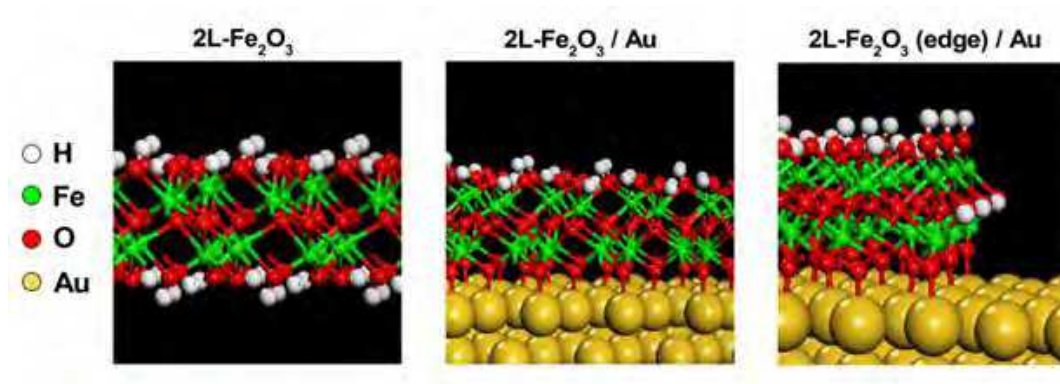


Figure 7. DFT-optimized structures of unsupported and Au(111)-supported, two-layer thick α -Fe₂O₃ (0001) structures [8].

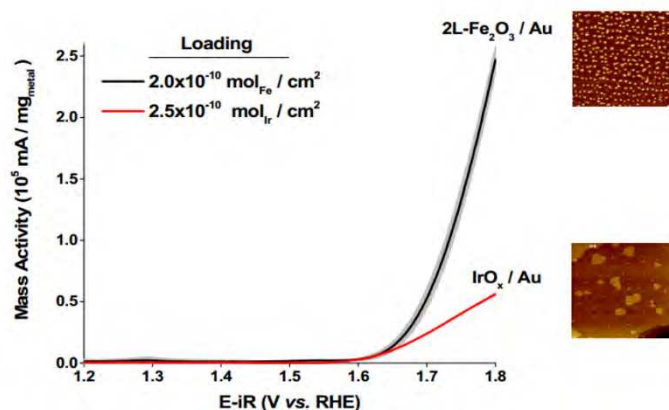


Figure 8. OER voltammograms of 2L-Fe₂O₃/Au and ultrathin IrO_x/Au catalysts at similar loadings (2.0×10^{-10} and 2.5×10^{-10} mol metal/cm², respectively). The 2L-Fe₂O₃/Au voltammogram represents the average of two independently synthesized samples and the shaded region represents the standard deviation. STM conditions: $I = 5$ pA, $V = 2.0$ V; image sizes: 200 nm x 200 nm [8]

Like for any other semi-conducting material, the catalytic activity of oxides toward OER is strongly influenced by their electrical conductivity. Especially in the case of Fe-based OER

catalysts, a layer of hydrous iron oxide forms at their surface during OER which displays a poor conductivity hence these catalysts only show poor catalytic activity for OER. In this context, the simplest way to increase the activity of metal oxide catalysts is to immobilize them on the surface of highly conducting carbon substrates such as graphene[9] or carbon nanotubes[10] or metal substrates such as Ni foam[11].. *etc.* These substrates not only increase the catalytic activity of metal oxides by insuring a fast electron transport but also increase the stability of the overall system by avoiding the aggregation of metal oxide NPs. Furthermore, the high surface area of these deposited catalysts reduces the resistance associated with the mass transfer process during OER. However, few results are yet reported in the literature.

As an example, in 2014, Liu and co-workers demonstrated that α -Fe₂O₃ nanorod arrays (NA) could grow on carbon cloth (CC), namely α -Fe₂O₃ NA/CC, by using a chemical bath deposition method (Figure 9). The as-synthesised α -Fe₂O₃ NA/CC could directly be used as an integrated binder-free 3D OER electrode in 1M KOH. This electrode exhibited an onset overpotential of 330 mV and a Tafel slope of 52mV/decade. Furthermore, it could afford a current density of 10mA/cm² at the small overpotential of 420 mV/decade and maintain its catalytic activity for at least 10 hours (Figure 10) [12]. The high performance of α -Fe₂O₃ NA/CC could be attributed to the strong adhesion between vertically aligned α -Fe₂O₃ nanorods and CC that allowed a fast electron transport and easy diffusion of the electrolyte.

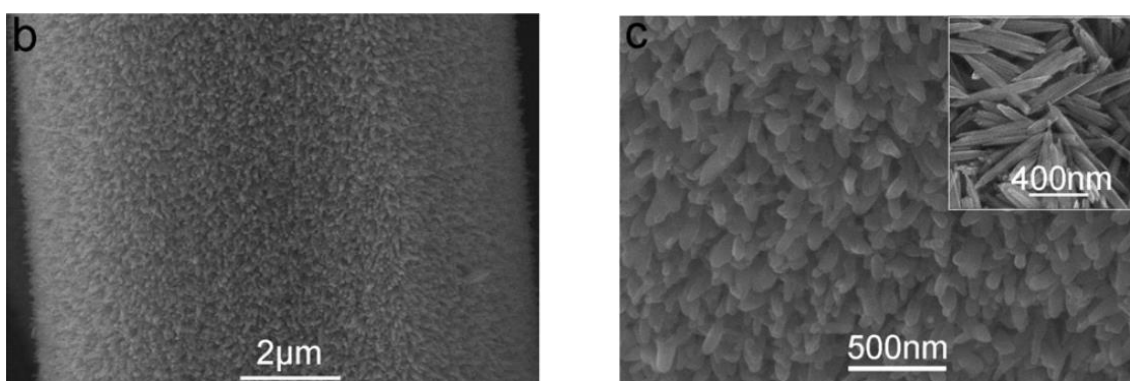


Figure 9. SEM images of α -Fe₂O₃ NA/CC [12].

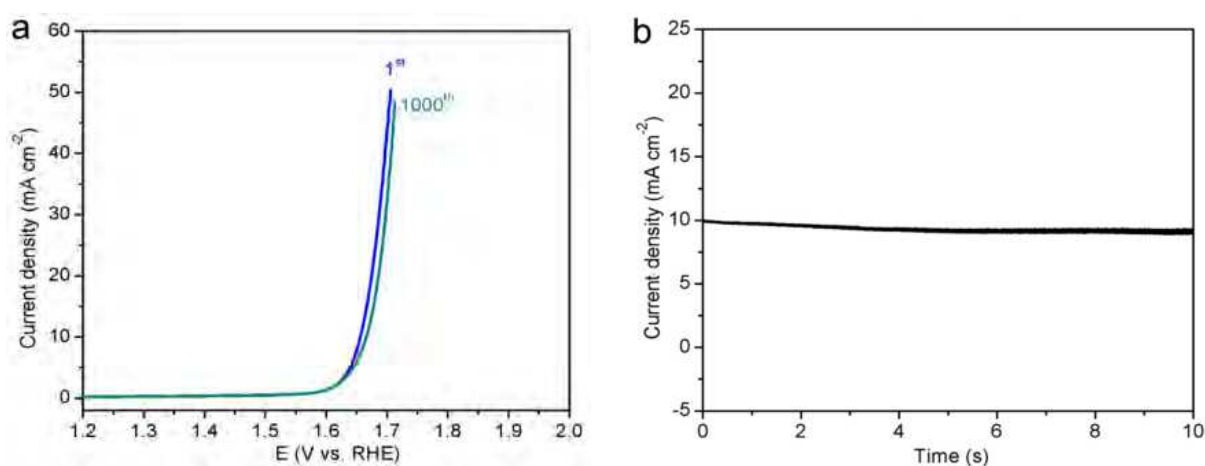


Figure 10. a) Polarization curves for α -Fe₂O₃ NA/CC in 0.1 M KOH initially and after 1000 CV scanning between +1.2 and +2.0 V (vs. RHE). (b) Time-dependent current density curve for α -Fe₂O₃ NA/CC in 0.1 M KOH at an overpotential of 420 mV over a period of 10 h [12].

In 2016, Bandal and co-workers [13] successfully synthesized polycrystalline hollow α -Fe₂O₃ nanorods on CNT by hydrolyzing FeCl₃ in the presence of CNT (Figure 11). These rods with approximately 35-45 nm in length and 5-10 nm in width, were present as large clusters that completely covered the surface of CNT (Figure 12). The combination of the larger electrochemical accessible surface area provided by these hollow α -Fe₂O₃ nanorods with the enhanced electrical conductivity provided by CNT resulted in a α -Fe₂O₃/CNT composite which exhibited a high electrocatalytic activity toward OER with good stability in alkaline conditions (1M KOH) as a current density of 10 mA/cm² was achieved at a low overpotential of 383 mV and the Tafel slope was 61 mV/decade. This value is significantly lower than the value recorded for α -Fe₂O₃ and CNT

in identical conditions, and the simple physical mixture of α -Fe₂O₃ and CNT (Figure 13). Unfortunately, the α -Fe₂O₃/CNTs catalyst displayed a poor stability as it lost 90% of its catalytic activity after 20 h. of reaction (Figure 13c).

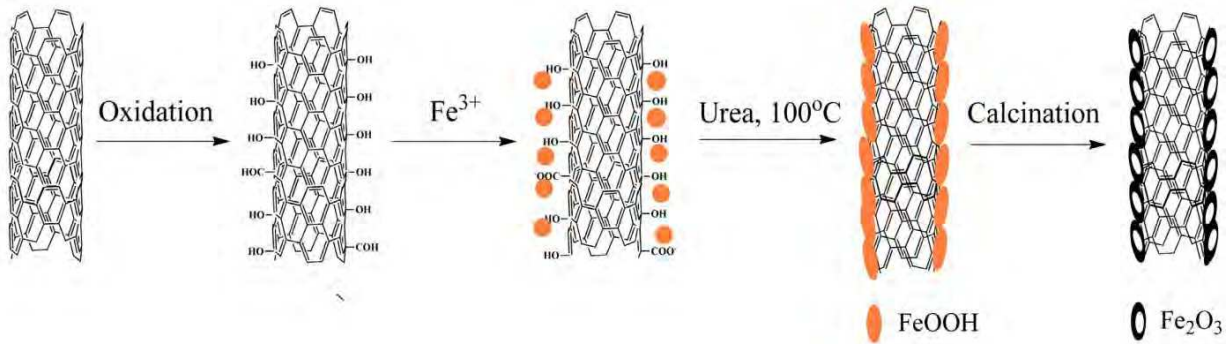


Figure 11. Schematic representation of the experimental procedure for the preparation of the α -Fe₂O₃/CNT composites[13].

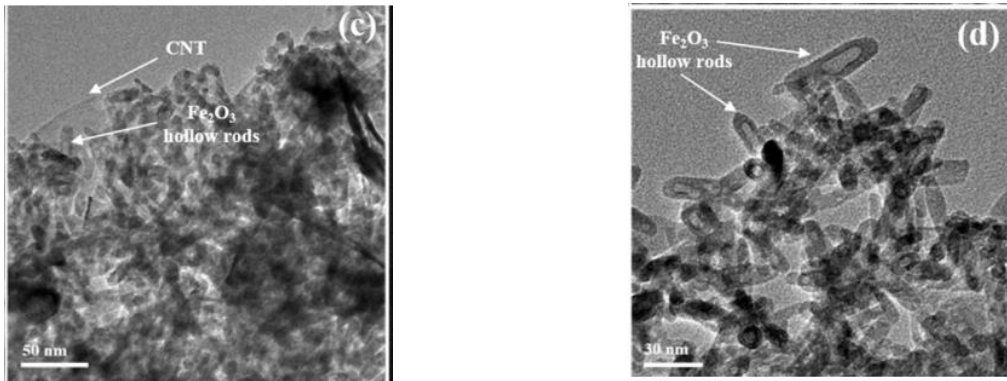


Figure 12. TEM images of α -Fe₂O₃/CNT composite[13].

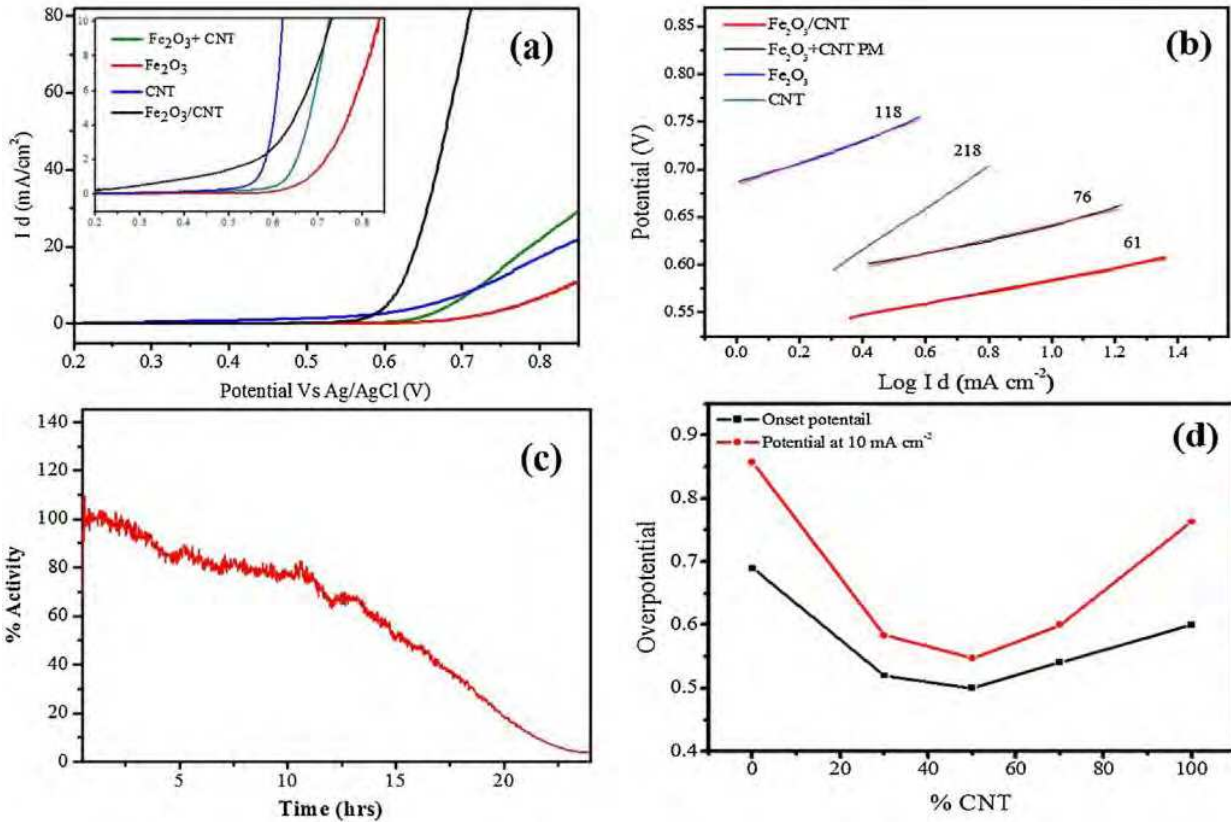


Figure 13. Comparison between the electrocatalytic activities of $\alpha\text{-Fe}_2\text{O}_3$ and $\alpha\text{-Fe}_2\text{O}_3/\text{CNT}$ composite (a) polarization curve from the catalyst deposited on glassy carbon electrode, (b) corresponding Tafel plots, (c) potentiostatic analysis at a constant potential of 600 mV vs. Ag/AgCl electrode, (d) effect of CNT loading on the onset potential and potential at a current density of $10 \text{ mA}/\text{cm}^2$ [13].

Following the same concept, Tavakkoli and co-workers synthesized a $\gamma\text{-Fe}_2\text{O}_3/\text{CNT}$ composite by adopting a CVD method to produce Fe NPs, followed by the *in situ* conversion of the Fe NPs into $\gamma\text{-Fe}_2\text{O}_3$ NPs and investigated their electrocatalytic activity for OER (Figure 14) [14].

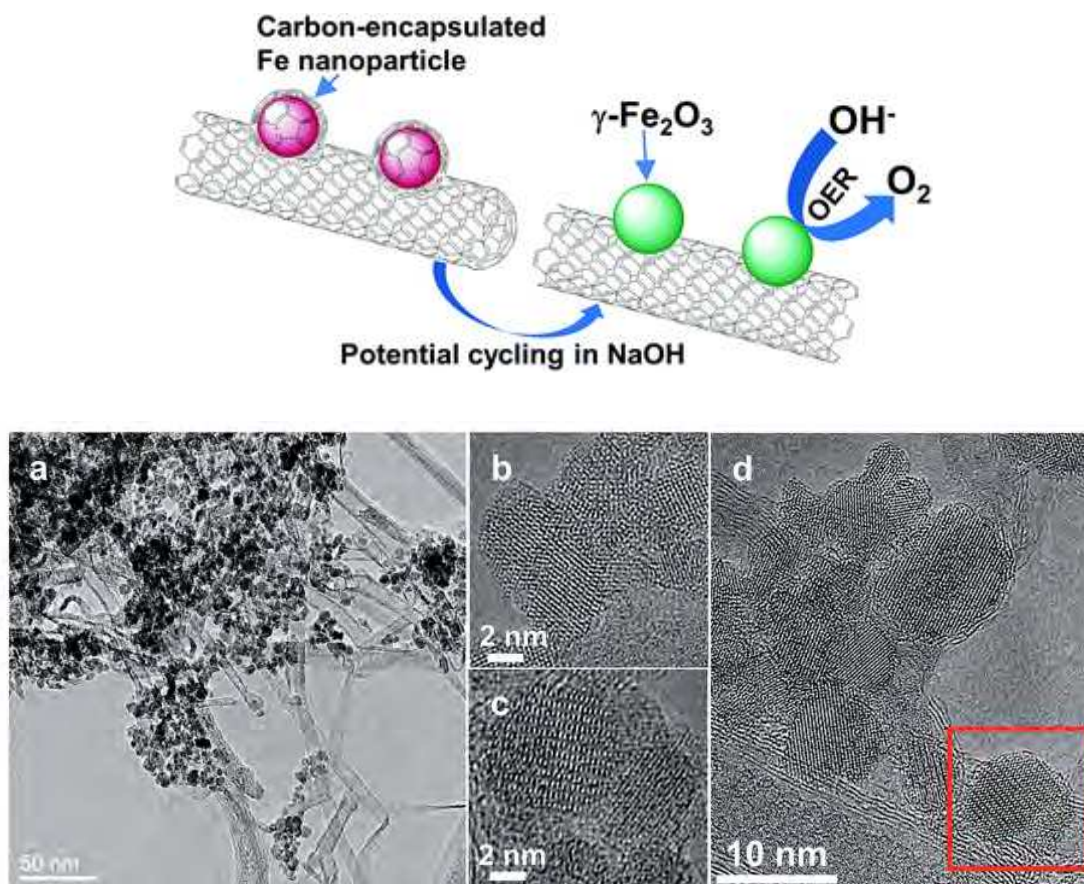


Figure 14. Top) Schematic synthesis pathway for $\gamma\text{-Fe}_2\text{O}_3/\text{CNTs}$ composite. Bottom) (a) Low- and (b-d) high- magnification TEM images of the $\gamma\text{-Fe}_2\text{O}_3$ NPs supported on CNTs[14].

The $\gamma\text{-Fe}_2\text{O}_3/\text{CNT}$ composite exhibited high catalytic activity for OER (current density of 10 mA/cm^2 at an overpotential of 340 mV and 380 mV in 1M and 0.1 M NaOH, respectively, Tafel slopes as small as 50 mV/decade and 45 mV/decade in 0.1M and 1M NaOH, respectively) (Figure 15).

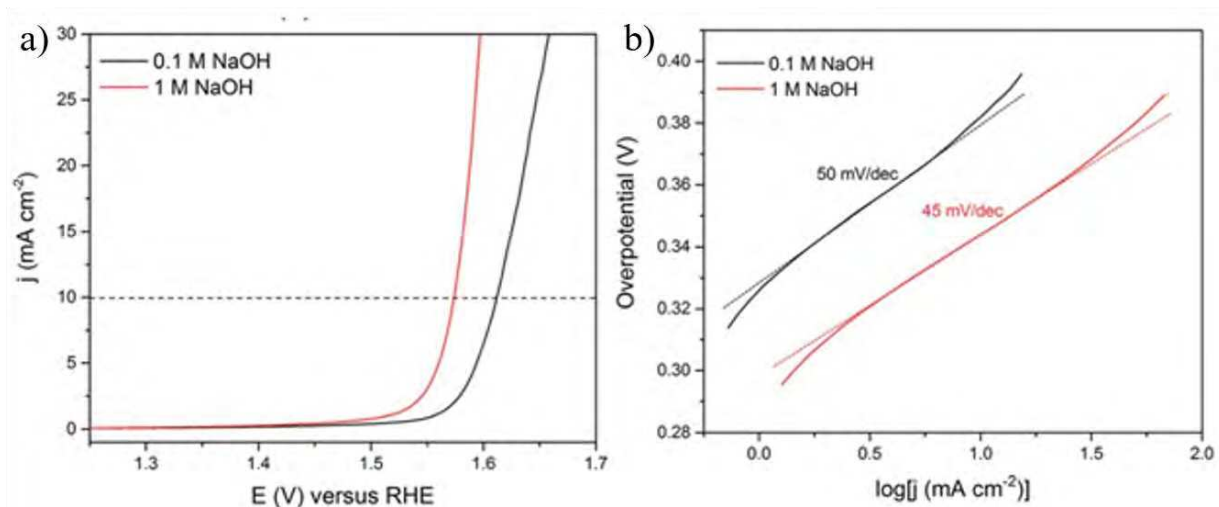


Figure 15. a) Rotating disk electrode (RDE) voltammogram with iR compensation and d) corresponding Tafel plots obtained with the γ -Fe₂O₃/CNT electrode in 0.1 M (black lines) and 1.0 M (red lines) NaOH. Potential scan rate of 5 mV/s and rotation of 1600 rpm [14].

Moreover, this catalyst displayed a better stability in comparison with the α -Fe₂O₃/CNT composite reported by Bandal and co-workers [13] as the γ -Fe₂O₃/CNT composite showed a stable performance during 25 h. at a potential of ~ 1.64 V vs. RHE (Figure 16).

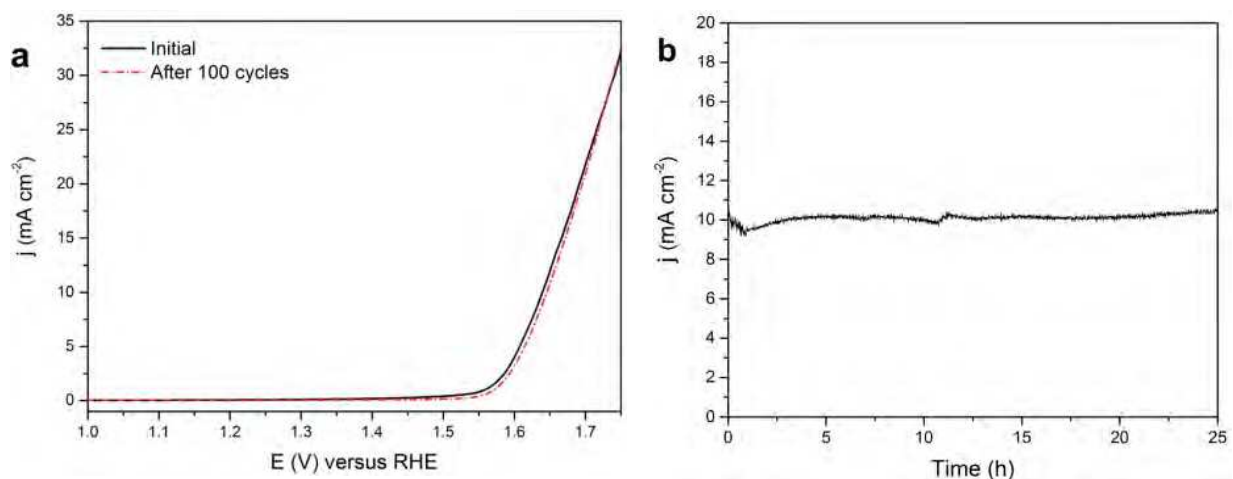


Figure 16. Stability test of the γ -Fe₂O₃/CNT catalyst for OER a) the polarization curves of γ -Fe₂O₃/CNT before the cycling durability test (black solid line) and after 100 cycles (red dash dot line) between the potential of 1 and 1.75 V vs. RHE. Potential scan rate of 50 mV/s b) time dependence of the current density obtained at a static potential of ~ 1.64 V vs. RHE in 0.1 M NaOH [14].

The difference in catalytic activity between α -Fe₂O₃/CNT and γ -Fe₂O₃/CNT composites can be attributed to the difference in crystal structure. In α -Fe₂O₃/CNT, the rhombohedral hematite phase, only octahedral sites are available, and occupied by the Fe³⁺ ions. Meanwhile, in the γ -Fe₂O₃/CNT composites, of cubic spinel structure, octahedral and tetrahedral sites are present and display cation vacancies[15]. Like crystal defects, these vacancies are supposed to play a beneficial role in the catalytic activity of OER catalysts, and maghemite is thus expected to be a better OER catalyst than hematite. Although the γ -Fe₂O₃/CNT composites displayed high activity and stability for OER, a drawback remains in the process used for their synthesis as it required complex instruments and very high temperature (up to 1100°C). In addition, the morphology and composition of the final material could not be controlled. In order to better understand and compare these Fe oxide-based nano-electrocatalysts for OER, Table 1 lists the documented parameters for the evaluation of their OER performances.

Considering all the methods described above for the synthesis of iron oxide OER catalysts, it is necessary to develop a method which would be much simpler, would require a lower temperature (to reduce the energy consumption) and provide a good control in size and morphology of the iron oxide catalyst. In this respect, the organometallic method could be a good alternative as it affords metal NPs with good control in size and morphology in mild conditions, the oxidation of which is expected to be controllable. However, downsizing the size of the NPs very often requires the introduction of a stabilizing agent, most of them being hydrophobic with very long alkyl chains as the solvent used for this method is an organic one. As a result, the NPs obtained are hydrophobic which is not suitable for a catalyst to be used in aqueous media. Therefore, it is necessary to proceed to a ligand exchange to make these NPs water-soluble.

Table 1: Summary of representative Fe oxide –based electrocatalysts for OER.

No.	Catalysts	Synthetic method	Morphology	Substrate	Electrolyte	Onset potential (V vs. RHE)	Over potential (V) at J=10mA/cm ² geometric area	Tafel slope (mV/dec)	TOF (s ⁻¹)	Ref.	Pub. year
1	Passive Fe oxide	_a	_Thin film?	Fe metal foil	NaOH 1M	–	–	≈ 46	–	[4]	2010
2	amorphous Fe ₂ O ₃	Photochemical metal-organic deposition at low-temperature process	Amorphous Thin film 100-200 nm	FTO electrode	KOH 0.1M	1.55	1.63V (j=0.5mA/cm ²)	40		[5]	2013
3	α-Fe ₂ O ₃ NA/CC	Chemical bath deposition	Nano array α-Fe ₂ O ₃ on carbon cloth	Carbon Cloth	KOH 0.1 M	1.56	0.42	52	–	[12]	2014
4	Fe ₂ O ₃ ^b	Commercial	NPs Size < 5μm	Glass carbon electrode	NaOH 1M	–	1.24 V	– ^c	–	[2]	2016
5	FeOx	Anodic electrodeposition	Thin film 2-5 nm	Au-coated 10 MHz quartz crystal substrate	KOH 1M	–	–	–	–	[6]	2016
6	Polycrystalline α-Fe ₂ O ₃ /CNT	Hydrolyzing FeCl ₃ on CNT	α-Fe ₂ O ₃ hollow nanorod	Glassy carbon	KOH 1M	–	0.383	68	–	[13]	2016

			~35-40 nm in length 5-10 nm in width								
8	γ -Fe ₂ O ₃ /CNT	CVD	6.3 nm NPs	Rotating disk (glassy carbon) electrode	NaOH 1M	–	0.340	54	–	[14]	2016
9	Crystalline Fe ₂ O ₃ (mixed of α -Fe ₂ O ₃ and γ -Fe ₂ O ₃)	Spray pyrolysis deposition	Polymorph film <1.5 μ m	Ti foils substrates	H ₂ SO ₄ 0.5M		0.65 V	56		[5]	2018
10	2L-Fe ₂ O ₃ /Au	UHV science surface	5-6 nm NPs to near monolayer of Fe ₂ O ₃ on Au substrates	Au electrode	KOH 0.1 M	1.55	–	77.6	36.8 (O ₂ /atom Fe)	[8]	2019

a: passive iron oxide layer on Iron metal polycrystalline anode (Fe metal foils).

b: α -Fe₂O₃ or γ -Fe₂O₃ phase not specified

c: the specific current density and the Tafel slope were not reported because the Fe₂O₃ NPs catalyst degraded during steady state measurement.

Surface modification of metal oxides by grafting organic molecules has been extensively studied in the literature. For metal oxides, ligands can be anchored *via* carboxylic acid, phosphonic acid, catechol[16], hydroxylamic acid, silanes, pyridine [17], or thiol [18] groups...Among them carboxylic acids and phosphonic acid groups are the most widely used to make a covalent binding on the surface. Phosphonic acids and their derivatives have a good affinity toward metal oxide surfaces such as indium-tin oxide, alumina oxide, iron oxide etc... [19, 20]. These groups can bind more strongly and to many different metal oxide ions *via* covalent P-O-M bond, in comparison to other anchors such as carboxylates, and remain adsorbed even in alkaline aqueous media[21]. Therefore, we focused on the use of phosphonic acids to modify the surface of iron oxide NPs.

Surface modification of iron oxide NPs with phosphonic acids is currently growing in interest for numerous applications for example, in magnetic resonance imaging (MRI), drug delivery, hyperthermia for cancer treatment [22, 23]. Indeed, it was recognized that greater grafting rates than with carboxylic acids could be achieved and the Fe-O-P bonds are more stable. In addition, surface modification of iron-oxide nanoparticles by a phosphonate monolayer has been shown to prevent aggregation of the NPs[24] which is important for catalysts to be used in water splitting. Furthermore, surface modification can be performed in water as the homocondensation does not occur, especially under mild conditions. [25].

On metal oxide, phosphonic acids can display up to three binding modes (monodentate, bidentate and tridentate) depending on the nature of the surface and the grafting conditions (Figure 17)[26].

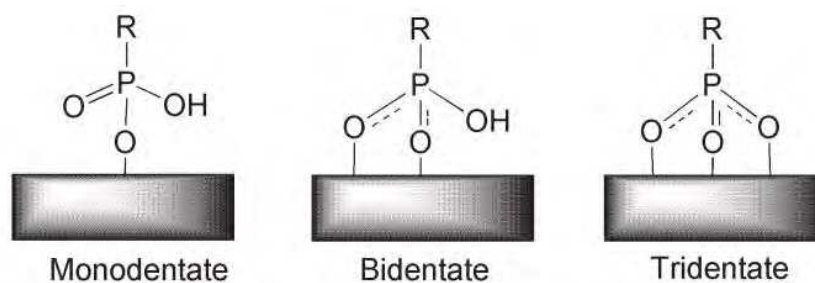


Figure 17. Different bonding modes of a phosphonate unit to a metal oxide surface[26].

It is worth noting that one possible drawback when using phosphonic acids to modify a metal oxide surface is the dissolution-precipitation of the metal oxide which may lead to the formation of a crystalline metal phosphonate (Figure 18) [26]. Working in a too acidic pH, grafting at high

temperature or too long reaction times favor this dissolution precipitation process, which has been reported for many metal oxide surfaces such as, TiO₂, Al₂O₃, ZrO₂ [27].

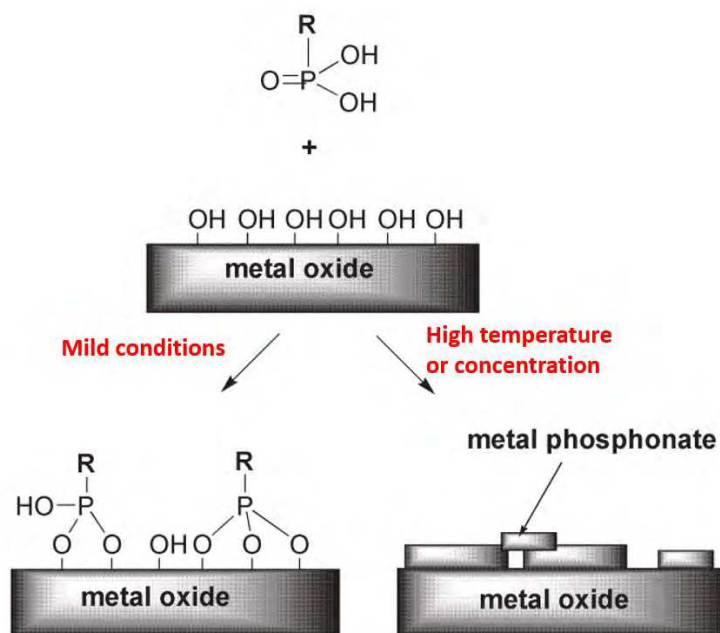


Figure 18. Competition between surface modification and dissolution-precipitation processes in the reaction between a metal oxide surface and a phosphonic acid[26].

Therefore, in this study we chose to graft amino phosphonic acid on iron oxide surface in mild conditions to avoid the formation of crystalline phosphate. A previous study in our group reported the modification of Fe NPs with 3-aminopropyl phosphonic acid at room temperature (r. t.). It was observed that the thin layer of iron oxide formed at the surface of the Fe NPs during water transfer process was beneficial to the grafting of the phosphonic acid ligand [28]. However, when trying to reproduce this protocol we observed that the stability of the core shell Fe@FeOx NPs, once grafted with 3-aminopropyl phosphonic acid in aqueous media was not good enough as they rapidly aggregated. This could result from a weak covalent Fe-O-P bond forming on the passivating iron oxide layer. Therefore, in this study we decided to improve the crystallinity of the oxide layer in order to reach a better stability of the final Fe@FeOx NPs in the aqueous phase. To do that, the reconstruction of the iron oxide surface was needed.

In this chapter, we report a new approach to size-controlled water soluble iron oxide NPs covalently grafted with different amino phosphonic acids via the phosphonic acid moiety. This

represents a model study before grafting a ruthenium complex photosensitizer bearing a pendant phosphonic acid group on Fe@FeOx NPs for light-driven OER.

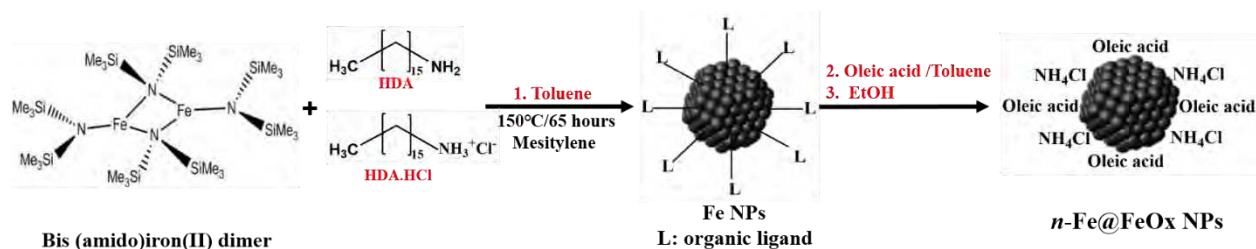
2. Results and discussion

2.1. Synthesis and characterization of nanomaterials

Based on the facts reported above, a three-step process was developed to synthesize the surface modified iron nanoparticles. The first step consisted in synthesizing Fe nanoparticles with an average size of *circa* 10 nm. The second step consisted in reconstructing the oxide shell to obtain the Fe@FeOx core-shell structures with an oxide shell well adapted to the grafting of the phosphonic groups. Then, in a third step, grafting of the target phosphonic acids was carried out on the surface oxide layer.

2.1.1. Synthesis and characterization of Fe@FeOx NPs

Fe NPs were prepared following the organometallic approach based on a recent publication[28], using $[\text{Fe}[\text{N}(\text{SiMe}_3)_2]_2]_2$ as a Fe precursor in a mixture of HDA/HDA.HCl, followed by treatment with oleic acid then with EtOH according to Scheme 1. This method has the advantage of avoiding the use of dihydrogen to reduce the Fe(II) precursor and of affording well crystalline NPs in high yield. After 65 hours of reaction in mesitylene at 150°C, a black powder was collected and washed with toluene, hereafter called FeNPs.



Scheme 1. Synthesis route for the iron-based catalyst

Figure 19a displays a representative TEM image of this black powder. These NPs are relatively uniform in size and shape with an average size of 7.9 ± 1.0 nm and narrow size distribution (Figure 19b). The same protocol was reproduced at least ten times with the same result, thus indicating that the reaction allows good control in the morphology of Fe NPs.

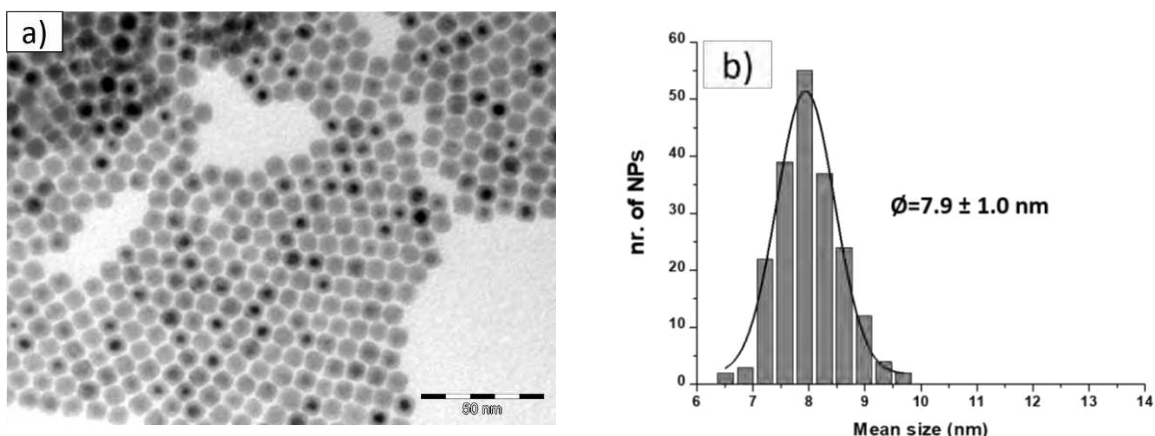


Figure 19. (a) TEM image of Fe-NPs (scale bar 50nm) and (b) corresponding size histogram.

FTIR spectroscopy was used to analyze the surface state of the NPs. The IR spectrum was relatively flat (Black trace, Figure 20). The two peaks at 2912 cm^{-1} and 2845 cm^{-1} were attributed to $\nu\text{C-H}$ stretching of alkyl chains (Figure 21a), but their intensity was very weak. Accordingly, the typical $\nu\text{N-H}$ vibration of HDA.HCl and HDA (expected to display even weaker intensity at around $3000\text{-}3400 \text{ cm}^{-1}$) were not observed on the spectrum. The peaks observed were then attributed to traces of HDA.HCl, the less soluble organic material in the medium, so the most difficult to remove through the purification steps (see experimental section). A low-intensity peak was also observed at 1393 cm^{-1} (Figure 21b) corresponding to the triply degenerated $\nu\text{N-H}$ vibrations of NH_4Cl [29], a product issued from a side reaction between HDA.HCl and HMDS [30](scheme 2).

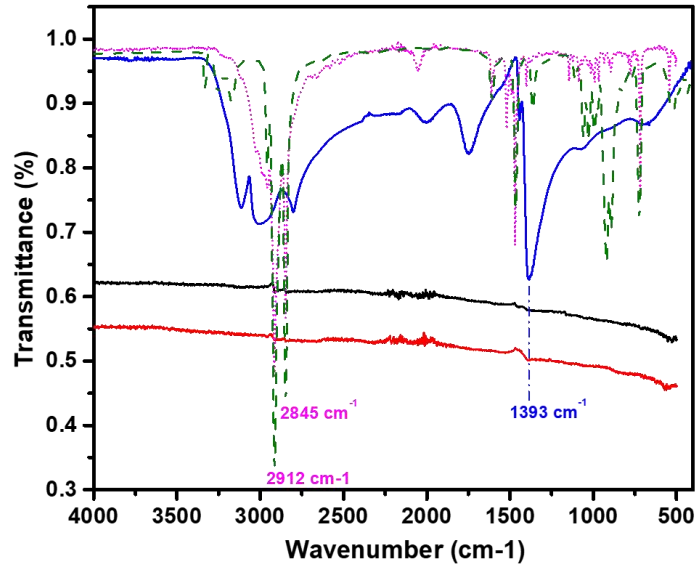


Figure 20. ATR-IR spectrum of Fe NPs (black solid line), n-Fe@FeOx NPs (red solid line) compared to HDA (green dash line), HDA.HCl (pink dot line) and NH₄Cl reference spectra (blue solid line).

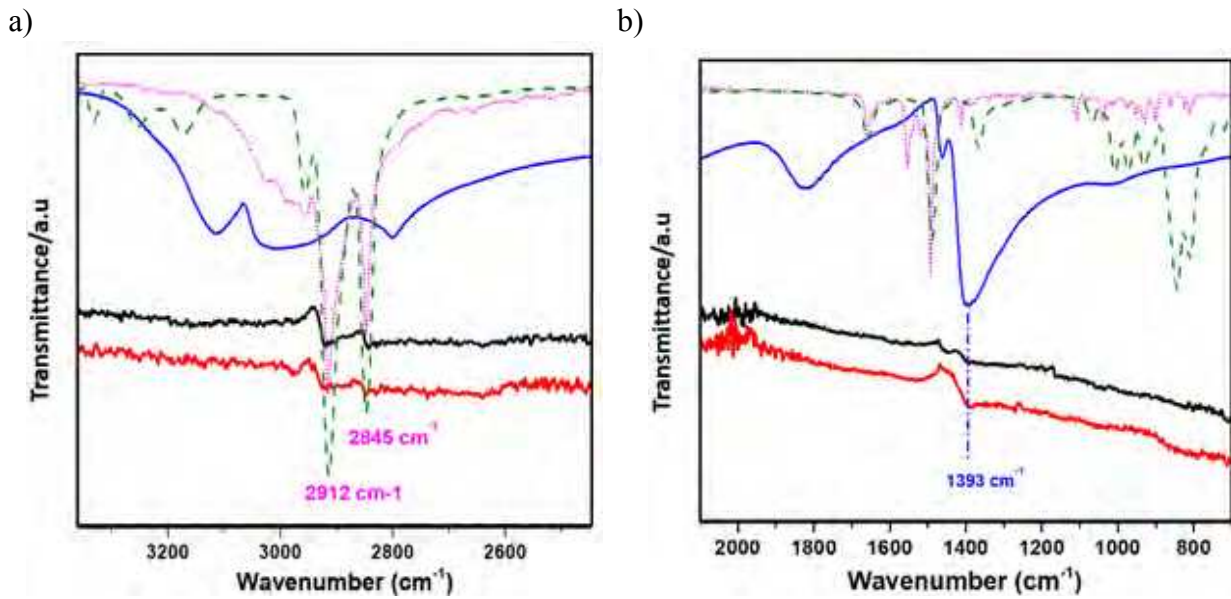
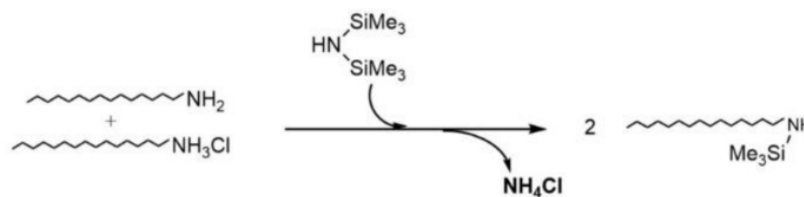


Figure 21. a) Zoom on the ν C-H stretching of alkyl chains b) zoom on the triply degenerate ν N-H vibrations of NH₄Cl.



Scheme 2. Formation of NH₄Cl and silylated amine[30].

Therefore, further reaction of the NPs with oleic acid then finally washing with ethanol replaced the possible HDA.HCl and NH₄Cl traces by an oleic acid surface layer. It afforded a black powder (hereafter referred to as *n*-Fe@FeOx NPs, displaying a large iron content (above 86w%), which could be easily dispersed in organic solvents.

The FT-IR spectrum of *n*-Fe@FeOx NPs is shown in Figure 22. The two peaks of weak intensity at 2912 cm⁻¹ and 2845 cm⁻¹ were attributed to νC-H stretching of alkyl chains (Figure 22) from oleic acid. Accordingly, the typical νCOO vibrations of coordinated oleic acid (expected to display weaker intensity at around 1650-1500 cm⁻¹) were not observed on the spectrum. A very low-intensity peak corresponding to νN-H vibrations of NH₄Cl also was observed in the same position as indicated in Figure 21b. The low solubility of NH₄Cl in distilled EtOH is the reason for a trace of NH₄Cl still remaining after the washing process. The very weak intensity of these peaks indicated that only traces of NH₄Cl and oleic acid remained. This is in agreement with the high iron content (86 w%) determined for the *n*-Fe@FeOx NPs by ICP-OES.

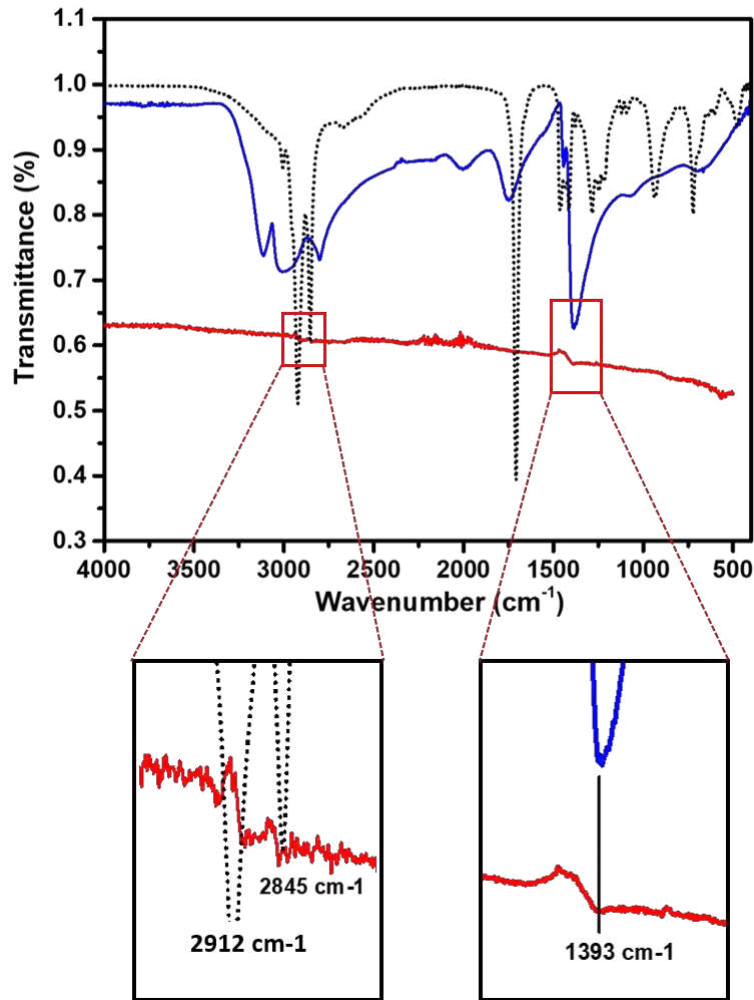


Figure 22. ATR-IR spectrum of *n*-Fe@FeOx NPs (red solid line) in comparison with oleic acid (black dotted line) and NH₄Cl (blue solid line).

Figure 23 shows the TEM images with corresponding size distribution of the *n*-Fe@FeOx NPs. An increase in the size distribution of the NPs from 7.9 ± 1.0 nm (Figure 19b) to 10.1 ± 1.1 nm (Figure 23b), was observed upon the last step of the synthetic process, which might be due to digestive Oswald ripening induced by oleic acid.

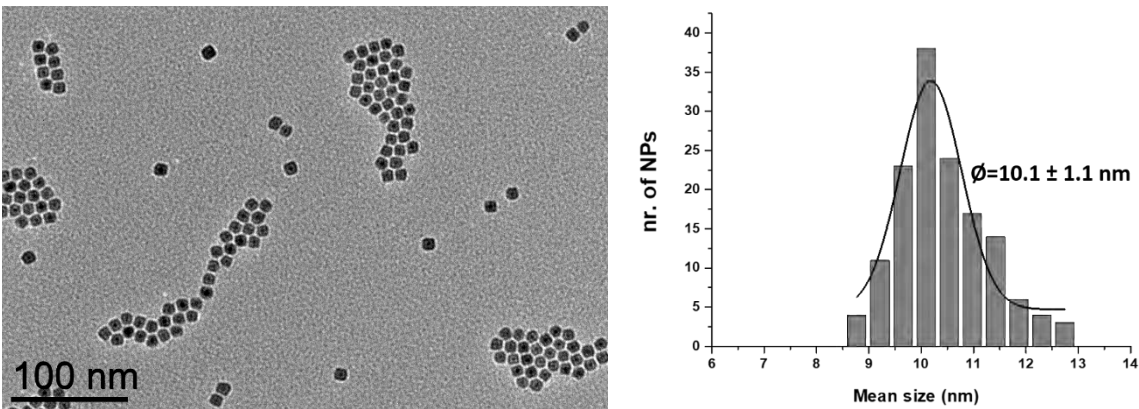


Figure 23. a) TEM images and b) corresponding size histograms of *n*-Fe@FeOx NPs Fe NPs.

The selected area electron diffraction (SAED) pattern (Figure 24b) from a large number of NPs (Figure 24a) displayed diffraction rings corresponding to bcc iron. Diffraction rings of weaker intensity and corresponding to larger interplanar distances were observed as well, suggesting partial oxidation of the material. The formation of a Fe oxide shell on some of the NPs was first observed as a lighter contrast layer surrounding the dark core on HR-TEM images (Figure 24a). Fast Fourier Transformation (FFT) was calculated from a typical HR-TEM image of one selected NP highlighted by the red-square in Figure 24a (Figure 24d). It indicated interplanar distances of 0.1442, 0.0984, and 0.2010 nm corresponding respectively to the (002), (202), and (101) lattice planes of bcc-Fe observed along the [001] direction. A distance of 0.2844 nm was also observed, once again suggesting the formation of oxide, but this distance couldn't be unambiguously attributed to any of the lattice plane spacing of either magnetite (Fe₃O₄) or maghemite (γ-Fe₂O₃). The thickness and crystallinity of the surface oxide layer varied from one NP to the other, as illustrated on Figure 24c and Figure 24e which display HR-TEM images of two different NPs from the same batch of nanomaterial. On the NPs imaged in Figure 24c, the size of the core was around 6.9 nm, and the shell thickness was estimated to be 2.4 nm meanwhile, on the NPs imaged in Figure 24e we could not clearly observe the oxide layer. Moreover, FFT calculations from most NPs observed in HR-TEM displayed only diffraction patterns that could be attributed to bcc Fe, suggesting that most of them consisted in a well-crystalline Fe core surrounded by an amorphous oxide layer (Figure 24e, 24f).

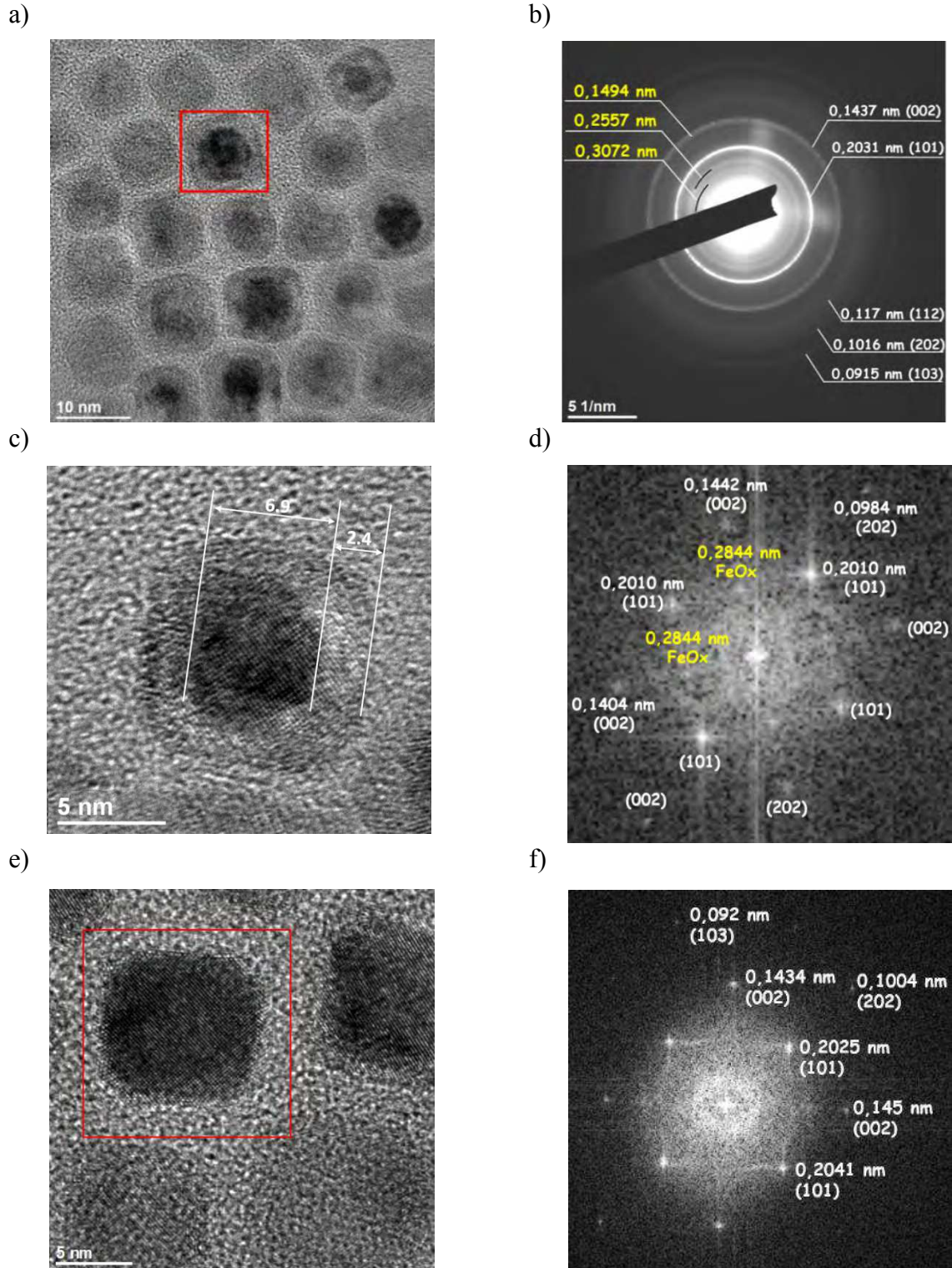


Figure 24. a) HR-TEM of NPs (*n-Fe@FeOx* NPs), b) selected area electron diffraction pattern, c) typical HR-TEM image of one NP (*n-Fe@FeOx* NP), d) FFT calculation on the NP highlighted by the red square in a), e) HR-TEM of *n-Fe@FeOx* NPs, f) FFT calculation on the NP highlighted by the red square in e).

To get a more statistical view of the nanomaterial, the crystallinity of these core-shell NPs was further investigated by Wide Angle X-Ray Scattering (WAXS) (Figure 25) which furthermore allowed us to investigate the nanomaterial in sealed capillaries (i.e. without any risk of air exposure). All diffraction peaks expected from bcc-Fe (reference pattern PDF-01-071-4648) were observed, in agreement with the SAED results. Other diffraction peaks at 10, 15 and 26 degrees were assigned to NH₄Cl (PDF 96-901-0007) in agreement with FT-IR analysis. No diffraction peaks corresponding to iron oxide phases could be clearly observed (Figure 25), confirming that the crystalline oxide part evidenced by SAED is only limited in the sample and may in part arise from the fact that air exposure of the sample could not be avoided during its introduction into the microscope chamber. Else oxidation traces could result from reaction with water traces present either in distilled EtOH or argon from the vacuum-argon line used during the washing process.

All the analysis above confirmed that the NPs consisted in a bcc-Fe core which was eventually surrounded by a thin and/or amorphous oxide layer the exact nature of which remained unknown. The same protocol was reproduced at least 10 times with the same result, thus indicating that the reaction allowed a good control in morphology of the NPs.

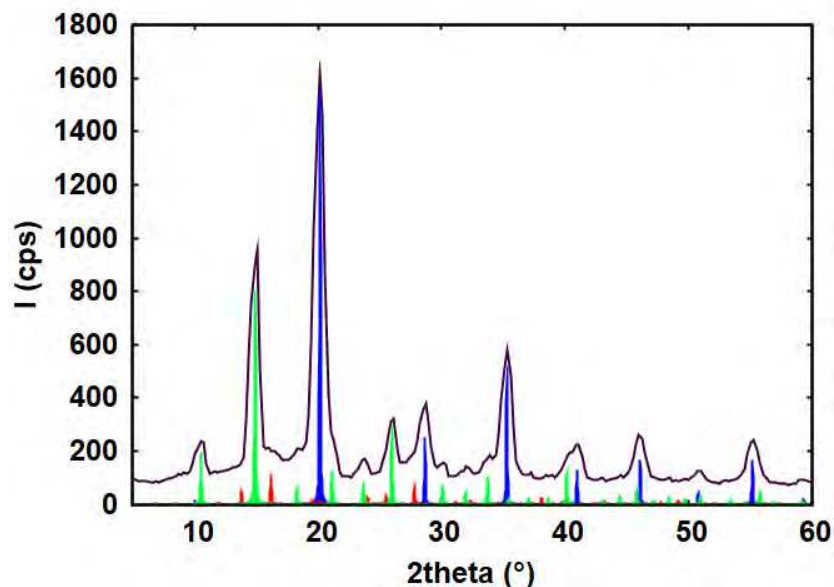
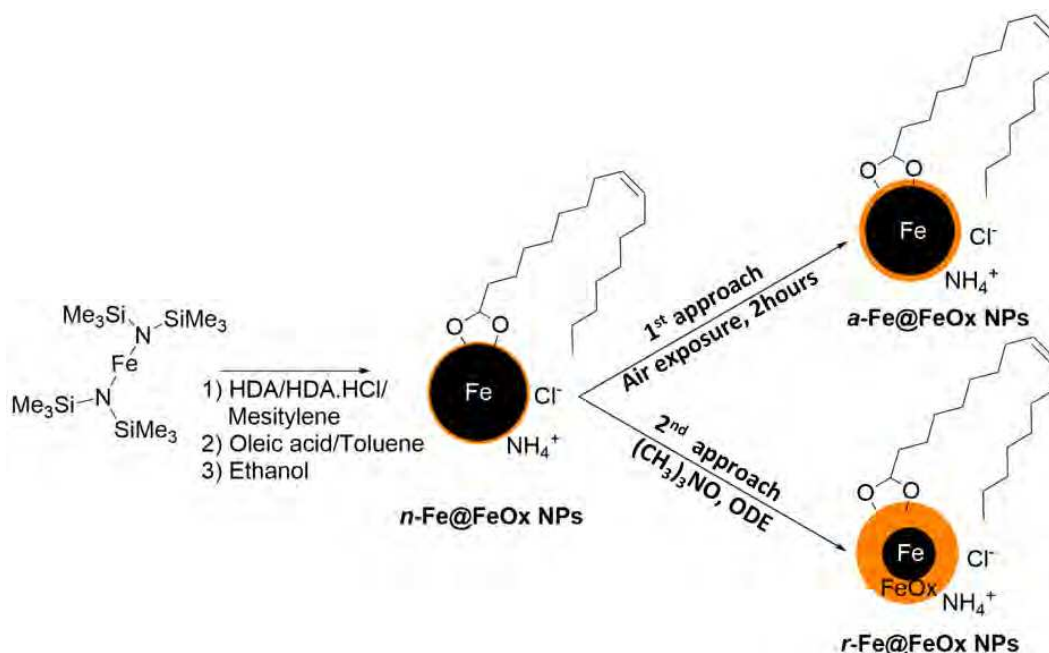


Figure 25. Wide-Angle X-Ray Scattering (WAXS) diagram of *n*-Fe@FeOx NPs (black solid line) in comparison with reference diagrams of bcc-Fe (PDF-01071-4648, in blue), NH₄Cl (PDF 96-901-0007, in green) and hypothetical maghemite γ -Fe₂O₃ (PDF-01-089-5894, in red).

2.1.2. Reconstruction of the iron oxide layer

As describe above the *n*-Fe@FeOx NPs samples are not homogeneous, some NPs have a thin amorphous oxide layer and others don't. Therefore, we have studied 2 approaches to afford a thicker and more crystalline iron oxide layer in all NPs in order to study the effect of the crystallinity of the iron oxide layer on the efficiency of the grafting of phosphonic acids. i) The first approach to obtain a homogeneous iron oxide layer consisted simply in exposing the *n*-Fe@FeOx NPs in air for 2 hours (See detail in Experimental Section- Section 2.2.2), hereafter referred to as *a*-Fe@FeOx NPs (*a* standing for air exposure, **scheme 5-1st approach**). ii) the second approach consisted in using an oxygen transfer agent (CH₃)₃NO, followed by a mild annealing process. This method was reported by Peng *et al.* to afford a thicker crystalline iron oxide layer, as well as to make the Fe@FeOx NPs more stable in both polar and non-polar solvents[31]. Hereafter, the nanoparticles with a reconstructed iron oxide layer will be referred to as *r*-Fe@FeOx NPs (*r* standing for *reconstructed*). See **Scheme 5-2nd approach** showing the corresponding synthesis pathway.



Scheme 3. Synthetic pathways of the *a*-Fe@FeOx NPs (1st approach), and reconstructed- iron/iron oxide core-shell NPs *r*-Fe@FeOx NPs (2nd approach).

The iron oxide layer is more obvious on samples *a*-Fe@FeOx and *r*-Fe@FeOx NPs (Figures 26 b and c, respectively) in comparison to *n*-Fe@FeOx NPs (Figure 26a) and definitely changing in morphology from one oxidation process to the other as observed when comparing sample *r*-Fe@FeOx NPs, (Figure 26c) with the other samples (*n*-Fe@FeOx NPs and *a*-Fe@FeOx NPs, Figure 26 (a and b respectively)). It is noteworthy that in the case of sample *a*-Fe@FeOx NPs, only a fraction of the sample could be dispersed to prepare the TEM grid, which then doesn't give a whole view of the sample. For this reason, a size histogram was not drawn for this sample. Still, Figure 26 doesn't show any significant change in the size of the NPs. A good dispersion could be achieved for the *r*-Fe@FeOx NPs, from which the average size of these NPs could determine by TEM at 11.5 ± 2.3 nm, *i.e.* identical to that of *n*-Fe@FeOx NPs.

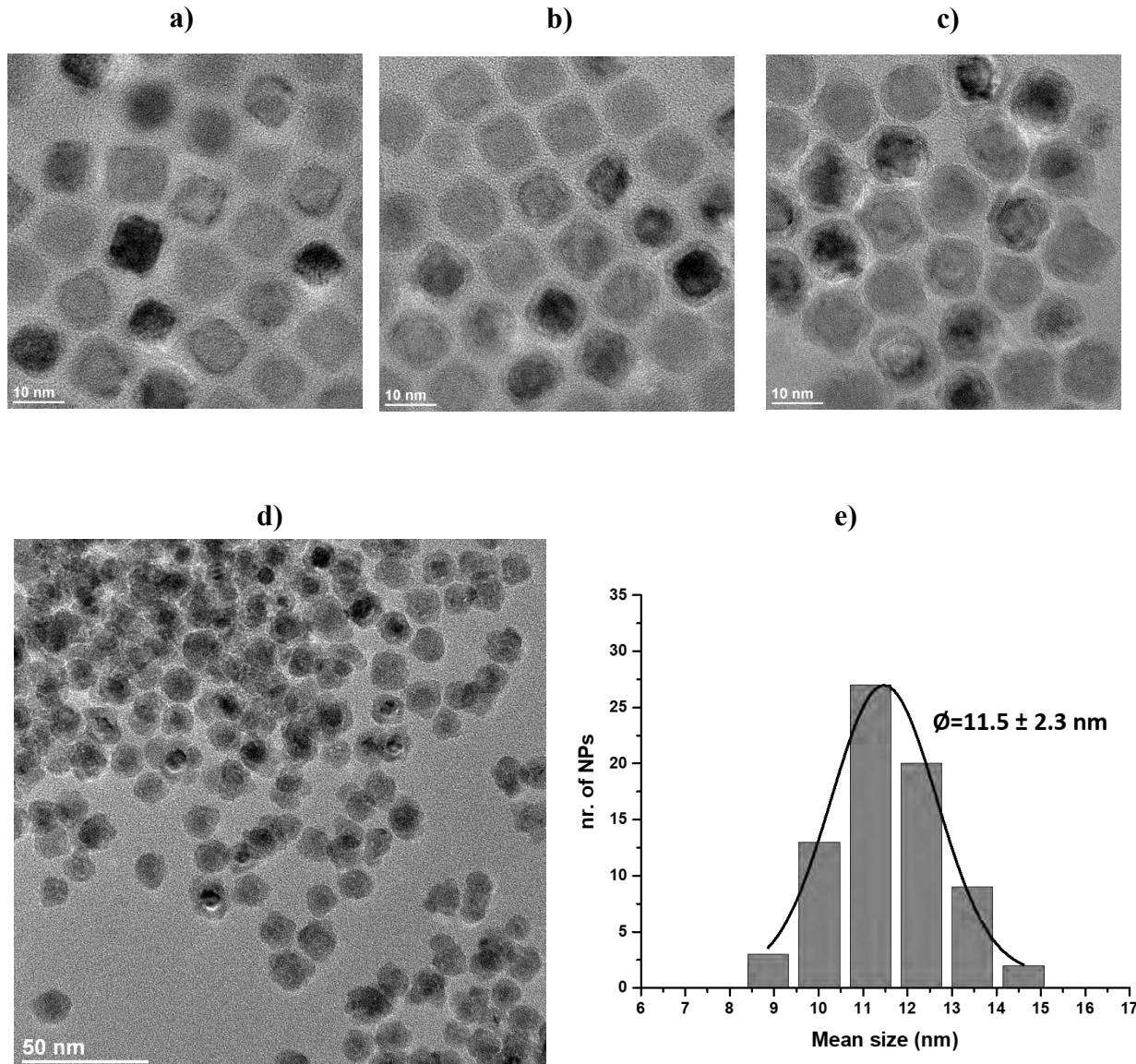


Figure 26. Typical HR-TEM images of a) *n*-Fe@FeOx NPs b) *a*-Fe@FeOx NPs, c-d) *r*-Fe@FeOx NPs and e) size histogram for *r*-Fe@FeOx NPs.

FFT calculation from a typical HR-TEM image of sample *a*-Fe@FeOx NPs displayed mostly diffraction patterns of bcc-Fe (202), (200), (101). As for sample *n*-Fe@FeOx NPs the distance of 0.2887 nm was observed and attributed to iron oxide (Figure 27), but this time WAXS analysis showed clearly one diffraction peak at 16 degrees which was attributed to either Fe₃O₄ or γ -Fe₂O₃ beside the peaks corresponding to bcc-Fe (Figure 28). This indicated a larger fraction of crystalline iron oxide in sample *a*-Fe@FeOx NPs.

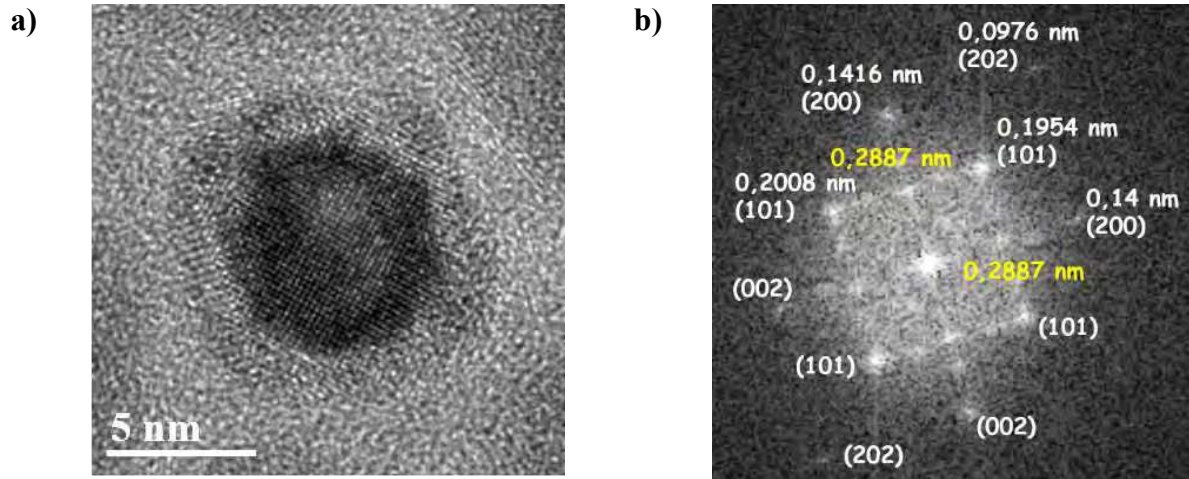


Figure 27. a) typical HR-TEM image of one α -Fe@FeOx NP, and b) corresponding FFT calculation.

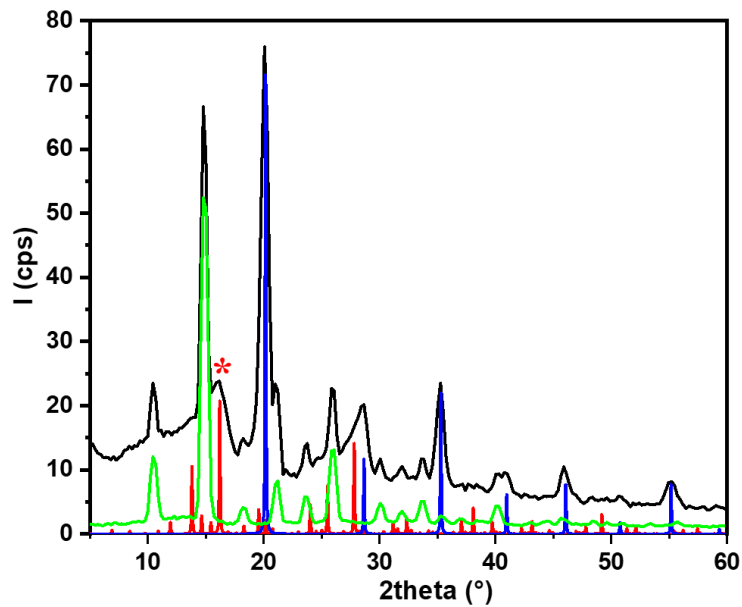


Figure 28. Wide-Angle X-Ray Scattering (WAXS) diagram of α -Fe@FeOx NPs (black solid line), in comparison with reference diagrams of bcc-Fe (PDF-01071-4648, in blue), NH_4Cl (PDF 96-901-0007, in green), and hypothetical maghemite ($\gamma\text{-Fe}_2\text{O}_3$) (PDF-01-089-5894, in red). *: highlight peak corresponding to maghemite.

The main features observed by high resolution TEM (HRTEM) were (i) a discontinuous oxide layer leading to nanoparticles with a “flower-like” morphology (Figures 29a, 29b) and (ii) an oxide shell of irregular thickness (Figure 29c). The maximum thickness of this layer was estimated to be ~ 3.9 nm (Figure 29d) and FFT calculation from this region showed only inter planar distances

corresponding to lattice plane of iron oxide (Figure 30), no lattice plane from bcc-Fe could be observed. Thus, the oxide shell of the nanoparticles consisted in well-defined iron oxide crystalline grains whose maximum thickness was estimated to be ~ 3.9 nm.

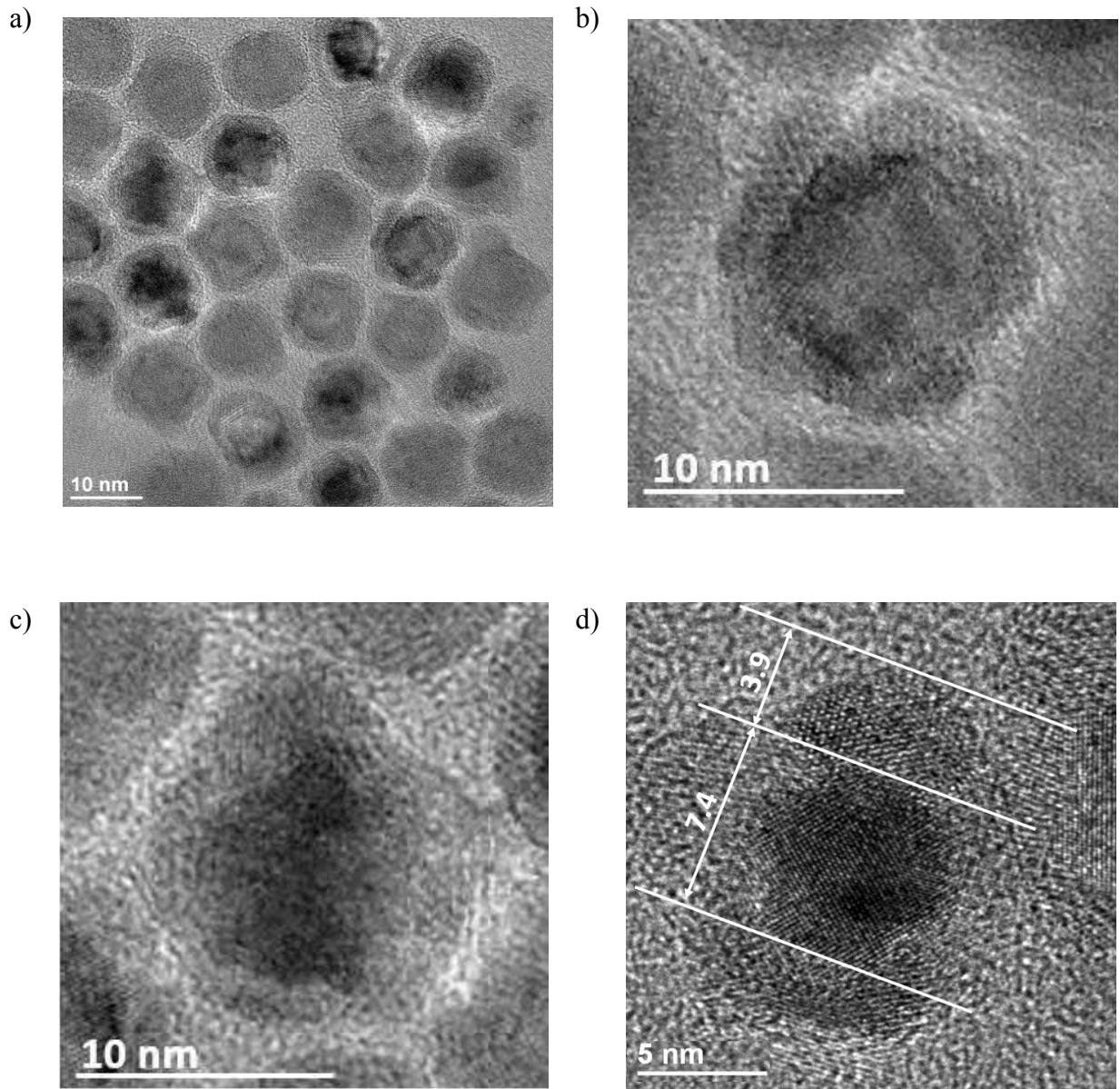


Figure 29. Typical HR-TEM images of nanoparticles from the r-Fe@FeOx NPs sample.

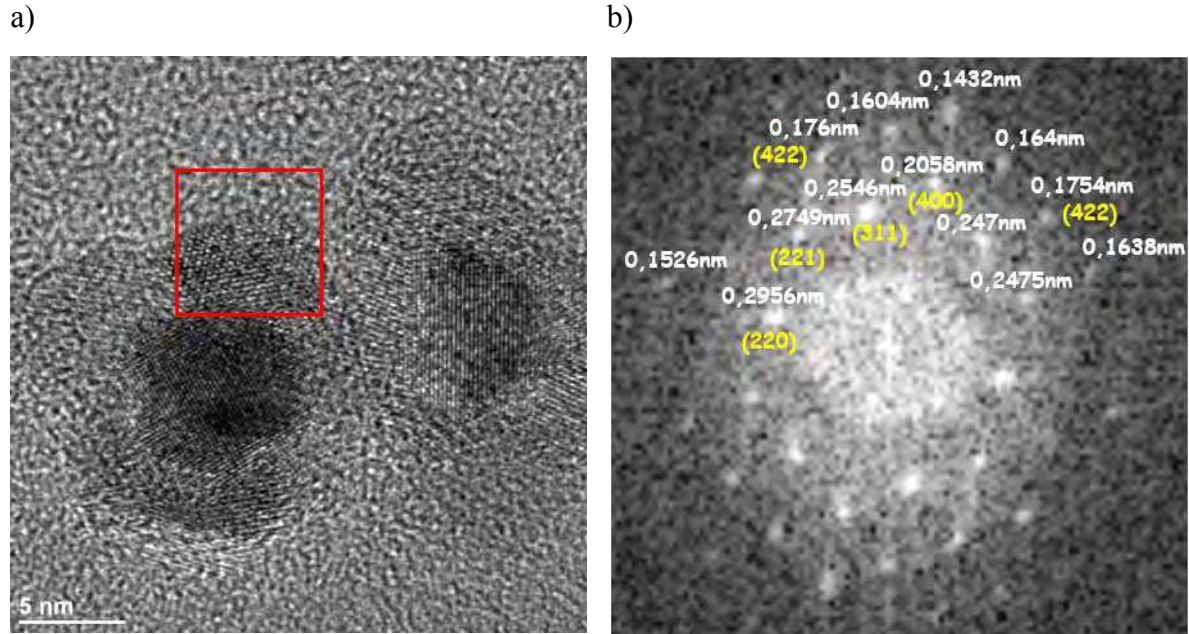


Figure 30. a) Typical HR-TEM image of a nanoparticle from *r-Fe@FeOx* NPs sample and b) FFT calculation from the iron oxide layer highlighted by red square.

Crystallinity of the oxide shell was highlighted by WAXS measurements carried out on the powder. The diagrams obtained for *r-Fe@FeOx* NPs is presented in Figure 31 together with those of bcc-Fe (alpha Fe), γ -Fe₂O₃, and NH₄Cl references. The peaks from NH₄Cl were still present. We observed new peaks at 13, 16, 18, 27 degrees assignable to γ -Fe₂O₃ and an obvious decrease of the intensities of the characteristic bcc-Fe peaks at 28, 41, 50 and 64 degrees. This clearly demonstrated the formation of a crystalline oxide shell at the expense of the bcc-iron core (Figure 32).

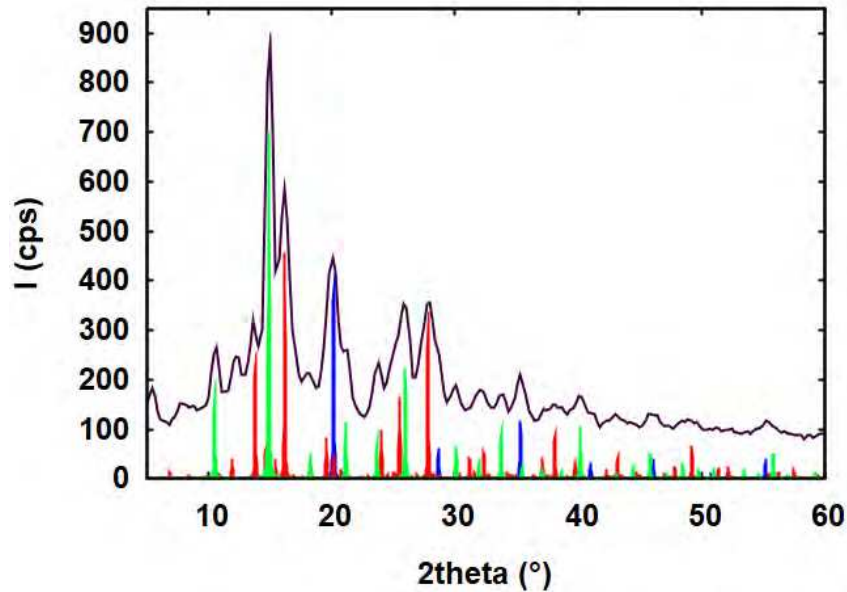


Figure 31. WAXS diagrams of $r\text{-Fe@FeO}_x$ NPs (black solid line) in comparison with bcc-Fe (PDF-01-071-4648, in blue), $\gamma\text{-Fe}_2\text{O}_3$ (PDF-01-089-5894, in red) and NH_4Cl (PDF 96-901-0007, in green) references.

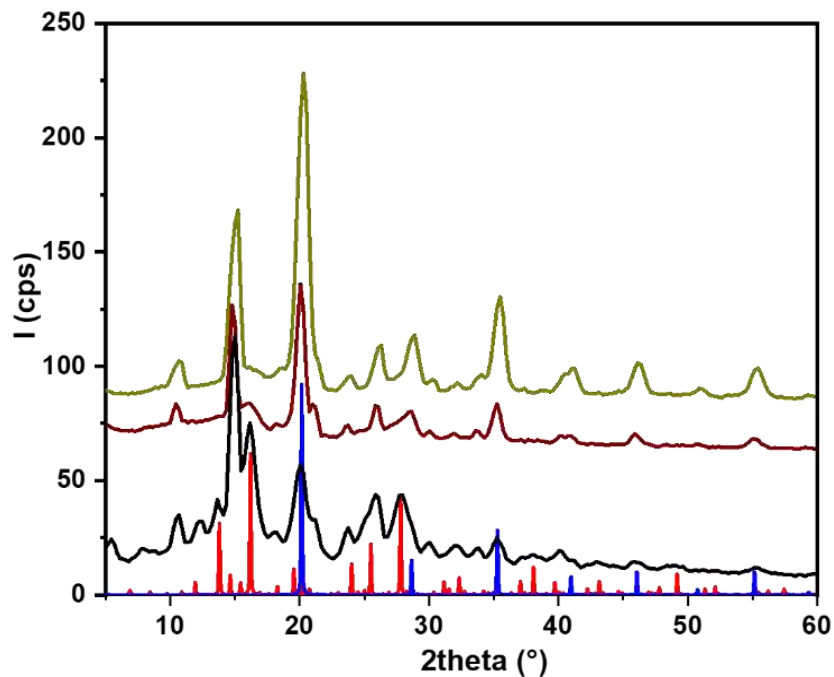


Figure 32. WAXS diagram of $n\text{-Fe@FeO}_x$ NPs (dark yellow line), $a\text{-Fe@FeO}_x$ NPs (burgundi line), $r\text{-Fe@FeO}_x$ NPs (black line), in comparison with bcc-Fe (PDF-01071-4648, blue line) and hypothetical maghemite ($\gamma\text{-Fe}_2\text{O}_3$) (PDF-01-089-5894, red line).

As will be explained later, the ***r*-Fe@FeOx NPs** provided a better starting material for the grafting of the phosphonic acids, so we investigated its properties in more details.

Especially, the persistence of the iron core was also probed by Extended X-Ray Absorption Fine Structure (EXAFS) at Fe *K* absorption edge. Indeed, contrarily to WAXS which puts strong emphasis on large crystalline domains, EXAFS is strictly limited to short range order. This limitation makes it much more sensitive for the analysis of small domains. Moreover, contributions not involving Fe atoms would be by principle rejected. Measurements were thus performed on the ***r*-Fe@FeOx NPs** sample. A pure Fe foil was also measured in the same conditions and additional reference data from pure γ -Fe₂O₃ was imported from the Farrel Lytle Database maintained by the International X-ray Absorption Society. Comparing the Chi function of the ***r*-Fe@FeOx NPs** sample with those of the two references (Figure 33), the pattern of γ -Fe₂O₃ was clearly observed, with however some discrepancies (e.g. 8.2 and 9.5 Å⁻¹).

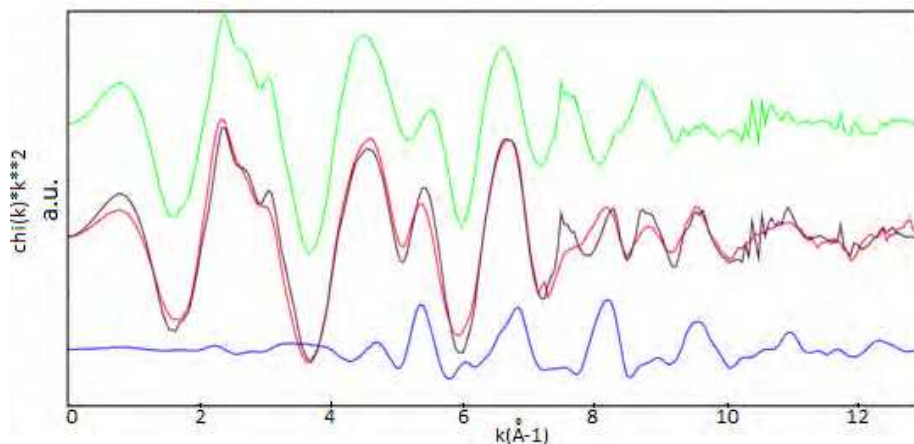


Figure 33. Comparison between *Chi(k)* functions of ***r*-Fe@FeOx NPs** (in black), maghemite (in green), and bcc-Fe (in blue), weighted sum of maghemite (90%) and iron (10%) (in red).

Interestingly, these discrepancies could be clearly attributed to metallic Fe features. Indeed, a model including the short Fe-O bonding distance and the longer Fe-Fe distance with O bridge typical for an iron oxide, as well as the metallic bonding Fe-Fe distance, allowed a good fit of the experimental data especially in the 6-10Å⁻¹ range (Figure 34).

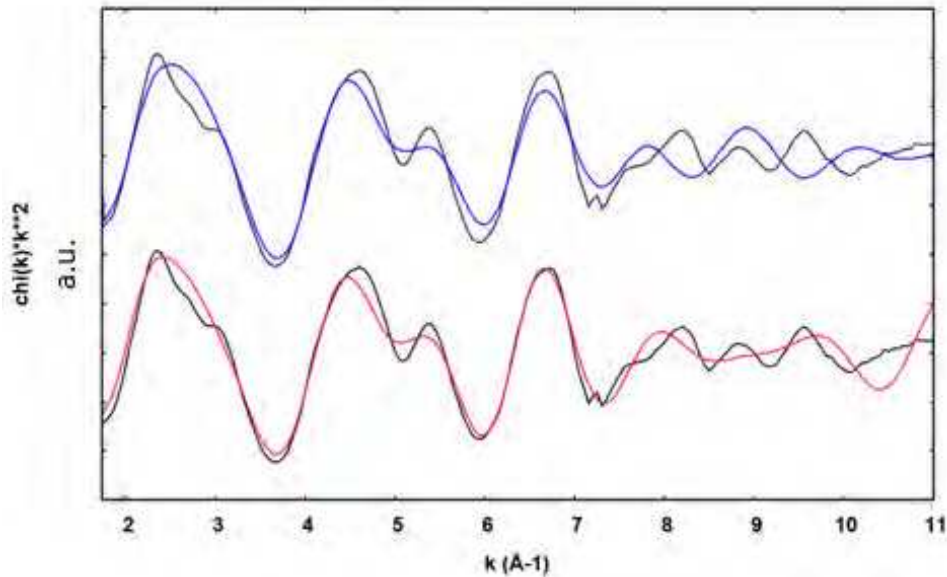


Figure 34. Overlap function $\chi(k)$ of $r\text{-Fe@FeOx}$ NPs (black line) with model 1 (blue line) and model 2 (pink line).

Very good agreement was also observed for the Fourier Transform (Figure 35). A model taking into account more shells could likely provide even better agreement however without providing more insight on a composite sample likely including Fe^{3+} oxide at different degrees of crystallization. For the same reasons quantitative evaluation of the Fe/Fe oxide ratio was not attempted even if a mixed organization is demonstrated.

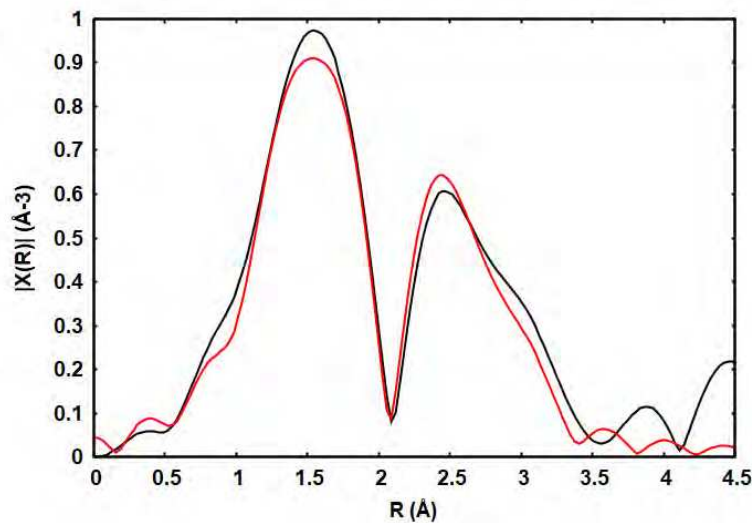


Figure 35. Magnitude of the Fourier Transform of function $\chi(k)$, $r\text{-Fe@FeOx}$ NPs (black line) and best fit achieved (red line)

From the Fe2p spectrum obtained by X-Ray Photoelectron Spectroscopy (XPS), (Figure 36), only binding energies corresponding to Fe³⁺ in an iron oxide environment (710.3 eV) and Fe(0) (706.7 eV) were observed. This confirmed the presence of a residual Fe core and that the oxide was most likely α - or γ - Fe₂O₃, even if the presence of FeOOH species on the top surface couldn't be excluded.

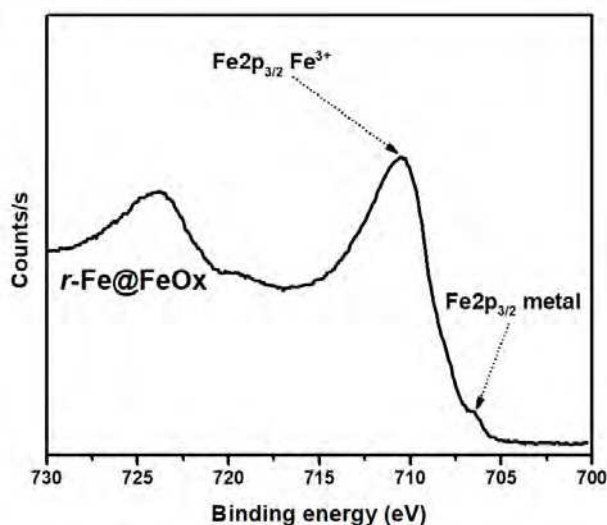


Figure 36. Fe2p XPS spectrum of r-Fe@FeOx NPs

To get a more quantitative evaluation of the Fe/FeOx ratio in the nanoparticles, a Mössbauer spectrum was recorded (Figure 37). The measurement was performed at 80K with a ⁵⁷Co source in a Rh matrix and was calibrated against bulk bcc-Fe. At this temperature and given the size of the nanoparticles, relaxation phenomena on the time scale of Mössbauer spectroscopy (10⁻¹¹ – 10⁻⁹ s) were initially expected to be negligible. Given the morphology of the nanoparticles, the defined lines observed on the spectrum could be attributed to contributions of ferromagnetic iron (FM Fe, 28.9 ± 0.5%) and iron oxide phases (FM Fe oxide, 42.9 ± 0.5%). However, to precisely adjust the experimental curve, two other contributions were introduced: a first one corresponding to iron oxide in superparamagnetic regime (SPM Fe oxide, 26.2 ± 0.5%), and a second one corresponding to a trace of paramagnetic iron (PM Fe, 2 ± 0.2%). Table 2 displays the hyperfine fields, quadrupolar splitting, and corresponding isomer shifts used to fit the spectrum. The parameters used to fit the iron oxide contributions are in good agreement with those expected for γ -Fe₂O₃ at

the nanoscale [32]. The two contributions observed (one FM and the other SPM) could reflect the heterogeneity of the iron oxide shell thickness and polycrystallinity.

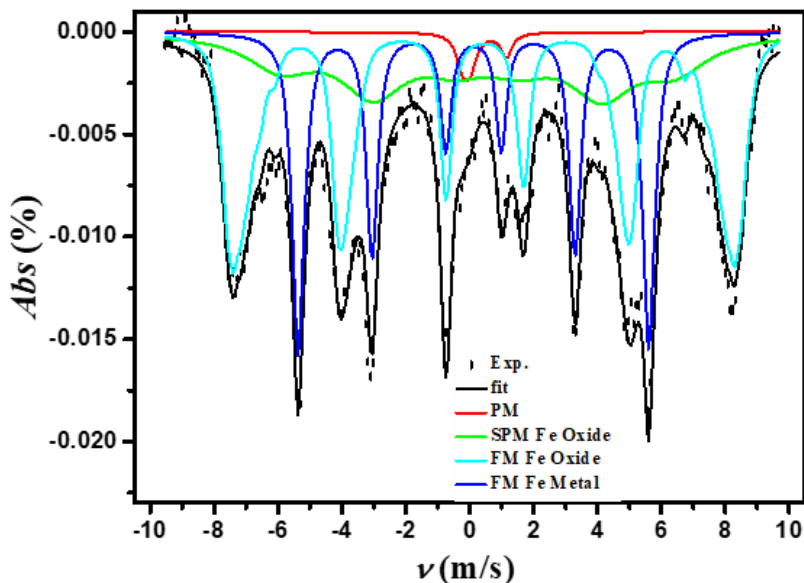


Figure 37. Mössbauer spectrum of *r-Fe@FeOx* NPs recorded at 80K (experimental data in diamonds), and best fit obtained (solid line) from a combination of iron and iron oxide contributions (see legend on the figure)

Table 2. Distributions of the isomeric shifts and hyperfine fields used to fit the experimental Mössbauer spectrum measured at 80 K.

Component	Isomeric shift (mm.s ⁻¹)	Quadrupolar splitting (mm.s ⁻¹)	Hyperfine field (T)
FM Fe	0.11	-	33
FM Fe oxide	0.46	-0.03	Distribution centered around 49 (Figure. 39)
SPM Fe oxide	0.40	-0.3	38.5
PM Fe ²⁺	0.45	1.4	-

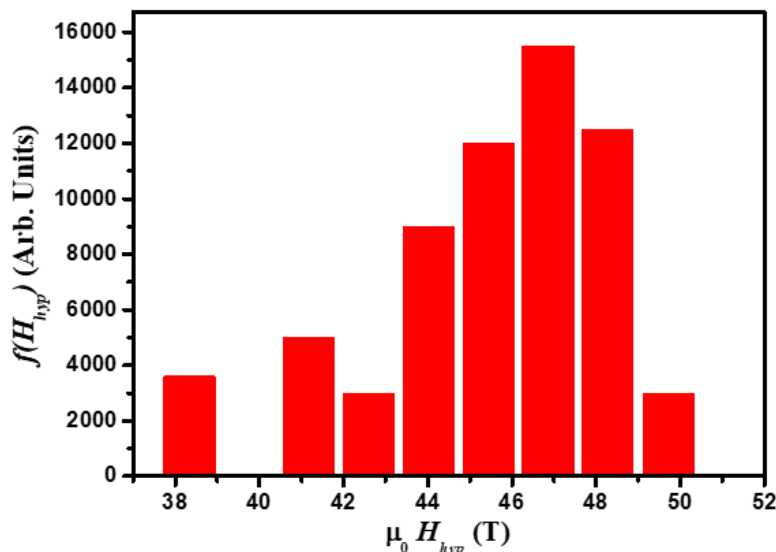


Figure 38. Distribution of hyperfine fields used to fit the FM Fe oxide contribution to the Mössbauer spectrum of the *r*-Fe@FeOx NPs.

From the morphological parameters of the *r*-Fe@FeOx NPs revealed by HR-TEM analysis Figure 29d (core size of *ca.* 7.4 nm and shell thickness of *ca.* 3.9 nm), a lower content of iron in the metallic state, *i.e.* being close to 23 at%, could be expected (See detail in Experimental Section - Section 7.1). The discrepancy between local and statistical investigations confirmed the heterogeneity of the oxide shell and the importance of more statistical analysis techniques to reach a good description of the nanomaterial. Here the average shell thickness should be lower than 3.9 nm. Indeed, the Fe(0)/Fe(III) atomic ratio extracted from fitting the Mossbauer spectrum indicated an average shell thickness of 2.6 nm (See experimental Section - Section 7.2). Thus, the *r*-Fe@FeOx NPs can be best described as core/shell Fe@ γ -Fe₂O₃ nanoparticles of a mean size of 11.5 ± 2.3 nm and an average shell thickness of 2.6 nm. In the following section, we describe the grafting of different amino phosphonic acids on the *r*-Fe@FeOx NPs in order to obtain the water soluble oxidation catalyst.

2.1.3. Water transfer of Fe@FeO_x NPs

In order to find out the effect of the preparation method of the iron oxide layer on the efficiency of the phosphonic acids grafting, the grafting of 3-aminopropyl phosphonic acid (APA) on

iron@iron oxide NPs was performed in identical conditions on both samples ***a*-Fe@FeOx NPs** and ***r*-Fe@FeOx NPs**.

A biphasic process was used following the previous work done by Gharbi *et al.*, in our group[28]. Briefly it consists in mixing an organic phase containing the NPs (here dichloromethane was used as solvent) and an aqueous phase containing the APA at a pH in the 7-8 range. Figure 39 shows the successful transfer of ***r*-Fe@FeOx NPs** from the CH₂Cl₂ phase to the aqueous phase by this process, leading to aqueous dispersions that were stable for a very long time. In the case of ***a*-Fe@FeOx NPs**, after 12 hours of mechanical stirring, the NPs also transferred to the aqueous phase, however they displayed a tendency to come back to the CH₂Cl₂ phase over time as can be seen in the Figure 40 where the ***a*-Fe@FeOx@APA NPs** are located mostly at the interface 1 day after stopping stirring. One possible explanation is that, as the oxidation of ***n*-Fe@FeOx NPs** into ***a*-Fe@FeOx NPs** (1st approach) was performed in the solid state, it might lead to very aggregated ***a*-Fe@FeOx NPs** (as stated above, this sample couldn't be fully dispersed in solution). Consequently, the accessible surface would be less than for the ***r*-Fe@FeOx NPs** sample leading to a lower grafting density of APA. As a result, the ***a*-Fe@FeOx@APA NPs** is not hydrophilic enough to afford water dispersion that would be stable over a long term, when in contact with the organic phase. Even trying to break the aggregates by crushing the ***a*-Fe@FeOx NPs** before grafting with APA, did not significantly improve the result as can be seen in Figure 40. In the 2nd approach, oxidation was performed in solution (with the NPs were dispersed in ODE), avoiding the aggregation of the NPs.

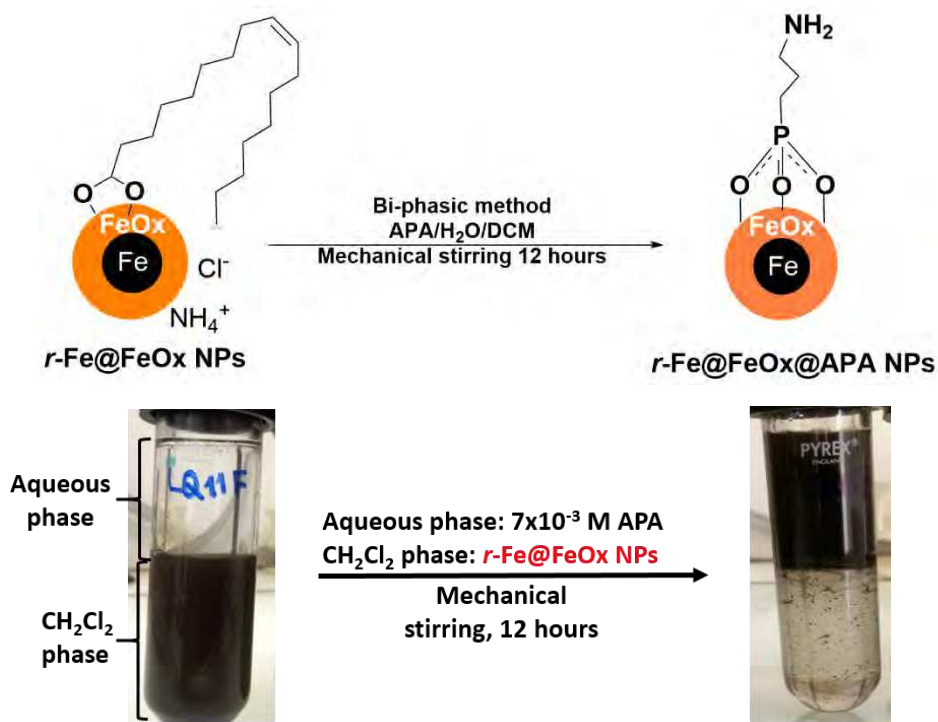


Figure 39. Synthesis pathway (top) and Photograph of the reaction medium when APA to **r-Fe@FeOx** NPs by a biphasic method (CH₂Cl₂/MilliQwater) (bottom).

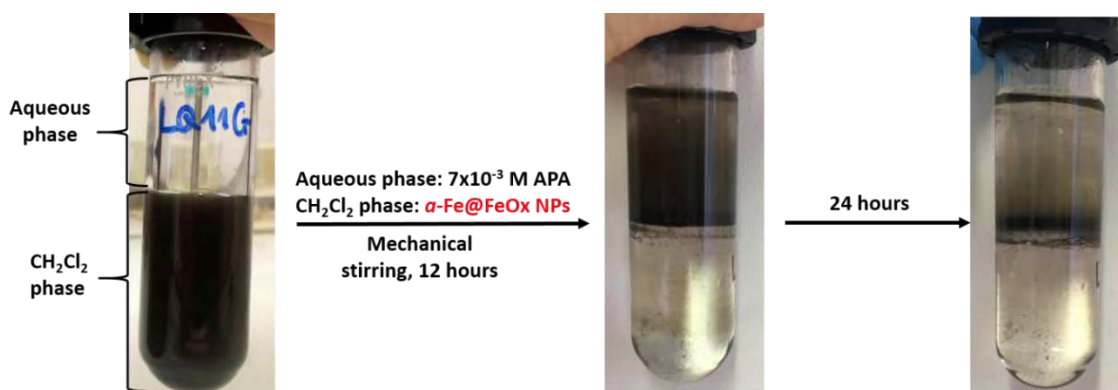


Figure 40. Photograph of the reaction medium when grafting APA to **α -Fe@FeOx** NPs by a biphasic method (CH₂Cl₂/MilliQwater).

The synthesized **r-Fe@FeOx@APA** NPs were then characterized by TEM and FT-IR.

The interaction between phosphonate derivatives and iron oxide NPs has been extensively studied[33] and FT-IR spectroscopy is one of the most effective techniques used to confirm the grafting of phosphonate derivatives on the surface of metal oxides. FT-IR spectra of *r*-Fe@FeOx NPs before and after grafting of APA are compared in Figure 41. The IR spectrum of *r*-Fe@FeOx NPs was relatively flat, and only traces of oleic acid and NH₄Cl could be observed. After grafting with APA, a broad band was observed in the 900-1168 cm⁻¹ range *i.e.* in a region where Fe-O-P vibrations are expected. This indicates that the 3- amino propyl phosphonic acid was successfully grafted through a covalent bonding [28, 34, 35]. This broad band was often observed after phosphatation of iron oxides such as hematite, goethite, and magnetite [36-38]. Furthermore, the presence of only one broad peak in this region also suggests that APA was probably grafted through a symmetrically tridentate binding mode rather than bidentate mode or mono-dentate mode (scheme 4) as we cannot observe any vibration of either P=O (1123 cm⁻¹) or P-OH (924 and 1004 cm⁻¹) bonds. It is worth to note that this analysis is in agreement with several studies published before[39, 40].

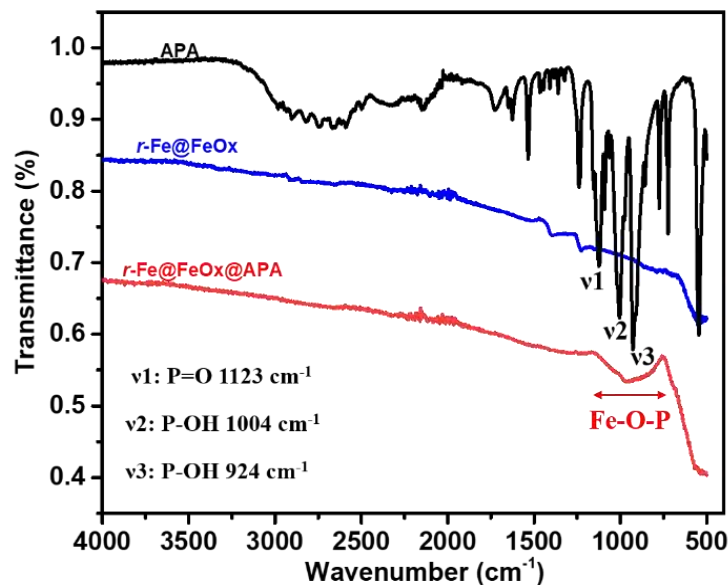
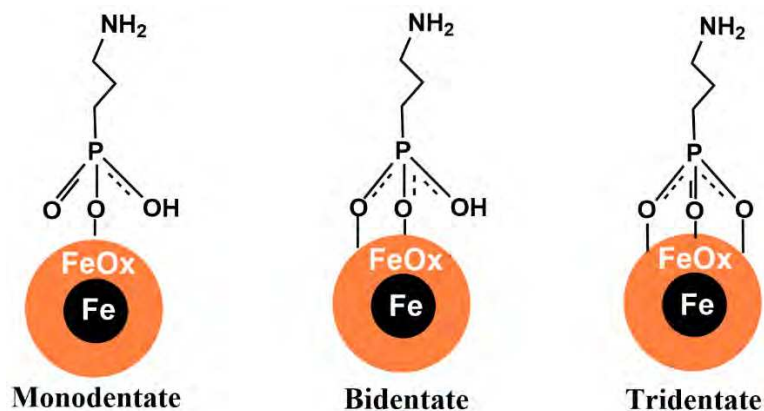


Figure 41. FT-IR of *r*-Fe@FeOx NPs, *r*-Fe@FeOx@APA NPs, and APA



Scheme 4. Possible bonding modes of APA

Figure 42 shows the TEM images of the NP before and after grafting with APA. It must be noted that the solvents used to disperse *r*-Fe@FeOx NPs and *r*-Fe@FeOx@APA NPs for drop-casting on the TEM grids were toluene and water, respectively. A layer of light contrast is observed at the surface of the NPs (Figure 42b). This layer could come from the organic layer of APA. This was also observed in the work of Basly *et al.*, in which they studied the grafting of phosphonate dendrons on the surface of iron oxide (Fe_{3-δ}O₄) NPs [35]. No significant change in the size of the NPs can be observed.

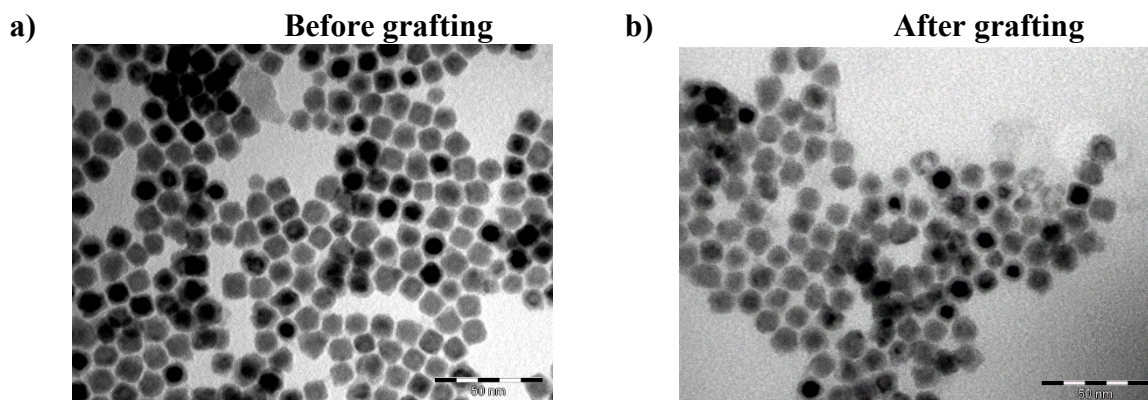


Figure 42. Typical HR-TEM images of a) *r*-Fe@FeOx NPs (scale bar= 50 nm), and b) *r*-Fe@FeOx@APA NPs (scale bar =50 nm)

For comparison purposes, a control experiment was performed on *r*-Fe@FeOx NPs where *r*-Fe@FeOx NPs were dispersed CH₂Cl₂ by sonication for 30 minutes. Then, MilliQ water was added and the immiscible mixture was mechanically stirred for 6 days. No color change of the

aqueous phase could be observed (Figure 43), indicating that in the absence of APA, the NPs couldn't be transferred into water (confirming their hydrophobic character).

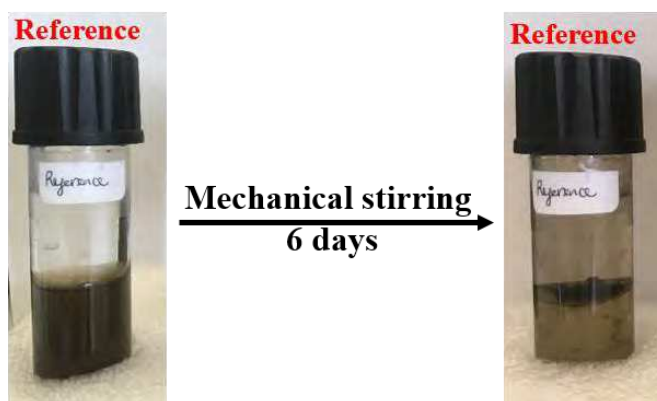
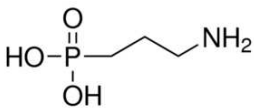
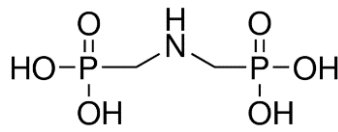
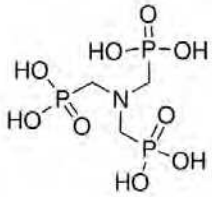
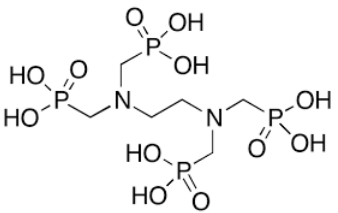


Figure 43. Photograph of the control experiment proving that without APA, the $r\text{-Fe@FeOx}$ NPs could not be transferred to the aqueous phase.

The same grafting procedure was then performed on other aminophosphonic acids presenting different numbers of phosphonic groups in their chemical structure (Table 3) to test the generality of the process. In this case, the pH of the aqueous phase was set above 9 for IMPA, ATMP, and EDTMPA solutions, as we observed that it favored the grafting of phosphonic acid group on the NP (see Experimental section – Section 2.2.4). After 6 days of mechanical stirring the NPs were successfully transferred to the aqueous phase, as can be seen in Figure 44. Collecting the grafted NPs from the aqueous phase, then washing them 5 times with MilliQ water, once time with ethanol, and finally with diethyl ether afforded NPs hereafter referred to as $r\text{-Fe@FeOx@IMPA}$ NPs, $r\text{-Fe@FeOx@ATMPA}$ NPs, and $r\text{-Fe@FeOx@EDTMPA}$ NPs.

Table 3. Aminophosphonic acids used in this study.

No.	Chemical name	Label	Chemical structure	pKa
1	3-aminopropyl phosphonic acids	APA		$pK_{a1}= 2.1, pK_{a2}= 6.4, pK_{a3}= 10.5$
2	Iminodi (methylphosphonic acid)	IMPA		values not found
3	Aminotris(methylenephosphonic acid)	ATMPA		$pK_{a1} < 2, pK_{a2} < 2, pK_{a3} = 4.30,$ $pK_{a4} = 5.4, pK_{a5} = 6.6, pK_{a6} = 12.3$
4	Ethylenediamine tetra (methylene phosphonic acid)	EDTMPA		$pK_{a4} = 1.16, pK_{a5} = 2.80, pK_{a6} = 5.00$ $pK_{a7} = 6.24, pK_{a8} = 7.72, pK_{a9} = 9.64$

For EDTMPA: pK_{a1} , pK_{a2} , and pK_{a3} could not be measured in water because they are too low and pK_{a10} could not be measured because it is too high[41].

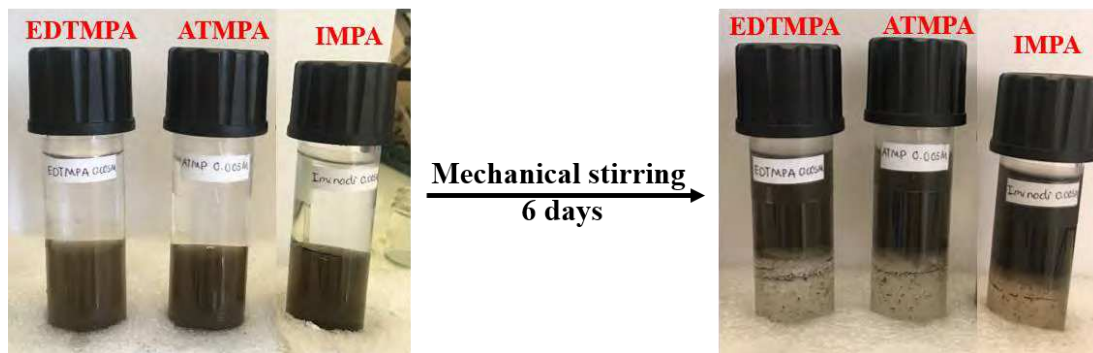


Figure 44. Photograph of the reaction medium when grafting EDTMPA, ATMPA, IMPA to $r\text{-Fe@FeOx}$ NPs by a biphasic method ($\text{CH}_2\text{Cl}_2/\text{MilliQwater}$).

FT-IR was used to characterize the grafted NPs as can be seen in Figure 45. The spectra of the grafted NPs ($r\text{-Fe@FeOx@IMPA}$ NPs, $r\text{-Fe@FeOx@ATMPA}$ NPs, and $r\text{-Fe@FeOx@EDTMPA}$ NPs) are relatively flat, only one broad band in the region dedicated to Fe-O-P ($900\text{-}1200\text{ cm}^{-1}$) bonds can be observed which indicates the possibility of grafting different aminophosphonic acids on the surface of $r\text{-Fe@FeOx}$ NPs.

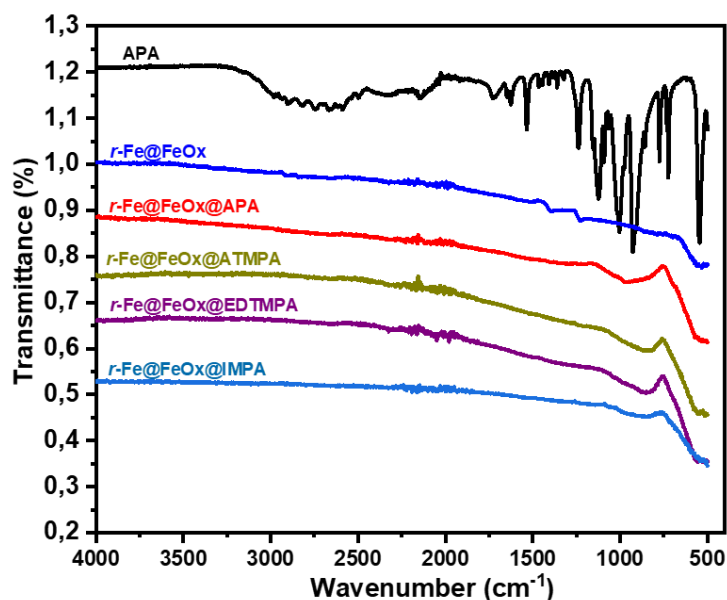


Figure 45. FT-IR of $r\text{-Fe@FeOx@APA}$ NPs (red curve), $r\text{-Fe@FeOx@ATMPA}$ NPs (dark yellow curve), $r\text{-Fe@FeOx@EDTMPA}$ NPs (purple curve), $r\text{-Fe@FeOx@IMPA}$ NPs (cyan curve) in comparison with pristine $r\text{-Fe@FeOx}$ NPs (blue curve), and APA (black curve).

The $r\text{-Fe@FeOx@IMPA}$ NPs, $r\text{-Fe@FeOx@ATMPA}$ NPs, and $r\text{-Fe@FeOx@EDTMPA}$ NPs were characterized by TEM as shown in Figure 46. After water transfer the NPs retain their initial shape even after a few months (note that the TEM images were recorded from drop casting of aged solutions).

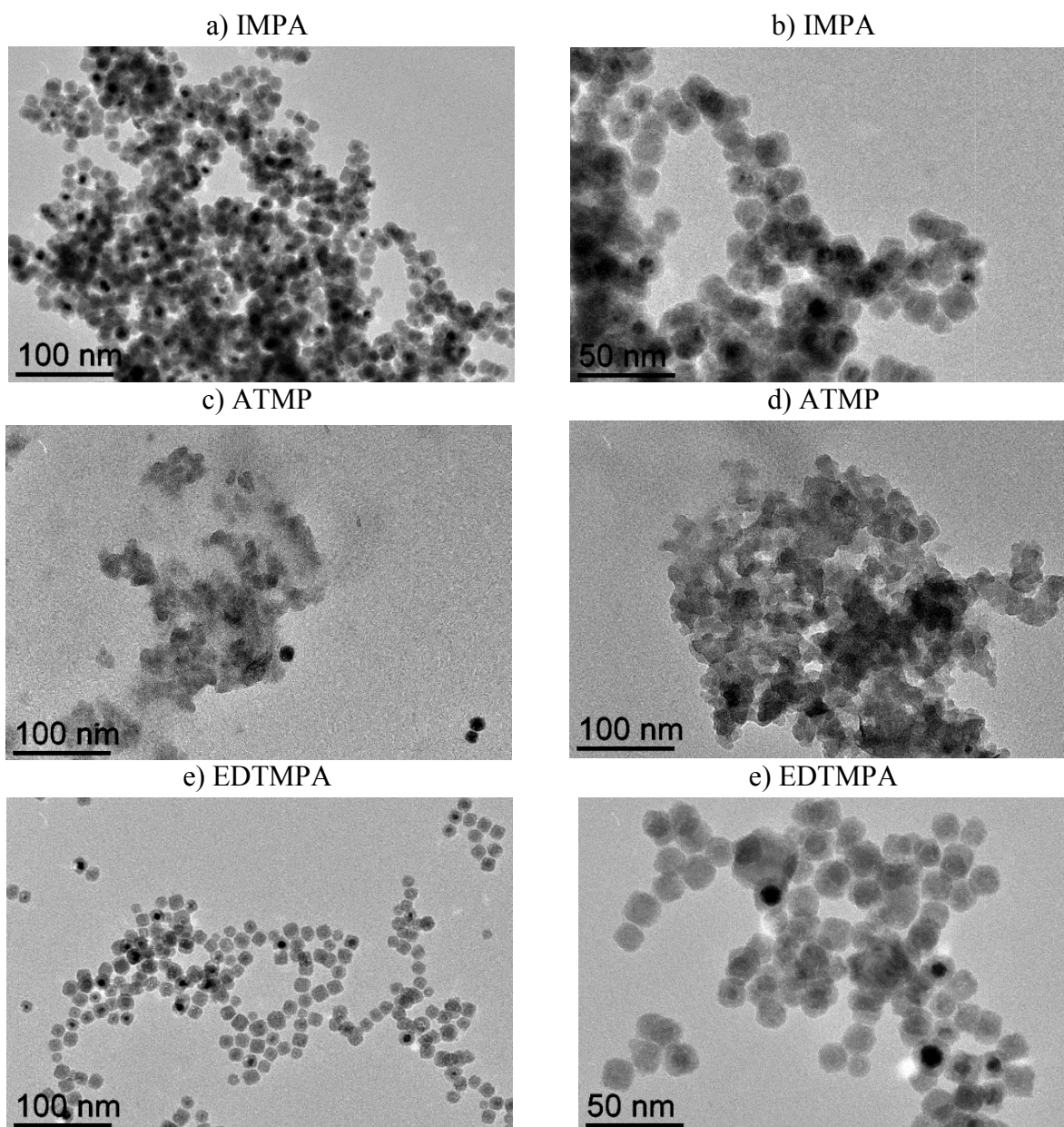


Figure 46. TEM images of Fe@FeOx NPs grafted with IMPA (a, b), ATMP (c, d), and EDTMPA (e, f) after purification process and 4 months of storage.

These experiments show that the process can be easily generalized to many aminophosphonic acids. In case of APA, the transfer could be achieved at slightly basic pH (7-8). Taking into account

the value of the pH_i of maghemite (*ca.* 7.5), the surface of the NPs should be close to neutral in these conditions, while the APA should be negatively charged given the value of its pK_a (see Table 3), leading to favorable interactions between APA and the NP. In comparison, grafting of IMPA, ATMP and EDTMPA was best achieved in more basic conditions, where both the aminophosphonic acid and the maghemite are supposed to be negatively charged thus inducing electrostatic repulsions between the reactants. Still, the grafting was efficient in agreement with an interaction that takes place only at the interface. It further shows that the key factor for an efficient grafting is the presence of deprotonated phosphonate groups.

We will now report on the studies of the catalytic activity of these nanomaterials in OER.

2.2. Electrocatalytic activity of *r*-Fe@FeOx NPs and *r*-Fe@FeOx@APAs NPs in OER

The electrocatalytic activity of a material for OER is primarily evaluated on the basis of the onset potential and Tafel slope. Whereas, the former represents the minimum potential required for OER, the latter characterizes the effect of an increase in applied potential on the current density. Besides, the potential required to achieve a current density of 10 mA/cm^2 is also an important parameter as it corresponds to a benchmark solar fuel generation efficiency of 10 %. The electrocatalytic performance of *r*-Fe@FeOx NPs in OER was studied in pH 7 (phosphate buffer 0.1M KPi) and in a pH 13 alkaline electrolyte (0.1 M NaOH) (see detail in section 3-experimental section). A catalyst ink made of *r*-Fe@FeOx NPs dispersed in a EtOH/water solvent mixture together with $1 \mu\text{l}$ Nafion 5% (w%) as a linker was drop-casted on a Fluorine-doped Tin Oxide (FTO) electrode at a mass loading density of $1.8 \times 10^{-4} \text{ g/cm}^2$ (Figure 47). The resultant catalyst electrode was then assayed by linear sweep voltammetry (LSV) at potential scan rate of 5mV/s in both pH 7 and pH 13. In pH 13, it operated with an onset potential of $\sim 1.75 \text{ V vs. RHE}$ and a Tafel slope value of 142 mV/decade could be deduced from the data (Figure 48, black trace). In pH 7, it showed a much higher onset potential of $\sim 1.95 \text{ V}$ as well as a higher Tafel slope value of 207 mV/decade (Figure 48, red trace). This assay demonstrated that the *r*-Fe@FeOx NPs sample is an active catalyst for OER, and that it is significantly more active in alkaline solution.



Figure 47. Drop-casting *r-Fe@FeOx* NPs on an FTO electrode for testing water oxidation catalytic activity at pH 7 and pH 13.

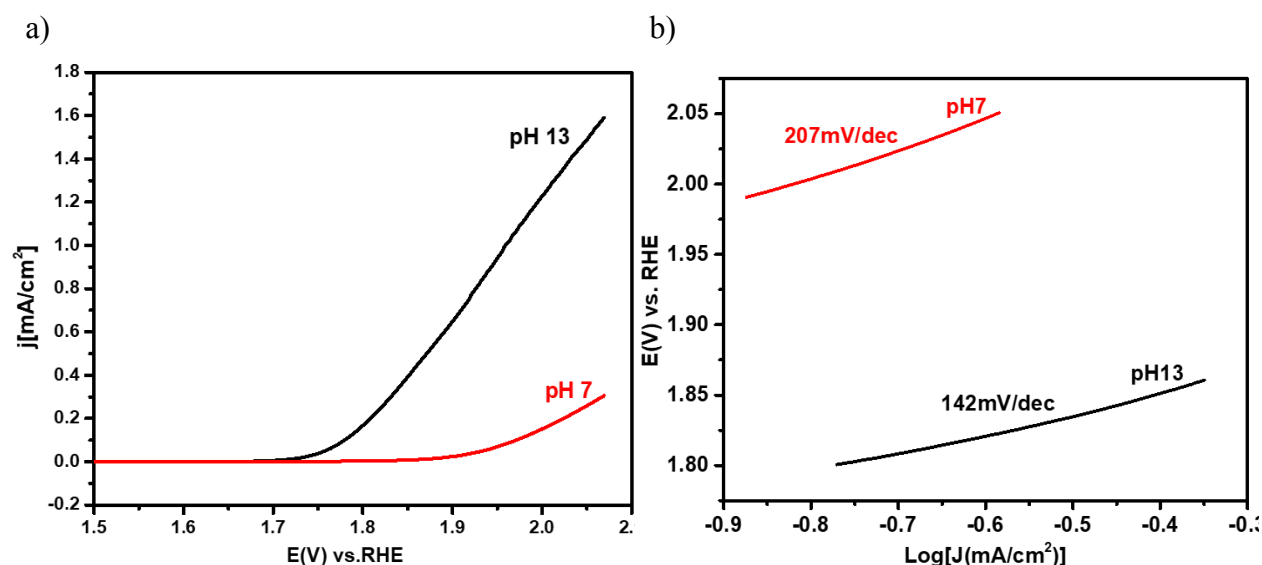


Figure 48. a) Polarization curves of a *r-Fe@FeOx* NPs electrode recorded in pH 7 (red line) and pH 13 (black line) electrolyte solutions, potential scan rate was 5 mV/s. b) Tafel slope of *r-Fe@FeOx* NPs electrode in pH 7 (red line) and pH 13 (black line).

For lack of time, we couldn't investigate the electrocatalytic activity of all the samples prepared, and only APA and EDTMPA functionalized NPs were studied. The electrocatalytic activity of *r-Fe@FeOx@APA* NPs, and *r-Fe@FeOx@EDTMPA* NPs are compared with that of the pristine *r-Fe@FeOx* NPs in Figure 49. Grafting APA on *r-Fe@FeOx* NPs obviously enhanced the catalytic activity of *r-Fe@FeOx* NPs as the onset potential shifted from 1.75 V to 1.62 V vs. RHE. The Tafel plot was drawn and it showed a strongly decreased slope from 142 mV/decade to 30 mV/decade for the pristine *r-Fe@FeOx* NPs and *r-Fe@FeOx@APA* NPs, respectively (Figure

50). Meanwhile, grafting EDTMPA on *r-Fe@FeOx* NPs did not show significant change in terms of catalytic current and Tafel slope.

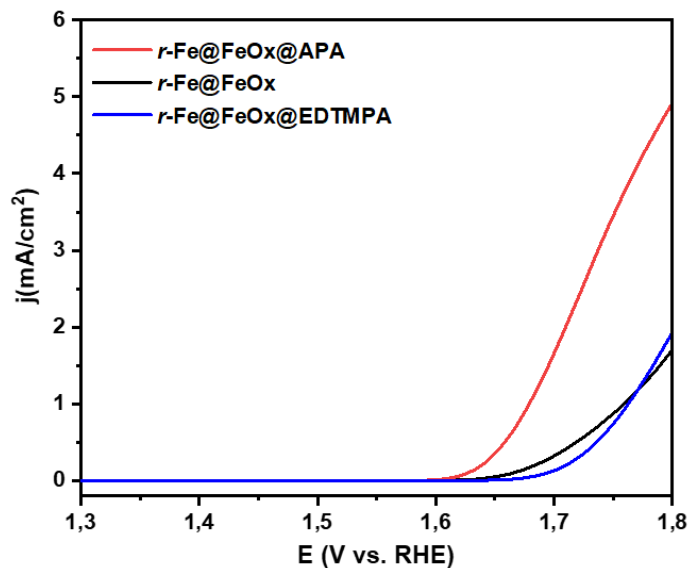


Figure 49. Polarization curves of a *r-Fe@FeOx* NPs (black trace), *r-Fe@FeOx@APA* NPs (red trace), and *r-Fe@FeOx@EDTMPA* NPs (blue trace) electrode recorded in pH 13 electrolyte solutions, potential scan rate was 5 mV/s.

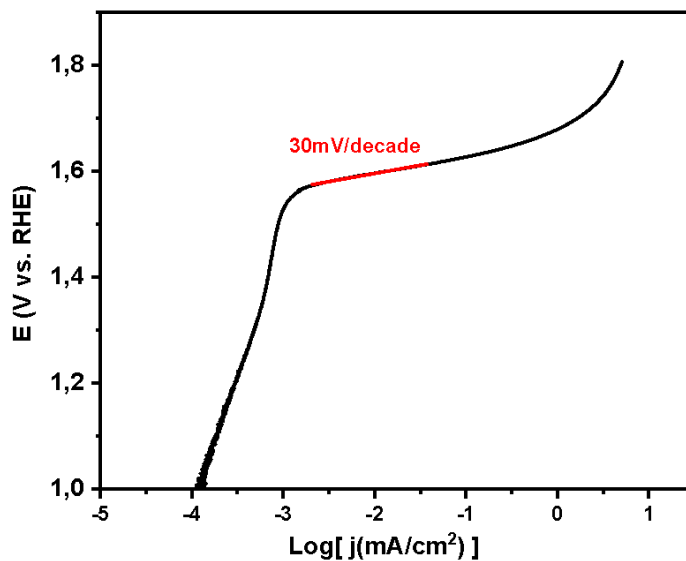


Figure 50. Tafel slope deduced from polarization curve of *r-Fe@FeOx@APA* NPs recorded in pH 13 electrolyte solutions, potential scan rate was 5 mV/s.

The electrocatalytic performances of *r*-Fe@FeOx NPs and *r*-Fe@FeOx@APA NPs were then compared with that of other electrocatalysts reported in the literature as depicted in Table 4, showing that the *r*-Fe@FeOx@APA NPs sample presents the lowest Tafel slope.

Table 4: Comparison of the results from our work to data from already reported Fe oxide –based electrocatalysts.

No.	Catalysts	Synthetic method	Morphology	Substrate	Electrolyte	η (mV vs. RHE)	η_{10} (V vs. RHE)	Tafel slope (mV/dec)	TOF (s ⁻¹)	Ref.	Pub. year
1	Passive Fe oxide	_a	_Thin film?	Fe metal foil	NaOH 1 M	–	–	≈ 46	–	[4]	2010
2	amorphous Fe ₂ O ₃	Photochemical metal-organic deposition at low-temperature process	Amorphous Thin film 100-200 nm	FTO electrode	KOH 0.1 M	320	0.4 (j=0.5mA/cm ²)	40	–	[5]	2013
3	α -Fe ₂ O ₃ NA/CC	Chemical bath deposition	Nano array α -Fe ₂ O ₃ on carbon cloth	Carbon Cloth	KOH 0.1 M	330	0.42	52	–	[12]	2014
4	Fe ₂ O ₃ ^b	Commercial vendors	NPs Size < 5 μ m	Glass carbon electrode	NaOH 1 M	–	1.24	– ^c	–	[2]	2016
5	FeOx	Anodic electrodeposition	Thin film 2-5 nm	Au-coated 10 MHz quartz crystal substrate	KOH 1 M	–	–	–	–	[6]	2016
	Polycrystalline		α -Fe ₂ O ₃ hollow nanorod		KOH				–	[13]	

6	α -Fe ₂ O ₃ /CNT	Hydrolyzing FeCl ₃ on CNT	~35-40 nm in length 5-10 nm in width	Glassy carbon	1M	–	0.383	68			2016
8	γ -Fe ₂ O ₃ /CNT	CVD	6.3 nm NPs	Rotating disk (glassy carbon) electrode	NaOH 1 M	–	0.340	54	–	[14]	2016
9	Crystalline Fe ₂ O ₃ (mixed of α -Fe ₂ O ₃ and γ -Fe ₂ O ₃)	Spray pyrolysis deposition	Polymorph film <1.5 μ m	Ti foils substrates	H ₂ SO ₄ 0.5 M		0.65	56		[5]	2018
10	2L-Fe ₂ O ₃ /Au	UHV science surface	5-6 nm NPs to near monolayer of Fe ₂ O ₃ on Au substrates	Au electrode	KOH 0.1 M	320	–	77.6	36.8 (O ₂ /atom Fe)	[8]	2019
11	<i>r</i> -Fe@ γ -Fe ₂ O ₃	Organometallic decomposition	NPs Size ~11.5 nm	FTO electrode	NaOH 0.1 M	~520	–	142		This work	2021
12	<i>r</i> -Fe@ γ -Fe ₂ O ₃ @APA	Organometallic decomposition	~11.5 nm	FTO electrode	NaOH 0.1 M	390	–	30		This work	2021

a: passive iron oxide layer on Iron metal polycrystalline anode (Fe metal foils).

b: α -Fe₂O₃ or γ -Fe₂O₃ phase not specified

c: the specific current density and the Tafel slope were not reported because the Fe₂O₃ NPs catalyst degraded during steady state measurement.

3. Conclusions

In summary, well-controlled *r*-Fe@FeOx core-shell nanoparticles were synthesized. These nanoparticles showed a better O₂-evolution electrocatalytic activity in alkaline conditions than in neutral ones, with an onset overpotential of 1.75 V and a Tafel slope value of 142 mV/decade at pH 13. Subsequently, these *r*-Fe@FeOx core-shell NPs were grafted with different aminophosphonic acids in order to improve the hydrophilicity of their surface and beyond their catalytic activity for OER. For lack of time, we couldn't investigate the electrocatalytic activity of all the samples prepared, and only APA and EDTMPA functionalized NPs were studied. This study shows for the first time that Fe@FeOx NPs grafted with APAs can be used as water oxidation catalyst.

Our studies open the door to a new strategy to synthesize OER nanocatalysts by the organometallic method as one of the simplest and powerful techniques in controlling the size and morphology of small NPs. Ligand exchange by phosphonic acids proves a good and general method to transfer these NPs into water and afford active catalysts in OER.

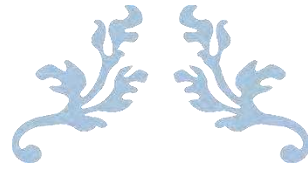
4. References

1. Song, F., et al., *Transition Metal Oxides as Electrocatalysts for the Oxygen Evolution Reaction in Alkaline Solutions: An Application-Inspired Renaissance*. Journal of the American Chemical Society, 2018. **140**(25): p. 7748-7759.
2. Jung, S., et al., *Benchmarking nanoparticulate metal oxide electrocatalysts for the alkaline water oxidation reaction*. Journal of Materials Chemistry A, 2016. **4**(8): p. 3068-3076.
3. Feng, C., et al., *Fe-Based Electrocatalysts for Oxygen Evolution Reaction: Progress and Perspectives*. ACS Catalysis, 2020. **10**(7): p. 4019-4047.
4. Lyons, M.E.G. and M.P. Brandon, *A comparative study of the oxygen evolution reaction on oxidised nickel, cobalt and iron electrodes in base*. Journal of Electroanalytical Chemistry, 2010. **641**(1): p. 119-130.
5. Smith, R.D.L., et al., *Photochemical Route for Accessing Amorphous Metal Oxide Materials for Water Oxidation Catalysis*. Science, 2013. **340**(6128): p. 60-63.
6. Morales-Guio, C.G., L. Liardet, and X. Hu, *Oxidatively Electrodeposited Thin-Film Transition Metal (Oxy)hydroxides as Oxygen Evolution Catalysts*. Journal of the American Chemical Society, 2016. **138**(28): p. 8946-8957.
7. Kwong, W.L., et al., *High-performance iron (III) oxide electrocatalyst for water oxidation in strongly acidic media*. Journal of Catalysis, 2018. **365**: p. 29-35.
8. Kauffman, D.R., et al., *Edge-Enhanced Oxygen Evolution Reactivity at Ultrathin, Au-Supported Fe₂O₃ Electrocatalysts*. ACS Catalysis, 2019. **9**(6): p. 5375-5382.
9. Zhao, Y., et al., *Graphene-Co₃O₄ nanocomposite as electrocatalyst with high performance for oxygen evolution reaction*. Scientific Reports, 2015. **5**(1): p. 7629.
10. Andersen, N.I., A. Serov, and P. Atanassov, *Metal oxides/CNT nano-composite catalysts for oxygen reduction/oxygen evolution in alkaline media*. Applied Catalysis B: Environmental, 2015. **163**: p. 623-627.
11. Yuan, W., et al., *Ni foam supported three-dimensional vertically aligned and networked layered CoO nanosheet/graphene hybrid array as a high-performance oxygen evolution electrode*. Journal of Power Sources, 2016. **319**: p. 159-167.
12. Liu, Q., A.M. Asiri, and X. Sun, *Hematite nanorods array on carbon cloth as an efficient 3D oxygen evolution anode*. Electrochemistry Communications, 2014. **49**: p. 21-24.
13. Bandal, H.A., et al., *Fe₂O₃ hollow nanorods/CNT composites as an efficient electrocatalyst for oxygen evolution reaction*. Electrochimica Acta, 2016. **222**: p. 1316-1325.
14. Tavakkoli, M., et al., *Maghemite nanoparticles decorated on carbon nanotubes as efficient electrocatalysts for the oxygen evolution reaction*. Journal of Materials Chemistry A, 2016. **4**(14): p. 5216-5222.
15. Gehring, A.U., et al., *High temperature stability of natural maghemite: a magnetic and spectroscopic study*. Geophysical Journal International, 2009. **179**(3): p. 1361-1371.
16. Li, S.-C., et al., *Correlation between Bonding Geometry and Band Gap States at Organic-Inorganic Interfaces: Catechol on Rutile TiO₂(110)*. Journal of the American Chemical Society, 2009. **131**(3): p. 980-984.
17. Takijiri, K., et al., *Highly stable chemisorption of dyes with pyridyl anchors over TiO₂: application in dye-sensitized photoelectrochemical water reduction in aqueous media*. Chemical Communications, 2017. **53**(21): p. 3042-3045.

18. Nann, T., et al., *Water Splitting by Visible Light: A Nanophotocathode for Hydrogen Production*. *Angewandte Chemie International Edition*, 2010. **49**(9): p. 1574-1577.
19. Queffelec, C., et al., *Surface Modification Using Phosphonic Acids and Esters*. *Chemical Reviews*, 2012. **112**(7): p. 3777-3807.
20. Guerrero, G., et al., *Phosphonate coupling molecules for the control of surface/interface properties and the synthesis of nanomaterials*. *Dalton Transactions*, 2013. **42**(35): p. 12569-12585.
21. Schuschke, C., et al., *Phosphonic Acids on Well-Ordered CoO Surfaces: The Binding Motif Depends on the Surface Structure*. *The Journal of Physical Chemistry C*, 2018. **122**(28): p. 16221-16233.
22. Pankhurst, Q.A., et al., *Applications of magnetic nanoparticles in biomedicine*. *Journal of Physics D: Applied Physics*, 2003. **36**(13): p. R167-R181.
23. Lu, A.-H., E.L. Salabas, and F. Schüth, *Magnetic Nanoparticles: Synthesis, Protection, Functionalization, and Application*. *Angewandte Chemie International Edition*, 2007. **46**(8): p. 1222-1244.
24. Basly, B., et al., *Dendronized iron oxide nanoparticles as contrast agents for MRI*. *Chemical Communications*, 2010. **46**(6): p. 985-987.
25. Guerrero, G., P.H. Mutin, and A. Vioux, *Anchoring of Phosphonate and Phosphinate Coupling Molecules on Titania Particles*. *Chemistry of Materials*, 2001. **13**(11): p. 4367-4373.
26. Mutin, P.H., G. Guerrero, and A. Vioux, *Hybrid materials from organophosphorus coupling molecules*. *Journal of Materials Chemistry*, 2005. **15**(35-36): p. 3761-3768.
27. Gao, W., et al., *Self-Assembled Monolayers of Alkylphosphonic Acids on Metal Oxides*. *Langmuir*, 1996. **12**(26): p. 6429-6435.
28. Gharbi, K., et al., *Alkyl phosphonic acid-based ligands as tools for converting hydrophobic iron nanoparticles into water soluble iron-iron oxide core-shell nanoparticles*. *New Journal of Chemistry*, 2017. **41**(20): p. 11898-11905.
29. Trivedi, M.K., et al., *Fourier Transform Infrared and Ultraviolet-Visible Spectroscopic Characterization of Ammonium Acetate and Ammonium Chloride: An Impact of Biofield Treatment*. *Modern Chemistry & Applications*, 2015. **3**(3).
30. Mathieu, P., et al., *Silica Coated Iron/Iron Oxide Nanoparticles as a Nano-Platform for T2 Weighted Magnetic Resonance Imaging*. *Molecules*, 2019. **24**(24): p. 4629.
31. Peng, S., et al., *Synthesis and Stabilization of Monodisperse Fe Nanoparticles*. *Journal of the American Chemical Society*, 2006. **128**(33): p. 10676-10677.
32. da Costa, G.M., E. De Grave, and R.E. Vandenberghe, *Mössbauer studies of magnetite and Al-substituted maghemites*. *Hyperfine Interactions*, 1998. **117**(1): p. 207-243.
33. Schmitt, C., *Surface modification of oxide nanoparticles using phosphonic acids : characterization, surface dynamics, and dispersion in sols and nanocomposites*. 2015, Université Montpellier.
34. Parikh, S.J. and J. Chorover, *ATR-FTIR Spectroscopy Reveals Bond Formation During Bacterial Adhesion to Iron Oxide*. *Langmuir*, 2006. **22**(20): p. 8492-8500.
35. Basly, B., et al., *Effect of the nanoparticle synthesis method on dendronized iron oxides as MRI contrast agents*. *Dalton Transactions*, 2013. **42**(6): p. 2146-2157.
36. Arai, Y. and D.L. Sparks, *ATR-FTIR Spectroscopic Investigation on Phosphate Adsorption Mechanisms at the Ferrihydrite-Water Interface*. *Journal of Colloid and Interface Science*, 2001. **241**(2): p. 317-326.

37. Luengo, C., et al., *Kinetics of phosphate adsorption on goethite: Comparing batch adsorption and ATR-IR measurements*. Journal of Colloid and Interface Science, 2006. **300**(2): p. 511-518.
38. Daou, T.J., et al., *Phosphate Adsorption Properties of Magnetite-Based Nanoparticles*. Chemistry of Materials, 2007. **19**(18): p. 4494-4505.
39. Mohapatra, S. and P. Pramanik, *Synthesis and stability of functionalized iron oxide nanoparticles using organophosphorus coupling agents*. Colloids and Surfaces A: Physicochemical and Engineering Aspects, 2009. **339**(1): p. 35-42.
40. Ramsier, R.D., P.N. Henriksen, and A.N. Gent, *Adsorption of phosphorus acids on alumina*. Surface Science, 1988. **203**(1): p. 72-88.
41. Di Marco, V., et al., *Complexation Properties of Ethylenediaminetetramethylenephosphonic Acid (EDTMP) with Al(III) and V(IV)*. European Journal of Inorganic Chemistry, 2004. **2004**(12): p. 2524-2532.

Chapter II – Fe@FeOx@APAs



Chapter III- Fe@FeOx NPs grafted with a Ru complex for photocatalysed water splitting



INSA – Toulouse – France 2020

Table of contents – Chapter III

1. Introduction.....	93
2. Synthesis and characterization of the [Ru-PO(OH) ₂]-Cl ₂ ·7H ₂ O.....	106
3. Synthesis and characterization of hybrid nanomaterials PS-Fe@FeO _x NPs.....	114
4. Photo-electrochemical water oxidation catalysis	127
5. Conclusion	133
6. References	137

Chapter III – Fe@FeOx@Ru photoanode

Chapter III- Fe@FeOx NPs grafted with a Ru complex for photocatalysed water splitting

This work was carried out in collaboration with Pr. Gilles Lemerrier and Dr. Elodie Rousset at ICMR (Institut de Chimie Moleculaire de Reims) for the synthesis of the Ru based photosensitizers.

1. Introduction

In general, a photoanode combines a *light-harvester* for photon harvesting and a *catalyst* for accelerating the OER. N-type semiconductors like TiO₂,[1] BiVO₄,[2-5] α -Fe₂O₃[6, 7] or molecular dyes like ruthenium trisbipyridine complexes,[8-10] perylene,[11-14] polyheptazine,[15-17] metal-free porphyrins,[18] and π -conjugated naphthalene benzimidazole polymers[19] have been assayed as light-harvesters in this context. Regarding the OER catalyst, oxides of transition metals like IrO₂,[20-27] CoOx,[28-32] Co-Pi,[33-37] or FeOOH[4, 38-41] have been investigated.

When a solid light-harvester and a solid OER catalyst are employed, they are generally interfaced without any specific linker to create a solid – solid junction.[4, 5, 29, 37, 42, 43]. As an example, deposition of a Co-based catalyst on BiVO₄ resulted in an obvious enhancement of the photocatalytic activity[43-46]. Electrodeposition of a thin layer (30 nm) of Co-Pi OER catalyst on BiVO₄ resulted in an enhancement of the photoanode activity as under AM1.5 a photocurrent of 1.7 mA/cm² was recorded at 1.23 V vs. RHE (Figure 1) while a value of only 0.7mA/cm² was measured in the absence of the Co-Pi deposit[43].

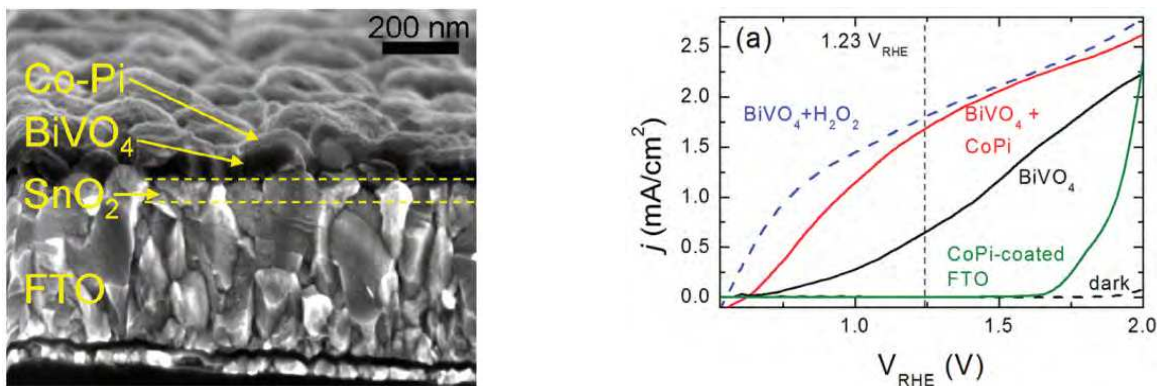


Figure 1. a) Cross section scanning electron microscope image of a 30 nm thick Co-Pi modified BiVO₄ photoanode and b) AM 1.5 photocurrent vs voltage curve for a BiVO₄ photoelectrode and a Co-Pi modified BiVO₄ photoelectrode recorded at a scan rate of 50 mV/s. The reference curves for Co-Pi coated FTO confirms the true photovoltaic nature of the photocurrents in BiVO₄ and rules out that they are caused by photoconductivity effects[43].

Regarding molecular catalysts, they can be just physically adsorbed on solid semiconducting light-harvesters. Physisorption of a [Ru(tpy)(ppy)Cl] (tpy = terpyridine, ppy = phenylpyridine) catalyst on a hematite (α -Fe₂O₃) photoanode is such a typical example (Figure 2c-top) [47]. In this design the combination between the molecular water oxidation catalyst and the light-harvester hematite creates a semiconductor-molecular heterojunction (Figure 2a-top), which is expected to not only facilitate the charge separation but also catalyze the water oxidation reaction by tuning the redox property of the organo-metallic molecule (Figure 2b-top). Furthermore, it is possible to covalently graft molecular catalysts such as [Ru(tpy)(dcbpy)Cl] (tpy = terpyridine, dcbpy = dicarboxylic bipyridine) and [Ru(tpy)(pba)Cl] (tpy = terpyridine, pba = pyridine benzoic acid) onto the surface of the semiconductor by modifying them with adequate functions such as carboxylic acid end-groups (Figure 2c-top), thus affording a hybrid photoanode of improved efficiency. As showed in Figure 2-bottom, the [Ru(tpy)(pba)Cl]/ α -Fe₂O₃ photoanode exhibited a photocurrent which was 2-fold higher than that obtained with the pristine α -Fe₂O₃ photoanode in pH 3 at 1.23 V vs. RHE. In addition, there was a large negative shift of the onset potential and a significant increment of the plateau current achieved at high potential[47].

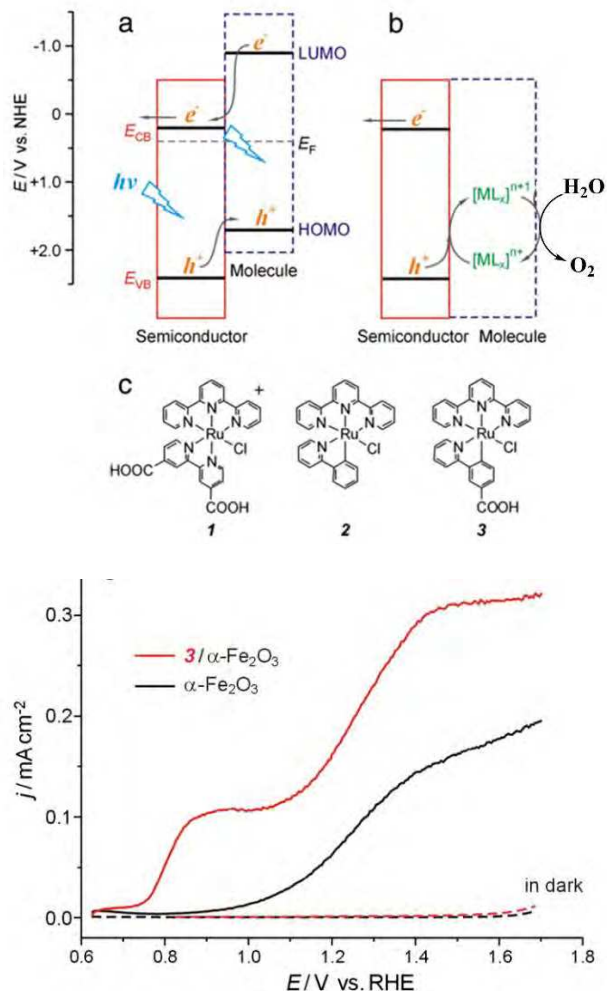


Figure 2. Top: scheme of the semiconductor/molecular catalyst photoanode for water splitting a) energetics of the heterojunction formed at the semiconductor/molecule interface. b) the molecular catalyst can mediate OER, adapted from ref. 47. c) the three Ru (II) complexes used by Chen et al., to promote OER. Bottom: photoelectrochemical behavior of the covalently grafted ruthenium terpyridine (tpy) pyridine benzoic acid (pba) $[Ru(tpy)(pba)Cl]$ molecular complex on $\alpha-Fe_2O_3$ photoanode in buffer solution ($pH=3$) at a scan rate 20 mV/s[47].

In a different approach, hybrid photoanodes can be engineered by covalent grafting of a molecular light-harvester onto the surface of a solid metal oxide catalyst. Such covalent grafting between the molecular light-harvester and solid catalyst is believed to offer (i) an efficient electron/hole transfer between the two components and beyond, an enhanced overall photocatalytic activity and, (ii) a more robust system preventing the leaching out of the light-harvester. However, it is worth noting

that to achieve such a molecular engineering, intensive efforts are needed to introduce appropriate functions to the light-harvester and/or catalyst component.

To the best of our knowledge, the first example of such a photoanode for solar water splitting was reported by Mallouk and co-workers in 2009 wherein a ruthenium tris-bipyridine complex acting as a light-harvester was covalently grafted through a malonate linker on IrO₂ nanoparticles, used here as a catalyst. The ruthenium tris-bipyridine complex was also covalently grafted on TiO₂ (Figure 3). A photocurrent density of 12.7 μA/cm² was generated by this hybrid TiO₂/ruthenium complex/IrO₂.nH₂O photoanode at an applied potential of 0 V vs. Ag/AgCl/KCl using 450 nm light at 7.8 mW/cm² intensity in 30 mM Na₂SiF₆ (buffered to pH 5.75 with NaHCO₃) and 500 mM Na₂SO₄ (Figure 4)[48].

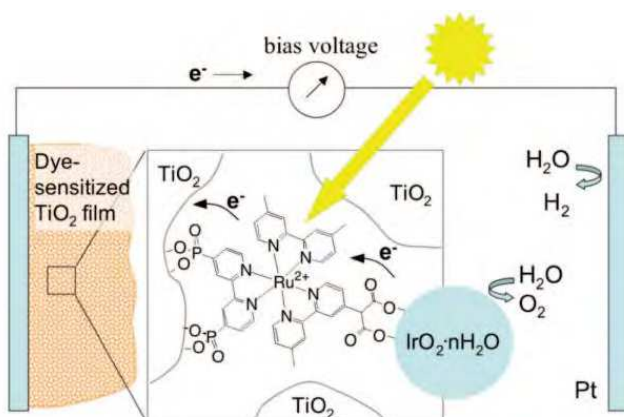
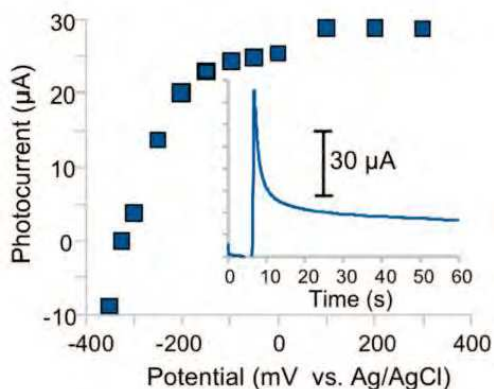


Figure 3. Schematic photoanode where a ruthenium complex is covalently grafted on IrO₂.n H₂O WOC NPs and on the TiO₂ electrode[48].



Chapter III – Fe@FeOx@Ru photoanode

Figure 4. Steady-state photocurrent vs anode potential curve recorded in a solution of 30 mM Na_2SiF_6 (buffered to pH 5.75 with NaHCO_3) and 500 mM Na_2SO_4 under light irradiation. Insert : transient photocurrent recorded at 0 mV vs. Ag/AgCl/saturated NaCl [48].

Since then, only a few other systems were published[11, 49, 50]. For example, Kirner *et al.*, investigated the benefit of coupling a perylene diimide (PDI) dye presenting phosphonic acids pendant groups to a CoOx catalyst. In this study, a thin film of perylene diimide dye functionalized with two phosphonic acid groups (N,N'-bis(phosphonomethyl)-3,4,9,10-perylenediimide (PMPDI)) was spin-coated on an ITO electrode on top of which a CoOx OER catalyst was deposited. (Figure 5). The ITO/PMPDI/CoOx photoanode showed an efficient visible-light assisted OER with a photocurrent of more than $150 \mu\text{A}/\text{cm}^2$ at 1 V applied bias vs. Ag/AgCl in 0.1 M pH 7 KPi buffer (Figure 6). Also in this study, an analogous photoanode was prepared from a PDI derivative which did not present any linking group was prepared, as a comparison point. The authors attributed the higher efficiency of ITO/PMPDI/CoOx photoanode as a result of the efficient coupling between the dye PMPDI and the CoOx OER catalyst through the phosphonic acid functional groups[11].

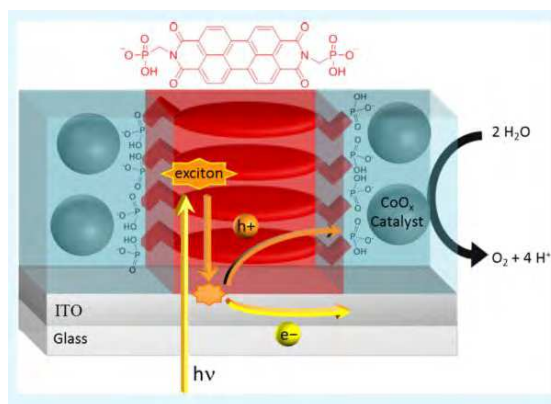


Figure 5. Schematic description of the hybrid ITO/ PMPDI/CoOx photoanode[11].

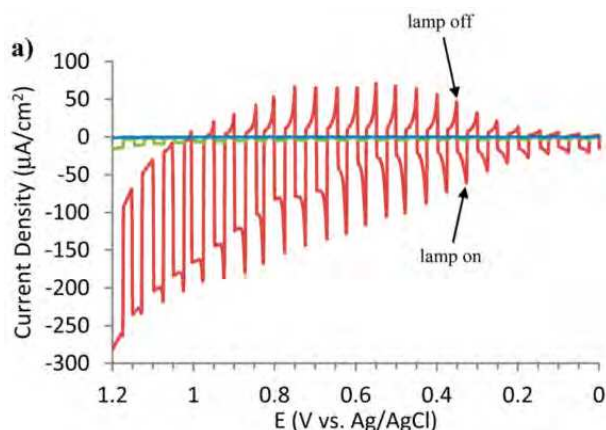


Figure 6. Photocurrent transients vs. applied potential for ITO/PMPDI/CoOx (red line), ITO/PMPDI (green line), and bare ITO (Blue line) photoanode in 0.1 M pH 7 KPi buffer, 5mV.s scan rate starting from 0 V (i.e., from right to left) with 5 s light transients[11].

Recently, our group reported the covalent grafting of a Ru complex light-harvester onto Co₃O₄ nanoparticles, using pendant phosphonic acid linkers as well, and its positive impact on the photoanode efficiency (Figure 7)[50]. In this work photosensitive polypyridyl - based Ru (II) complexes with different numbers of phosphonic acid groups (PS1: two phosphonic groups and PS2: 4 phosphonic groups) were covalently grafted on the surface of Co₃O₄ NPs OER catalyst in order to afford hybrid photocatalysts. The photocatalytic activity of the hybrid systems for OER using visible light and S₂O₈²⁻ as sacrificial electron acceptor at pH 5.6 was evaluated. The results showed that the Ru (II) PS with four phosphonic acid pending groups had a better efficiency compared with the one with 2 phosphonic pending groups based on the TON and TOF values (82/2.05 min⁻¹ and 5.4/0.90 min⁻¹ in the case of 4 and 2 phosphonic pending groups, respectively) (Table 1). The better catalytic performance was attributed to the higher grafting density achieved with the PS presenting the higher number of phosphonic pending groups (19PS and 32PS per Co₃O₄ NPs for PS with 2 and 4 phosphonic pending groups, respectively). The results also express the important role of the covalent grafting between PS and WOC for minimizing the catalyst aggregation under working conditions.

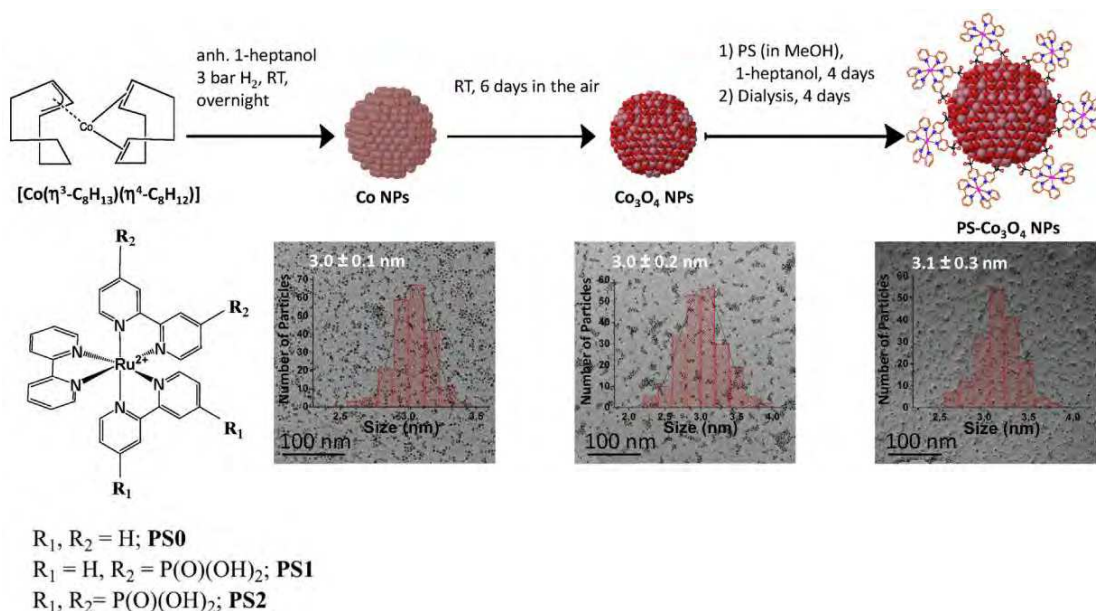


Figure 7. Synthetic pathway for hybrid PS-Co₃O₄ photocatalysts[50].

Table 1. TON and TOF (min⁻¹) per NP and per PS obtained as a function of the PS nature for the photochemical water oxidation reaction with single Co₃O₄ NPs and hybrid PS-Co₃O₄ NPs at pH 5.6 [50].

Entry	System	PS:Co ₃ O ₄ ratio	TON (O ₂ /NP)	TOF min ⁻¹ (O ₂ /NP)	TON (O ₂ /PS)	TOF min ⁻¹ (O ₂ /PS)
1	Co ₃ O ₄ + PS0	6.0:1.0	453	49.4	0.35	0.038
2	Co ₃ O ₄ + PS1	6.0:1.0	566	67.9	0.44	0.053
3	Co ₃ O ₄ + PS2	6.0:1.0	604	36.2	0.47	0.028
4	Co ₃ O ₄ + PS1	0.09:1.0	<1	—	<0.1	—
5	Co ₃ O ₄ + PS2	0.15:1.0	<1	—	<0.1	—
6	PS1-Co ₃ O ₄	0.09:1.0	5.4	0.90	0.28	0.046
7	PS2-Co ₃ O ₄	0.15:1.0	82.0	2.05	2.53	0.063

Relating to the benefit of covalent grafting in the design of hybrid photoanodes, another approach has been presented in which both PS and OER catalyst are covalently grafted on the surface of the photoanode [51-53]. In 2012 Zhao and co-workers covalently grafted a Ru polypyridine photosensitizer bearing three phosphonic acid end groups (3P-Ru) and a IrO₂ WOC on a TiO₂ photoanode. They showed that the performance of the system could be further improved by incorporating an electron transfer mediator, benzimidazole-phenol (BIP), between the IrO₂ nanoparticle and the ruthenium dye, mimicking the tyrosine- histidine pair present in photosystem II (Figure 8). This mediator helps accelerate the electron transfer between Ir(IV) and Ru(III)

centers resulting in a more efficient (by a factor of three) water splitting photoanode (Figure 9) [51].

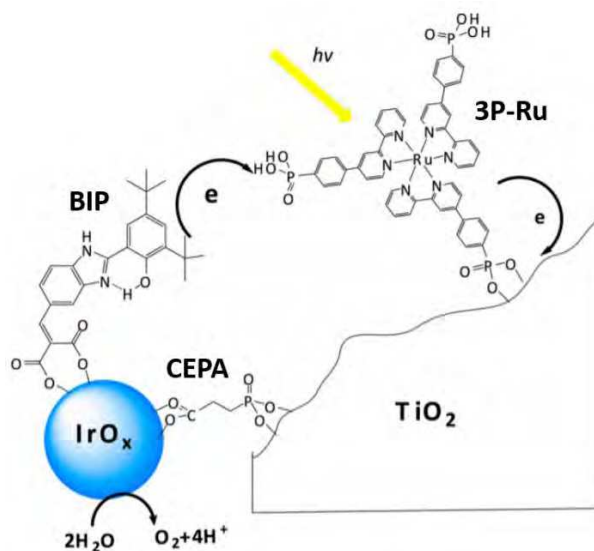


Figure 8. Schematic presentation of the electron transfers and water oxidation reaction in the mediator-based, dye sensitized TiO₂ photoanode showing molecular structures of benzimidazole-phenol (BIP) mediator, 3P-Ru dye, and 2-carboxyethyl phosphonic acid (CEPA) anchoring group[51].

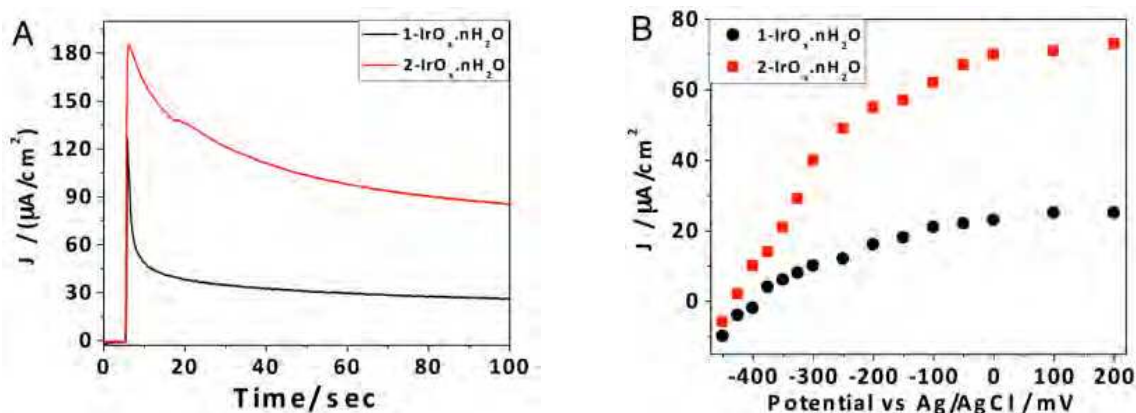


Figure 9. (A) photocurrent density vs. time for TiCl_4 - treated porous TiO_2 electrode with co-adsorbed 3P-Ru dye and 1-IrO_x.nH₂O (CEPA capped IrO_x.nH₂O) or 2-IrO_x.nH₂O (BIP and CEPA capped IrO_x.nH₂O) NPs (Dye:Ir=1:5) in pH 5.8 silicate buffer at 0 V vs. Ag/AgCl. The initial sharp spike in current corresponds to switching from dark to light conditions. B) Steady - state photocurrent vs. anode potential[51].

More recently, Na *et al.*, investigated the behavior of a TiO_2 photoanode on which a Ru-polypyridyl complex bearing two phosphonic acid functions (Ru-P) was grafted, together with Co_3O_4 NPs. In this study, the photoanode was assembled by first sensitizing the TiO_2 electrode with the Ru-P complex and then with 4-formyl benzoic acid. Afterwards, the Co_3O_4 NPs, surfaced-modified with 3-aminopropyl triethoxysilane (APTES), were integrated into the device by a fast Schiff base reaction between the amino group present at their surface and the 4-formylbenzoic acid (Figure 10). This strategy resulted in an enhancement of the transient photocurrent which was 8 times higher than that measured without the Co_3O_4 catalyst (Figure 11)[53].

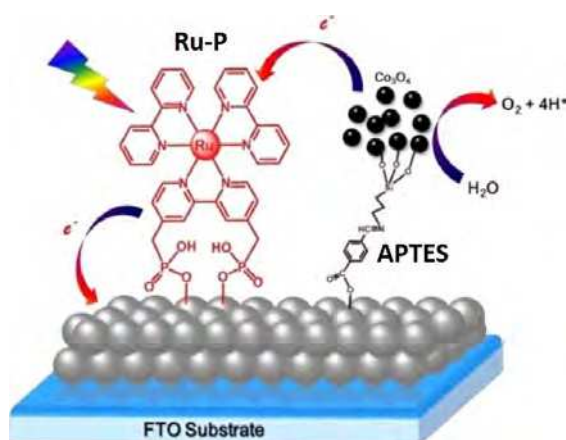


Figure 10. Schematic illustration of the TiO_2 electrode (grey balls) co-sensitized by a Ru-polypyridyl complex (RuP) and surface modified Co_3O_4 NPs. reproduced from ref. [53].

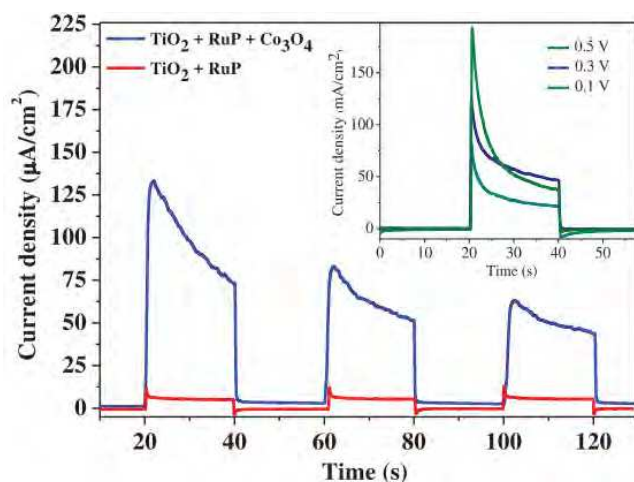


Figure 11. The transient current response with 0.3 V vs. Ag/AgCl bias potential for the photoanodes $\text{TiO}_2/\text{RuP}/\text{Co}_3\text{O}_4$, and TiO_2/RuP , 1 cm^2 active area in $\text{pH}=6.8$ phosphate buffer solution upon the on-off cycles of illumination (500 W Xe lamp coupled to a 400 nm long-pass filter, $100 \text{ mW}/\text{cm}^2$). Insert: the photocurrent transient for the photoanode ($\text{TiO}_2/\text{RuP}/\text{Co}_3\text{O}_4$) under different applied potential[53].

To complete this literature survey, Table 1 reports other examples of hybrid photoanode systems. However, as the methods used to evaluate the photocatalytic efficiencies of these photoanodes were not always identical, no clear comparison can be made.

Table 1: Summary of the representative photocatalytic activity toward OER using hybrid photoanodes based on a molecular dye covalent grafted MOx catalyst.

No.	Substrate /PS/ WOC	PS:WOC ratio	Electrolyte	V _{onset} (V vs. RHE)	Photocurrent/testing conditions	TON	TOF	Ref
1	[Ru(bipy) ₂ (bipy(COO) ₂)]/ [Mn ₄ O ₄ ((MeOPh) ₂ PO ₂) ₆]	4.5:1	Na ₂ SO ₄ 0.1M, pH 6.5	-	-	-	0.013 O ₂ .cluster ⁻¹ s ⁻¹	[54]
2	[Ru(bpy)(4,4'-(PO ₃ H ₂) ₂ bpy) ₂](Cl) ₂ / Co ₃ O ₄	0.15:1	Na ₂ SiF ₆ - NaHCO ₃ (0.02-0.04 M, pH 5.6)	-	-	2.53 O ₂ .PS ⁻¹	0.001 O ₂ .PS ⁻¹ .s ⁻¹	[50]
3	TiO ₂ /[Ru(bpy) ₃] ²⁺ modified malonate ligand/IrO ₂ .nH ₂ O	-	Na ₂ SiF ₆ - NaHCO ₃ 0.02M pH 5.75	-	12.7 μA/cm ² At 0 V vs. Ag/AgCl/KCl Under 450 nm light (7.8mW/cm ²)	-	-	[48]

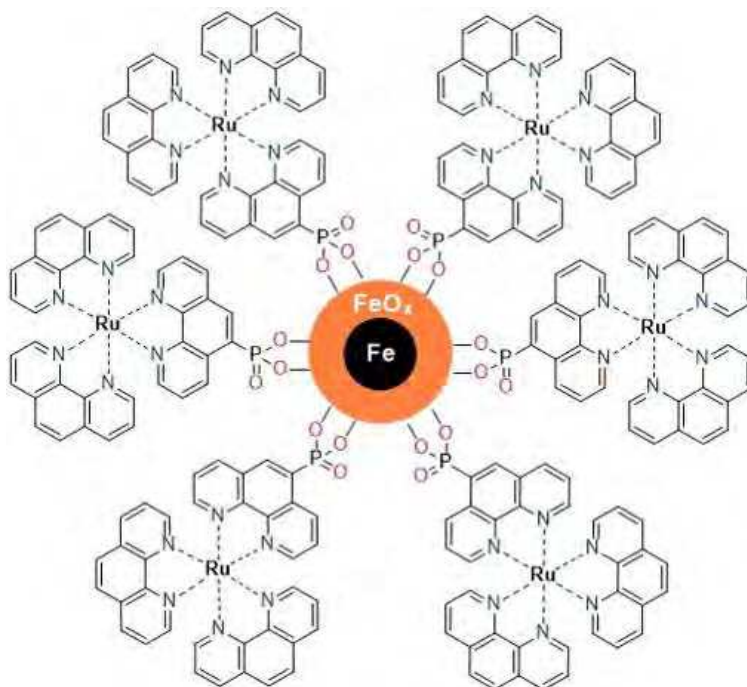
Chapter III – Fe@FeOx@Ru photoanode

4	ITO/PMPDI/CoOx	-	0.1 M pH 7 KPi	-	150 $\mu\text{A}/\text{cm}^2$ at 1 V vs. Ag/AgCl simulated sunlight (100 mW/cm^2)	-	-	[11]
---	----------------	---	-------------------	---	---	---	---	------

Chapter III – Fe@FeOx@Ru photoanode

Based on the above considerations, we designed a new hybrid photocatalyst for solar water splitting where ruthenium trispolypyridyl complexes (as light-harvester) are grafted on core-shell iron@iron oxide nanoparticles, Fe@FeOx NPs (as OER catalyst). Indeed, ruthenium trispolypyridyl complexes have been widely used for more than 50 years as they are archetypal compounds for solar energy harvesting[55-57]: they present large extinction coefficients over a broad range of the visible spectrum, long-lived excited state and high luminescent quantum yields. This allows an efficient energy/electron transfer to the catalyst. Their scaffold is also highly tunable, allowing the fine tuning of the optical and redox properties, to drive both water oxidation and hydrogen reduction reactions.

Here, a Ru(II) tris(1,10-phenanthroline) complex was selected because of its well-known propensity to promote singlet-triplet intersystem crossing which often results in quite long excited state lifetimes and thus efficient charge separation. This type of complex is also air-stable and displays a high thermal stability allied to a remarkable chemical inertness[58, 59] On one of the 1,10-phenanthroline ligands, we introduced a pendant phosphonic acid group which we assume to afford a covalent grafting onto iron oxide surfaces (Scheme 1) based on literature data[60-63]. In this model, the Ru complex can serve not only as an effective stabilizer for the Fe@FeOx NPs but also as a photosensitizer that can absorb energy from sunlight to drive the thermodynamically uphill conversion of water into oxygen and hydrogen.

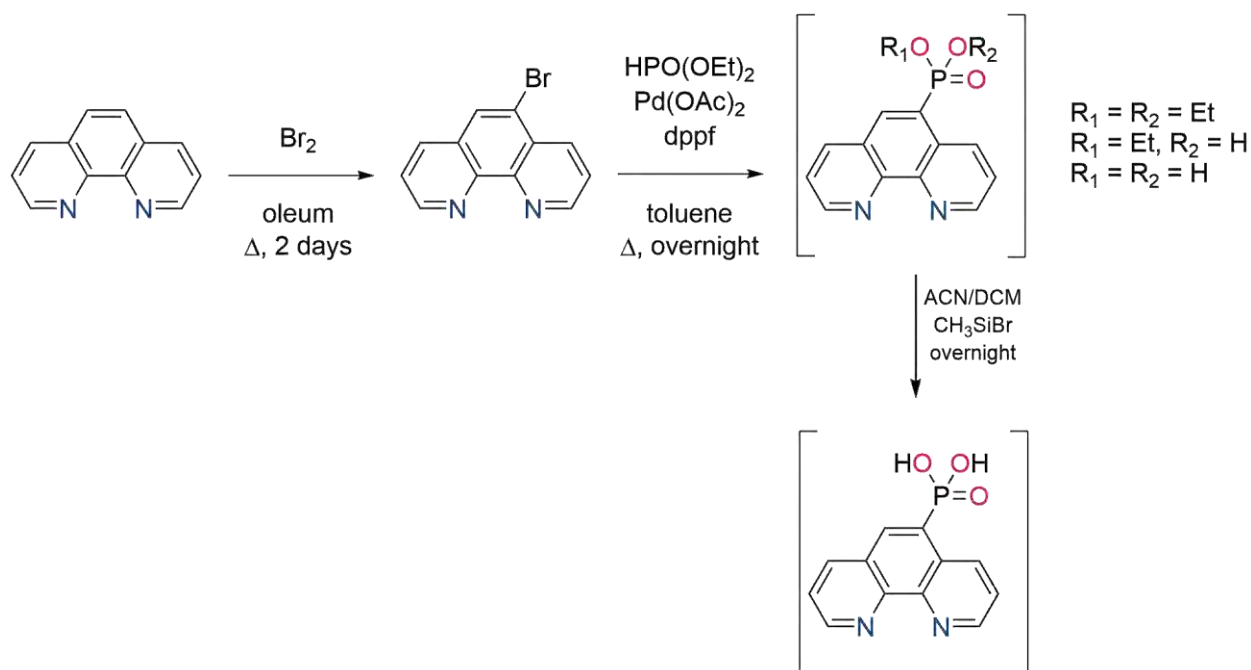


Scheme 1. Proposed structure of Fe@FeOx@Ru NPs, the nanohybrid targeted in this study.

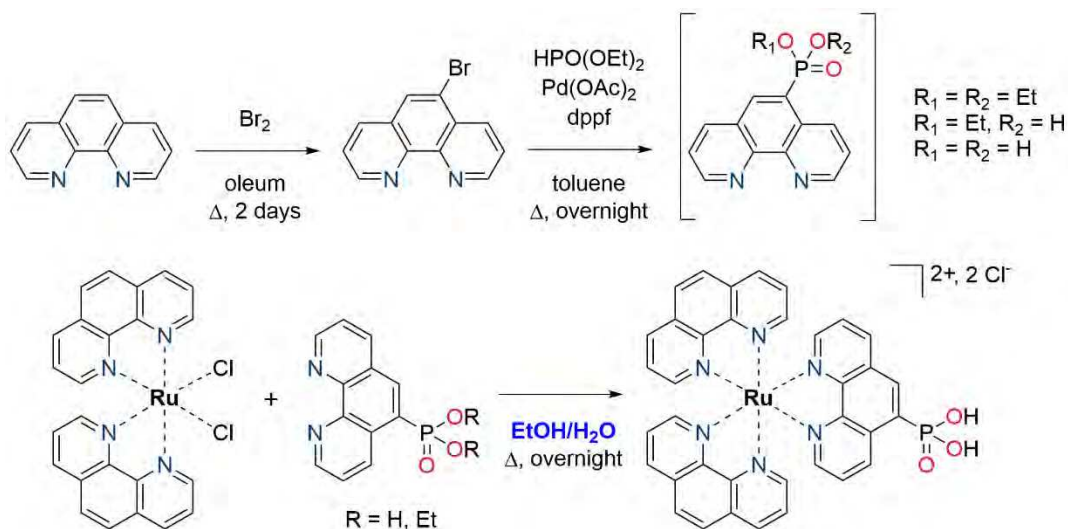
2. Synthesis and characterization of the [Ru-PO(OH)₂]₂·Cl₂·7H₂O.

Although the archetypal [Ru(bpy)₃]²⁺ photosensitizer is mainly used in the development of photoelectrocatalytic systems, their phenanthroline-based analogues attract a wide interest as the latter ligands are more rigid and conjugated [64, 65]. The fifth position of the 1,10-phenanthroline ligand is usually substituted, as the corresponding carbon atom is the most reactive in the bromination conditions used herein. In addition, the fifth position is the less sterically hindered in the resulting complex, potentially allowing its easier grafting on the nanoparticles. While the 1,10-phenanthroline precursor is commercially available, the synthesis of the 5-phosphonic 1,10-phenanthroline, hereafter referred to as **1,10-phen-PO(OH)₂**, was initially carried out following a three-step procedure as reported for 2, 2'-bipyridine[66], and reported in scheme 2. The first step, corresponding to the bromination of 1,10-phenanthroline in the fifth position, is already reported and widely used to modify the scaffold of such a synthon[67, 68]. The second step consists in the synthesis of the 5-diethylphosphonate analogue through a palladium-catalyzed coupling of 5-bromo-1,10-phenanthroline in presence of dppf (dppf = 1,1'-Bis(diphenylphosphino)ferrocene)[66]. The hydrolysis deprotection step was carried out in the

presence of triethylamine, following the similar reaction carried on 2,2'-bipyridine[69]. However, a mixture of the same species (with protected, partially deprotected, and fully deprotected phosphonate group), albeit in a different ratio, was obtained. Although the three species could be separated by silica gel chromatography, we observed as well that the reaction of the mixture with the $[\text{Ru}(\text{phen})_2\text{Cl}_2]$ (*vide infra*), yielded a unique complex species containing solely the fully deprotected **1,10-phen-PO(OH)₂** ligand. To save time and reactant, the functionalized phenanthroline was therefore synthesized in two steps only and used as a mixture of the three species for the complexation (Scheme 3).



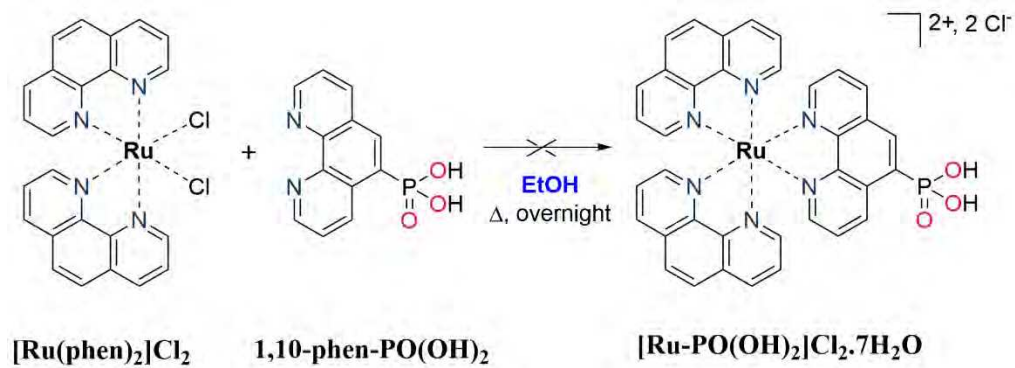
Scheme 2. Synthetic pathway towards the **1,10-phen-PO(OH)₂** ligand by the three-step procedure.



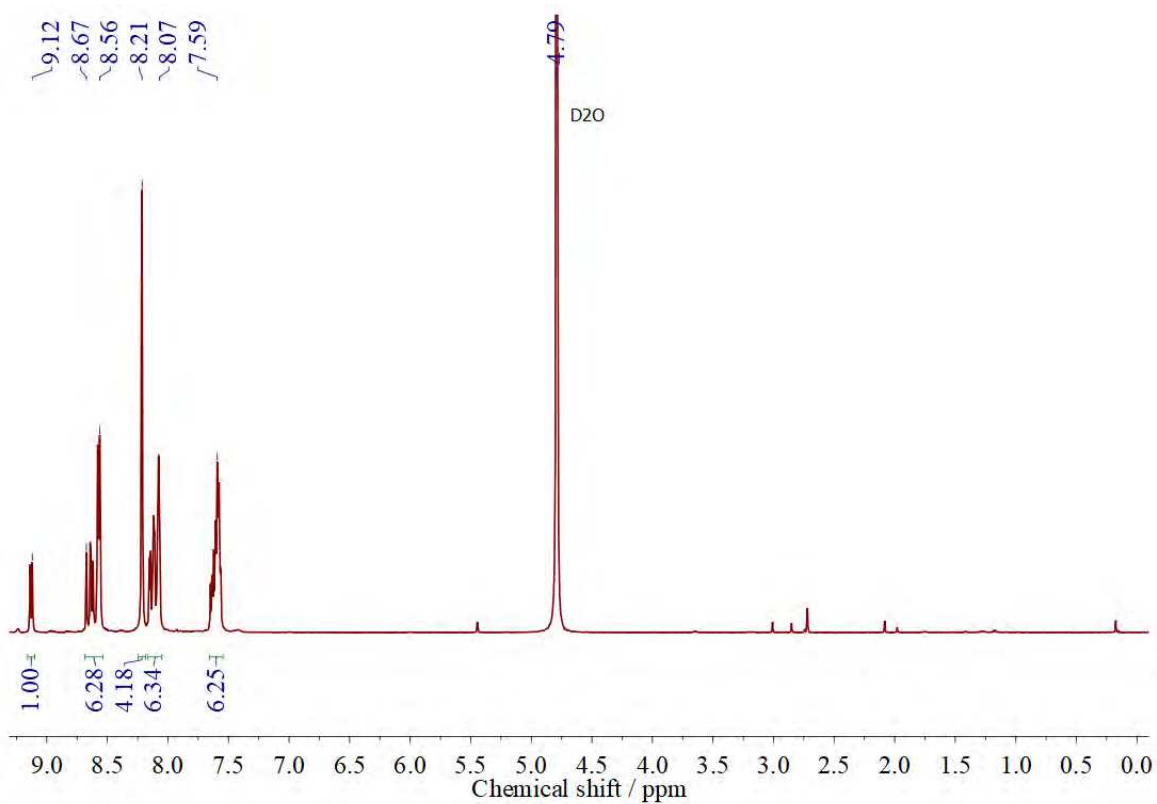
Scheme 3. Synthetic pathways towards the 1,10-phen-PO(OH)₂ ligand (2 step-procedure, top) and its corresponding [Ru-PO(OH)₂]₂Cl₂·7H₂O complex (bottom).

The widely used stepwise synthesis of *bis*-heteroleptic ruthenium(II) complexes *via* the [Ru(phen)₂Cl₂] precursor complex [70, 71], followed by the addition of one equivalent of the 1,10-phen-PO(OH)₂ ligand in ethanol (Scheme 4) was not successful for the targeted complex [Ru-PO(OH)₂]²⁺. Therefore, the reaction was carried out in a mixture of ethanol/water (1:1) as we suspected the equilibrium between the neutral and zwitterionic forms of the 1,10-phen-PO(OH)₂ ligand to prevent the coordination on the metal center [72] (Scheme 3). The complex was first isolated as a chloride salt [Ru-PO(OH)₂]₂Cl₂ before being precipitated as a hexafluorophosphate salt [Ru-PO(OH)₂]₂(PF₆)₂ to ease the purification. As the synthesis of the hybrid nanomaterials required to be carried out in an aqueous media (*vide infra*), the pure [Ru-PO(OH)₂]₂(PF₆)₂ was converted back to [Ru-PO(OH)₂]₂Cl₂ using a Dowex® 1x8,50-100 mesh ion-exchange resin. The nature of the complex was confirmed by ¹H (Figure 12), ³¹P NMR (Figure 13) and mass spectrometry (Figure 14). Finally, the compound was identified as [Ru-PO(OH)₂]₂Cl₂·7H₂O by elemental analysis.

Chapter III – Fe@FeOx@Ru photoanode



Scheme 4. Hypothetical synthetic pathway of the $[\text{Ru-PO}(\text{OH})_2]\text{Cl}_2 \cdot 7\text{H}_2\text{O}$ complex following the usual conditions.



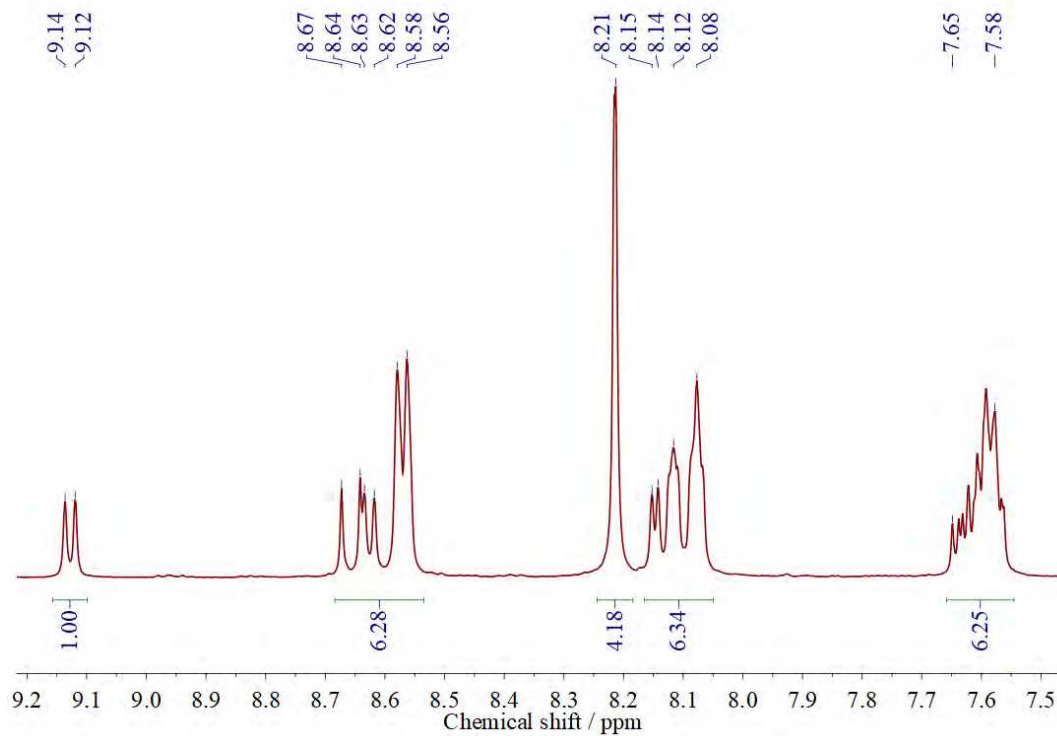


Figure 12. ^1H NMR spectrum in D_2O of $[\text{Ru-PO}(\text{OH})_2]\text{Cl}_2 \cdot 7\text{H}_2\text{O}$ (top), and Zoom on the aromatic spectral range of the ^1H NMR spectrum in D_2O of $[\text{Ru-PO}(\text{OH})_2]\text{Cl}_2 \cdot 7\text{H}_2\text{O}$ (bottom).

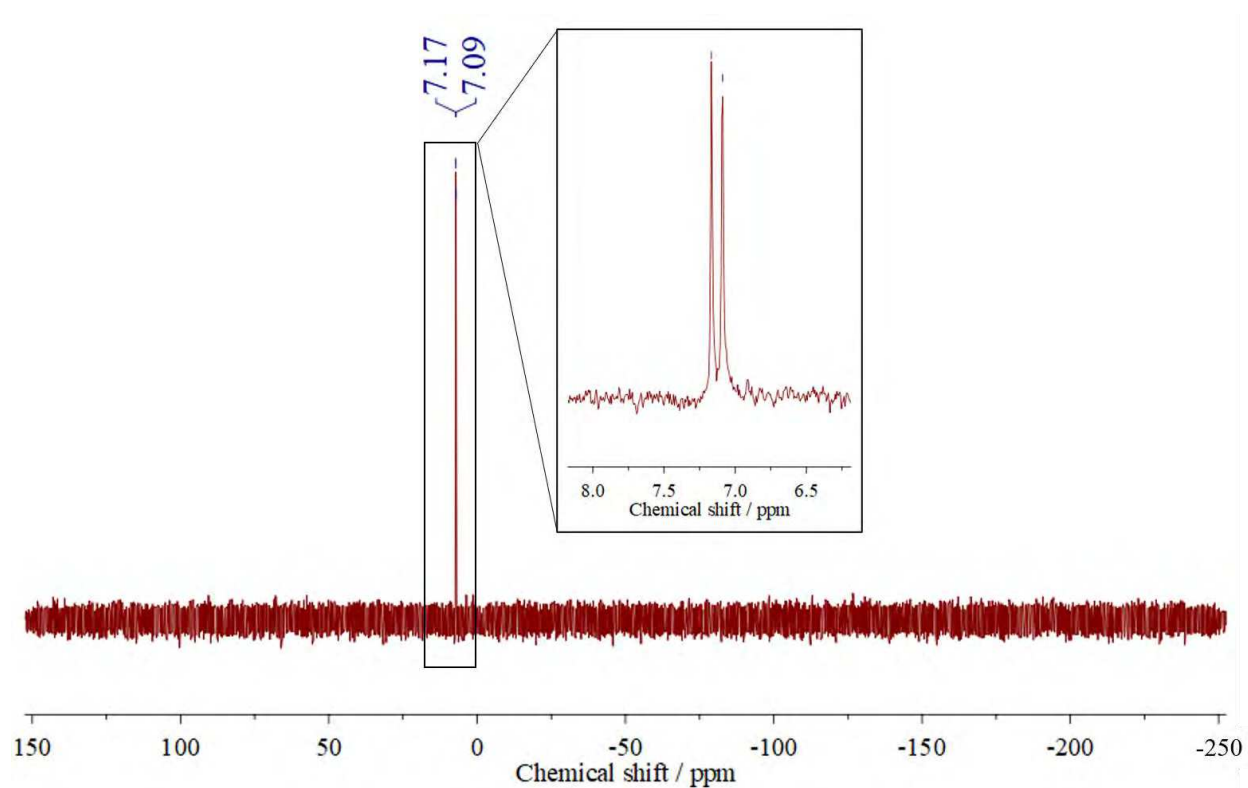


Figure 13. ^{31}P NMR spectrum in D_2O of $[\text{Ru-PO}(\text{OH})_2]\text{Cl}_2 \cdot 7\text{H}_2\text{O}$

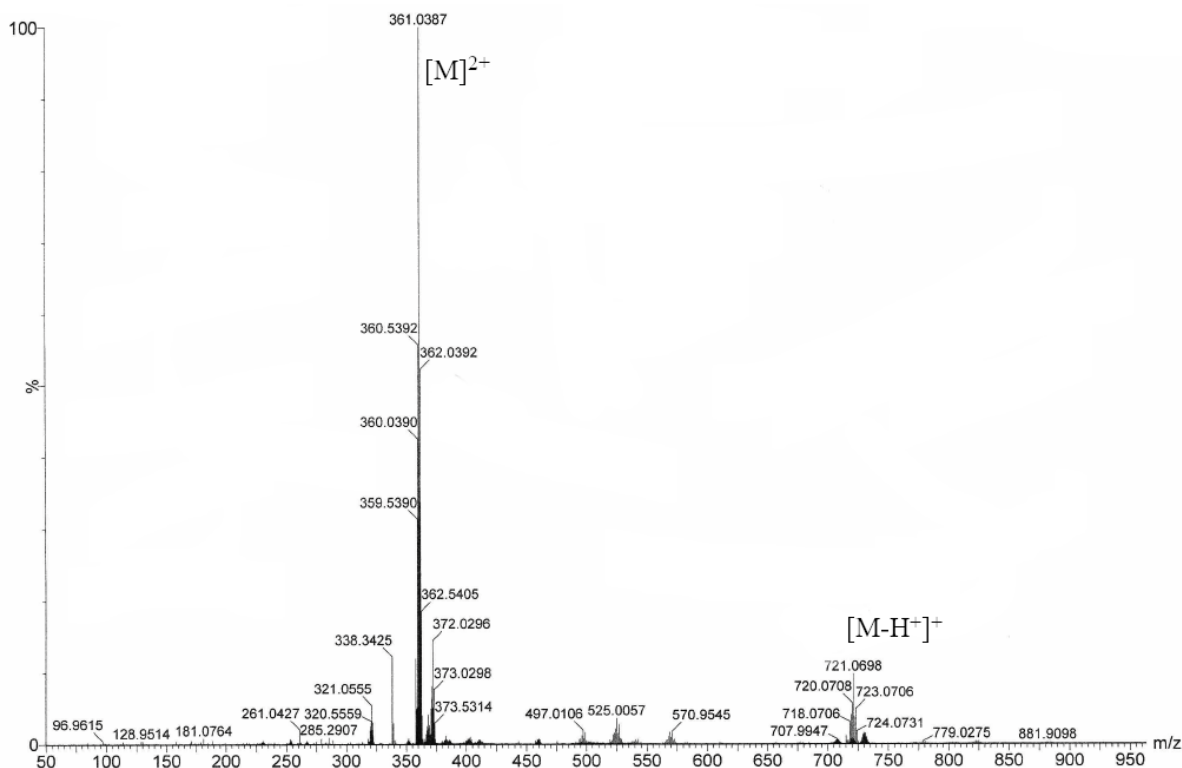


Figure 14. HRMS data of $[\text{Ru-PO(OH)}_2]\text{Cl}_2 \cdot 7\text{H}_2\text{O}$. The $[\text{M}]^{2+}$ fragment is defined as $[\text{Ru(phen)}_2(\text{phen-PO(OH)}_2)]^{2+}$ and the $[\text{M-H}]^+$ as the mono-deprotonated species $[\text{Ru(phen)(phen-PO(OH)}_2)(\text{phen-PO(OH)(O}^-))]^+$.

The photophysical properties of $[\text{Ru-PO(OH)}_2] \cdot (\text{PF}_6)_2$ were investigated in acetonitrile to allow an easier comparison with literature values. The complex presents the typical bands for such polypyridine ruthenium(II) derivatives[73] (Figure 15) (i) a Ligand Centered (LC) $\pi_L \rightarrow \pi_L^*$ electronic transition at 264 nm ($\epsilon \approx 82600 \text{ L mol}^{-1} \text{ cm}^{-1}$) and (ii) a broad band presenting a shoulder around 415 nm and centred at 447 nm ($\epsilon \approx 12800 \text{ L mol}^{-1} \text{ cm}^{-1}$), which may be attributed to a Metal to Ligand Charge Transfer (MLCT) by analogy with the parent $[\text{Ru(phen)}_3]^{2+}$ complex (Figure 16). Although usually identified as Metal-to-Ligand-Charge-Transfers (MLCT), it is worth noting that the transition occurring around 450 nm has also been found in the literature to include Intra-Ligand Charge Transfers character, especially in its highest energy range, between 300 and 400 nm. The large band width of 410 nm can, therefore, be ascribed either to such phenomenon or to vibronic broadenings and the overlap of bands involving different close-lying electronic transitions.

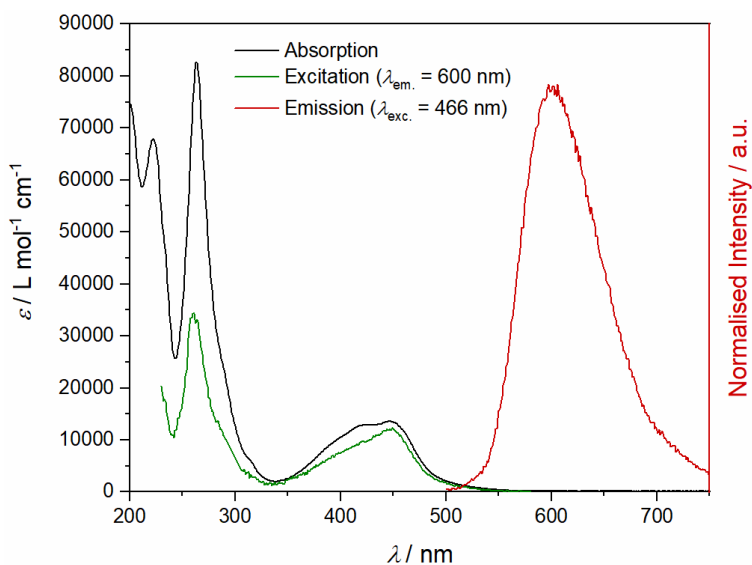


Figure 15. Photo-physical characterization of complex $[\text{Ru-PO(OH)}_2](\text{PF}_6)_2$ in acetonitrile ($3.6 \times 10^{-6} \text{ mol.L}^{-1}$). In black: UV-vis absorption spectrum; in red: emission profile ($\lambda_{\text{exc.}} = 450 \text{ nm}$); in green: the corresponding excitation spectrum ($\lambda_{\text{em.}} = 600 \text{ nm}$).

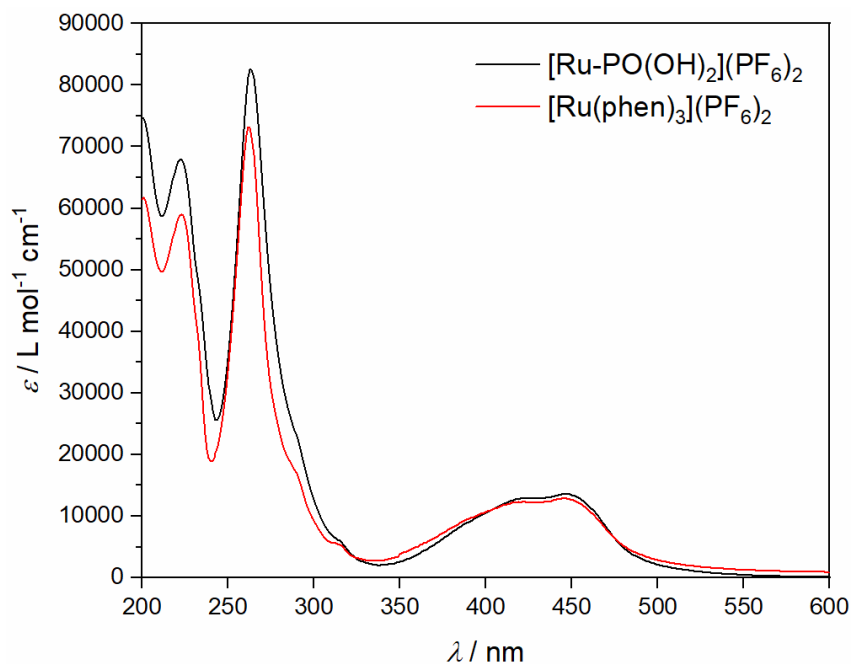


Figure 16. Comparison of the absorption spectra of $[\text{Ru-PO(OH)}_2](\text{PF}_6)_2$ (in black) and the parent $[\text{Ru(phen)}_3](\text{PF}_6)_2$ (in red) spectra in acetonitrile ($8.2 \times 10^{-6} \text{ mol.L}^{-1}$).

The broad emission band originating from the lowest in energy $^3\text{MLCT}$ excited state is centred around 600 nm. The triplet character of the excited state was evidenced by the $^3\text{O}_2$ quenching of the luminescence intensity and the related Stern-Volmer plot (Figure 17). This spectroscopic investigation shows that the complex $[\text{Ru-PO}(\text{OH})_2]^{2+}$ presents the required characteristics to be used as a suitable photosensitizer as it absorbs in the visible domain and is emissive through its $^3\text{MLCT}$ excited state. In other words, the presence of the phosphonic acid group does not seem to affect the photophysical properties of the archetypal $[\text{Ru}(\text{phen})_3]^{2+}$ (Figure 16) which can therefore be used as a reference in the photo-electrocatalysis studies presented herein, and the $[\text{Ru-PO}(\text{OH})_2]^{2+}$ complex is fully qualified to be used as a light harvester to build a hybrid photocatalyst for the visible light driven solar water splitting.

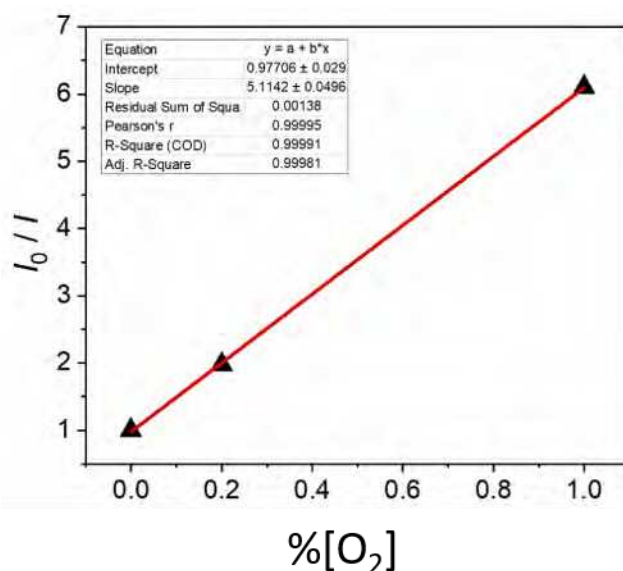
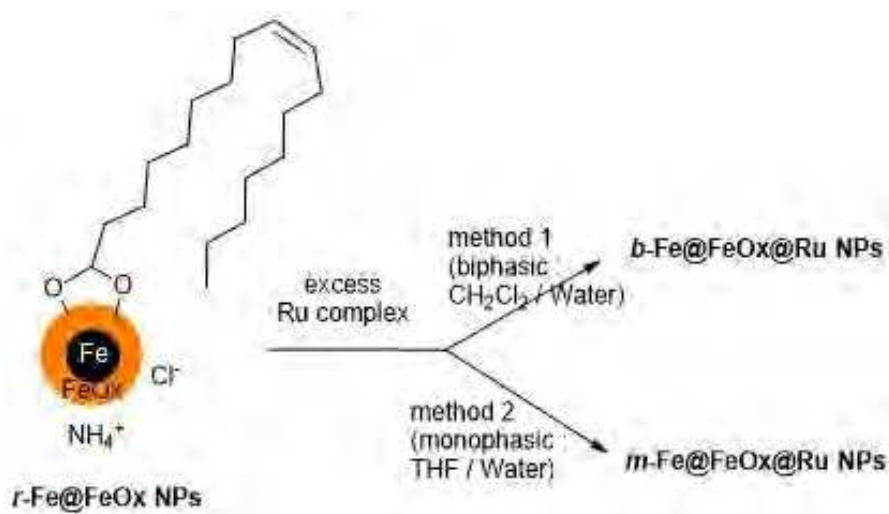


Figure 17. Stern-Volmer plot for the $[\text{Ru-PO}(\text{OH})_2](\text{PF}_6)_2$ complex in acetonitrile.

3. Synthesis and characterization of hybrid nanomaterials PS-Fe@FeOx NPs.

As we have seen in chapter II, the grafting of APA is more efficient on the reconstructed *r*-Fe@FeOx NPs. Grafting of the $[\text{Ru-PO}(\text{OH})_2]\text{Cl}_2$ complex was thus performed only on *r*-Fe@FeOx NPs. It was carried out following two strategies yielding the target PS-Fe@FeOx NPs, as displayed in Scheme 5: a biphasic method (*Method 1*) and a monophasic method (*Method 2*).

Hereafter, the resulting hybrid nanomaterials are respectively labelled ***b*-Fe@FeO_x@Ru** (*b* for biphasic) and ***m*-Fe@FeO_x@Ru** (*m* for monophasic).



Scheme 5. Synthetic pathways for the hybrid catalysts prepared in biphasic (***b*-Fe@FeO_x@Ru NPs**) and monophasic (***m*-Fe@FeO_x@Ru NPs**) media.

In the biphasic method 1, the *r*-Fe@FeO_x NPs were dispersed in CH₂Cl₂ while the ruthenium complex was dissolved in MilliQ water leading to a yellow solution. The resulting mixture was mechanically stirred for three days. The efficiency of this grafting method was first evidenced by the aqueous phase turning black, indicating that the NPs were successfully transferred from the organic dispersion in CH₂Cl₂ to the aqueous phase (Figure 18). The two phases were separated and the magnetic component of the aqueous one recovered by magnetic separation. The resulting ***b*-Fe@FeO_x@Ru** was washed intensively with MilliQ water, ethanol then diethyl ether in order to remove the non-grafted excess of ruthenium photosensitiser. In the monophasic method 2, a similar protocol was followed to obtain the ***m*-Fe@FeO_x@Ru**, replacing the dichloromethane by tetrahydrofuran, which is miscible with water, to disperse the NPs (Figure 19).

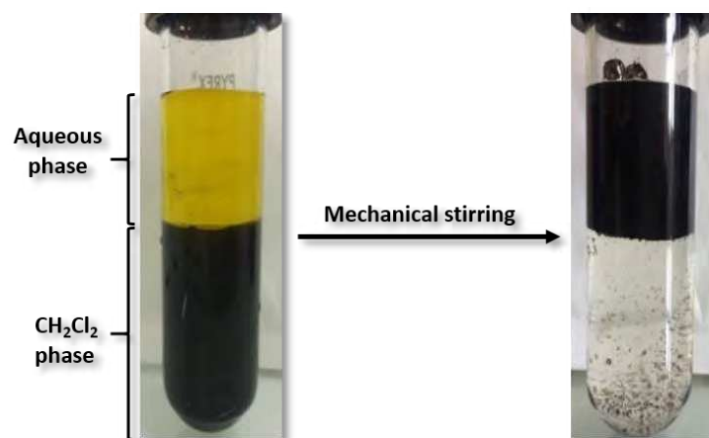


Figure 18. Photograph of the grafting steps when grafting the Ru complex to *r*-Fe@FeO_x NPs by the biphasic method 1.

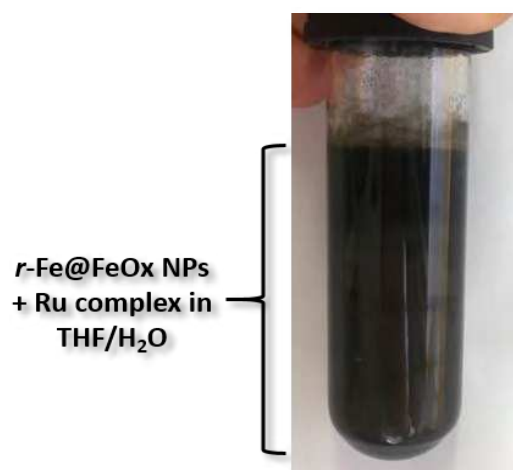


Figure 19. Photograph of *r*-Fe@FeO_x NPs and Ru complex in a homogeneous THF/MilliQ water medium (monophasic method 2).

Analysis of High Resolution - High Angle Annular Dark Field - Scanning Transmission Electron Microscopy (HR-HAADF-STEM) images of *b*-Fe@FeO_x@Ru NPs and *m*-Fe@FeO_x@Ru NPs indicated that the size and core-shell morphology of the NPs were retained after grafting the ruthenium complex on their surface (Figure 20).

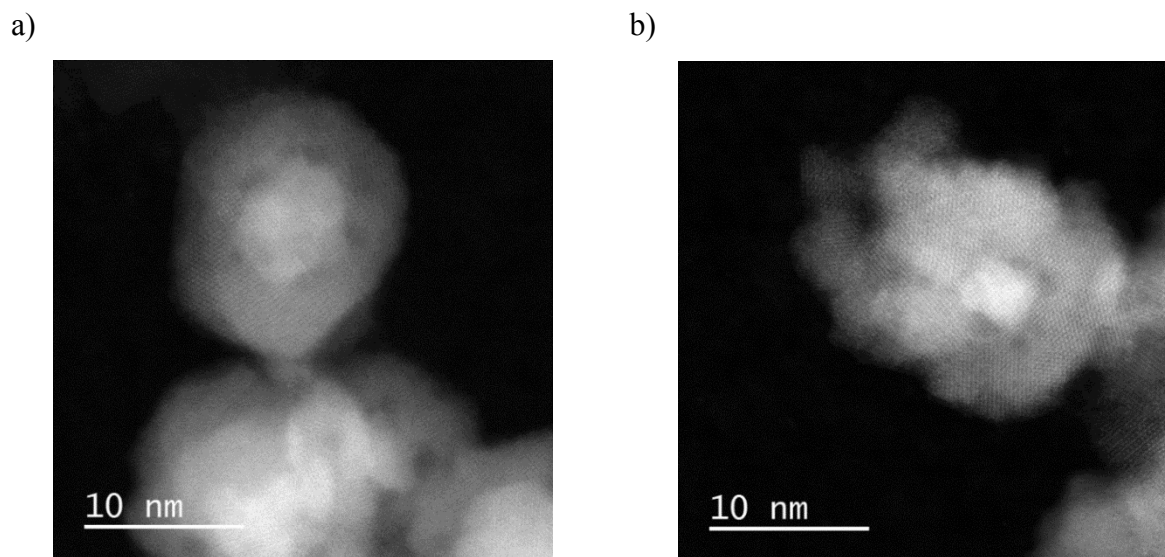


Figure 20. HR-HAADF-STEM images of a) *b*-Fe@FeO_x@Ru NPs and b) *m*-Fe@FeO_x@Ru NPs.

WAXS measurement on *m*-Fe@FeO_x@Ru NPs confirmed the persistence of a crystalline Fe oxide layer as all the diffraction peaks matched well with the maghemite diffraction diagrams (Figure 21). The presence of the shoulder at $2\theta = 20^\circ$ and peaks at $2\theta = 35^\circ$ suggests the presence of a very small contribution of metallic Fe (Figure 21), that could not be confirmed, nor disproved. It is worth noting that no contribution from NH₄Cl (present in *r*-Fe@FeO_x NPs as discussed in Chapter 2) was detected suggesting its removal during the grafting process (Figure 22).

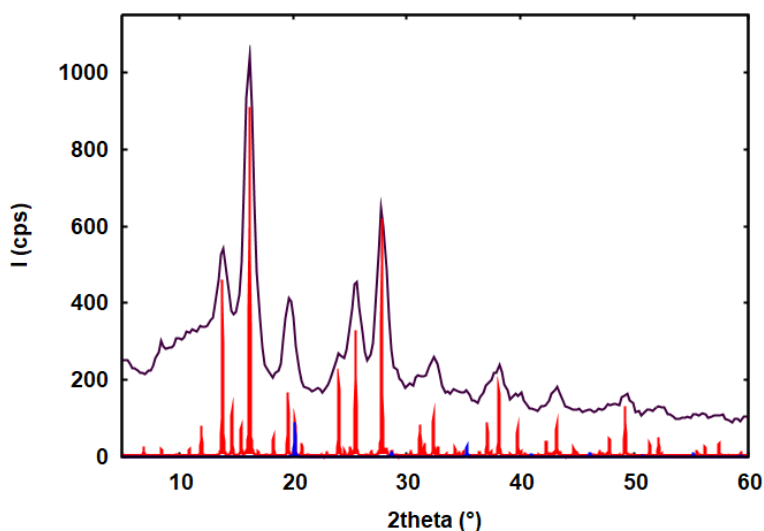


Figure 21. WAXS diagram of *m*-Fe@FeO_x@Ru NPs (solid line) in comparison with Fe₂O₃ (PDF-01-089-5894, in red) and bcc-Fe (PDF-01071-4648, in blue).

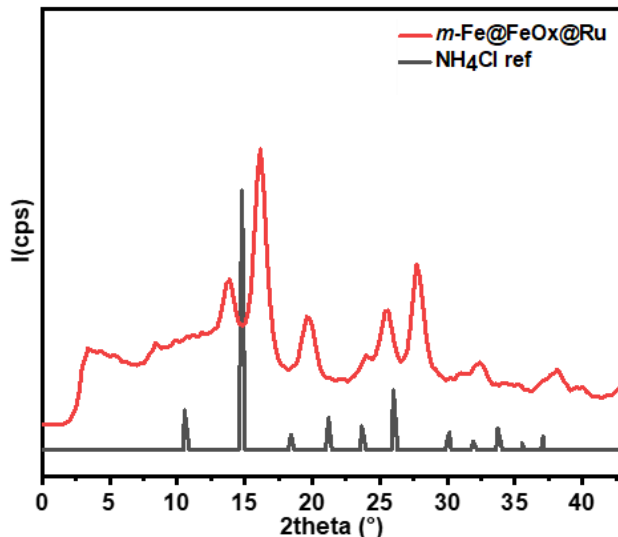


Figure 22. WAXS diagram of *m-Fe@FeO_x@Ru* NPs in comparison with *NH₄Cl* (PDF 96-901-0007).

Figure 23 shows the Radial Distribution Function (RDF) of the nanoparticles at the different steps of their elaboration. As expected, the RDF of *n-Fe@FeO_x* is very close to the one computed from the Fe alpha bcc structure (spherical model, 3.8nm in diameter). Agreement for *r-Fe@FeO_x* is significantly worse, indicating that at this point NPs were more disordered and still included elements from the metallic Fe structure (distance at 0.86 nm is typical). Finally, the RDF of *m-Fe@FeO_x@Ru* is in nearly perfect agreement with the one computed from the Fe₂O₃ structure (5.0 nm in diameter).

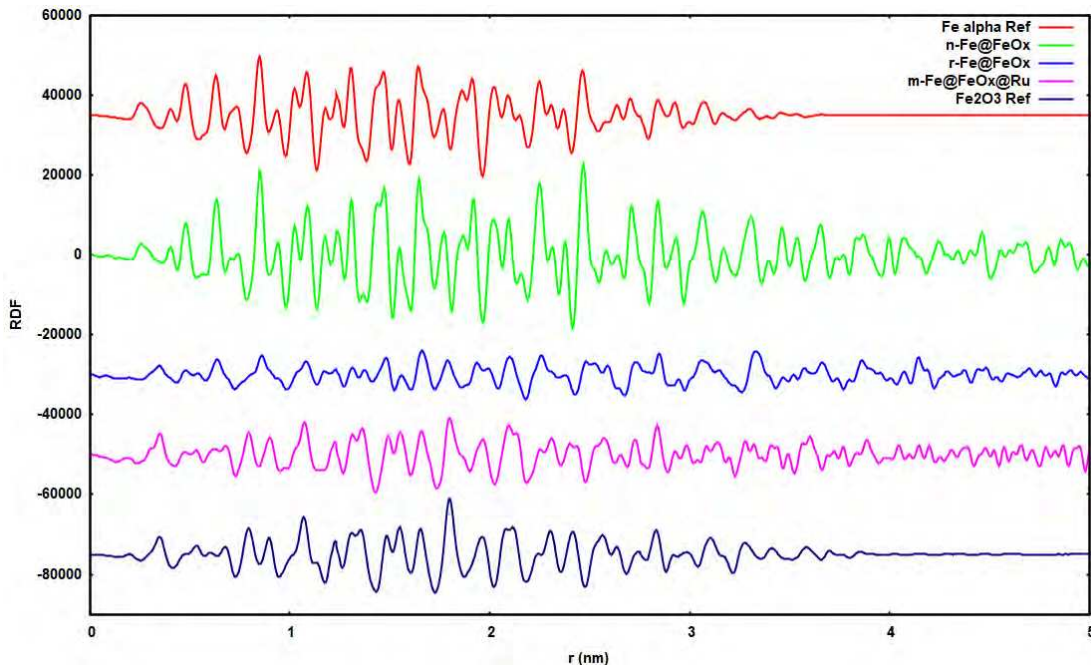


Figure 23. Comparison between RDF of, from top to bottom, model bcc-Fe NPs, **n-Fe@FeO_x** NPs, **r-Fe@FeO_x** NPs, **m-Fe@FeO_x@Ru** NPs, and model γ -Fe₂O₃ NPs showing the evolution from a nanomaterial with a high bcc Fe content to one with a high crystalline maghemite content.

This study clearly shows that, in water, the oxide layer doesn't protect the inner metallic iron core from oxidation. Unfortunately, a too limited quantity of **b-Fe@FeO_x@Ru** NPs was recovered precluding any WAXS analysis on this sample. But, we can expect a similar evolution for this material.

The presence of Ru atoms was first detected by HR-HAADF-STEM measurements (Figure 24a). Small bright dots were observed on the NPs in sample **m-Fe@FeO_x@Ru** NPs. As the atomic number *Z* of a ruthenium atom is higher than that of an iron atom, these bright dots were tentatively attributed to Ru atoms from the complex. No such dots were observed in the sample of **b-Fe@FeO_x@Ru** NPs (Figure 24b), suggesting that the biphasic grafting *method 1* is less efficient than the monophasic *method 2*.

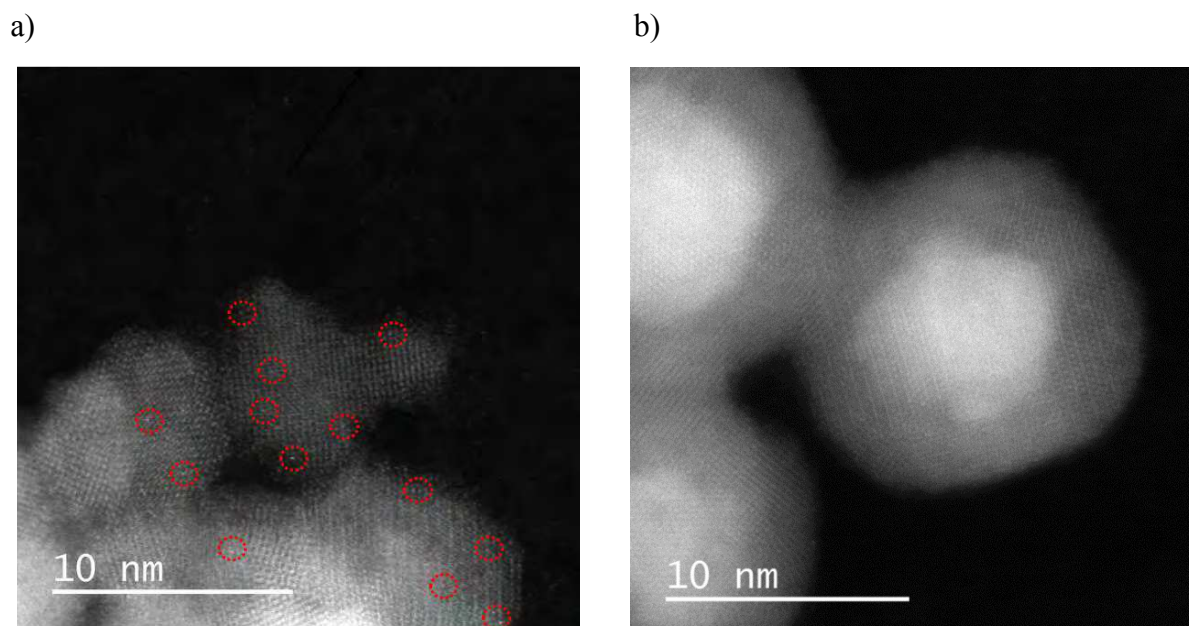


Figure 24. Atomic resolution micrographs obtained by HR-HAADF-STEM of a) *m-Fe@FeO_x@Ru* NPs, highlighting the presence of ruthenium atoms and b) *b-Fe@FeO_x@Ru* NPs

More evidence for the presence of Ru complexes on the NPs was found using XPS, although the ruthenium content in *b-Fe@FeO_x@Ru* NPs seemed too low to be studied. The data obtained from *m-Fe@FeO_x@Ru* NPs are reported in Table 2, compared to the references *r-Fe@FeO_x* NPs and the free ruthenium photosensitiser [Ru-PO(OH)₂]Cl₂.

The Ru 3d and C1s energy ranges were expected to overlap. In this region, the spectrum of the free ruthenium complex presented a peak at 280.7 eV attributed to the Ru3d_{5/2} contribution, being characteristic for -Ru-N environment[74]. The associated Ru3d_{3/2} peak was observed at 285 eV (see Table 2). The same two peaks were observed in *m-Fe@FeO_x@Ru* NPs, but not in *r-Fe@FeO_x@Ru* NPs, clearly confirming the presence of the Ru complex in the hybrid nanomaterial obtained by *method 2* and the better efficiency of this method over *method 1*. (Figure 25 and Table 2).

In *m-Fe@FeO_x@Ru* NPs a strong contribution, characteristic of C-C/C-H bonds, was also evidenced at 284.7 eV; as well as a peak at 285.8 eV which could correspond to the contribution of both C-N from the phenanthroline ligand, as in the free complex, and to C-O from oleic acid. The presence of oleic acid remaining at the surface of the NPs is further confirmed in the C1s regions of the XPS spectra of *r-Fe@FeO_x* NPs and *m-Fe@FeO_x@Ru* NPs (Figure 25), both

clearly displaying a peak at 288 eV assigned to C=O/O=C=O bonds. Such a result suggests that the exchange of the carboxylic acid coating of the NP to phosphonates is difficult at room temperature, even when an excess is introduced. For example, similar results have been obtained by Basly et al. when trying to exchange oleic acid for dendrons with phosphonic acid end groups at the surface of magnetite NPs[61].

Further confirmation of the presence of the Ru complex was found also in the N1s energy range (Figure 26). The XPS N1s spectrum of *m*-Fe@FeOx@Ru NPs displayed a main peak at 399.8 eV attributed to the nitrogen in the phenanthroline ligand of the Ru complex. Interestingly, we didn't observe any contribution from nitrogen in an ammonium environment (expected at 401.9 eV[75]), confirming the elimination of the ammonium chloride during the grafting process, as observed in the WAXS measurements. Another peak was found at 398.4 eV which was assigned to N-pyridinic (which may come from traces of free ligand).

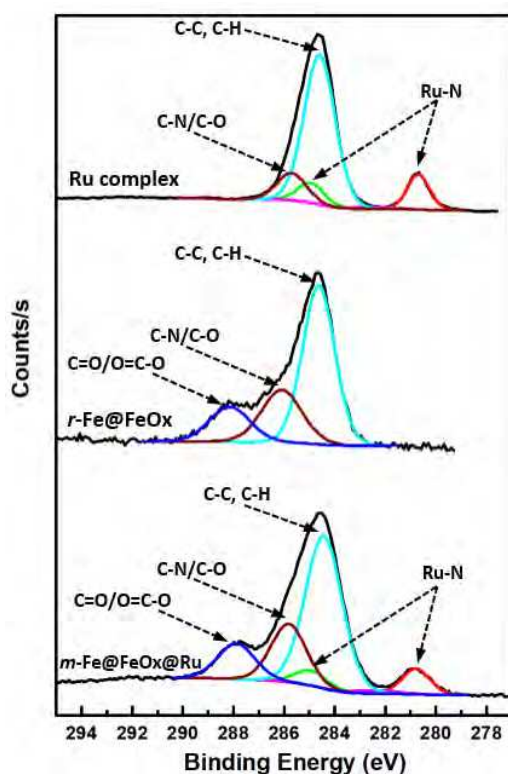


Figure 25. XPS spectra of the free ruthenium complex $[Ru-PO(OH)_2]Cl_2$ (top), *r*-Fe@FeOx NPs (middle) and *m*-Fe@FeOx@Ru NPs (bottom) in the C1s - Ru 3d region (red and green curves: Ru-N 3d_{5/2} and 3d_{3/2} signals, respectively; cyan curve: C-C/C-H signal; brown curve: C-N/C-O signal; blue curve: C=O/O=C-O signal).

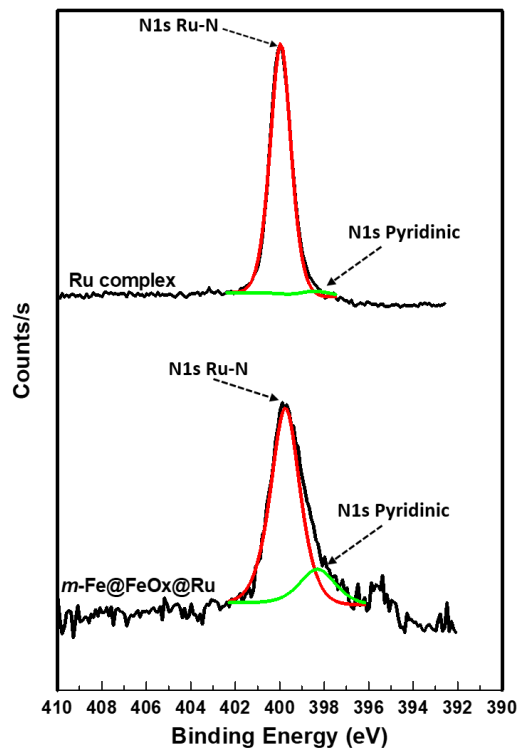


Figure 26. XPS spectra of the free Ru complex (top), and *m*-Fe@FeOx@Ru NPs (bottom) in the N1s region.

In the Fe2p region only one peak at 710.2 eV, attributed to Fe³⁺, was observed (Figure 27). The absence of Fe metal signal emphasized the further oxidation of the Fe core during the grafting process, confirming the first conclusion made based on WAXS data.

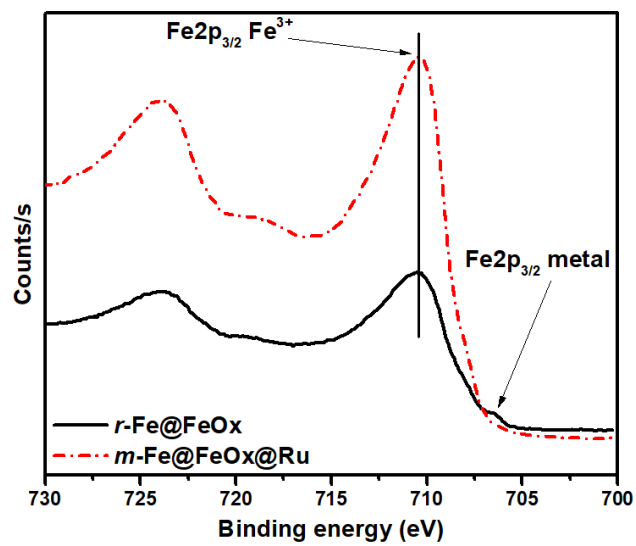


Figure 27. Overlap of the XPS spectra of the r-Fe@FeOx NPs, and m-Fe@FeOx@Ru NPs in the Fe2p region.

Table 2. Binding energies, full width at half maximum (FWHM) and percentage of Ru3d, C1s, N1s, P2p, O1s and Fe2p_{3/2} for [Ru-PO(OH)₂]Cl₂, r-Fe@FeOx NPs and m-Fe@FeOx@Ru NPs.

		[Ru-PO(OH) ₂]Cl ₂			r-Fe@FeOx NPs			m-Fe@FeOx@Ru NPs		
		B.E. (eV)	FWHM (eV)	% atomic	B.E. (eV)	FWHM (eV)	% atomic	B.E. (eV)	FWHM (eV)	% atomic
Ru3d	Ru3d _{5/2} (Ru in complex)	280.7	1.0	1.3	-	-	-	280.8	1.3	0.2
	Ru3d _{3/2} (Ru in complex)	285.0	1.2		-	-	-	285.0	1.4	
C1s	C-C, C-H	284.6	1.4	63.9	284.6	1.5	8.7	284.5	1.7	13.3
	C-N/C-O	285.7	1.4	11.0	286.1	1.8	3.6	285.8	1.6	4.9
	C=O/O=C-O	-	-	-	288.2	1.9	2.4	287.9	1.7	3.1
N1s	N pyridinic	398.4	1.8	0.3	-	-	-	398.3	1.9	0.3
	Ru-N-	399.9	1.1	7.8	-	-	-	399.8	1.5	1.2
P2p	P2p _{3/2} P-C	131.0	2.1	0.5	-	-	-	-	-	-
	P2p _{1/2} P-C	131.8	2.2		-	-	-	-	-	

Chapter III – Fe@FeOx@Ru photoanode

	P2p _{3/2} C-P=O	132.4	1.6	1.7	-	-	-	132.3	1.4	0.3
	P2p _{1/2} C-P=O	133.2	1.7		-	-	-	133.2	1.4	
Fe2p _{3/2}	Fe (0)	-	-	5.4	706.7	-	-	-	-	18.1
	Fe (III)	-	-		710.3	-	710.2	-		

Chapter III – Fe@FeO_x@Ru photoanode

The ratio of ruthenium complex per NP was quantitatively determined on the basis of ICP-OES results. Based on these results, calculations indicated an average of 9 Ru complexes per NP in the hybrid nanomaterial ***b*-Fe@FeO_x@Ru NPs** and approximately 56 Ru complexes per NP in the hybrid nanomaterial ***m*-Fe@FeO_x@Ru NPs** (see Experimental Section – Section 7.3 for details on the calculations). Those results confirmed the much lower ratio obtained for ***b*-Fe@FeO_x@Ru NPs** than for ***m*-Fe@FeO_x@Ru NPs**, as suspected from the XPS measurements. The higher grafting density obtained by the monophasic ***method 2*** could be related to the increased interactions between the ruthenium complexes and the NPs when compared to the biphasic ***method 1*** in which the interactions happened only at the water/dichloromethane interface.

To get a clear view of the chemical bonding of the complex on the NPs surface, it would have been interesting to study the P2p or O energy ranges. However, if we could detect the signal of phosphorus in the XPS spectrum of the nanohybrid, the signal/noise ratio was too weak to make a clear interpretation (Figure 28). While, in the O energy range, contributions from both carboxylate and phosphonate environments complicated too much the spectrum. Consequently, no indication on the coordination mode of the phosphonate group on the iron oxide surface could be obtained based on XPS results.

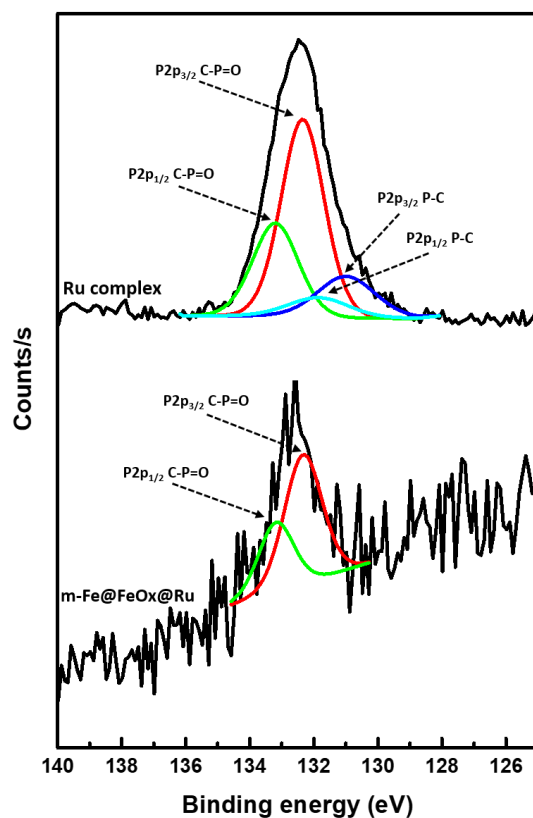


Figure 28. Overlap of the XPS spectra of the free Ru complex, and *m*-Fe@FeO_x@Ru NPs in the P2p region.

4. Photo-electrochemical water oxidation catalysis

In the (*m/b*)-Fe@FeO_x@Ru hybrid systems prepared, the role of the molecular complex is to harvest solar energy while the nanoparticles aim to accelerate the water oxidation reaction. Thus, before investigating the photocatalytic activity of these hybrid systems, the electrocatalytic activity of the *r*-Fe@FeO_x NPs used to build them was evaluated in a pH 7 phosphate buffer (KPi 0.1 M) and a pH 13 alkaline electrolyte (NaOH 0.1M). The results show that the *r*-Fe@FeO_x NPs is an active catalyst for the O₂ evolution reaction (OER), and that it is significantly more active in an alkaline solution (see Section 2.2- Chapter II). We then investigated the photocatalytic activity of the (*m/b*)-Fe@FeO_x@Ru NPs hybrid nanomaterials to understand in what extend a covalent linkage between the molecular light-harvester and the nanocatalyst, can benefit to its overall operation, working in alkaline solution. To this end, an ink was prepared from the (*m/b*)-Fe@FeO_x@Ru NPs samples and deposited onto a FTO electrode as described for the *r*-Fe@FeO_x

Chapter III – Fe@FeOx@Ru photoanode

NPs (see Experimental section –Section 4). The light source was provided by a Xe arc lamp equipped with a UV filter. We employed the back-illumination mode in which the incident light went through the transparent FTO electrode to the catalyst. The incident light intensity reaching the FTO electrode was set to 100 mW/cm².

It is interesting to note that the ink obtained from the NPs bearing Ru complexes at their surface, was more homogenous and allowed to reach a more homogenous deposit on the FTO electrode than when working with *r*-Fe@FeOx NPs, as shown in Figure 29 for *m*-Fe@FeOx@Ru NPs, as an example.

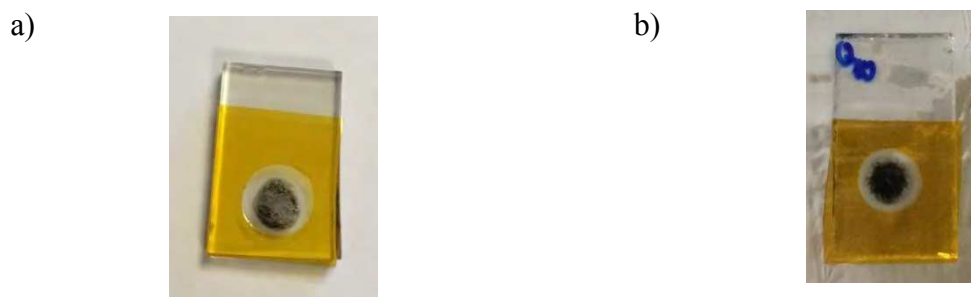


Figure 29. Photograph images of a) *r*-Fe@FeOx photoanode and b) *m*-Fe@FeOx@Ru photoanode by drop-casting on FTO electrodes for testing their photocatalytic activity.

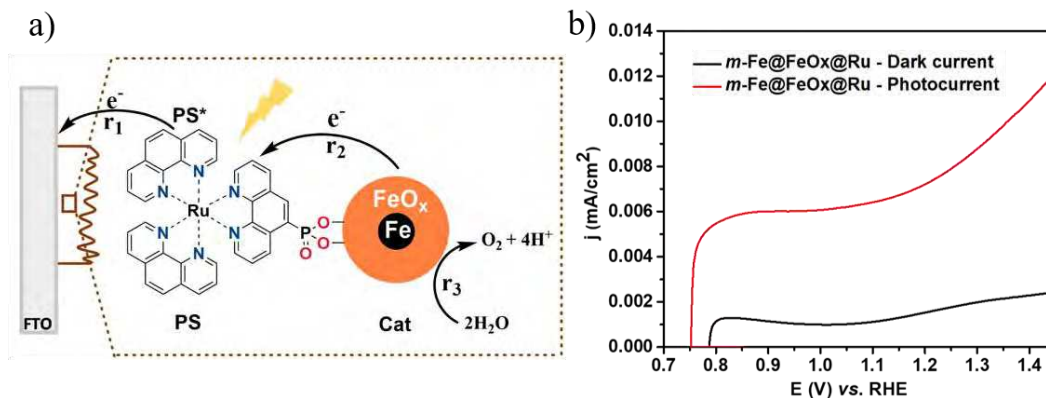


Figure 30. a) Simplified scheme for the photocatalytic water oxidation (left) where PS and PS* stand for the photosensitizer in its ground and excited states respectively, and cat stands for catalyst (here Fe@FeOx nanoparticles); b) Dark current density (black curve) and photocurrent density (red curve) of *m*-Fe@FeOx@Ru NPs photoanode measured in pH 13 (NaOH 0.1M) at scan rate 10 mV/s under 1 Sun illumination.

Chapter III – Fe@FeOx@Ru photoanode

Figure 30a (left) shows a simplified overview of the electron and energy transfers involved during the operation of the hybrid photocatalyst. In this model the overall oxygen production rate is determined by the slowest step of the elemental reactions 1, 2, and 3, in which: (i) $r1$ represents the rate of the oxidation of the excited photosensitizer (PS*) by an oxidative potential applied to the FTO electrode. Thus, $r1$ is expected to increase when increasing the oxidative potential applied; (ii) $r2$ represents the electron transfer rate from the catalyst to the oxidized photosensitizer (PS⁺) (*i.e.* the hole transfer rate from PS⁺ to the catalyst) and (iii) $r3$ represents the O₂ production rate on the surface of the water oxidation catalyst, *i.e.* on the surface of the Fe@FeOx component of the hybrid nanomaterial.

Herein, the photocatalytic activity of ***m*-Fe@FeOx@Ru NPs** electrode for the water oxidation reaction was assayed at pH 13 where $r3$ is assumed to be optimal. Figure 30b shows current density-voltage (J - V) curves recorded for this electrode with (red trace) and without (black trace) light illumination. In the absence of light, the dark current was almost negligible at applied potentials up to 1.5 V *vs.* RHE. Under light illumination, the onset potential for generating a photocurrent was found to be 0.75 V *vs.* RHE. An almost constant photocurrent density was observed when increasing the applied potential up to 1.1V *vs.* RHE. This means that the overall rate of water oxidation remained unchanged in this potential window even if $r1$ should increase when increasing the applied oxidative potential. In other words, the charge transfers between the Ru light-harvester and the Fe@FeOx nanocatalyst, namely $r2$, limited the whole operation in this potential range.

In order to emphasize the benefit of engineering a covalent grafting between the light-harvester and the catalyst, we also recorded the photocatalytic activity of a simple mixture of ***r*-Fe@FeOx NPs** and ruthenium tris-phenanthroline chloride, [Ru(phen)₃]Cl₂, in the same Ru per NP ratio (*i.e.* 56) as in the ***m*-Fe@FeOx@Ru NPs** sample, hereafter labeled ***r*-Fe@FeOx//Ru**. [Ru(phen)₃]Cl₂ was chosen as a reference photosensitizer given its comparable photophysical properties to those of [Ru-PO(OH)₂]Cl₂, (see Figure 16) and was expected to adsorb only physically onto the ***r*-Fe@FeOx** nanoparticles given the absence of pendant grafting group. A control electrode was also fabricated by loading only ***r*-Fe@FeOx** nanoparticles at an identical mass loading density without adding any Ru complex. Figure 31a shows the I - t curves recorded at 1.0 V *vs.* RHE under chopped

light mode using electrodes made of *m*-Fe@FeOx@Ru NPs (red trace), *r*-Fe@FeOx//Ru (blue trace) and *r*-Fe@FeOx NPs (black trace). The *r*-Fe@FeOx NPs photoanode generated a negligible photocurrent density of *ca.* 0.5 $\mu\text{A}/\text{cm}^2$.

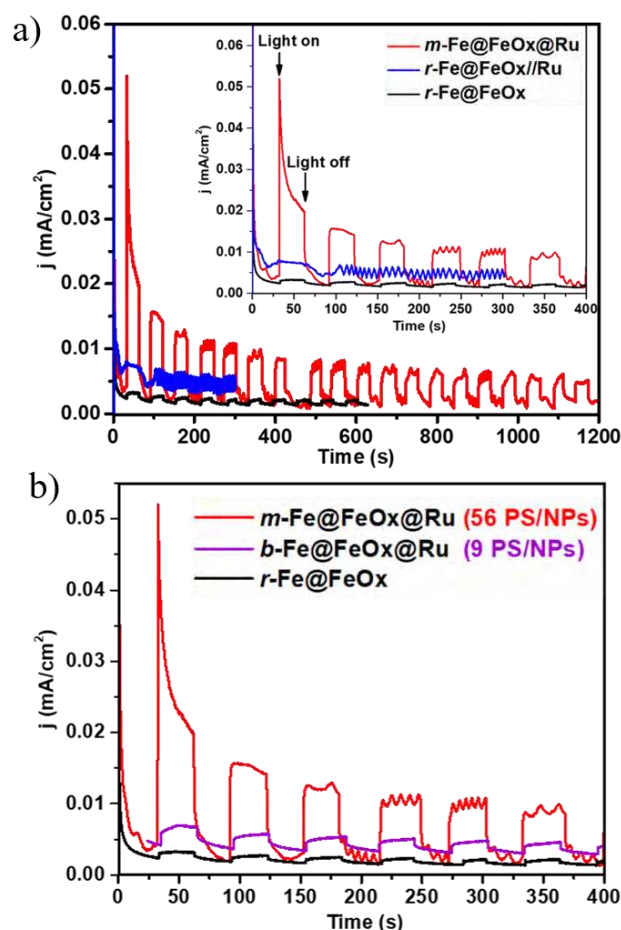


Figure 31. (a) *I-t* curves recorded on *m*-Fe@FeOx@Ru NPs (red trace), *r*-Fe@FeOx//Ru (blue trace) and *r*-Fe@FeOx NPs (black trace) photoanodes; (b) *I-t* curves recorded on *m*-Fe@FeOx@Ru NPs (red trace), *b*-Fe@FeOx@Ru NPs (purple trace) and *r*-Fe@FeOx (black trace) photoanodes. Applied potential: 1.0 V vs. RHE. Electrolyte: pH 13 NaOH solution. Incident light power: 100 mW/cm².

The *r*-Fe@FeOx//Ru (simple mixture) showed a higher photocurrent density (2.3 $\mu\text{A}/\text{cm}^2$) demonstrating the improvement in light harvesting brought by the Ru complex. Interestingly, a significantly higher photocurrent density of *ca.* 20 $\mu\text{A}/\text{cm}^2$ was achieved for the *m*-Fe@FeOx@Ru NPs electrode (where the Ru complex is covalently grafted on the *r*-Fe@FeOx nanocatalyst). This value corresponds to *ca.* 9-folds and 40-folds higher activities than those

Chapter III – Fe@FeOx@Ru photoanode

obtained with the *r*-Fe@FeOx//Ru and *r*-Fe@FeOx electrodes, respectively. This result clearly demonstrates the usefulness of a covalent grafting between the Ru light-harvester and the Fe@FeOx catalyst to promote the charge transfer and therefore increase the overall photocatalytic activity. This result is in perfect line with the few previous studies where a covalent grafting between light-harvesters and water oxidation catalysts was shown to be more efficient in comparison with a simple mixture of both[50, 76].

By repeating the on-off light illumination cycle, the *m*-Fe@FeOx@Ru NPs photoanode was found to still produce ~50% of the initial photocurrent density (determined in the first on-off cycle) after 20 minutes assay, whereas the non-bonded *r*-Fe@FeOx//Ru counterpart did not generate any noticeable photocurrent from the second on-off cycle onwards. This degradation can be attributed to a fast detachment of [Ru(phen)₃]Cl₂ from the electrode surface because of the lack of covalent bonding and the high solubility of this complex in water. Thus, covalent grafting also improves the stability of the *m*-Fe@FeOx@Ru NPs hybrid system.

As described above, *b*-Fe@FeOx@Ru NPs had a much lower Ru complex grafting density than *m*-Fe@FeOx@Ru NPs, that is 9 Ru complexes vs. 56 Ru complexes per nanoparticle. At identical mass loading density, the *b*-Fe@FeOx@Ru NPs photoanode showed a 7-fold lower photocurrent density than the *m*-Fe@FeOx@Ru NPs photoanode did, that is ~3 vs. ~20 $\mu\text{A}/\text{cm}^2$ (Figure 31b, purple and red traces). However, comparable photocatalytic performances were deduced for these two photoanodes when normalizing the catalytic activity per number of photosensitizer (PS), *i.e.* per number of grafted Ru complex. (see Experimental section - Section 7 for details on normalization), thus confirming that the rate limiting step involves the Ru complex. Turn over frequencies per Ru complex (TOF_{Ru}) of 0.015 s^{-1} and 0.02 s^{-1} were calculated for the photoanodes prepared with *b*-Fe@FeOx@Ru NPs and *m*-Fe@FeOx@Ru NPs, respectively, which represents the best TOF value reported so far when comparing to the literature data published for comparable systems (see Table 3). The similarity of the values obtained for *b*-Fe@FeOx@Ru NPs and *m*-Fe@FeOx@Ru NPs photoanodes further confirmed that the charge transfer between the Ru light-harvester and the Fe@FeOx nanocatalyst is the main limiting factor. A higher density of Ru light-harvester would thus increase the overall performance of the system.

Looking back to the first on-off light illumination cycle recorded with *m*-Fe@FeOx@Ru NPs, a high transient photocurrent ($\Delta j_{\text{transient}}$) of 33 $\mu\text{A}/\text{cm}^2$ (Figure 32) was observed. This suggested an important charge recombination within the system[77, 78]. More studies are required to understand this phenomenon, but this recombination may be related to the fact that the (luminescent) $^3\text{MLCT}$ excited state of the Ru-light-harvester[79] might be quenched by the oxygen molecules which are generated locally on the surface of the *r*-Fe@FeOx nanoparticles. Such a quenching was indeed demonstrated in solution, as mentioned earlier in this study (Figure 17). If so, quickly removing oxygen from the catalyst surface would reduce the charge recombination and thus represents a good strategy to increase the performance of the hybrid photocatalyst.

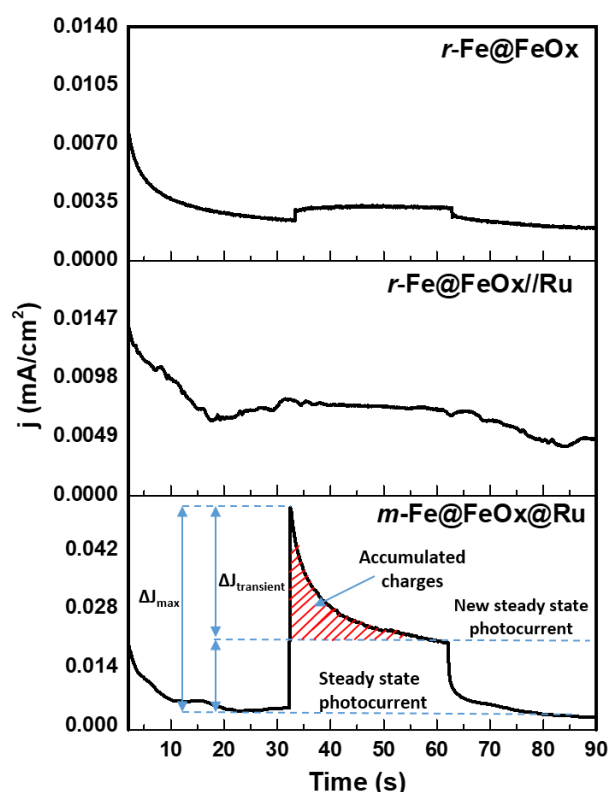


Figure 32. Focus on photocurrent-time plot in the first chop-light cycle of *r*-Fe@FeOx NPs, *r*-Fe@FeOx//Ru NPs, and *m*-Fe@FeOx@Ru NPs photoanodes at applied potential 1.0 V vs RHE, pH 13.

Finally, as shown in Figure 33, the photocatalytic activity of *b*-Fe@FeOx@Ru NPs was first studied in pH 13, but also in pH 7 to compare with the results obtained on *r*-Fe@FeOx NPs (see

Results and Discussion - Section 2.2- Chapter 2). In pH 13, a photogenerated current of $3 \mu\text{A}/\text{cm}^2$ was recorded, while in pH 7 it was much lower, *circa* $1.4 \mu\text{A}/\text{cm}^2$. After 9 min of operation under chop-light, the ***b*-Fe@FeOx@Ru** photoanode retained 40 % of its initial photocurrent in pH 13 and 54 % in pH 7 in identical conditions. The lower activity of ***b*-Fe@FeOx@Ru** complex in pH 7 in comparison with pH 13 was already seen on ***r*-Fe@FeOx** NPs *i.e.* in the absence of Ru complex (see Results and Discussion - Section 2.2- Chapter 2).

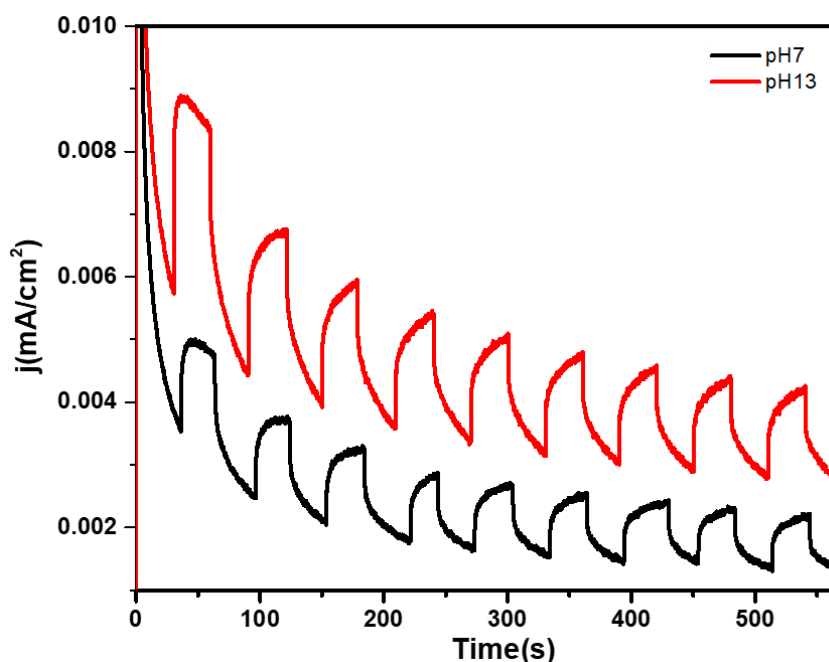


Figure 33. Chopped light measurement at an applied potential 1.0 V vs. RHE of ***b*-Fe@FeO_x@Ru** photoanodes in pH 7 and pH 13 under 1 Sun illumination.

5. Conclusion

This chapter reports the successful construction of a novel hybrid photocatalyst for the solar driven water splitting by covalently grafting a Ru-phenanthroline light-harvester onto ***r*-Fe@FeOx** core/shell nanoparticles through a phosphonate linker. First, a successful synthetic strategy was developed to prepare the phosphonate-derivative 1,10-phenanthroline ligand and the corresponding *bis*-heteroleptic ruthenium(II) complex from the [Ru(phen)₂Cl₂] precursor. Two synthetic pathways were investigated to graft the Ru light-harvester at the surface of the ***r*-Fe@FeOx** nanoparticles described in Chapter II, namely *via* mono- and biphasic processes in

Chapter III – Fe@FeOx@Ru photoanode

THF/H₂O or CH₂Cl₂/H₂O solvent mixtures, respectively. The monophasic process was found to be more efficient as it provided a higher grafting density at the surface of the nanoparticles, 7-folds higher than that obtained by the biphasic process (56 and 9 Ru complexes per nanoparticles for the mono- and biphasic processes, respectively). Then, the efficient photocatalytic activity of the hybrid system prepared in monophasic conditions was demonstrated. At an applied potential of +1.0 V vs. RHE and under a simulated 1 sun illumination, a catalytic rate of 0.02 O₂.Ru⁻¹.s⁻¹ was deduced. They compare well with previous data from the literature (see Table 3). The results obtained also evidenced that the charge transfer between the grafted Ru light-harvester and the *r*-Fe@FeOx nanocatalyst is the bottleneck in the operation of these hybrid systems. Thus, increasing the grafting density of Ru light-harvester could be a way to improve the overall performance. Moreover, the covalent grafting was found to not only improve the photocatalytic activity (by *ca.* 9 folds compared with a counterpart system based on a simple physical adsorption) but also to significantly improve the stability of the photocatalyst. However, the charge recombination within the system remained important as evidenced by a rather high transient current. This may result from the quenching of the excited state of Ru(II) complex by the O₂ molecules accumulating on the surface of the Fe@FeOx catalyst until a steady state in their evolution is reached. If so, a better evacuation of O₂ might improve the overall performance of the hybrid photocatalyst as well.

In the future, and in line with previous results from Mallouk and co-workers[48], the covalent grafting of the hybrid *m*-Fe@FeOx@Ru NPs on the FTO electrode could be envisaged to avoid any possible leaching of the catalyst and to limit back electron transfer events happening during photo-catalytic conditions.

Table 3: Summary of the representative photocatalytic activity toward OER using hybrid photoanodes based on a molecular dye covalently grafted on a MOx catalyst.

No.	Substrate /PS/ WOC	PS:WOC ratio	Electrolyte	V _{onset} (V vs. RHE)	Photocurrent/testing conditions	TON	TOF	Ref
1	[Ru(bipy) ₂ (bipy(COO) ₂) ₂]/ [Mn ₄ O ₄ ((MeOPh) ₂ PO ₂) ₆]	4.5:1	Na ₂ SO ₄ 0.1M, pH 6.5	-	-	-	0.013 O ₂ .cluster ⁻¹ s ⁻¹	[54]
2	[Ru(bpy)(4,4'-(PO ₃ H ₂) ₂ bpy) ₂] (Cl) ₂ / Co ₃ O ₄	0.15:1	Na ₂ SiF ₆ - NaHCO ₃ (0.02-0.04 M, pH 5.6)	-	-	2.53 O ₂ .PS ⁻¹	0.001 O ₂ .PS ⁻¹ .s ⁻¹	[50]
3	TiO ₂ /[Ru(bpy) ₃] ²⁺ modified malonate ligand/IrO ₂ .nH ₂ O	-	Na ₂ SiF ₆ - NaHCO ₃ 0.02M pH 5.75	-	12.7 μA/cm ² At 0 V vs. Ag/AgCl/KCl Under 450 nm light (7.8mW/cm ²)	-	-	[48]
4	ITO/PMPDI/CoOx	-	0.1 M pH 7 KPi	-	150 μA/cm ² at 1 V vs. Ag/AgCl simulated sunlight (100 mW/cm ²)	-	-	[11]

Chapter III – Fe@FeOx@Ru photoanode

5	FTO/[Ru(phen)₂(phen-PO(OH)₂] (Cl)₂/ <i>r</i>-Fe@FeOx = <i>m</i>-Fe@FeOx@Ru NP	85:1	0.1M NaOH pH13	0.75	20 $\mu\text{A}/\text{cm}^2$ At 1 V vs. RHE 1 Sun illumination (100 mW/cm²)	0.67 O₂.PS⁻¹	0.02 O₂.PS⁻¹.s⁻¹	This work
---	---	------	-------------------------------	-------------	--	---	--	----------------------

6. References

1. Fujishima, A. and K. Honda, *Electrochemical Photolysis of Water at a Semiconductor Electrode*. Nature, 1972. **238**(5358): p. 37-38.
2. Kim, T.W., et al., *Simultaneous enhancements in photon absorption and charge transport of bismuth vanadate photoanodes for solar water splitting*. Nature Communications, 2015. **6**(1): p. 8769.
3. Tayebi, M. and B.-K. Lee, *Recent advances in BiVO₄ semiconductor materials for hydrogen production using photoelectrochemical water splitting*. Renewable and Sustainable Energy Reviews, 2019. **111**: p. 332-343.
4. Kim, T.W. and K.-S. Choi, *Nanoporous BiVO₄ Photoanodes with Dual-Layer Oxygen Evolution Catalysts for Solar Water Splitting*. Science, 2014. **343**(6174): p. 990-994.
5. Seabold, J.A. and K.-S. Choi, *Efficient and Stable Photo-Oxidation of Water by a Bismuth Vanadate Photoanode Coupled with an Iron Oxyhydroxide Oxygen Evolution Catalyst*. Journal of the American Chemical Society, 2012. **134**(4): p. 2186-2192.
6. Sivula, K., *Nanostructured α -Fe₂O₃ Photoanodes*, in *Photoelectrochemical Hydrogen Production*, R. van de Krol and M. Grätzel, Editors. 2012, Springer US: Boston, MA. p. 121-156.
7. Shen, S., et al., *Hematite heterostructures for photoelectrochemical water splitting: rational materials design and charge carrier dynamics*. Energy & Environmental Science, 2016. **9**(9): p. 2744-2775.
8. Berardi, S., et al., *Molecular artificial photosynthesis*. Chemical Society Reviews, 2014. **43**(22): p. 7501-7519.
9. Sherman, B.D., et al., *Light-Driven Water Splitting by a Covalently Linked Ruthenium-Based Chromophore–Catalyst Assembly*. ACS Energy Letters, 2017. **2**(1): p. 124-128.
10. He, J., et al., *Ruthenium-Based Photosensitizers for Dye-Sensitized Solar Cells*, in *Organometallics and Related Molecules for Energy Conversion*, W.-Y. Wong, Editor. 2015, Springer Berlin Heidelberg: Berlin, Heidelberg. p. 91-114.
11. Kirner, J.T., et al., *Visible-Light-Assisted Photoelectrochemical Water Oxidation by Thin Films of a Phosphonate-Functionalized Perylene Diimide Plus CoOx Cocatalyst*. ACS Applied Materials & Interfaces, 2014. **6**(16): p. 13367-13377.
12. Ronconi, F., et al., *Modification of Nanocrystalline WO₃ with a Dicationic Perylene Bisimide: Applications to Molecular Level Solar Water Splitting*. Journal of the American Chemical Society, 2015. **137**(14): p. 4630-4633.
13. Kamire, R.J., et al., *Photodriven Oxidation of Surface-Bound Iridium-Based Molecular Water-Oxidation Catalysts on Perylene-3,4-dicarboximide-Sensitized TiO₂ Electrodes Protected by an Al₂O₃ Layer*. The Journal of Physical Chemistry C, 2017. **121**(7): p. 3752-3764.
14. Kirner, J.T. and R.G. Finke, *Sensitization of Nanocrystalline Metal Oxides with a Phosphonate-Functionalized Perylene Diimide for Photoelectrochemical Water Oxidation with a CoOx Catalyst*. ACS Applied Materials & Interfaces, 2017. **9**(33): p. 27625-27637.
15. Bledowski, M., et al., *Visible-light photocurrent response of TiO₂–polyheptazine hybrids: evidence for interfacial charge-transfer absorption*. Physical Chemistry Chemical Physics, 2011. **13**(48): p. 21511-21519.

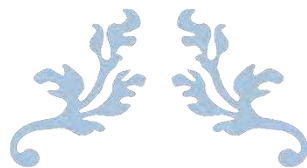
16. Wang, L., et al., *Dynamics of Photogenerated Holes in TiO₂-Polyheptazine Hybrid Photoanodes for Visible Light-Driven Water Splitting*. Journal of The Electrochemical Society, 2012. **159**(7): p. H616-H622.
17. Wang, L., et al., *Ultrasmall CoO(OH)_x Nanoparticles As a Highly Efficient “True” Cocatalyst in Porous Photoanodes for Water Splitting*. ACS Catalysis, 2017. **7**(7): p. 4759-4767.
18. Swierk, J.R., et al., *Metal-free organic sensitizers for use in water-splitting dye-sensitized photoelectrochemical cells*. Proceedings of the National Academy of Sciences, 2015. **112**(6): p. 1681-1686.
19. Bornoz, P., et al., *Direct Light-Driven Water Oxidation by a Ladder-Type Conjugated Polymer Photoanode*. Journal of the American Chemical Society, 2015. **137**(49): p. 15338-15341.
20. Lee, Y., et al., *Synthesis and Activities of Rutile IrO₂ and RuO₂ Nanoparticles for Oxygen Evolution in Acid and Alkaline Solutions*. The Journal of Physical Chemistry Letters, 2012. **3**(3): p. 399-404.
21. Nong, H.N., et al., *IrO_x core-shell nanocatalysts for cost- and energy-efficient electrochemical water splitting*. Chemical Science, 2014. **5**(8): p. 2955-2963.
22. Chandra, D., et al., *Highly Efficient Electrocatalysis and Mechanistic Investigation of Intermediate IrO_x(OH)_y Nanoparticle Films for Water Oxidation*. ACS Catalysis, 2016. **6**(6): p. 3946-3954.
23. Guan, J., et al., *Synthesis and Demonstration of Subnanometric Iridium Oxide as Highly Efficient and Robust Water Oxidation Catalyst*. ACS Catalysis, 2017. **7**(9): p. 5983-5986.
24. Kan, M., et al., *Highly Active IrO_x Nanoparticles/Black Si Electrode for Efficient Water Splitting with Conformal TiO₂ Interface Engineering*. ACS Sustainable Chemistry & Engineering, 2017. **5**(11): p. 10940-10946.
25. Li, G., et al., *Nanoporous IrO₂ catalyst with enhanced activity and durability for water oxidation owing to its micro/mesoporous structure*. Nanoscale, 2017. **9**(27): p. 9291-9298.
26. Badam, R., et al., *Synthesis and electrochemical analysis of novel IrO₂ nanoparticle catalysts supported on carbon nanotube for oxygen evolution reaction*. International Journal of Hydrogen Energy, 2018. **43**(39): p. 18095-18104.
27. Jiang, B., et al., *Efficient oxygen evolution on mesoporous IrO_x nanosheets*. Catalysis Science & Technology, 2019. **9**(14): p. 3697-3702.
28. Deng, X. and H. Tüysüz, *Cobalt-Oxide-Based Materials as Water Oxidation Catalyst: Recent Progress and Challenges*. ACS Catalysis, 2014. **4**(10): p. 3701-3714.
29. Gujral, S.S., et al., *Highly Dispersed Cobalt Oxide on TaON as Efficient Photoanodes for Long-Term Solar Water Splitting*. ACS Catalysis, 2016. **6**(5): p. 3404-3417.
30. Huang, J., Y. Zhang, and Y. Ding, *Rationally Designed/Constructed CoO_x/WO₃ Anode for Efficient Photoelectrochemical Water Oxidation*. ACS Catalysis, 2017. **7**(3): p. 1841-1845.
31. Ahmed, M.S., B. Choi, and Y.-B. Kim, *Development of Highly Active Bifunctional Electrocatalyst Using Co₃O₄ on Carbon Nanotubes for Oxygen Reduction and Oxygen Evolution*. Scientific Reports, 2018. **8**(1): p. 2543.
32. Tüysüz, H., et al., *Mesoporous Co₃O₄ as an electrocatalyst for water oxidation*. Nano Research, 2013. **6**(1): p. 47-54.
33. Kanan, M.W. and D.G. Nocera, *In Situ Formation of an Oxygen-Evolving Catalyst in Neutral Water Containing Phosphate and Co²⁺*. Science, 2008. **321**(5892): p. 1072-1075.

34. Kanan, M.W., Y. Surendranath, and D.G. Nocera, *Cobalt–phosphate oxygen-evolving compound*. Chemical Society Reviews, 2009. **38**(1): p. 109-114.
35. Lutterman, D.A., Y. Surendranath, and D.G. Nocera, *A Self-Healing Oxygen-Evolving Catalyst*. Journal of the American Chemical Society, 2009. **131**(11): p. 3838-3839.
36. Kanan, M.W., et al., *Structure and Valency of a Cobalt–Phosphate Water Oxidation Catalyst Determined by in Situ X-ray Spectroscopy*. Journal of the American Chemical Society, 2010. **132**(39): p. 13692-13701.
37. Zhong, D.K., et al., *Photo-assisted electrodeposition of cobalt–phosphate (Co–Pi) catalyst on hematite photoanodes for solar water oxidation*. Energy & Environmental Science, 2011. **4**(5): p. 1759-1764.
38. Chemelewski, W.D., et al., *Amorphous FeOOH Oxygen Evolution Reaction Catalyst for Photoelectrochemical Water Splitting*. Journal of the American Chemical Society, 2014. **136**(7): p. 2843-2850.
39. Feng, J.-X., et al., *FeOOH/Co/FeOOH Hybrid Nanotube Arrays as High-Performance Electrocatalysts for the Oxygen Evolution Reaction*. Angewandte Chemie International Edition, 2016. **55**(11): p. 3694-3698.
40. Hu, J., et al., *Understanding the Phase-Induced Electrocatalytic Oxygen Evolution Reaction Activity on FeOOH Nanostructures*. ACS Catalysis, 2019. **9**(12): p. 10705-10711.
41. Mukai, K., et al., *High-pressure synthesis of ϵ -FeOOH from β -FeOOH and its application to the water oxidation catalyst*. RSC Advances, 2020. **10**(73): p. 44756-44767.
42. Lichterman, M.F., et al., *Enhanced Stability and Activity for Water Oxidation in Alkaline Media with Bismuth Vanadate Photoelectrodes Modified with a Cobalt Oxide Catalytic Layer Produced by Atomic Layer Deposition*. The Journal of Physical Chemistry Letters, 2013. **4**(23): p. 4188-4191.
43. Abdi, F.F. and R. van de Krol, *Nature and Light Dependence of Bulk Recombination in Co-Pi-Catalyzed BiVO₄ Photoanodes*. The Journal of Physical Chemistry C, 2012. **116**(17): p. 9398-9404.
44. Abdi, F.F., et al., *Efficient solar water splitting by enhanced charge separation in a bismuth vanadate-silicon tandem photoelectrode*. Nature Communications, 2013. **4**(1): p. 2195.
45. Zachäus, C., et al., *Photocurrent of BiVO₄ is limited by surface recombination, not surface catalysis*. Chemical Science, 2017. **8**(5): p. 3712-3719.
46. Nellist, M.R., et al., *Potential-Sensing Electrochemical AFM Shows CoPi as a Hole Collector and Oxygen Evolution Catalyst on BiVO₄ Water-Splitting Photoanodes*. ACS Energy Letters, 2018. **3**(9): p. 2286-2291.
47. Chen, X., et al., *Promoting the photoanode efficiency for water splitting by combining hematite and molecular Ru catalysts*. Electrochemistry Communications, 2013. **27**: p. 148-151.
48. Youngblood, W.J., et al., *Photoassisted Overall Water Splitting in a Visible Light-Absorbing Dye-Sensitized Photoelectrochemical Cell*. Journal of the American Chemical Society, 2009. **131**(3): p. 926-927.
49. Lee, S.-H.A., et al., *Electron transfer kinetics in water splitting dye-sensitized solar cells based on core–shell oxide electrodes*. Faraday Discussions, 2012. **155**(0): p. 165-176.
50. De Tovar, J., et al., *Light-driven water oxidation using hybrid photosensitizer-decorated Co₃O₄ nanoparticles*. Materials Today Energy, 2018. **9**: p. 506-515.

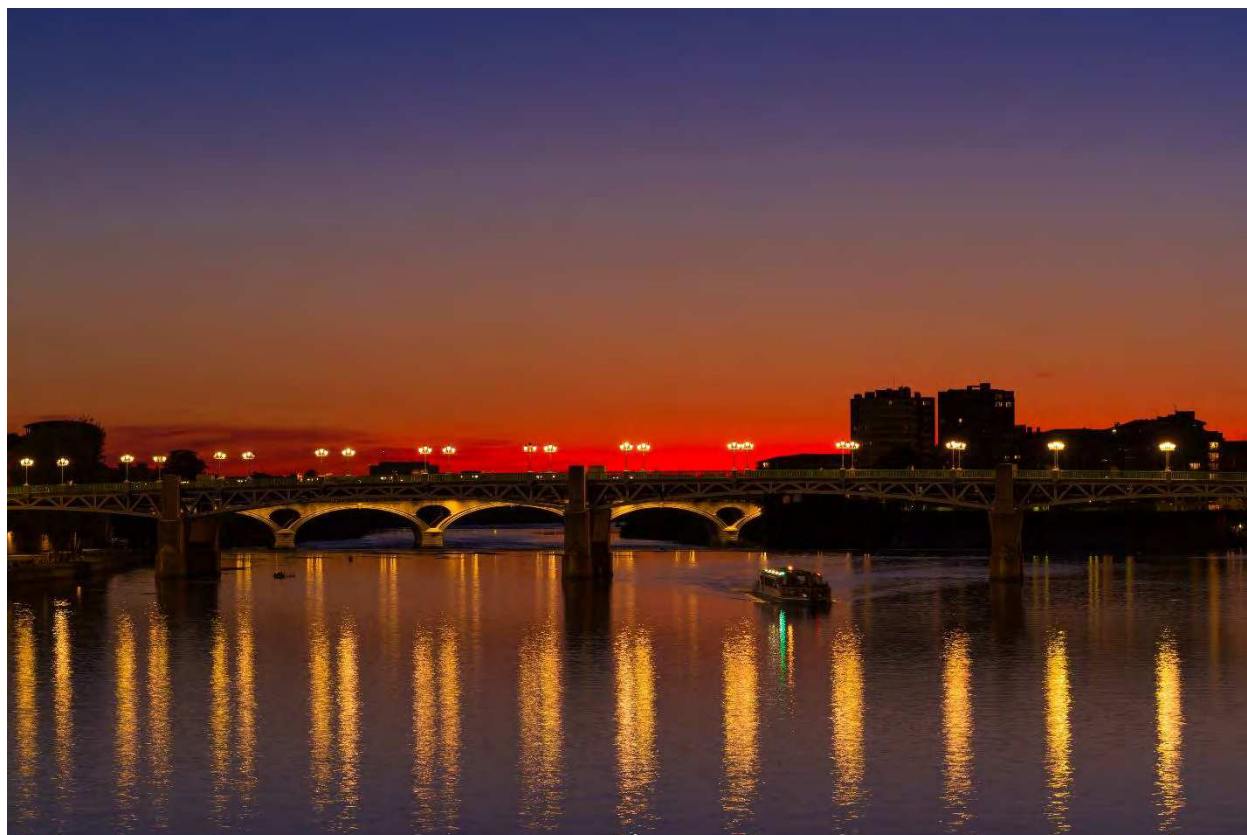
51. Zhao, Y., et al., *Improving the efficiency of water splitting in dye-sensitized solar cells by using a biomimetic electron transfer mediator*. Proceedings of the National Academy of Sciences, 2012. **109**(39): p. 15612.
52. Michaux, K.E., et al., *Visible Photoelectrochemical Water Splitting Based on a Ru(II) Polypyridyl Chromophore and Iridium Oxide Nanoparticle Catalyst*. The Journal of Physical Chemistry C, 2015. **119**(29): p. 17023-17027.
53. Wei, P., et al., *New strategy to incorporate nano-particle sized water oxidation catalyst into dye-sensitized photoelectrochemical cell for water splitting*. Journal of Energy Chemistry, 2016. **25**(3): p. 345-348.
54. Brimblecombe, R., et al., *Solar Driven Water Oxidation by a Bioinspired Manganese Molecular Catalyst*. Journal of the American Chemical Society, 2010. **132**(9): p. 2892-2894.
55. Hagfeldt, A. and M. Grätzel, *Molecular Photovoltaics*. Accounts of Chemical Research, 2000. **33**(5): p. 269-277.
56. Kuang, D., et al., *High Molar Extinction Coefficient Heteroleptic Ruthenium Complexes for Thin Film Dye-Sensitized Solar Cells*. Journal of the American Chemical Society, 2006. **128**(12): p. 4146-4154.
57. Balzani, V., et al., *Autonomous artificial nanomotor powered by sunlight*. Proceedings of the National Academy of Sciences, 2006. **103**(5): p. 1178-1183.
58. Girardot, C., et al., *Ruthenium(II) Complexes for Two-Photon Absorption-Based Optical Power Limiting*. ChemPhysChem, 2008. **9**(11): p. 1531-1535.
59. Four, M., et al., *A novel ruthenium(ii) complex for two-photon absorption-based optical power limiting in the near-IR range*. Physical Chemistry Chemical Physics, 2011. **13**(38): p. 17304-17312.
60. Parikh, S.J. and J. Chorover, *ATR-FTIR Spectroscopy Reveals Bond Formation During Bacterial Adhesion to Iron Oxide*. Langmuir, 2006. **22**(20): p. 8492-8500.
61. Basly, B., et al., *Effect of the nanoparticle synthesis method on dendronized iron oxides as MRI contrast agents*. Dalton Transactions, 2013. **42**(6): p. 2146-2157.
62. Mohapatra, S. and P. Pramanik, *Synthesis and stability of functionalized iron oxide nanoparticles using organophosphorus coupling agents*. Colloids and Surfaces A: Physicochemical and Engineering Aspects, 2009. **339**(1): p. 35-42.
63. Daou, T.J., et al., *Phosphate Adsorption Properties of Magnetite-Based Nanoparticles*. Chemistry of Materials, 2007. **19**(18): p. 4494-4505.
64. Heinemann, F., J. Karges, and G. Gasser, *Critical Overview of the Use of Ru(II) Polypyridyl Complexes as Photosensitizers in One-Photon and Two-Photon Photodynamic Therapy*. Accounts of Chemical Research, 2017. **50**(11): p. 2727-2736.
65. Stephenson, M., et al., *Ru(II) Dyads Derived from 2-(1-Pyrenyl)-1H-imidazo[4,5-f][1,10]phenanthroline: Versatile Photosensitizers for Photodynamic Applications*. The Journal of Physical Chemistry A, 2014. **118**(45): p. 10507-10521.
66. Alexandre Mitrofanov, A.B.L., Christine Stern, Roger Guillard*, Nataliya Gulyukina, Irina Beletskaya*, *Palladium-Catalyzed Synthesis of Mono- and Diphosphorylated 1,10-Phenanthrolines*. Synthesis 2012. **44**(24): p. 3805-3810.
67. Girardot, C., et al., *Novel ruthenium(ii) and zinc(ii) complexes for two-photon absorption related applications*. Dalton Transactions, 2007(31): p. 3421-3426.

68. Girardot, C., et al., *Novel 5-(oligofluorenyl)-1,10-phenanthroline type ligands: synthesis, linear and two-photon absorption properties*. Tetrahedron Letters, 2008. **49**(11): p. 1753-1758.
69. Montalti, M., et al., *Luminescent Ruthenium(II) Bipyridyl-Phosphonic Acid Complexes: pH Dependent Photophysical Behavior and Quenching with Divalent Metal Ions*. Inorganic Chemistry, 2000. **39**(1): p. 76-84.
70. Giordano, P.J., C.R. Bock, and M.S. Wrighton, *Excited state proton transfer of ruthenium(II) complexes of 4,7-dihydroxy-1,10-phenanthroline. Increased acidity in the excited state*. Journal of the American Chemical Society, 1978. **100**(22): p. 6960-6965.
71. Hackett, J.W. and C. Turro, *Luminescent Ru(phen)*n*(bpy)*3-n*2*n*-4 Complexes (n = 0–3) as Probes of Electrostatic and Hydrophobic Interactions with Micellar Media*. Inorganic Chemistry, 1998. **37**(8): p. 2039-2046.
72. Norris, M.R., et al., *Synthesis of Phosphonic Acid Derivatized Bipyridine Ligands and Their Ruthenium Complexes*. Inorganic Chemistry, 2013. **52**(21): p. 12492-12501.
73. Juris, A., et al., *Ru(II) polypyridine complexes: photophysics, photochemistry, electrochemistry, and chemiluminescence*. Coordination Chemistry Reviews, 1988. **84**: p. 85-277.
74. Agnès, C., et al., *XPS study of ruthenium tris-bipyridine electrografted from diazonium salt derivative on microcrystalline boron doped diamond*. Physical Chemistry Chemical Physics, 2009. **11**(48): p. 11647-11654.
75. Touihri, S., G. Safoula, and J.C. Bernède, *Properties of chlorine-doped poly(N-vinylcarbazole) thin films*. Polymer Degradation and Stability, 1998. **60**(2): p. 481-485.
76. Youngblood, W.J., et al., *Visible Light Water Splitting Using Dye-Sensitized Oxide Semiconductors*. Accounts of Chemical Research, 2009. **42**(12): p. 1966-1973.
77. Le Formal, F., K. Sivula, and M. Grätzel, *The Transient Photocurrent and Photovoltage Behavior of a Hematite Photoanode under Working Conditions and the Influence of Surface Treatments*. The Journal of Physical Chemistry C, 2012. **116**(51): p. 26707-26720.
78. Hu, L., et al., *Organic optoelectronic interfaces with anomalous transient photocurrent*. Journal of Materials Chemistry C, 2015. **3**(20): p. 5122-5135.
79. Lemerrier, G., et al., *3MLCT excited states in Ru(II) complexes: Reactivity and related two-photon absorption applications in the near-infrared spectral range*. Comptes Rendus Chimie, 2008. **11**(6): p. 709-715.

Chapter III – Fe@FeOx@Ru photoanode



Chapter IV – Investigation of the catalytic activity of NiFeO_x NPs



Pont saint pierre – Toulouse – France 2020

Table of contents – Chapter IV

1. Introduction	3
1.1 Some hypothesis on the origin of activity enhancement.....	145
1.2 Optimal composition.....	147
1.3 Synthesis methods for NiFe-based thin films and main results in electrocatalysis thereof	148
1.4 Synthesis of NiFe based NPs and main results in electrocatalysis thereof	154
2. Description of the nanomaterials used in this work	160
2.1 Ni and Fe oxide reference samples	161
2.2 Synthesis and characterization of the Fe-rich sample (1Ni/9Fe oxide NPs)	166
2.3 Synthesis and characterization of NiFeO_x NPs with compositions 1Ni/1Fe and 2Ni/1Fe	169
2.4 Water transfer of NiFeO_x NPs using 3-amino propyl phosphonic acid:	175
3. Evaluation of the nanomaterials in WOC	180
3.1 Electrocatalytic activity in OER.....	180
3.2 Electrocatalytic Stability	182
3.3. Cyclic Voltametry studies	183
4. Conclusions	188
5. References	191

Chapter IV – NiFeO_x NPs as an OER catalyst

Chapter IV- Investigation of the catalytic activity of NiFeO_x NPs

This work was carried out in collaboration with François Robert, PhD student in our group, for the synthesis of the FeNi nanoparticles.

1. Introduction

Several advantages are mentioned for the use of bimetallic catalysts. A bimetallic bond often involves redistribution of charges around the metal centers. Bimetallic catalysts may thus exhibit superior catalytic performances and show greater stability than their parent metals. Also, the active metal can be confined to the surface, offering an ultra-high specific surface area. Alternatively the distribution of the two metals on the surface can be engineered to create new active sites [1]. Among all bimetallic compounds that have been investigated for the OER, the NiFe – based compounds, mainly including NiFe-based oxides, and NiFe-based (oxy) hydroxides, have gained attention due to their low-cost, abundance and excellent catalytic activity for OER especially in alkaline solution[2-5]. In this section, we present the early discoveries and recent progresses on NiFe oxide - based OER electrocatalysts concerning the relation between chemical properties, synthetic methodologies and catalytic performances. Main features are reported in Table 1 for comparison purposes.

Chapter IV – NiFeOx NPs as an OER catalyst

Table 1: Summary of the main characteristics of representative NiFe oxide –based electrocatalysts for OER

No.	Catalyst	Ni:Fe ratio	Synthetic method	Morphology	Substrate	Electrolyte	Overpotential (mV) J=10mA/cm ²	Tafel slope (mV.dec ⁻¹)	TOF	Ref	Pub. year
1	Ni _{0.9} Fe _{0.1} Ox	9:1	Solution synthesis, spin coating	Thin film 2-3 nm	Au/Ti QCM or ITO	KOH 1M	336	30	0,21 s ⁻¹ ($\eta=0.3V$)	[2]	2012
2	Fe:NiOx	–	Sputtering	film	–	KOH 1N	80 mA/cm ² at $\eta=362$ mV	40	–	[6]	1997
3	NiO/NiFe ₂ O ₄	1:2	E ISA	powder	Carbon paper	KOH 1M	–	–	–	[7]	2012
4	NiFeOx	0.1% Fe in NiOx electrode	Electrodeposition	Thin film	–	25 w/o KOH	233	25	–	[8]	1987
5	[Ni _{1-x} Fe _x (OH) ₂](NO ₃) _y (OH) _{x-y} .nH ₂ O	22% Fe	Pulsed laser ablation in liquids	NPs 12 nm	Graphite electrode	KOH 1M	260	47	–	[9]	2014
6	NiFeOx	–	Electrodeposited	–	Glassy carbon electrode	NaOH 1M	360	–	–	[10]	2013
7	NiFe-LDH	–	Exfoliation	nanosheet	Glassy carbon electrode	KOH 1M	302	40	0.05.s ⁻¹ ($\eta=0.3V$)	[11]	2014
8	NiFe-LDH bulk	–	Hydrothermal	Submicrometre	Glassy carbon electrode	KOH 1M	347	–	–	[11]	2014
9	NiFe-LDH	–	–	–	Glassy carbon electrode	KOH 1M	315	40	–	[12]	2015
10	NiFe-LDH	–	Solvothermal	nanoplates ~50nm	CNTs	KOH 1M	–	31	0.56 s ⁻¹ ($\eta=0.3V$)	[5]	2013

Chapter IV – NiFeOx NPs as an OER catalyst

11	Mesoporous NiFe hydroxide	–	electrodeposition	Thickness ~10nm Lateral extension 50-several hundred nm	Nickel foam	KOH 1M	215	28	0.075 s ⁻¹ ($\eta=0.4V$)	[13]	2015
12	Ni ₄₅ Fe ₅₅	45:55	solvothermal	–	Glassy carbon electrode	NaOH 0.1M	180	35	0.1 s ⁻¹ ($\eta=0.3V$)	[14]	2017
13	NiFe ₂ O ₄	1:2	Commercial vendors	30nm	–	NaOH 1M	510	–	–	[15]	2016
14	Ni _{2/3} -Fe _{1/3} LDH	2:1	Homogeneous precipitation, exfoliated method	- Lateral size (NS) ~few hundred nm -Thickness ~0.8 nm	rGO	KOH 1M	210	40	0.2 s ⁻¹ ($\eta=0.3V$)	[16]	2015
15	Ni _{0.69} Fe _{0.31} Ox	7:3	Solution phase nanocapsule	Amorphous Ni- Fe oxide NP ~4 nm	Carbon vulcan	KOH 1M	280	30	0.2 s ⁻¹ ($\eta=0.3V$)	[17]	2014
16	NiOx-NiOx/FeOx	–	Thermal decomposition organometallic	NPs ~19.8 nm	Au electrode	KOH 1M	320	–	1.175 s ⁻¹ ($\eta= ? V$)	[18]	2018
17	NiFeO	3:2	Direct pyrolysis	Nano cube ~60 nm	Glassy carbon electrode	KOH 1M	240	41	0.093 s ⁻¹ at ($\eta=0.25V$)	[19]	2019
18	FeNi ₃ @Ni	1:3	Co-decomposition organometallic	NPs ~18.6 nm	Glassy carbon electrode	KOH 1M	330	–	–	[20]	2020

1.1 Some hypothesis on the origin of activity enhancement

Ni-Fe oxide – based catalysts are significantly more active for the OER in alkaline solution than either Ni-based or Fe-based ones. The enhancement of OER electrocatalytic activity observed upon combining Ni and Fe is reported to result not only from a change in the electronic structure of the catalyst and improvement of its conductivity, but also from the increased number of redox active centers[21].

It was discovered that even a very small amount of iron can improve the OER activity of NiOx catalysts. For example, in 1984 Mlynarek and co- workers studied the effect of surface-poisoning of a nickel hydroxide electrode by ferric ions [22]. They reported that Fe₃O₄ islands form on the surface of the electrode before the oxidation of the insulating Ni(OH)₂ into the conductive (and so more active) NiO(OH) catalyst. As Fe₃O₄ has a much better electron conductivity than Ni(OH)₂, an increase in OER efficiency at the Ni(OH)₂-Fe₃O₄ interface is expected, in agreement with the decrement of the overpotential observed when the electrode is poisoned by ferric ions. [23].

Three years later, in 1987 Corrigan *et al.*, also studied the influence of intentional iron incorporation into a Ni oxide layer at the surface of a Ni electrode [8]. First, the authors observed that in KOH electrolyte, Fe impurities co-precipitated with nickel oxide onto a nickel foil electrode after a series of 100 potential sweep experiments. As shown in Figure 1, 1 ppm of Fe caused not only a dramatic increment of the OER current density but also an decrement of the overpotential.

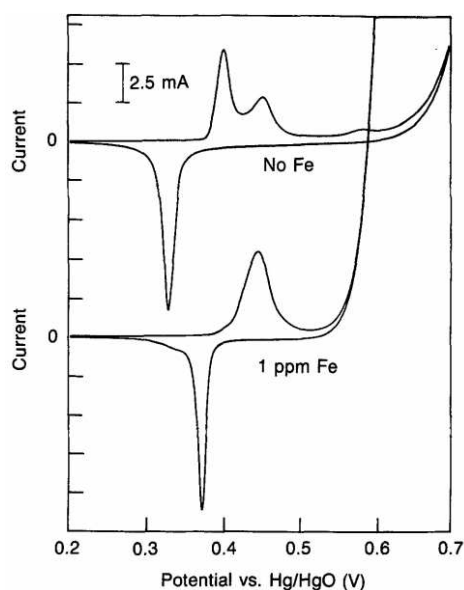


Figure 1. Effect of iron on a nickel electrode voltammograms (scan rate 10 mV/s, KOH electrolyte)[8].

This effect on the overpotential could be detected at an iron loading on the thin film nickel oxide electrode as low as 0.01 at.% (Figure 2a). A dramatic drop of the Tafel slope was observed upon increasing the iron content, from 70mV/decade in the absence of iron down to 25 mV/decade at high iron loading (10 at.%) (Figure 2b and Table 2) [8]. According to the authors, these observations (decrement of overpotential and Tafel slope when increasing the iron loading) could result from the fact that iron could provide more stable active sites or improve the conductivity of the resistive nickel oxide layers.

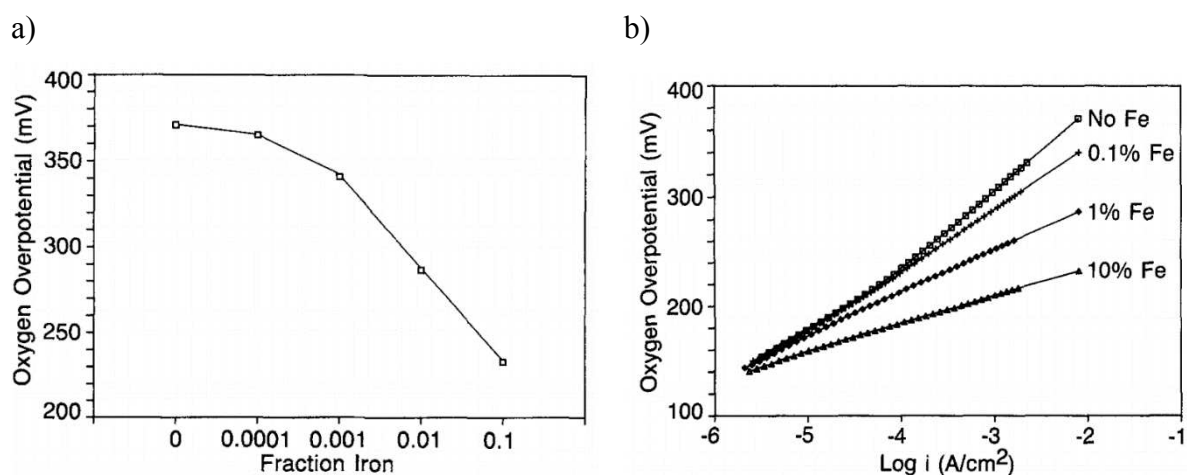


Figure 2. Effect of coprecipitated iron a) on the overpotential (results from steady-state polarization measurements at 8 mA/cm²) and b) on the Tafel plots (results from open-circuit decay measurements) for OER at nickel oxide thin film electrodes[8].

Table 2. Effect of iron co-precipitation on Oxygen evolution kinetics [8].

Fraction iron	Oxygen overpotential (mV) ^a	Tafel slope (mV/decade) ^a	Exchange current density (A/cm ²) ^b	Pseudo-capacitance (Farads/cm ²) ^c
0	371	72	5.8×10^{-8}	0.045
0.0001	365	70	5.0×10^{-8}	0.046
0.001	341	57	9.7×10^{-9}	0.046
0.01	287	39	3.1×10^{-10}	0.055
0.05	245	27	6.6×10^{-12}	0.069
0.1	233	25	4.5×10^{-12}	0.096
0.5	231	21	6.0×10^{-14}	0.033
0.6	256	17	1.5×10^{-17}	0.005
0.75	274	19	2.4×10^{-17}	0.0005

^a At 8 mA/cm² current density.

^b Extrapolated from overpotential and Tafel slope at 8 mA/cm² current density.

^c Calculated from time constant τ of open-circuit decay experiment.

Later on, in 2014 Trotochaud *et al.*, also observed that incorporation of iron in a nickel (II) hydroxide thin film could dramatically increase the conductivity of this film. It can be seen in Figure 3, that when increasing the iron content from strictly 0 to impurity level, then to 15 at.%, the conductivity increases from a close to 0.2 mS.cm⁻¹ value (pure Ni(OH)₂ being insulating), to already around 2.5 mS.cm⁻¹ and then 6.2 mS.cm⁻¹ respectively, representing a close to 30-fold jump in conductivity. However the change in conductivity was not sufficient to explain the observed change in OER activity. Indeed, a further increase in iron content was accompanied by a significant decrease in conductivity, while the activity of the catalyst still increased [3]. It was suggested by the authors that the increase in OER activity was due to a Fe-induced partial-charge transfer mechanism, which activated the Ni centers throughout the catalyst film.

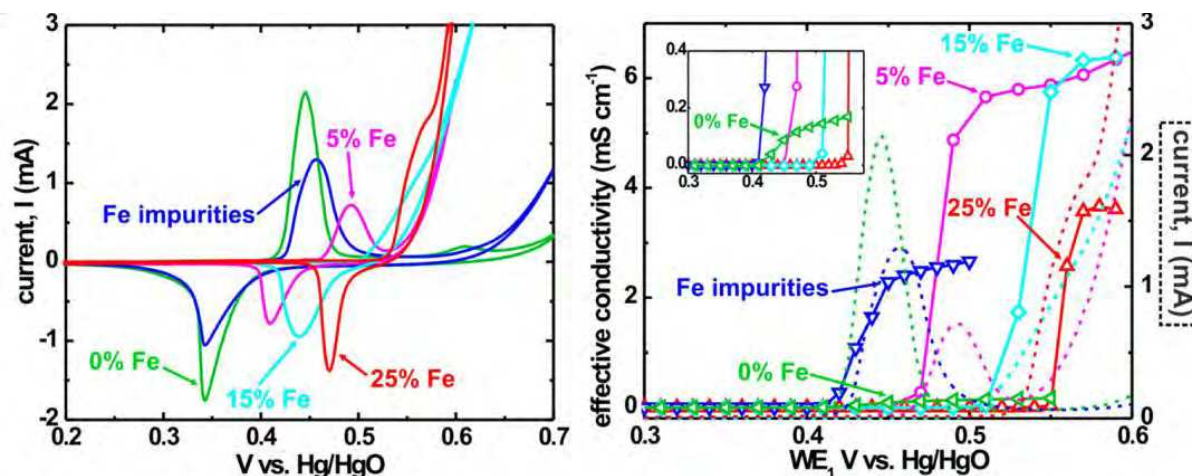


Figure 3. left: CV scan of Ni_{1-x}Fe_x(OH)₂/Ni_{1-x}Fe_xOOH films deposited on Au/Ti/quartz interdigitated (IDA) electrodes; right: conductivity data (points with solid connecting lines) for the corresponding films. The potential onset of conductivity correlates with the position of the hydroxide/oxyhydroxide oxidation wave shown as dotted lines for each film. The insert shows an enlarged region to make apparent the conductivity turn-on for the rigorously Fe-free film [3].

1.2 Optimal composition

Numerous studies indicated that the catalysts consisting of 60-90 wt% of Ni show the best OER activity[24]. At the end of a detailed study, Bell and co-workers demonstrated that the optimal OER activity of NiFe oxides was obtained at a Fe:Ni composition of 2:3 (~60 wt% of Ni). Combined electrochemical and *in situ* X-ray absorption spectroscopy measurements showed that, at the catalyst rest potential, these iron-doped nickel oxide films could be well described by a layered double hydroxide (LDH) structure of general formula : Ni(II)₁₋

$x\text{Fe(III)}_x(\text{OH})_2(\text{SO}_4)_{x/2}(\text{H}_2\text{O})_y$. It was also observed that the potential of the Ni(II)/Ni(III) couple shifted anodically when the film contained more iron[4].

Ma *et al.*, presented a systematic study of the influence of the composition of Ni-Fe LDH on the catalytic activity of these anodes in alkaline solution. Increasing the iron content in the Ni-Fe LDH nanosheets (NS) was found to increase the catalytic activity (Figure 4). The NS of composition $\text{Ni}_{2/3}\text{Fe}_{1/3}$ ($\text{Ni}_{2/3}\text{Fe}_{1/3}$ -NS) was the most efficient water oxidation catalyst in KOH 1M in comparison with $\text{Ni}_{3/4}\text{Fe}_{1/4}$ -NS and $\text{Ni}_{4/5}\text{Fe}_{1/5}$ -NS.

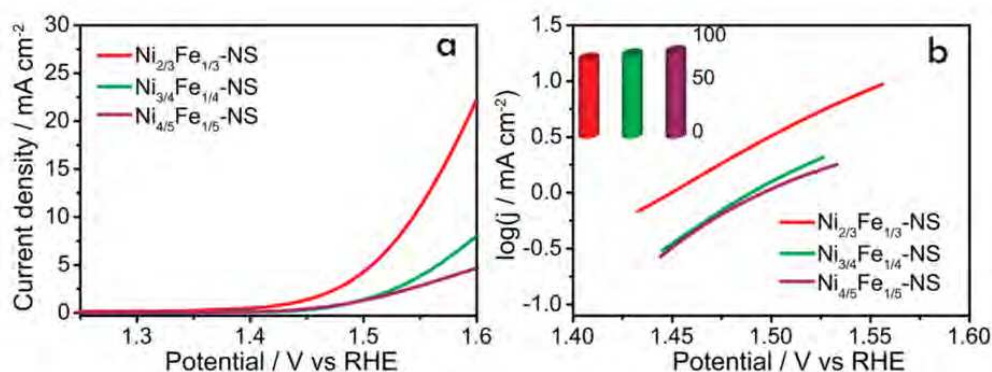


Figure 4. a) *iR*-corrected polarization curves and b) Tafel slopes of $\text{Ni}_{2/3}\text{Fe}_{1/3}$ -NS, $\text{Ni}_{3/4}\text{Fe}_{1/4}$ -NS, and $\text{Ni}_{4/5}\text{Fe}_{1/5}$ -NS (inset: histogram of corresponding Tafel slopes)[16].

The fabrication of highly efficient OER catalysts thus requires a precise control of the metal composition, an increased number of accessible active sites, and enhanced electronic conductivity. To reach this goal, different synthesis routes, including liquid-phase chemical method, electrodeposition, photochemical metal-organic deposition (PMOD), *etc.*, were developed to fabricate NiFe oxide NPs with tailored morphologies and/or properties for high performance OER catalysis as described in the following of this chapter.

1.3 Synthesis methods for NiFe-based thin films and main results in electrocatalysis thereof

Ni-Fe Oxide films can be prepared by different methods. The easiest one, reported by Miller and co-workers, consists in co-depositing Fe and Ni from NiFe alloy targets by reactive sputtering in a 20 % oxygen/argon atmosphere[6]. An improvement in activity upon Fe incorporation into the Ni oxide film was obtained as shown in Figure 5a. The best sample achieved a current density of 80 mA/cm² at an overpotential of 362 mV with a Tafel slope of

less than 40 mV/decade (Figure 5b). In addition, the sputtered NiFe oxide film showed an impressive durability of over 7000 hours due to the crystallinity of the sputtered NiFe oxide.

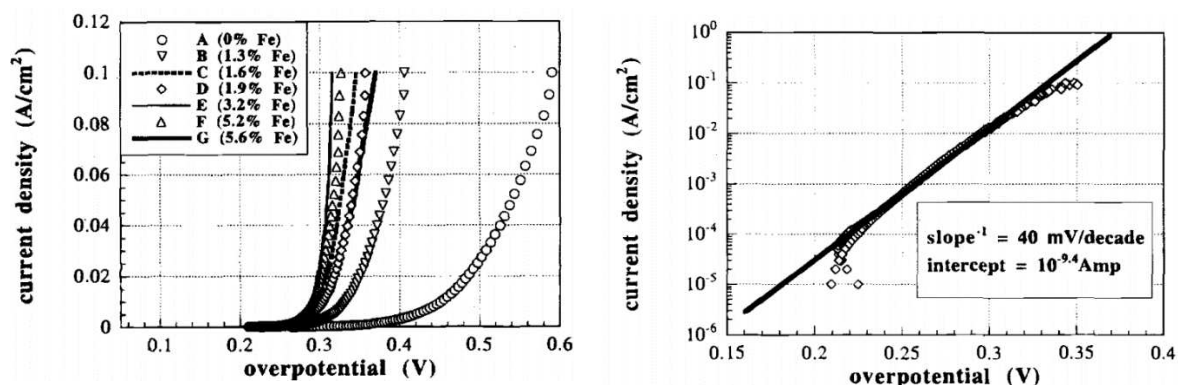
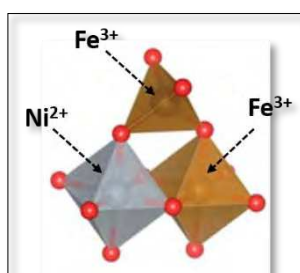


Figure 5. a) Steady-state polarization plots of Fe:NiOx anode and b) Tafel plot showing extrapolation to obtain the Tafel slope and exchange current density in 1M KOH[6].

When the Ni/Fe ratio is 1:2, a nickel ferrite can form (NiFe₂O₄). It has an inverse spinel oxide structure in which the divalent cation Ni²⁺ occupies octahedral sites and the trivalent cation Fe³⁺ occupies octahedral and tetrahedral sites (scheme 1).



Scheme 1. structure of the inverse spinel oxide NiFe₂O₄.

In 2012, Landon and co-workers fabricated mixed Ni-Fe oxides by three different methods such as, evaporation induced self-assembly (EISA), hard templating, and dip-coating[7]. In each case, they observed that at *circa* 10 at.% Fe content, the mixed metal oxide was substantially more active than the parent metal oxide electrocatalysts in KOH 1M (Figure 6), which could not be explained by variations in the electrocatalyst surface area (measured by Brunauer-Emmett-Teller (BET) method). Indeed, at 10 at.% Fe, the mixed Ni-Fe oxide did not have the highest surface area (Table 3). Therefore, there had to be an intrinsic reason for the increase in the surface activity for the mixed oxide sample near 10 at.% Fe.

Table 3. BET surface areas for mixed Ni-Fe oxide catalyst produced by the EISA method[7].

catalyst	surface area (m ² /g)
NiO	14
3 mol % Fe	18
4 mol % Fe	19
5 mol % Fe	19
10 mol % Fe	18
15 mol % Fe	26
20 mol % Fe	31
Fe ₂ O ₃	13

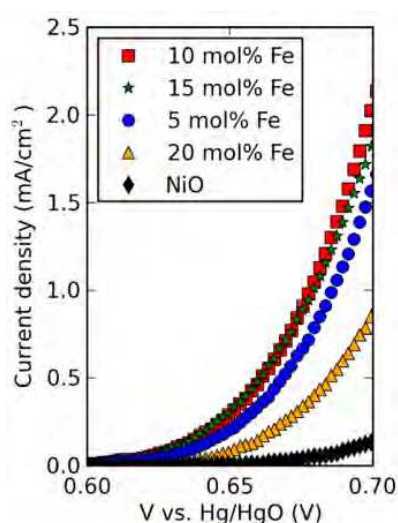


Figure 6. Geometric area - normalized polarization (scan rate = 1mV.s⁻¹) data of mixed Ni-Fe oxide catalyst (synthesis by the EISA method) showing the highest activity for 10 at.% Fe. The equilibrium potential for O₂ evolution is approximately 0.308 V vs Hg/HgO[7].

XRD analysis of the catalysts at different Fe contents showed that although the Fe content increased up to 10 at.%, the peaks positions from the NiO lattice remained constant. This suggests that Fe was not substitutionally incorporated into the NiO lattice (Figure 7). The formation of a mixed NiO/NiFe₂O₄ phase at low Fe concentrations and formation of Fe₂O₃ were observed as the Fe content was increased above 25 at.%.

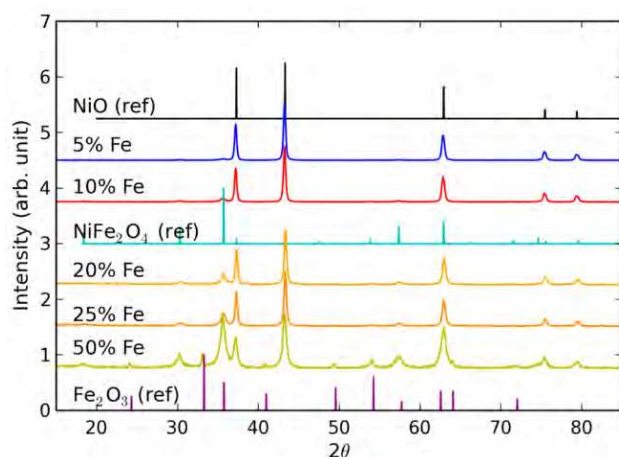


Figure 7. XRD patterns of the 5, 10, 20, 25, and 50 at.% Fe mixed samples. Lattice constants for NiO and all mixed Ni-Fe oxides were found to be 4.18 \AA , suggesting Fe was not substitutionally incorporated into the NiO lattice[7].

In situ EXAFS experiments on the Fe and Ni K-edges were conducted on the 10 at.% Fe mixed oxide powder in air, under open-circuit conditions in alkaline electrolyte, and under electrochemical OER conditions. The Ni K-edge didn't change during catalytic conditions while an increase in octahedrally coordinated Fe (as in NiFe₂O₄) was observed (Figure 8) demonstrating that the NiFe₂O₄ phase plays a significant role in improving OER activity of the mixed Ni-Fe oxide.

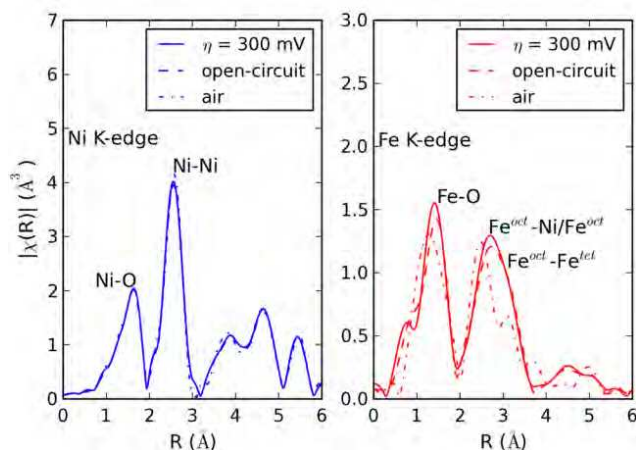
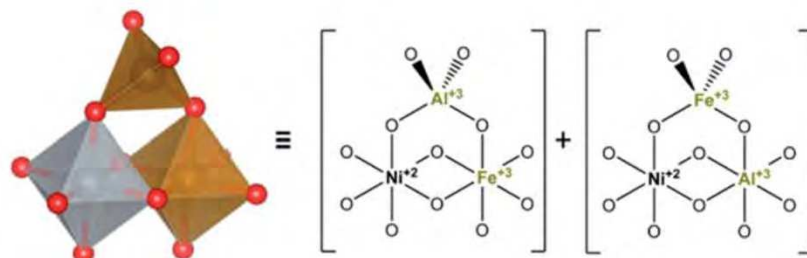


Figure 8. Fourier transform magnitudes of k_2 -weighted EXAFS data for the Ni and Fe K-edges of the 10 at.% Fe mixed Ni-Fe oxide catalyst in air, under open circuit conditions in alkaline electrolyte, and at an overpotential of 300 mV under OER conditions[7].

Gerken *et al.*, found out that introducing the trivalent cation Al³⁺ into the crystal structure of NiFe₂O₄ led to a significant enhancement in the catalytic activity in comparison with the pure NiFe₂O₄ ferrite[25]. These Al-Ni-Fe oxides adopted the inverse spinel structure NiFeAlO₄ in

which the divalent cation Ni^{2+} occupies an octahedral site and the trivalent cations, Al^{3+} and Fe^{3+} , occupy both octahedral and tetrahedral sites (scheme 2)[26].



Scheme 2. Simplified structural representation of NiFeAlO_4 showing only site occupancy of the metals. M^{II} ion (grey) occupies an octahedral site while M^{III} ions (brown) occupy both octahedral and tetrahedral sites, reproduced from ref [26].

The electrocatalytic activity of this kind of material was further studied by Jamie *et al.*, [26]. As shown in Figure 9 and Table 4, an enhancement in term of kinetics was achieved for NiFeAlO_4 (red curve) in comparison with NiFe_2O_4 (blue curve) and NiAl_2O_4 (green curve) as the Tafel slope was the lowest for this composition.

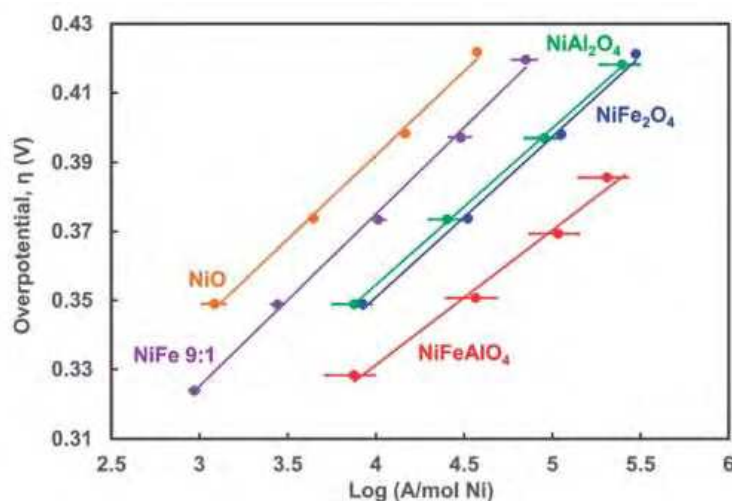


Figure 9. Steady - state Tafel plots of oxides in the low current density linear regime. Data shown are the average of three trials with error bars indicating one standard deviation[26].

Table 4. Tafel slope values for the different systems studied in [26].

	NiO	NiFe 9:1	NiFe ₂ O ₄	NiAl ₂ O ₄	NiFeAlO ₄
Tafel Slope (mV/dec)	49	50	47	41	37

Chapter IV – NiFeO_x NPs as an OER catalyst

In 2013, Trotochaud *et al.* reported the solution cast-method for the deposition of a thin metal oxide film (thickness between 2 to 3 nm) such as NiO_x, CoO_x, Ni_yCo_{1-y}O_x, Ni_{0.9}Fe_{0.1}O_x, IrO_x, MnO_x and FeO_x catalyst onto Au/Ti quartz crystal microbalance electrode (QCM) (Figure 10)[2]. In their experiment, the as-prepared thin film Ni_{0.9}Fe_{0.1}O_x demonstrated remarkable electrocatalytic activity for OER in KOH 1M. To achieve the current density of 10 mA/cm², an overpotential of only 336 mV was required with a Tafel slope as small as 30 mV/decade, namely lower than the one reported for the NiFeAlO₄ catalyst in Table 4 (Table 5). It is noteworthy that this Ni_{0.9}Fe_{0.1}O_x thin film was the most active of all thin films prepared and especially displayed a 10-fold higher OER catalytic activity in alkaline medium than a reference IrO_x thin film prepared and measured in the same conditions (Table 5). The high activity of this Ni_{0.9}Fe_{0.1}O_x catalyst was attributed to the *in situ* formation of layered Ni_{0.9}Fe_{0.1}OOH oxyhydroxide species in which nearly every Ni atom was electrochemically active.

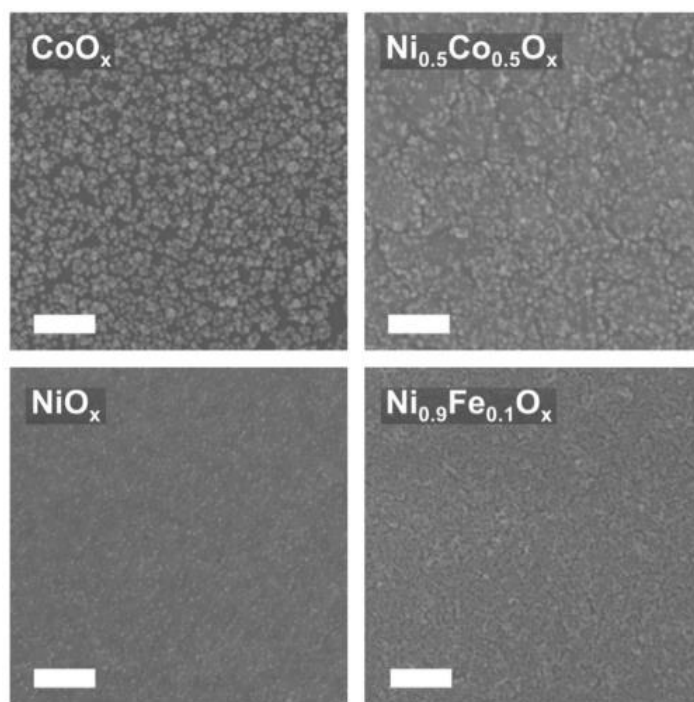


Figure 10. SEM image of selected thin films (CoO_x, Ni_{0.5}Co_{0.5}O_x, NiO_x and Ni_{0.9}Fe_{0.1}O_x) deposited on a Si electrode by the solution deposition method. Scale bars are 100 nm[2].

Table 5. Comparison between metal oxide thin film OER activities in KOH IM

	η (@ 1 mA cm ⁻²) (mV)	dry film loading ($\mu\text{g cm}^{-2}$)	J (@ $\eta = 0.3$ V) (mA cm ⁻²)	mass activity (@ $\eta = 0.3$ V) (A g ⁻¹)	TOF (s ⁻¹) @ $\eta = 0.3$ V	Tafel slope (mV dec ⁻¹)
MnO _x	514 ± 22	1.13 ± 0.08	0.002 ± 0.0009	1.8 ± 0.8	0.0004 ± 0.0002	49 ± 3
FeO _x	405 ± 4	1.63 ± 0.08	0.012 ± 0.007	7.6 ± 4.5	0.0015 ± 0.0009	51 ± 3
IrO _x	378 ± 4	4.12 ± 0.14	0.063 ± 0.036	15 ± 8.7	0.0089 ± 0.0050	49 ± 1
CoO _x	381 ± 12	1.32 ± 0.14	0.020 ± 0.009	15 ± 6.8	0.0032 ± 0.0014	42 ± 1
Ni _{0.25} Co _{0.75} O _x	341 ± 5	1.62 ± 0.09	0.079 ± 0.018	49 ± 11	0.0099 ± 0.0023	36 ± 1
Ni _{0.5} Co _{0.5} O _x	320 ± 4	1.06 ± 0.08	0.30 ± 0.07	280 ± 70	0.056 ± 0.014	35 ± 2
Ni _{0.75} Co _{0.25} O _x	312 ± 1	1.04 ± 0.09	0.47 ± 0.05	452 ± 64	0.089 ± 0.013	33 ± 1
NiO _x	300 ± 3	1.13 ± 0.10	1.01 ± 0.22	896 ± 206	0.17 ± 0.04	29 ± 0.4
Ni _{0.9} Fe _{0.1} O _x	297 ± 0.3	1.17 ± 0.14	1.24 ± 0.04	1065 ± 129	0.21 ± 0.03	30 ± 1

In the past few years, special interest has grown on the synthesis and application of amorphous metal oxide materials for electro-catalysis[27-29], and they have been demonstrated to be excellent OER catalysts[30-32]. It was suggested that this resulted from the presence of under-coordinated sites and tunable electronic structure [33].

In the literature, an increasing number of amorphous metal oxide catalysts has been reported but most of them have been produced by electrochemical deposition or photochemical metal organic deposition (PMOD), which allow to easily access amorphous films but are not suitable for the large scale synthesis of materials. Therefore, it would be interesting to develop a suitable synthesis route for the formation of amorphous materials which is not only scalable but also affords nanomaterials of high catalytic activity in OER.

1.4 Synthesis of NiFe based NPs and main results in electrocatalysis thereof

In comparison to thin films, nanoparticles provide more active sites on a mass basis on which higher OER catalytic activity could be achieved [34]. Also, a catalyst with nanoscale dimensions can be readily integrated into a functional photoelectrochemical cell. However, to the best of our knowledge most of the publications on Ni-Fe based OER catalysts investigate the activity of thin-films and only a few studies have been focused so far on the use of Ni-Fe nanoparticles[17-20]. We report hereafter the more significant examples found in the recent literature.

For example, Qiu *et al.*, investigated the catalytic activity of amorphous Ni_yFe_{1-y}O_x NPs deposited on a carbon support. The NPs (*circa* 4 nm large) were prepared by reduction of a mixture of Ni(II) and Fe(III) acetylacetonates by lithium triethylborohydride, in the presence of oleic acid and oleyl amine as stabilizing agents and of a carbon support (Vulcan carbon black).

The powder was handled and stored in air, leading to amorphous oxide phases. At the $\text{Ni}_{0.69}\text{Fe}_{0.31}\text{O}_x$ composition, the nanomaterial displayed a good electrocatalytic activity with an overpotential of 280 mV at $j = 10\text{mA}/\text{cm}^2$ in KOH 1M associated with a TOF value of $0.21\cdot\text{s}^{-1}$ at $\eta=300$ mV[17]. However, as we have already discussed in Chapter 1, a conductive support always increases the activity of the electrocatalyst. So here, the intrinsic properties of the NPs cannot be discussed.

As a further example, in 2018 Manso *et al.*, reported a scalable synthesis approach based on the thermal decomposition of organometallic complexes that enables controlling the morphology and crystallinity of NiFe oxide NPs[18]. NiFe oxide NPs with different morphologies (*i.e.* NiOx-FeOx or FeOx-NiOx core-shell NPs, and NiOx/FeOx alloyed NPs) were synthesized *via* either sequential or simultaneous injection of the two precursors in the reacting medium. The results highlight that the amorphous, disordered nature of the NiOx core allowed the diffusion of Ni into the FeOx shell to form NiOx-NiOx/FeOx core-mixed shell NPs with an average size of 16.8 ± 0.2 nm (Figure 11). In contrast, the crystalline FeOx core in the FeOx-NiOx core-shell morphology prevented Fe diffusion into the NiOx shell. As a consequence, the catalytic activity of the NiOx component was not promoted (Figure 12).

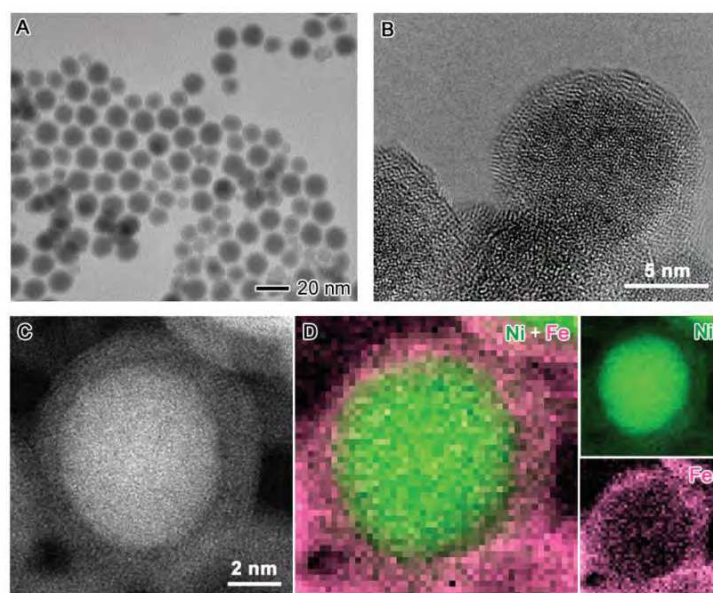


Figure 11. Electron microscopy characterization of NiOx-NiOx/FeOx core-mixed shell NPs A) TEM image overview of the NPs with an average diameter of 16.8 ± 2.0 nm: B) HR-TEM and HAADF-STEM images displaying a representative NP in A which is mostly amorphous; (D) Electron energy loss spectroscopy (EELS) mapping of the NP in C with Ni (green), Fe (pink), and Ni-Fe overlaid maps indicating a NiOx-NiOx/FeOx core-mixed shell morphology. The Ni/Fe atomic ratio of the shell is 0.39:1[18].

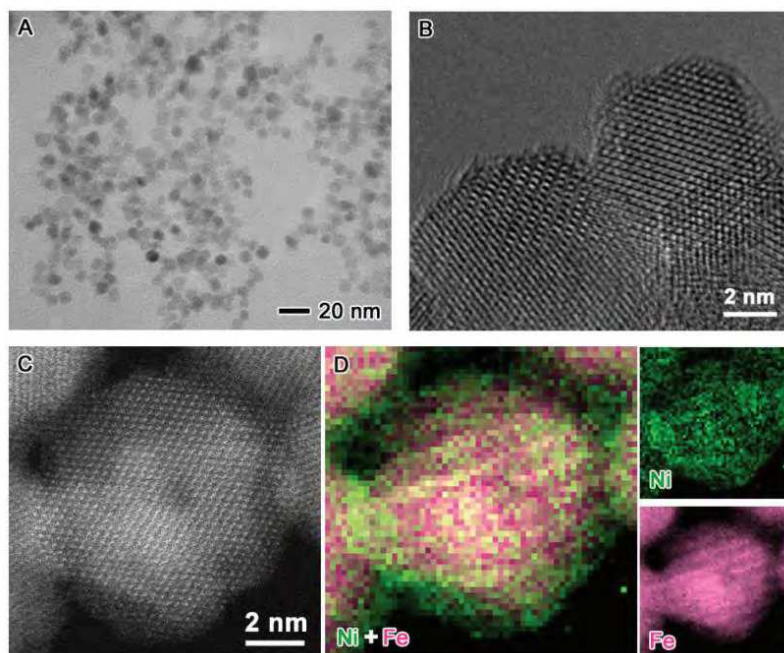


Figure 12. Electron microscopy characterization of FeOx-NiOx core-mixed shell NPs A) TEM image overview of the NPs with an average diameter of 9.8 ± 1.6 nm; B) HR-TEM and HAADF-STEM images displaying a representative NP in A with a crystalline core and a thin amorphous shell; (D) EELS mapping of the NP in C with Ni (green), Fe (pink), and Ni-Fe overlaid maps confirming the core-shell structure[18].

The NiOx-NiOx/FeOx core-shell NPs show the highest catalytic activity for OER in alkaline solution as it has the lowest overpotential (Figure 13) and the highest TOF value in comparison to FeOx-NiOx core-shell, NiOx/FeOx alloy, FeOx, and NiOx NPs.

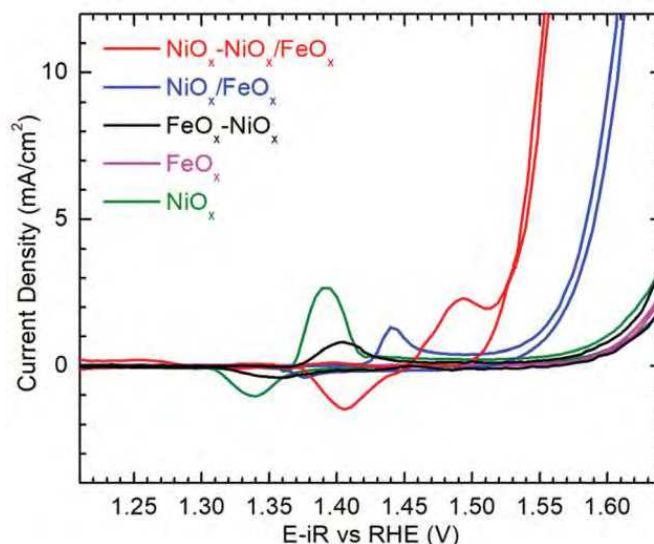


Figure 13. Cyclic voltammograms of the NPs catalysts obtained in 1M KOH at a scan rate of 10 mV.s⁻¹: NiOx-NiOx/FeOx core-mixed shell (red), NiOx-FeOx alloy (blue), FeOx-NiOx core-shell (black), FeOx (pink), and NiOx (green)[18].

In addition, the stability of the nanocatalysts was studied by chronopotentiometry (CP) for 2 hours in 1M KOH (Figure 14). It showed that the NiOx-NiOx/FeOx core-shell NPs had the lowest degradation rate (5.4 mV.h⁻¹) in comparison with NiOx/FeOx alloy (10.9 mV.h⁻¹), FeOx-NiOx core-shell (34.2 mV.h⁻¹), FeOx (24.2 mV.h⁻¹), and NiOx (26.2 mV.h⁻¹).

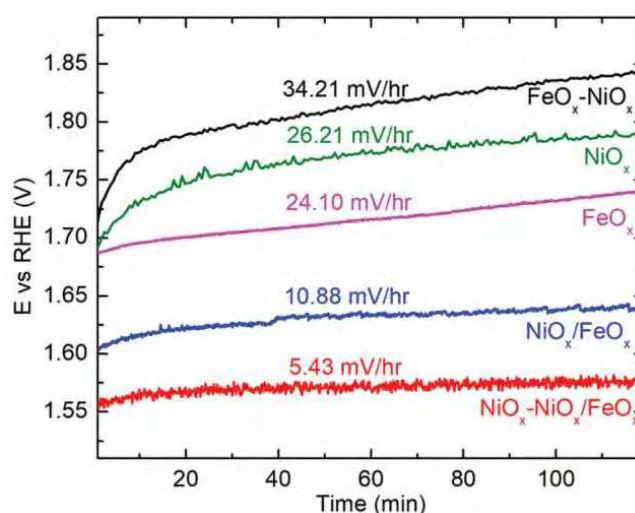


Figure 14. CP of the nanocatalyst obtained in 1M KOH at a current density of 10 mA/cm² for 2 h: NiOx-NiOx/FeOx core-mixed shell (red line), NiOx/FeOx alloy (blue), FeOx-NiOx core-shell (black), FeOx (pink), and NiOx (green)[18].

Another example is the work of Quiao and co-workers, reported in 2019. Spinel mesoporous NiFe oxide nanocubes (NCs) with Fe:Ni ratio equal to 2:3 could be obtained via direct pyrolysis

Chapter IV – NiFeOx NPs as an OER catalyst

of nickel hexacyanoferrate (NiHCF) NCs in air at three different temperatures (300°C, 400°C and 500°C) hereafter referred to as NiFeO-300 NiFeO-400, and NiFeO-500 respectively [19]. The NiFeO-400 NCs, with an average size of 60 nm (Figure 15), afforded a current density of 10 mA/cm² at a low overpotential of 240 mV and a small Tafel slope of 41 mV/decade in alkaline solution (Figure 16), as well as a TOF value of 0.093 s⁻¹ at the overpotential of 250 mV. Furthermore, NiFeO-400 NC also showed a long term stability as no significant loss of the OER activity was observed over a 100h polarization period at the overpotential of 300 mV (geometric current density fairly stable, around 38 mA/cm²). In addition the overpotential of 300 mV could be held for 100 h at the geometric current density of 40 mA/cm² (Figure 17).

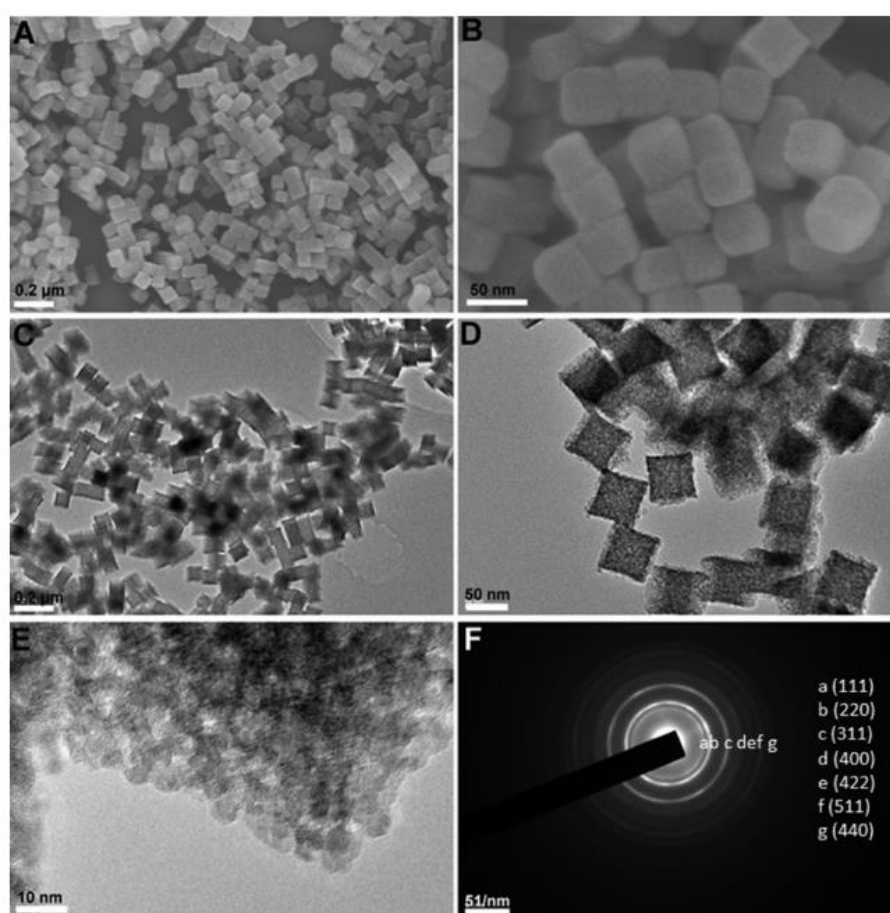


Figure 15. A-B) SEM images of NiFeO-400 NCs under different magnifications: (A) 0.2 μm, (B) 50 nm. (C,D,E) TEM images of NiFeO-400 NCs under different magnifications: (C) 0.2 μm, (D) 50 nm and (E) 10 nm. (F) SAED pattern of NiFeO-400 NCs[19].

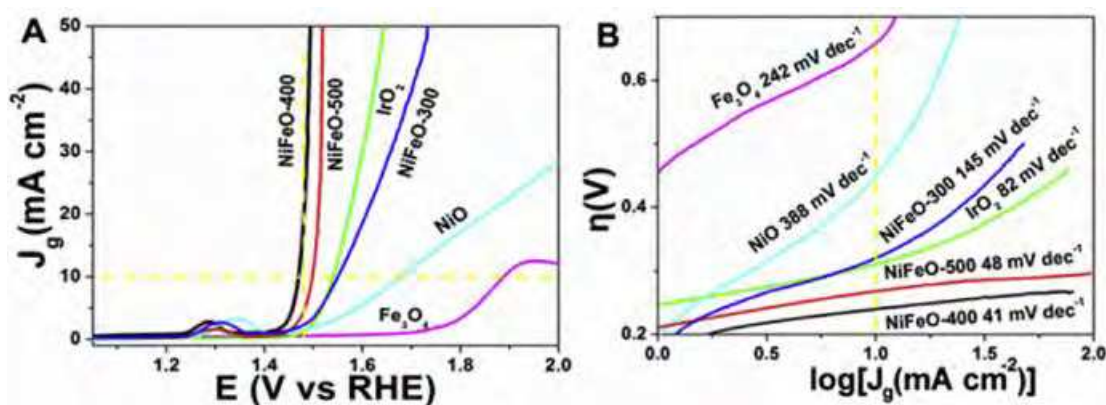


Figure 16. A) the iR-corrected LSV curves of NiFe oxide NCs compared with IrO₂, NiO, and Fe₃O₄ in 1M KOH solution at the scan rate of 10 mV/s and B) the corresponding Tafel plots at the current density of 10 mA/cm² [19].

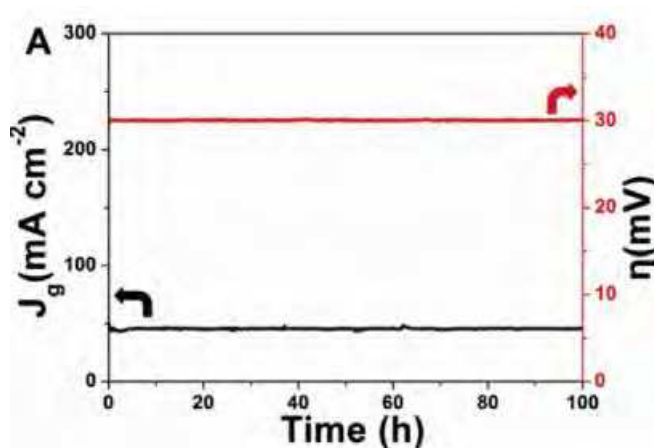


Figure 17. The chronoamperometry (CA) of NiFeO-400 NC at the overpotential of 300 mV, and CP curves of NiFeO-400 at geometric current density of 40 mA/cm² [19].

More recently, Gatard *et al.*, reported FeNi₃@Ni NPs (FeNi₃ core and Ni enriched surface) with an average size of 18.6 nm (Figure 18) synthesized by co-decomposition of organometallic precursors in the presence of a stabilizer, palmitic acid [20]. The FeNi₃@Ni NPs could reach a current density of 10 mA/cm² at an overpotential of 330 mV in 1M KOH solution (see Table 1).

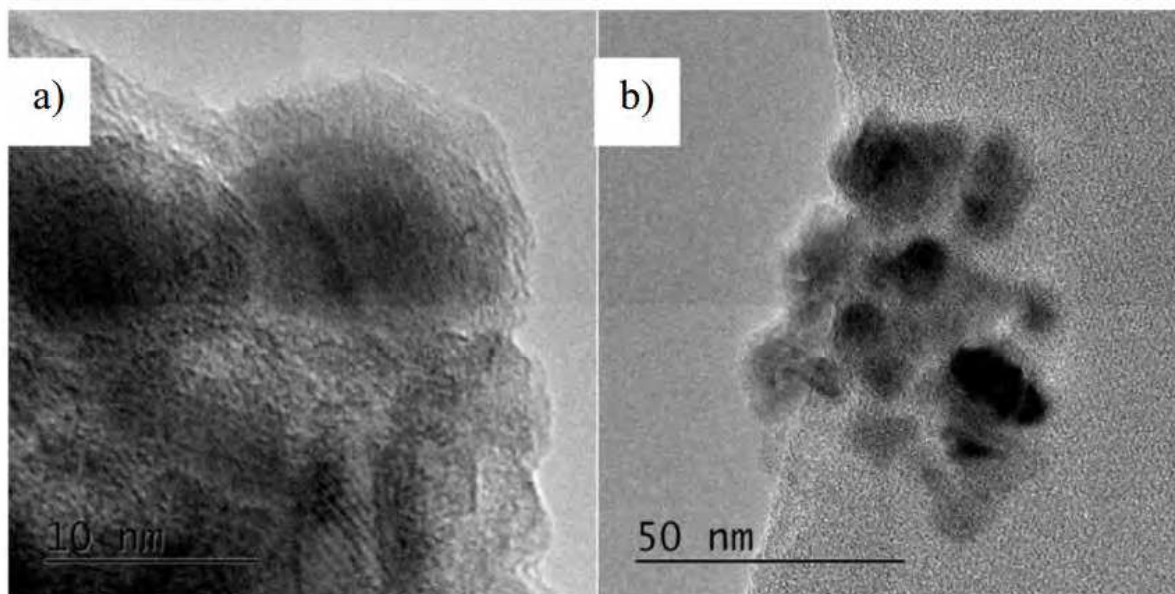


Figure 18. TEM images of FeNi₃@Ni NPs[20].

In this chapter we present new NiFe Oxide NPs having different Ni/Fe ratios. We targeted sizes below 4 nm by applying a simple organometallic synthesis method to reach a high surface specific area. This method provided first well defined, non oxidized NiFe NPs which were subsequently oxidized into NiFeOx NPs. The catalytic properties of these NPS for the OER were assayed in an alkaline electrolyte solution.

2. Description of the nanomaterials used in this work

All samples were obtained after oxidation of preformed metal nanoparticles for 4 days in air, in the solid state.

2.1 Ni and Fe oxide reference samples

Ni and Fe oxide reference samples were prepared following the synthetic pathways described in Figure 19.

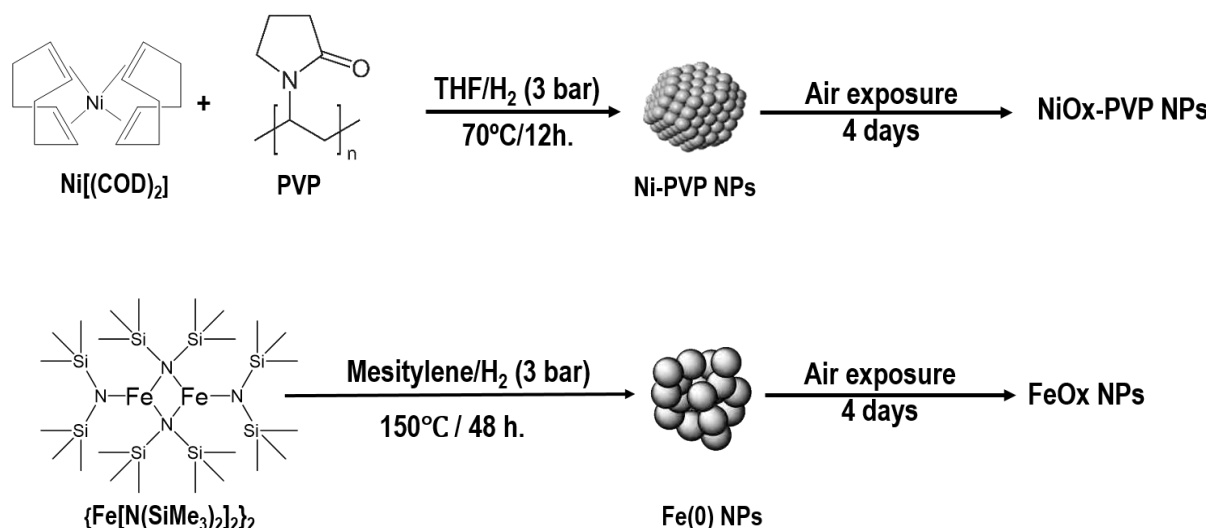


Figure 19. synthetic pathway to Ni (top) and Fe (bottom) oxide reference samples

First, Ni[35] and Fe[36] NPs were synthesized following procedures described in previous publications from our group. Briefly, the Ni NPs were obtained by hydrogenation of the bicyclooctadiene nickel(0) organometallic complex in THF at 70°C for 12 h. in the presence of polyvinylpyrrolidone (PVP) as stabilizer leading to a nanomaterial with a Ni loading of 9.0 wt% based on ICP-OES data. Fe NPs were synthesized by hydrogenation of the di-bis(bistrimethylsilylamido)iron (II) complex, $[\text{Fe}(\text{N}(\text{SiMe}_3)_2)_2]_2$, in mesitylene at 150°C for 48h. The Fe NPs thus obtained are stabilized by hexamethyldisilazane (HMDS) which forms *in situ*. The Fe content determined by ICP-OES is 56%.

The as-prepared Ni and Fe NPs were oxidized in air for 4 days, in the solid state. They are hereafter denoted as NiOx-PVP NPs and FeOx-HDMS NPs. TEM images of NiOx-PVP NPs as shown in Figure 20 revealed the presence of mostly spherical particles with an average size of 3.9 ± 2.1 nm (Figure 20b). Analysis of the TEM images of the FeOx NPs indicates that the nanoparticles are also spherical in shape with an average size of 1.6 ± 0.7 nm (Figure 21).

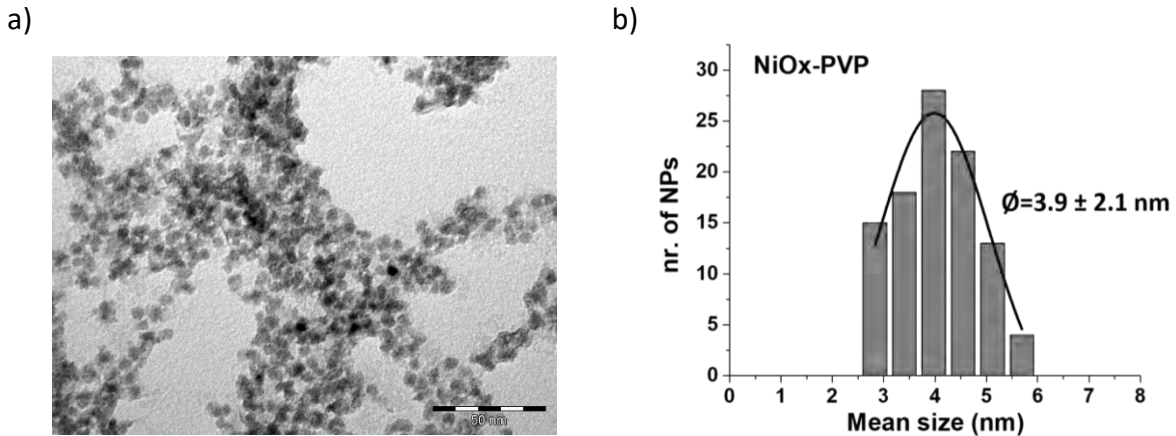


Figure 20. TEM image of a) NiOx-PVP NPs (scale bar = 50 nm) and b) corresponding size histogram $d = 3.9 \pm 2.1 \text{ nm}$.

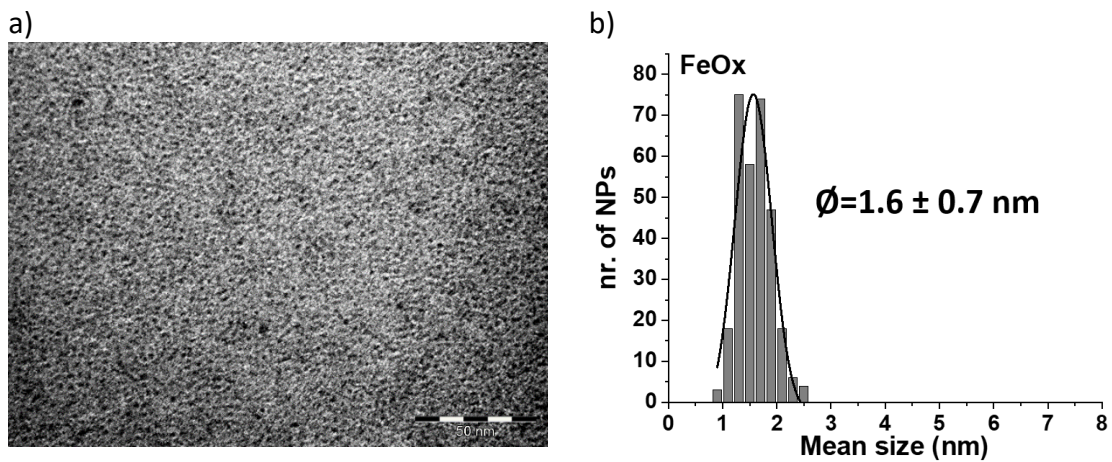


Figure 21. TEM image of a) FeOx NPs (scale bar = 50 nm) and b) corresponding size histogram $d = 1.6 \pm 0.7 \text{ nm}$.

Structural and electronic characterization of the NiOx-PVP NP sample:

The sample was first analyzed by X-Ray diffraction to identify the type of oxide formed (Figure 22). Upon oxidation, an increment in the amorphous contribution is noted, but no new diffraction peaks can be observed. Rather, the fcc Ni contribution which is clearly observed in the Ni NPs diagram still dominates the NiOx-PVP diagram. This indicates that oxidation of the Ni NPs in dry conditions produces a passivating amorphous surface layer.

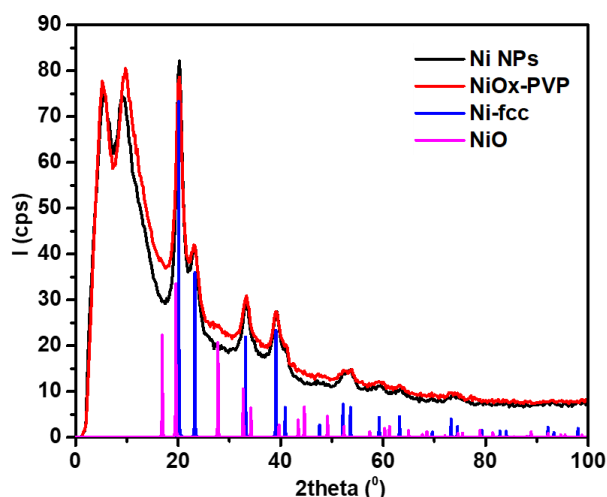


Figure 22. X-Ray diffraction diagrams of Ni-NPs reproduced from ref. [35], NiOx-PVP NPs, Ni-fcc (PDF 04-010-6148), and NiO reference pattern (PDF 04-010-6148)

To identify this amorphous layer, an XPS study was attempted. An aqueous dispersion of the sample was drop casted on a FTO electrode (in conditions used to assess the catalytic activity of the NPs in OER) and studied by XPS. The Ni2p spectrum showed two peaks at 855.9 eV and 861.5 eV which were assigned to Ni²⁺ in a hydroxide environment (Ni(OH)₂) (Figure 23). No peaks of Ni metal were found in this sample. Given the depth probed by XPS (*circa* 5 nm) and the average size of the NPs (3.9 ± 2.1 nm), this suggests that the passivation afforded by the amorphous surface layer formed upon air oxidation in the solid state was not effective in water. As the NiOx-PVP NPs quickly evolved upon dispersion in water, we thus couldn't identify this first formed amorphous layer.

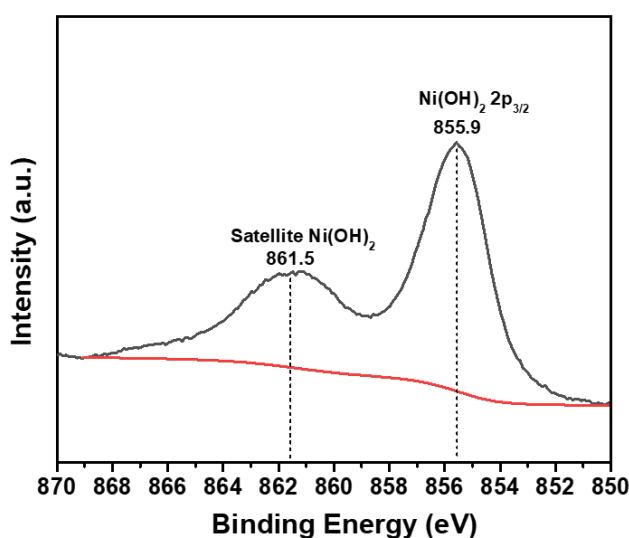


Figure 23. Ni 2p XPS spectrum of NiOx-PVP NPs deposited on a FTO substrate.

Structural and electronic characterization of the FeOx-NP sample:

Given the small size of the NPs, Wide Angle X-Ray Scattering measurements were performed on this sample (Figure 24).

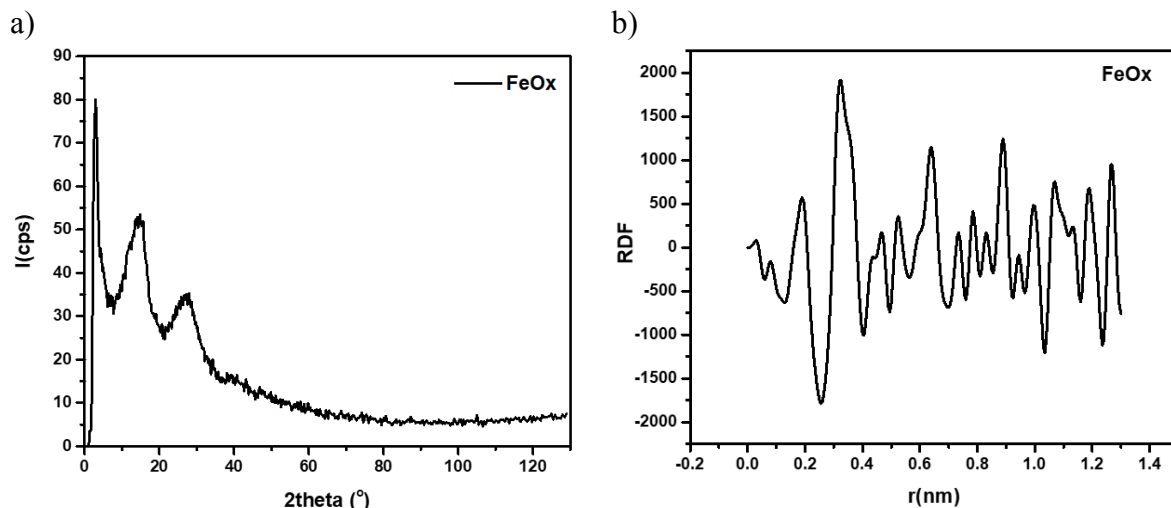


Figure 24. a) WAXS diagram and b) RDF of Fe(0) NPs after oxidation in air for 4 days.

The experimental WAXS diagram (left) and radial distribution function (RDF) of FeOx-HMDS NPs are compared to the data computed from models of hematite (α -Fe₂O₃), lepidocrocite (γ -FeO(OH)), Fe(OH)₃, and goethite (α -FeO(OH)) as presented in Figure 25.

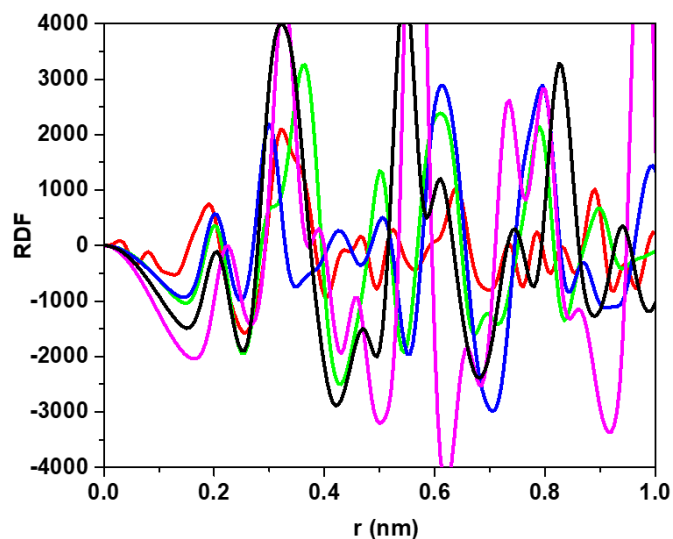
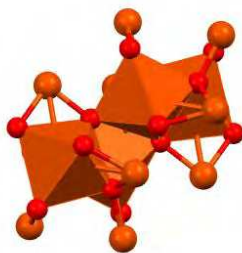


Figure 25. Radial distribution function in real space of FeOx-HMDS NPs (red line) compared with hematite (green line), lepidocrocite (blue line), iron (III) hydroxide (pink line), and goethite (black line) models.

As can be seen in this Figure, it is clear that the structure of FeOx-HMDS NPs does not correspond to any of the structures known for iron 3+. But in the short distances it is quite close

to the hematite structure. More obviously, when it was compared with a hematite model of only 30 atoms (Scheme 3) a better agreement was obtained in real space (Figure 26).



Scheme 3. model of hematite with only 30 atoms.

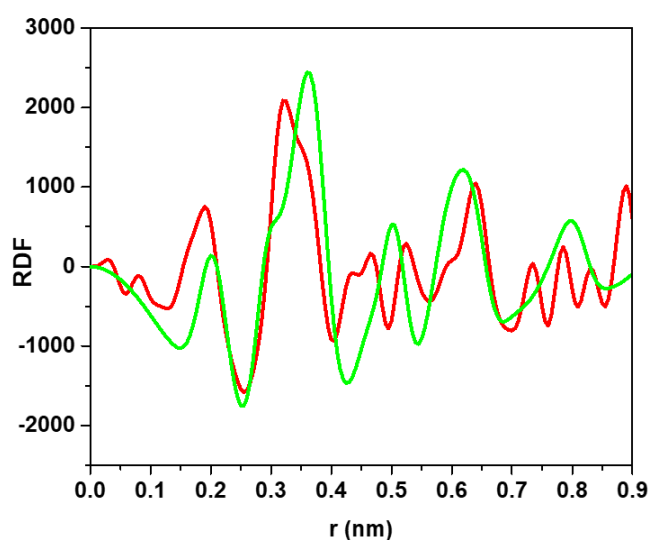


Figure 26. Radial distribution function of FeOx-HMDS (red line) compared with a simple model of hematite with 30 atoms (green line)

This analysis shows that FeOx-HMDS NPs consist in an amorphous oxide with a short range order probably close to the one in hematite.

A XPS analysis was carried out after drop-casting a dispersion of the sample in a mixture of EtOH/H₂O/Nafion (see experimental part - preparation of catalyst ink) on a FTO support. Figure 27 shows the Fe 2p XPS spectrum of the FeOx-HMDS NPs. Only one Fe 2p peak can be observed. The binding energy (711.5 eV) corresponds to Fe³⁺ ions thus pointing to NPs of Fe₂O₃, FeO(OH) or Fe(OH)₃. It is noteworthy that even if the hydroxylated species were not evidenced by WAXS, they could form upon exposure of the FeOx-HMDS NPs to water during the preparation and casting of the ink on the electrode. It is thus difficult to conclude on the exact nature of the nanomaterial, once deposited.

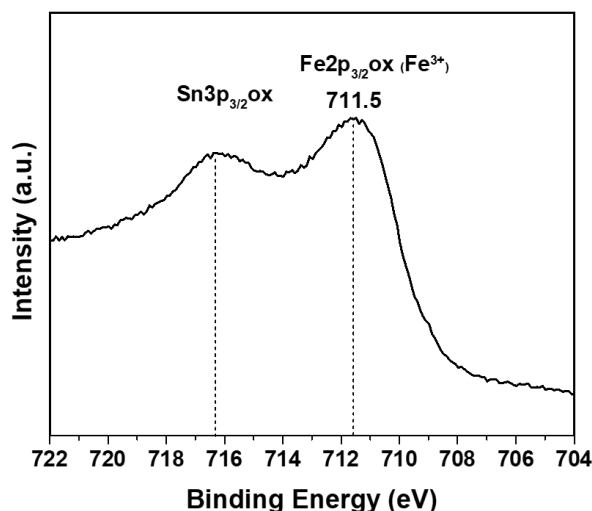


Figure 27. Fe 2p XPS spectrum of FeOx NPs deposited on FTO.

2.2 Synthesis and characterization of the Fe-rich sample (1Ni/9Fe oxide NPs)

Introduction of 10 at.%Ni in the Fe NPs described above was performed using the corresponding ratio of the Ni and Fe precursors, namely 1 Ni(COD)₂, 4.5 [Fe(N(SiMe₃)₂)₂]₂, and the synthesis pathway used to prepare the reference FeNPs (Figure 19, bottom). As for the Fe NPs, the final nanomaterial consisted in NPs stabilized by HMDS formed *in situ*. The Fe content was 59 wt% based on ICP analysis.

Once oxidized, the sample (hereafter referred to as 1Ni/9Fe oxide-HMDS NPs) was characterized by TEM, WAXS and XPS. The TEM image of sample 1Ni/9Fe oxide-HMDS NPs is shown in Figure 28a. It shows well dispersed NPs with a mean size of 1.3 ± 0.6 nm (Figure 28b).

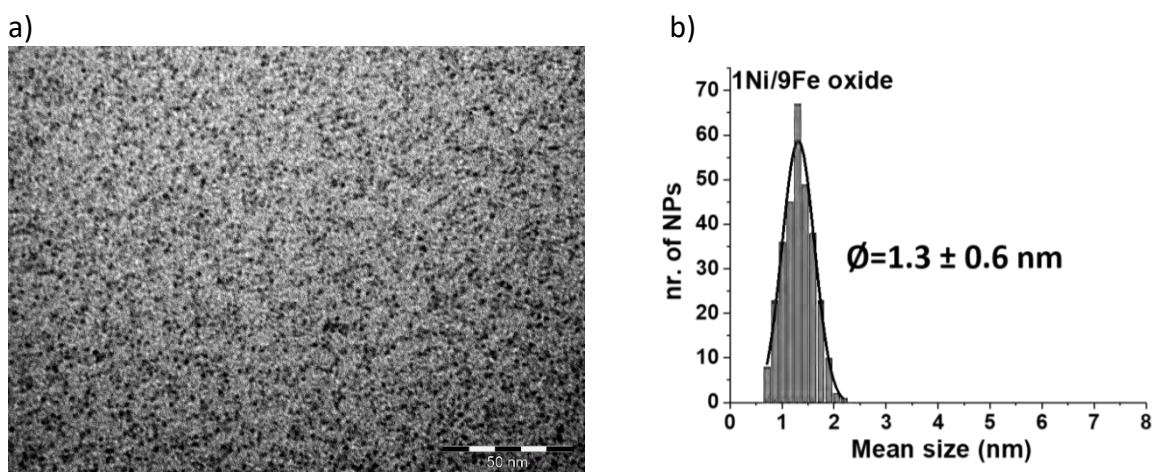


Figure 28. TEM image of a) 1Ni/9Fe oxide-HMDS NPs (scale bar = 50 nm) and b) corresponding size histogram $d=1.3 \pm 0.6$ nm.

To ascertain the structure of the NPs, a WAXS analysis was performed before and after oxidation of this sample as shown in Figure 29. Before oxidation the NPs display a β -Mn structure. In comparison, the structure is strongly altered after air exposure. Figure 30 shows the overlap of the WAXS diagrams and RDFs of samples 1Ni/9Fe oxide-HMDS NPs and FeOx-HMDS NPs. As can be seen from this figure, the structure of sample 1Ni/9Fe oxide –HMDS NPs presents only a short range order, as in sample FeOx-HMDS NPs, close to the one in hematite.

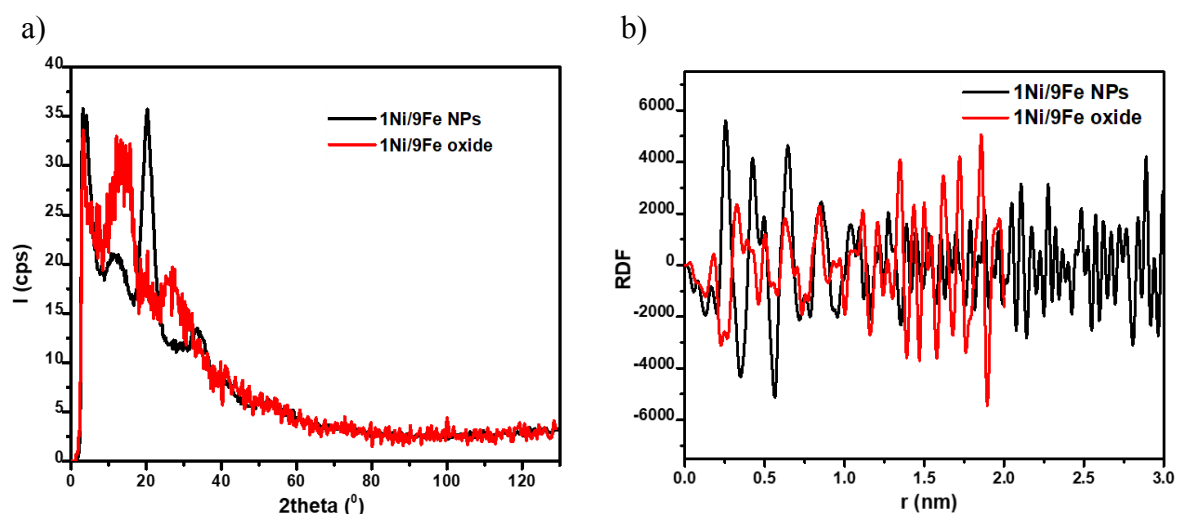


Figure 29. a) WAXS diagrams and b) RDFs of 1Ni/9Fe oxide-HMDS NPs before and after oxidation in air for 4 days.

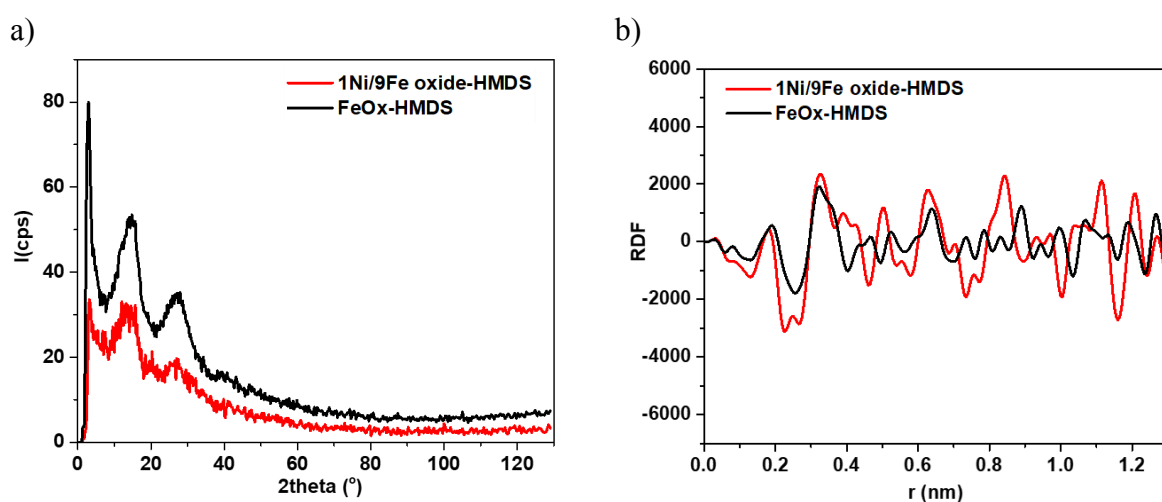


Figure 30. Overlap of a) WAXS diagrams and b) RDFs of 1Ni/9Fe oxide-HMDS NPs and FeOx-HMDS NPs

XPS analysis was carried out after drop-casting of a dispersion of the sample in a mixture of EtOH/H₂O/Nafion (see experimental part - preparation of catalyst ink) on a FTO support to evidence any possible evolution of the sample following its deposition on the electrode. The

Fe2p XPS spectrum of 1Ni/9Fe oxide NPs presents one peak located at 711.6 eV characteristic of Fe³⁺ as in Fe₂O₃, FeO(OH) or Fe(OH)₃ (Figure 31). The Ni2p spectrum displays a main peak at 856.1 eV attributed to Ni(OH)₂. The presence of Ni metal in the sample is ambiguous due to the poor signal/noise ratio in the 852-853eV region (Figure 32).

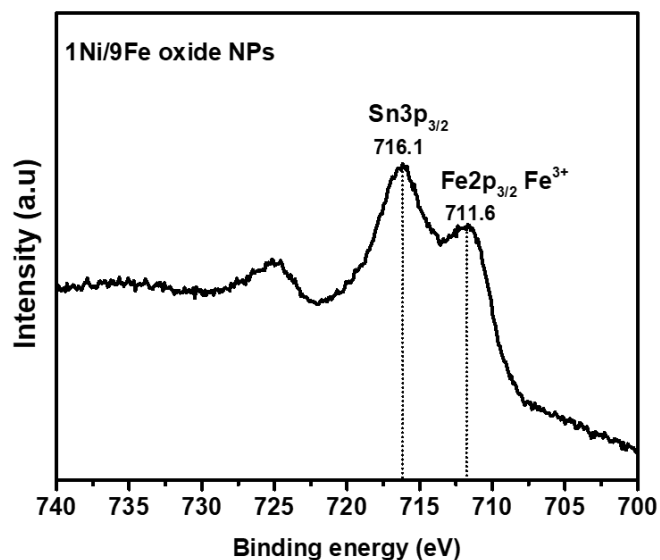


Figure 31. Fe 2p XPS spectrum of 1Ni/9Fe oxide NPs deposited on FTO

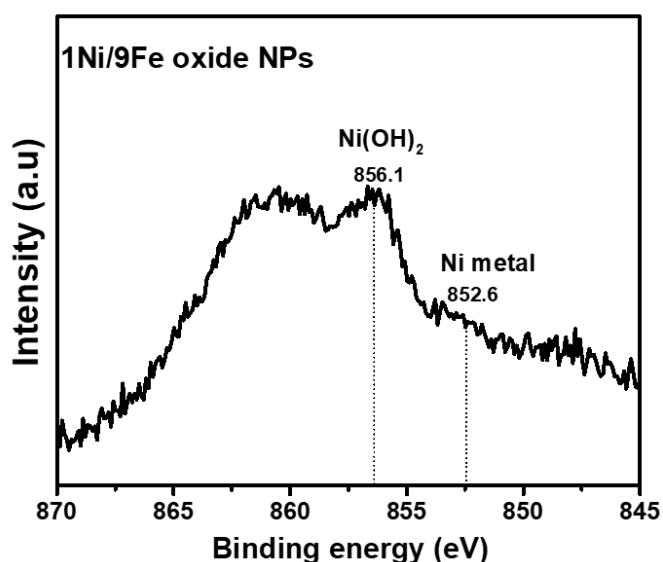


Figure 32. Ni 2p XPS spectrum of 1Ni/9Fe oxide NPs deposited on FTO

We will hereafter consider that these NPs consist in an amorphous NiFe oxide of 1Ni9Fe composition bearing only HMDS ligands at their surface.

2.3 Synthesis and characterization of NiFeOx NPs with compositions 1Ni/1Fe and 2Ni/1Fe

Following the synthetic pathway described in Figure 19 bottom, increasing the Ni/Fe precursor ratio over 1/4.5 led only to ill-defined NPs, not homogeneous in composition. The sample 1Ni/1Fe was thus synthesized following the procedure published by O. Margeat *et al.*,^[37] which uses hexadecylamine (HDA) to control the growth of the NPs and stabilize the final dispersion, as described in Figure 33. The same protocol led to 2Ni/1Fe NPs by adjusting the initial Ni(COD)₂/[Fe(N(SiMe₃)₂)₂]₂ molar ratio to 2/0.5. According to already published results^[37], this protocol leads to hydrophobic core-shell NPs with a core enriched in Ni while Fe is preferentially located on the surface of the NPs, as a consequence of the faster decomposition of the nickel precursor. The as-synthesized NPs were exposed to air for 4 days to form a passivating metal oxide layer on their surface. This passivating oxide played an important role not only in the protection of the residual Ni core but also enabled further functionalisation, a key step to afford NPs that could be dispersed in water.

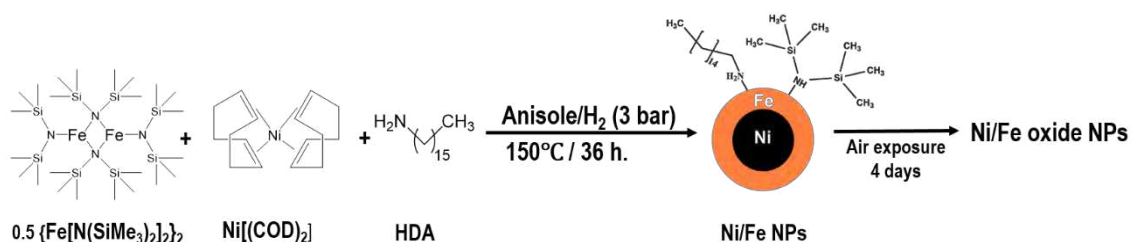
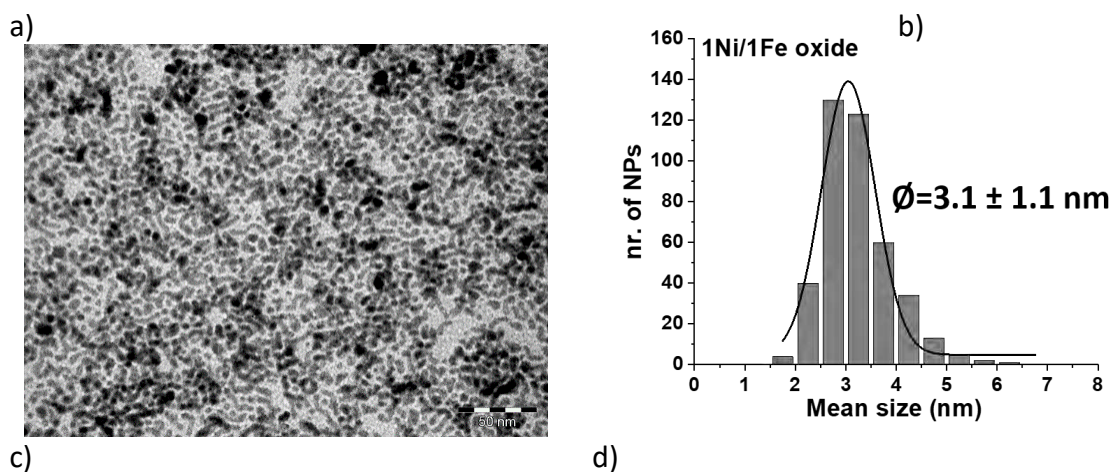


Figure 33. synthetic pathway to NiFeOx NPs with composition 1Ni/1Fe

Figure 34 displays representative TEM images of the NPs after the oxidation step. The NPs are relatively uniform in shape with an average diameter of 3.1 ± 1.1 nm (Figure 34a, b), and 3.6 ± 1.5 nm (Figure 34c, d) for samples with Ni/Fe ratios of 1/1 and 2/1, respectively.



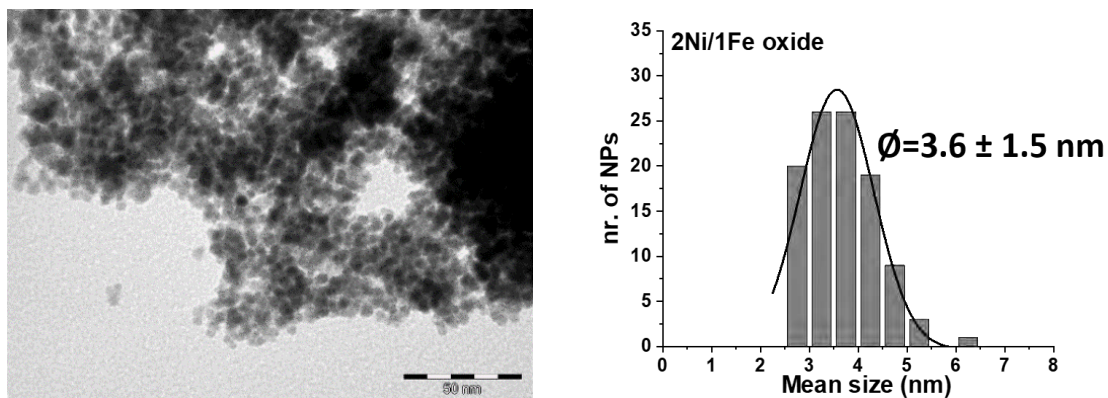


Figure 34. TEM image of a) sample 1Ni/1Fe oxide NPs (scale bar = 50 nm) with b) corresponding size histogram with the average diameter of 3.1 ± 1.1 nm, and TEM image of c) sample 2Ni/1Fe oxide NPs with d) corresponding size histogram with the average diameter of 3.6 ± 1.5 nm.

Atom Resolved TEM (ARM) was used to try and determine the atomic distribution in samples 1Ni/1Fe and 2Ni/1Fe NPs. Figures 35 and 36 show ARM images of these two samples. It clearly confirms that both Ni and Fe are present in the NPs. Drawing any firm conclusion on the distribution of Ni and Fe inside the NPs is difficult at such small size, especially as ARM is far from being a statistical method. Still, it can be observed that STEM-EELS analysis of a few NPs from sample 2Ni/1Fe oxide NPs do not show any clear segregation of the two elements. Analysis of sample 1Ni/1Fe NPs is even less conclusive. Under high resolution imaging conditions, three populations of NPs are evidenced: the smallest spherical NPs, in which no clear segregation of the two elements can be distinguished, the largest spherical NPs which present a surface enriched in Fe (Figure 36a), and NPs of irregular shape (Figure 36b) showing a shell enriched in Ni. These results must be taken with great care as no statistical data can be obtained from ARM investigations.

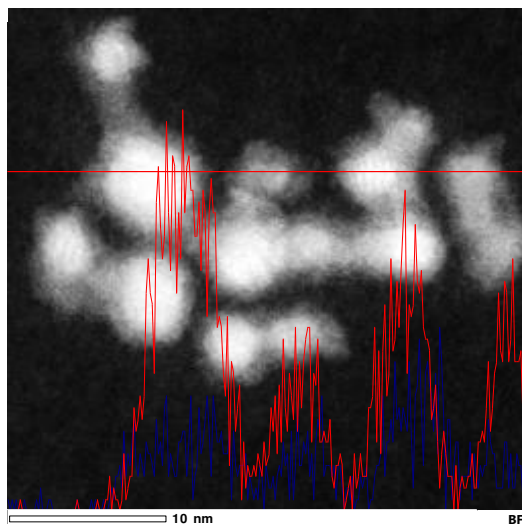


Figure 35. ARM image of sample 2Ni/1Fe oxide NPs, red and blue curves represent the Fe and Ni contents along the red line.

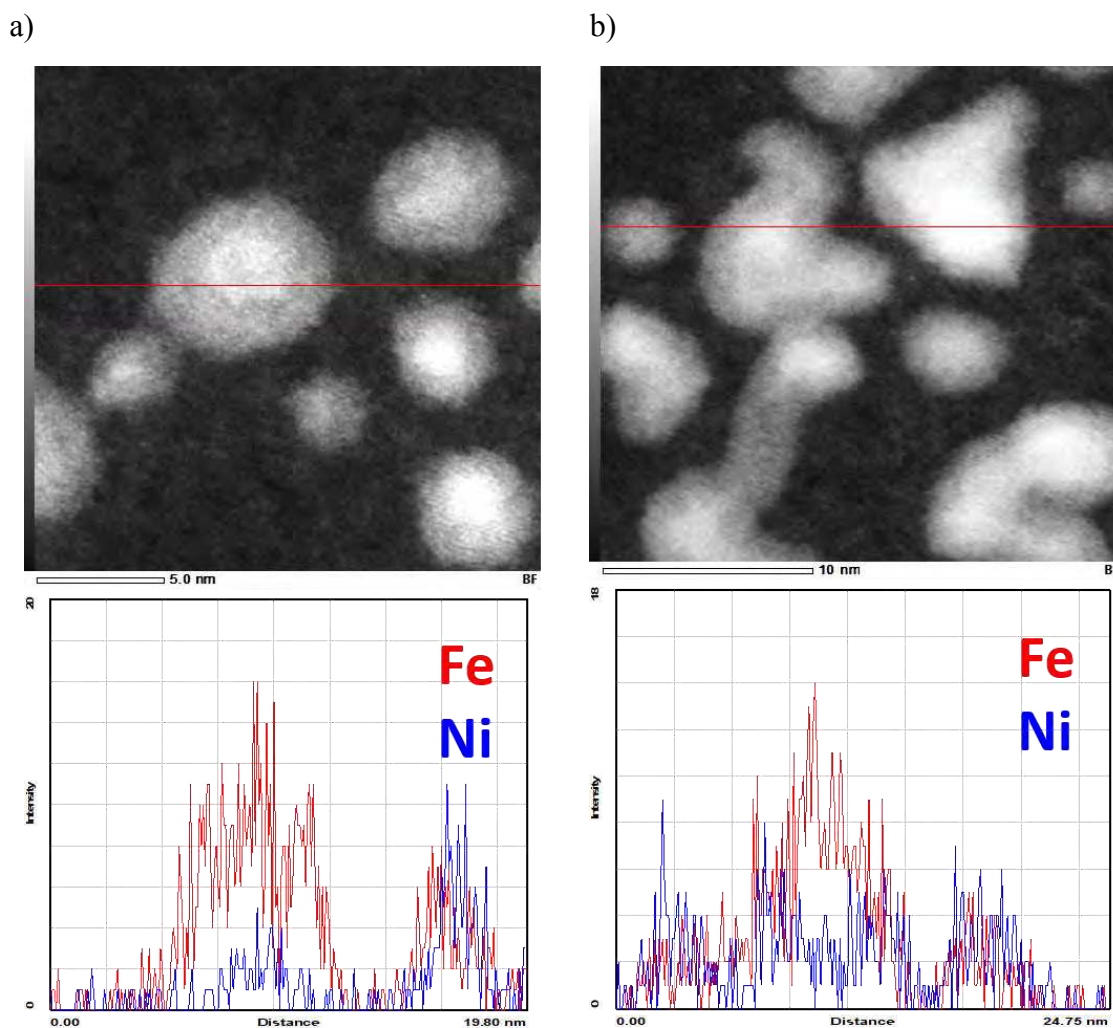


Figure 36. ARM images of sample 1Ni/1Fe oxide NPs and corresponding elemental analysis

WAXS was used to investigate the structure of the NiFe oxidized samples. This technique gives access to a more representative description of the sample. Figure 37 shows the overlap of the data recorded from sample 1Ni/1Fe before and after 4 days of air exposure. The WAXS diagram of the as-prepared 1Ni/1Fe NPs shows four peaks at 20, 23, 33, and 39° characteristic of faced centered cubic (fcc) nickel. No contribution from any Fe species can be observed pointing to an amorphous component. This observation is in agreement with the publication of O. Margeat *et al.*,[37]. After oxidation, new peaks are noted at 16 and 27° which fit well with the pattern of maghemite (or magnetite as these two oxides cannot be distinguished with this experimental set-up). A strong decrease of the intensity of the main peak attributed to fcc Ni is also observed, together with an increase in the amorphous contribution. This points to an oxidation of Ni into an amorphous oxide or hydroxide species. The presence of crystalline NiO is difficult to confirm or disprove as the experimental peaks are quite large due to the small size of the crystalline domains and its typical diffraction peaks are expected to be close to those of Fe₂O₃ and/or Ni. It is noteworthy that a small contribution from fcc Ni is still visible in the diagram. It suggests that 1Ni/1Fe oxide NPs consist in a Ni core surrounded by an oxide layer comprising both Ni and Fe.

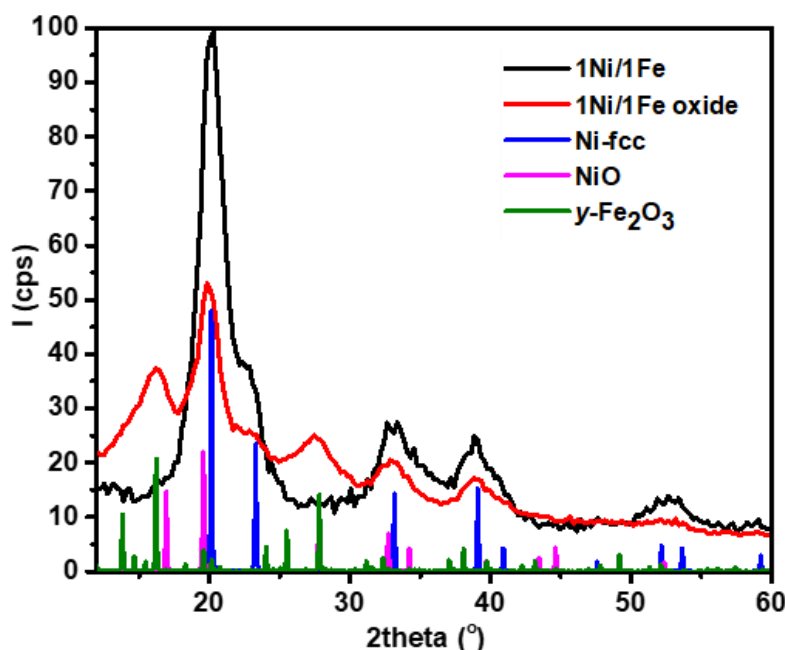


Figure 37. WAXS diagram of 1Ni/1Fe NPs before and after air exposure as well as reference fcc-Ni (PDF 04-010-6148), NiO (PDF 00-044-1159), and γ -Fe₂O₃ (PDF-01-089-5894) diagrams.

Similarly, in Figure 38 before the oxidation process, the WAXS diagram of 2Ni/1Fe NPs displayed only peaks corresponding to fcc Ni. After oxidation, additional peaks at 16 and 27° corresponding to maghemite (or magnetite) could be assigned. No clear oxidation of Ni could

be detected, nor disproved. Still, the persistence of a large fcc Ni contribution suggests the formation of a passivating oxide layer which could be part NiO, part FeOx. Anyways, these observations point out that, contrarily to what ARM studies suggested, the main part of the 2Ni/1Fe NPs sample may be constituted by NPs with a nickel rich core.

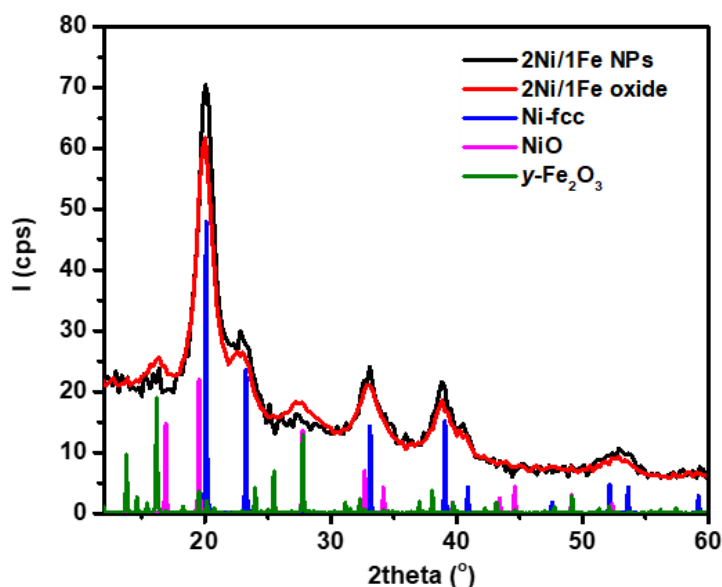


Figure 38. WAXS diagram of 2Ni/1Fe NPs before and after air exposure as well as reference fcc-Ni (PDF 04-010-6148), NiO (PDF 00-044-1159), and γ -Fe₂O₃ (PDF-01-089-5894) diagrams.

The surface state of 1Ni/1Fe NPs and 2Ni/1Fe NPs after oxidation was analyzed by FT-IR. A typical spectrum is given in Figure 39 for the 2Ni/1Fe oxide NPs sample. The two peaks at 2912 cm⁻¹ and 2845 cm⁻¹ were attributed to ν C-H stretching modes of alkyl chains, as in HDA. As well, the peaks at 1466 cm⁻¹ and 723 cm⁻¹ were attributed to respectively, the CH bending, and CH₂ rocking modes of an alkyl chain, confirming the presence of HDA. Meanwhile, the peak at 2956 cm⁻¹ was attributed to the CH stretching mode observed in the HMDS spectrum, in agreement with the *in situ* formation of this species. ICP-OES analysis indicated the presence of a large amount of these ligands in the samples. Indeed, the percentage of metal was no larger than 49 (wt%) and 31 (wt%) in 1Ni/1Fe and 2Ni/1Fe NPs samples, respectively. This explains why the NPs were highly soluble in any hydrophobic solvent but not in water. Therefore, in order to investigate the catalytic activity of these NiFe oxide NPs for the OER, a ligand exchange was definitely necessary in order to impart a hydrophilic coating to the NPs.

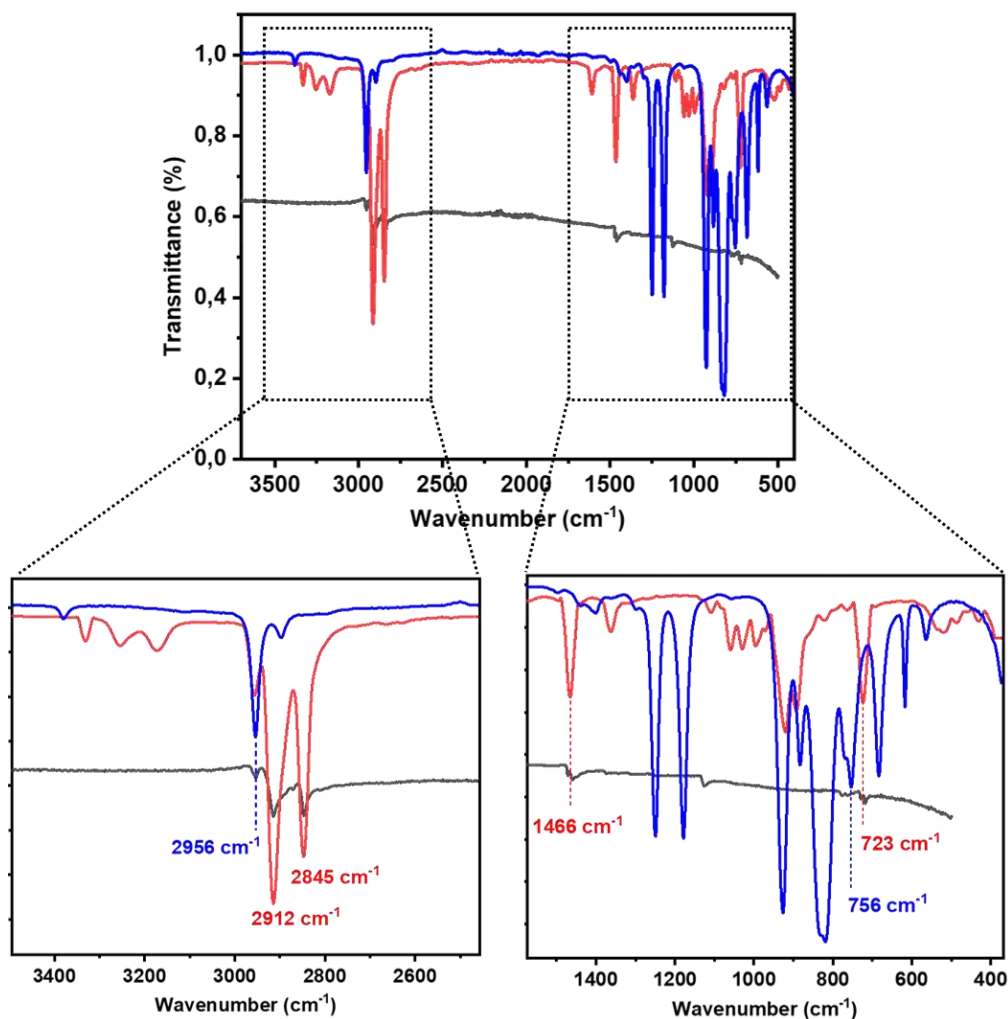
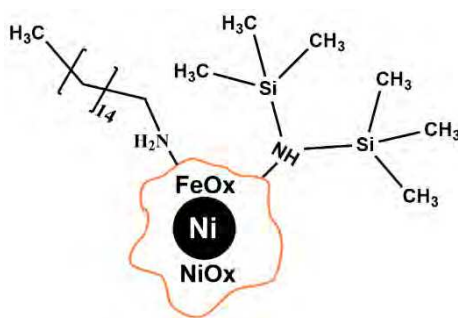


Figure 39. FT-IR spectrum of 2Ni/1Fe oxide NPs (black line) compared to HDA (red line) and HDMS (blue line) reference spectra.

To conclude, these NPs are best described by a Ni core surrounded by a mixed NiOx/FeOx surface layer, in which the Ni/Fe ratio will vary depending on the composition of the initial NiFe NPs, and bearing HDA and HMDS ligands at the surface as schematically drawn in scheme 4.



Scheme 4. tentative description of NPs in samples 1Ni1Fe NPs and 2Ni1Fe NPs

2.4 Water transfer of NiFeOx NPs using 3-amino propyl phosphonic acid:

Due to their PVP coating, the reference NiOx-PVP NPs were easily dispersed in water. As well, a satisfactory dispersion could be achieved with the HMDS coated FeOx and 1Ni9Fe oxide NPs, most probably due to the large quantity of ligand forming multilayers finally exposing the amine function of HMDS.

However, as noted above, the native 1Ni/1Fe oxide and 2Ni/1Fe oxide NPs couldn't be dispersed in water. Their transfer from the organic phase to the aqueous phase was achieved by exchanging HDA and HMDS for 3-aminopropyl phosphonic acid (APA) adapting a process already published by our group[38] and applied to Fe@FeOx NPs in Chapter 2. In brief, a solution of APA in water was added to a solution of the NiFeOx NPs in dichloromethane. The pH of the aqueous phase was adjusted to 8 by adding NaOH (1M). This biphasic system was mechanically stirred for 7 days upon which time the phosphonic group was successfully anchored on the surface of the NiFeOx NPs that were successfully transferred to the aqueous phase. The color change of the aqueous phase, from colorless to black, was an easy way to follow the process (Figure 40). Then the NPs were magnetically separated and purified by washing intensively with water, ethanol, diethyl ether and finally dried in air. The obtained NPs will be hereafter referred to as 1Ni/1Fe oxide-APA NPs and 2Ni/1Fe oxide-APA NPs.

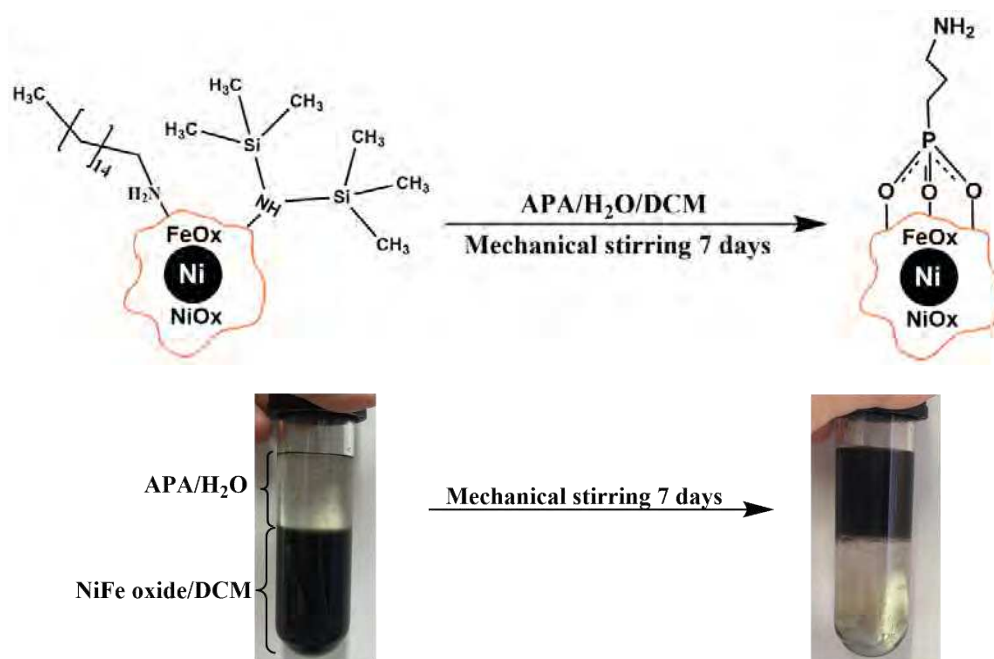


Figure 40. Synthetic pathway (top) and photograph of the ligand exchange process (bottom).

Infrared spectroscopy was used to confirm the bonding between the surfactant and metal oxide NPs and investigate its nature. FT-IR spectra (recorded in ATR mode) of 2Ni/1Fe oxide NPs before and after reaction with 3-aminopropyl phosphonic acid are combined in Figure 41. After ligand exchange, the IR spectrum of 2Ni/1Fe oxide-APA NPs is flat in the 2000-4000 cm^{-1} window. The absence of the CH stretching vibrations of HDA (expected at 2912 cm^{-1} and 2845 cm^{-1}) indicates that almost all the initial organic ligands present in the nanomaterial were removed. Furthermore, a broad band is observed at around 990 cm^{-1} *i.e.* in a region where Fe-O-P vibrations are expected. It indicates that the 3-aminopropyl phosphonic acid was successfully grafted on the surface of 2Ni/1Fe oxide NPs through a covalent Fe-O-P bonding [38-40]. The presence of only one broad peak in this region also suggests that APA is probably grafted in a symmetrically tridentate binding mode rather than in a bidentate or mono-dentate mode (see Scheme 4 Chapter 2), as we cannot observe any P=O or P-OH vibration. This analysis is in agreement with several studies published before [41, 42].

The same observation holds for sample 1Ni/1Fe oxide-APA NPs as shown in Figure 41.

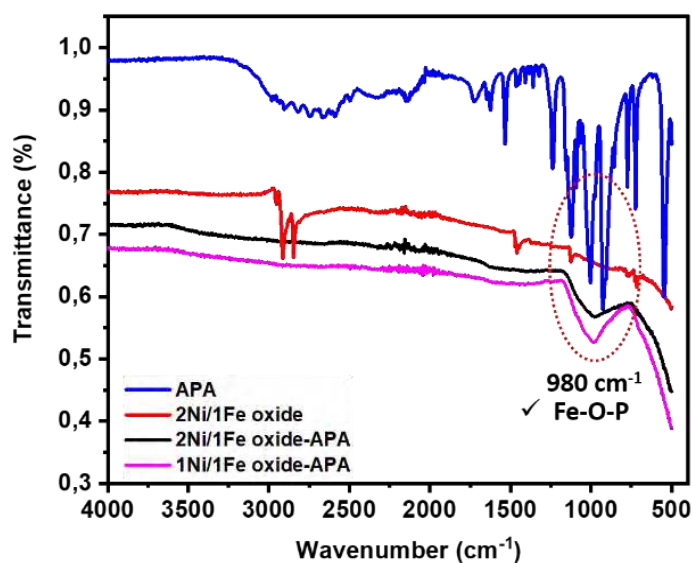


Figure 41. FT-IR spectra of 2Ni/1Fe oxide NPs, 2Ni/1Fe oxide-APA NPs, 1Ni/1Fe oxide-APA NPs, and APA.

Further confirmation of the anchoring of APA on NiFeOx NPs was found by XPS (Figure 42). A peak at 133.6 eV is observed in the XPS P2p spectrum of each sample. This binding energy is in a good agreement with those reported for phosphated magnetite NPs [43].

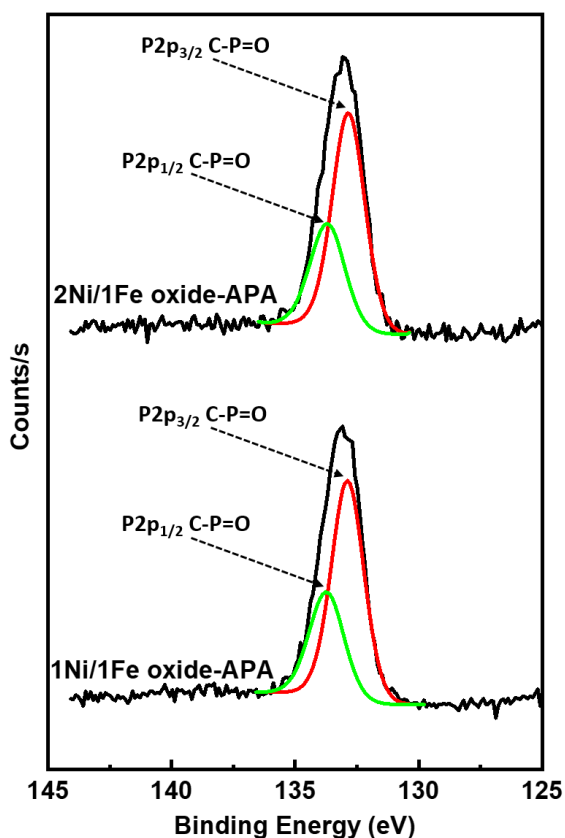


Figure 42. P2p XPS spectra of 1Ni/1Fe - oxide APA NPs (top) and 2Ni/1Fe oxide - APA NPs (bottom).

XPS also revealed the chemical valence state of Ni and Fe in the different samples.

The Fe2p spectra reported Figure 43 show peaks at 711.0 eV and 724.4 eV that were assigned respectively to Fe2p_{3/2} and Fe2p_{1/2} orbitals of Fe³⁺ ions in both 1Ni/1Fe oxide-APA NPs and 2Ni/1Fe oxide-APA NPs samples. These binding energies are in good agreement with those reported for maghemite[44, 45].

Concerning Ni2p_{3/2} spectra, the intense peak observed at 855.6 eV as well as the satellite peak at 861.5 eV confirms the presence of Ni(OH)₂ species in both 1Ni/1Fe oxide-APA NPs and 2Ni/1Fe oxide-APA NPs samples (Figure 44). This indicates that during the reaction, part of Ni was exposed to water. In addition, the peak at 852.7 eV could be assigned to the Ni2p_{3/2} signal of Ni metal, indicating the persistence of a Ni core in the sample after their transfer into water. From the spectra recorded, the presence of Ni oxide in 2Ni/1Fe oxide-APA and 1Ni/1Fe oxide-APA could not be confirmed nor disproved as there is an overlap between the satellite peak for Ni metal and the main peak for Ni(OH)₂ in the region expected for the Ni2p peak of NiO.

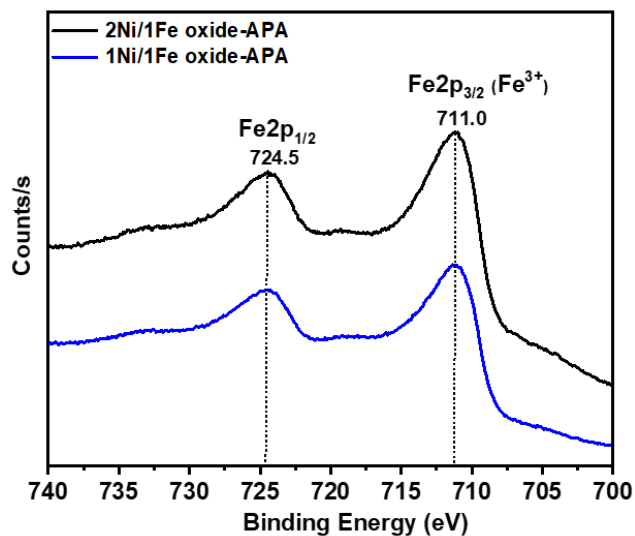


Figure 43. XPS Fe2p spectra of sample 2Ni/1Fe oxide-APA NPs (top, black curve) and sample 1Ni/1Fe oxide-APA NPs (bottom, blue curve).

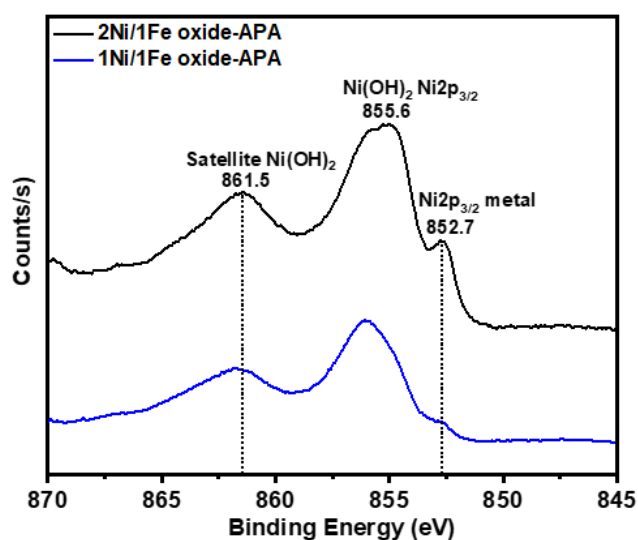


Figure 44. XPS Ni2p spectra of sample 2Ni/1Fe oxide-APA NPs (top, black curve) and sample 1Ni/1Fe oxide-APA NPs (bottom, blue curve).

Interestingly, the ratios of Ni in the metallic state, extracted from the XPS data for sample 2Ni/1Fe before (2Ni/1Fe oxide) and after ligand exchange with APA (2Ni/1Fe oxide-APA), were 0.3 and 0.16, respectively. These values suggest that oxidation progresses during ligand exchange (Figure 45).

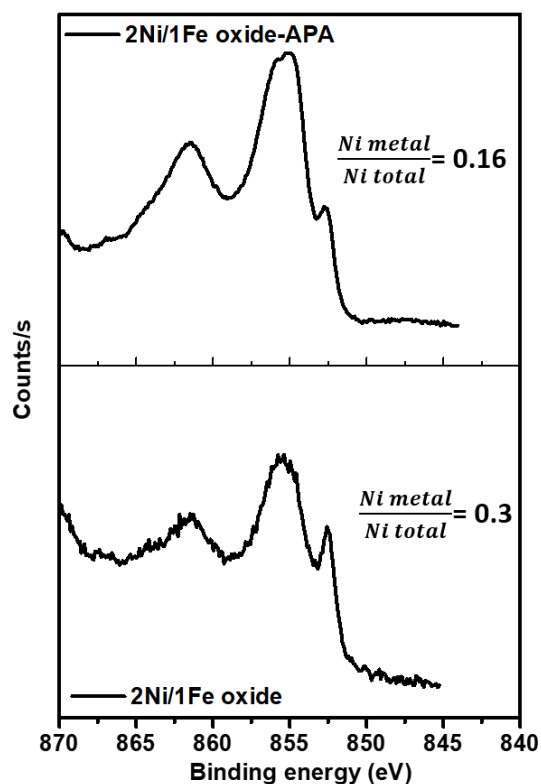
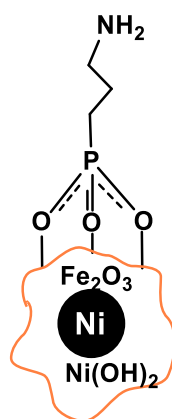


Figure 45. XPS Ni_{2p} spectra of sample 2Ni/1Fe oxide-APA NPs (top) and sample 2Ni/1Fe oxide (bottom)

To conclude, these NPs are best described by a Ni core surrounded by a mixed Ni(OH)₂/Fe₂O₃ surface layer, in which the Ni/Fe ratio will vary depending on the composition of the initial NiFeNPs, and bearing APA ligands at the surface as tentatively drawn in Scheme 5.



Scheme 5. Tentative representation of samples 1Ni1Fe oxide-APA and 2Ni1Fe oxide-APA NPs

3. Evaluation of the nanomaterials in WOC

3.1 Electrocatalytic activity in OER

The electrochemical performances of NiFeO_x-APA NPs with different Ni/Fe ratios were investigated in a 1M KOH solution using a standard three-electrodes configuration.

The catalyst was dispersed in water in the presence of Nafion and drop-casted on an FTO electrode with a loading of 2.6×10^{-4} g/cm² (*see detail in experimental section*). The electrocatalytic activity for OER was assayed by linear sweep voltammetry (LSV) at a scan rate of 5mV/s. The LSV OER activity of 2Ni/1Fe oxide-APA NPs was compared with those of 1Ni/1Fe oxide-APA NPs, 1Ni/9Fe oxide-HMDS NPs, NiO_x-PVP NPs and FeO_x-HMDS NPs studied in similar conditions (Figure 46a). Among all samples, the 2Ni/1Fe oxide-APA NPs displayed the best catalytic activity as it afforded the highest current density at a given overpotential. To reach a catalytic current density (*j*) of 10 mA/cm², this catalyst required 320 mV, which is 40, 130, and 250 mV less than 1Ni/1Fe oxide-APA NPs, 1Ni/9Fe oxide-HMDS, and FeO_x-HMDS NPs samples, respectively. The overpotential at *j*=10 mA/cm² for sample NiO_x-PVP NPs could not be recorded due to the fast detachment of the NPs during LSV measurements. These results show that NiFeO_x NPs have higher catalytic activity than pure FeO_x and NiO_x, indicating a synergetic effect between Ni and Fe. The catalytic activity of the NiFe NPs having a Ni core and Ni(OH)₂/Fe₂O₃ shell vary in function of their chemical composition : the system with the higher Ni content displays the higher catalytic current (rate) at a given applied potential.

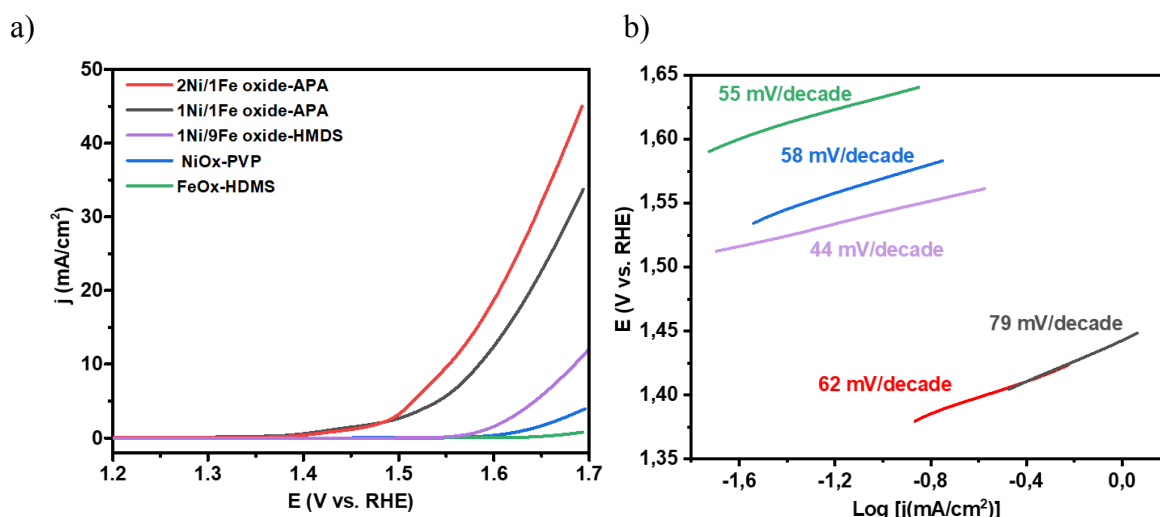


Figure 46. a) LSV curves and b) corresponding Tafel plots of 2Ni/1Fe oxide-APA NPs (red line), 1Ni/1Fe oxide-APA NPs (black line), 1Ni/9Fe oxide-HMDS NPs (purple line), NiOx-PVP NPs (blue line) and FeOx-HMDS NPs (green line) in KOH 1M, scan rate 5mV/s.

To gain more information on the OER kinetics, the Tafel plots were drawn and analyzed (Figure 46b). The Tafel slopes of 2Ni/1Fe oxide-APA NPs, 1Ni/1Fe oxide-APA NPs, 1Ni/9Fe oxide-HMDS NPs, NiOx-PVP NPs, and FeOx-HMDS NPs were 62, 79, 44, 58, and 55 mV/decade, respectively. Table 6 lists the values of the overpotentials at $j=10 \text{ mA/cm}^2$ and Tafel slopes for all studied samples for comparison purposes. These results are in line with those published by Ma *et al.*, who studied the influence of the Ni:Fe ratio in Ni-Fe layered double hydroxide (LDH) on the catalytic activity in alkaline solution and observed also that LHD nanosheets of composition $\text{Ni}_{2/3}\text{Fe}_{1/3}$ were most efficient water oxidation catalysts in KOH 1M than those of $\text{Ni}_{3/4}\text{Fe}_{1/4}$ and $\text{Ni}_{4/5}\text{Fe}_{1/5}$ composition[16].

Table 6. Overpotentials values at 10 mA/cm^2 , corresponding Tafel slopes and positions of the redox peaks observed in cyclic voltametry for all studied samples.

	2Ni/1Fe oxide - APA NPs	1Ni/1Fe oxide - APA NPs	1Ni/9Fe oxide - APA NPs	FeOx NPs	NiOx NPs
$\eta_{10} \text{ (mA/cm}^2\text{)}$	320	360	450	570	—
Tafel slope (mV/decade)	62	79	44	55	58
Reduction peak (V vs.RHE)	+1.35 + 1.24	+1.38	+1.37	—	+1.38
Oxidation peak (V vs.RHE)	+1.45	+1.45	—	—	+1.48

To further evaluate the electrocatalytic activity of the NiFe oxide APA NPs, determination of the TOF value would have been interesting. However, due to the limited quantity of material prepared, we couldn't determine the real metal content in each sample.

3.2 Electrocatalytic Stability

The stability and durability of 2Ni/1Fe oxide-APA, 1Ni/1Fe oxide-APA, 1Ni/9Fe oxide-HMDS and FeOx-HMDS NPs catalysts were evaluated by performing chronoamperometric (CA) measurements at a current density of $j=10 \text{ mA/cm}^2$ in 1M KOH. The NiOx-PVP sample showed to be the less stable, and by far, as it readily detached from the electrode during OER. As shown in Figure 47a, the electrocatalytic activity of 2Ni/1Fe oxide-APA NPs, 1Ni/1Fe oxide-APA, and 1Ni/9Fe oxide-HMDS NPs were stable over 16 h of measurement. This is thus independent of the surface coating (APA or HMDS). Contrarily, sample FeOx-HMDS NPs showed first a fast degradation of its activity which then remained stable at $\sim 5 \text{ mA/cm}^2$. This result expresses the synergistic effect of combining Ni with Fe in bimetallic NPs. LSV measurements recorded for 2Ni/1Fe oxide - APA NPs after the chronoamperometric experiments showed that the sample displayed almost the same activity as before (Figure 47b). The same observation was also made for samples 1Ni/1Fe oxide-APA, and 1Ni/9Fe oxide-HMDS NPs. The only noticeable difference was an increase in the intensity of the pre-oxidation peak after the chronoamperometric experiments.

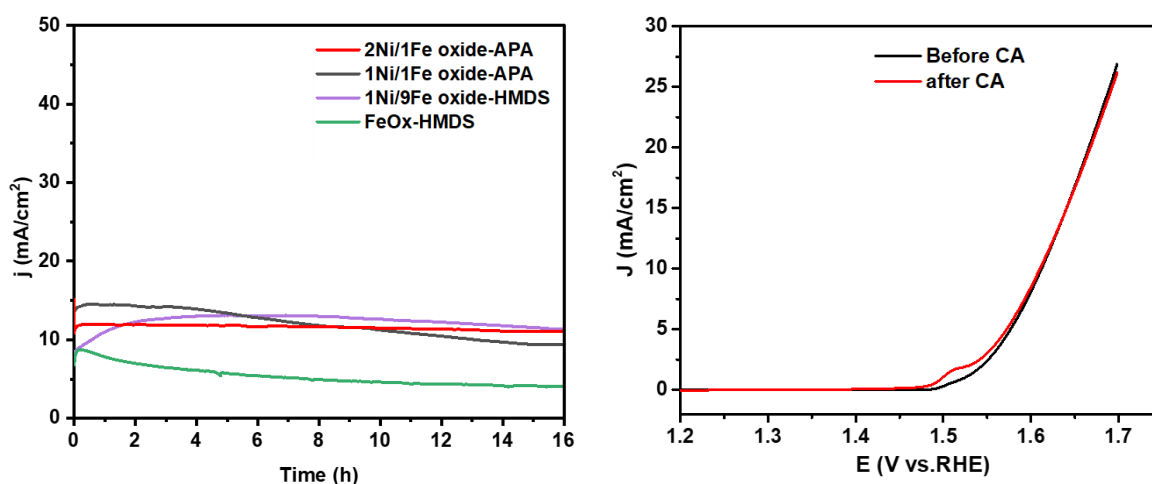


Figure 47. a) CA assessment of 2Ni/1Fe oxide-APA NPs (red line), 1Ni/1Fe oxide-APA NPs (black line), 1Ni/9Fe oxide-HMDS NPs (purple line), and FeOx-HMDS NPs (green line) at $j=10 \text{ mA/cm}^2$ in 1M KOH; b) LSV curves of sample 2Ni/1Fe oxide-APA NPs before and after the CA test.

2Ni/1Fe oxide-APA NPs are much more stable than amorphous NiFe oxide NPs of *similar size* (~ 4nm) incorporated in carbon black (stability at $j = 10 \text{ mA/cm}^2$ for 16h. for our systems compared to only for 6h. [17], in identical conditions). The stability of 2Ni/1Fe oxide-APA NPs can also be compared to that of nanocatalysts of larger size (~19.8 nm) but *comparable surface state* from Manso *et al.*[18]: in this work NPs with a NiOx core and mixed NiOx/FeOx shell showed a stability for 2 h. at $j = 10 \text{ mA/cm}^2$ in 1M KOH (same testing conditions). Comparison with literature data thus emphasizes the good stability of the new NiFe nanocatalysts reported herein, and the interest of combining both a reduced size and mixed Ni(OH)₂/Fe₂O₃ surface.

3.3. Cyclic Voltametry studies

Cyclic voltammograms (CVs) were recorded as soon as the samples reached the steady state during LSV measurements (namely steady I-V curves were obtained). Representative CVs for NiOx-PVP NPs and FeOx-HMDS NPs are shown in Figure 48 and Figure 50, respectively. Figure 48 shows a series of 50 CVs collected for NiOx NPs. Prior to occurrence of the O₂-evolution catalytic event (at an onset potential of 1.53 V *vs.* RHE), a quasi-reversible redox event was observed (oxidation peak potential at 1.48 V and reduction peak at 1.38 V *vs.* RHE) which was attributed to the Ni³⁺/Ni²⁺ couple. No obvious change in the electrochemical behavior of the electrode occurred upon repeating the potential scanning, except from a slight decrement of the catalytic current. It can be due to the detachment of NiOx-PVP in alkaline solution as the PVP matrix is highly soluble in water. Indeed, a phase transition from oxides to hydroxides and oxyhydroxides phases is often observed in the catalysts during electrocatalytic water oxidation[46, 47]. The modification of NiOx catalysts upon CV studies was thus attributed to the *in situ* formation of Ni(OH)₂/NiOOH hydroxide/oxyhydroxide species during the electrochemical conditioning process (Scheme 6) in alkaline conditions. Observation of the Ni²⁺ oxidation wave at 1.48 V *vs.* RHE is thus assigned to the reversible Ni(OH)₂/NiOOH redox reaction, as already reported in the literature [2, 8, 48, 49].



Scheme 6. oxidation of Ni(OH)₂ into NiOOH in alkaline solution.

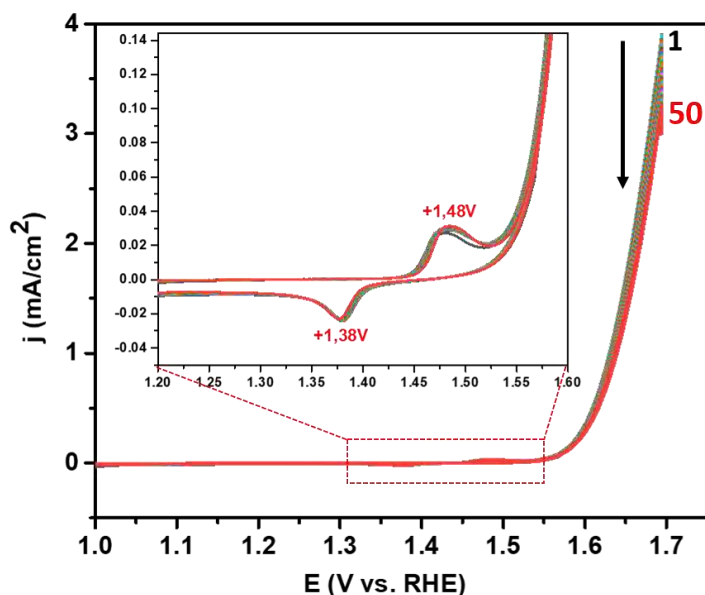


Figure 48. Cyclic voltammograms (CVs) for NiOx-PVP NPs and b) FeOx-HMDS NPs in 1M KOH electrolyte. Black arrow emphasizing the decrease in catalytic activity upon consecutive scans.

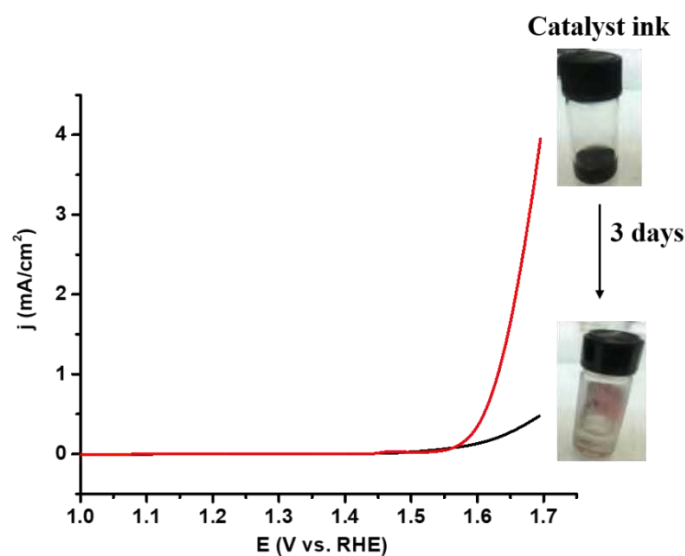


Figure 49. LSV curves for sample NiOx-PVP NPs prepared from a fresh (red curve) and aged (black curve) ink.

We then examined the potential influence of an air-oxidation on the electrochemical behavior of the NiOx-PVP NPs. To this end, the catalyst ink made of the dispersion of NiOx-PVP NPs in the EtOH/H₂O/Nafion solution was kept in the open air for 3 days. An obvious color change was observed, e.g. from black to colorless dispersion. The aged catalyst ink was then drop-casted on a FTO substrate and then assayed in the same 1M KOH electrolyte. It showed almost no catalytic activity (Figure 49). The actual reason behind this phenomenon should be

investigated. At this time, we hypothesize that the acidic activity of Nafion could cause the dissolution of NiOx-PVP NPs generating Ni^{2+} dissolved in the solution. We also noted that such a color change was not observed for the other catalyst inks, namely 2Ni/1Fe oxide-APA, 1Ni/1Fe oxide-APA, 1Ni/9Fe oxide-APA and FeOx HMDS NPs indicating their better stability.

In a parallel assay using the FeOx-HMDS catalyst, no pre-catalytic redox event was observed. The catalytic activity was significantly degraded upon repeating the potential cycling (Figure 50). It indicates a rapid detachment of the FeOx-HMDS NP catalyst from the electrode surface.

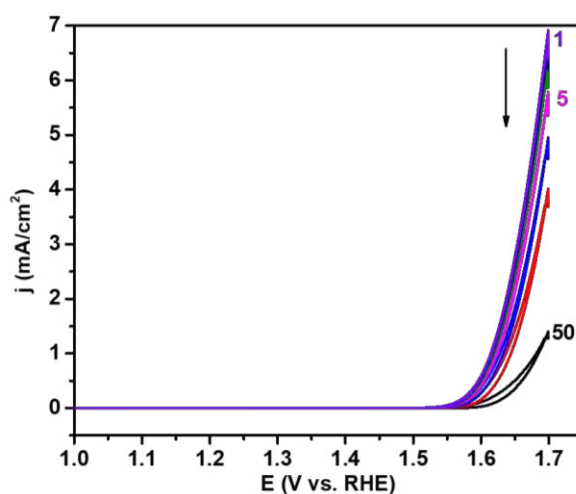


Figure 50. Superposition of 50 Cyclic voltammograms (CVs) for FeOx-HMDS NPs in 1M KOH electrolyte. Black arrow emphasizing the decrease in catalytic activity upon consecutive scans.

A similar study was carried out for the mixed NiFe oxide electrocatalysts. A superposition of the first 50 CVs is shown in Figure 51a, b, c, for 2Ni/1Fe oxide-APA, 1Ni/1Fe oxide-APA, and 1Ni/9Fe oxide-HMDS NPs respectively. The CVs are characterized by two primary features: the OER (already studied by LSV) and the $\text{Ni}(\text{OH})_2/\text{NiOOH}$ redox couple. Concerning the latter, a pre-oxidation peak at around +1.45 V (2Ni/1Fe oxide-APA), and +1.53 V (1Ni/1Fe oxide-APA) is observed, but such a peak is almost negligible for sample 1Ni/9Fe oxide-APA NPs. Nonetheless, the CVs of all three samples clearly show a reduction peak at +1.35 V (2Ni/1Fe oxide-APA), +1.38 V (1Ni/1Fe oxide-APA), and +1.36 V (1Ni/9Fe oxide-APA) which could correspond to the reduction peak of Ni^{3+} (as in NiOOH) to Ni^{2+} in $\text{Ni}(\text{OH})_2$. This reduction peak is more obvious for the sample with the highest Ni content, 2Ni/1Fe oxide-APA NPs.

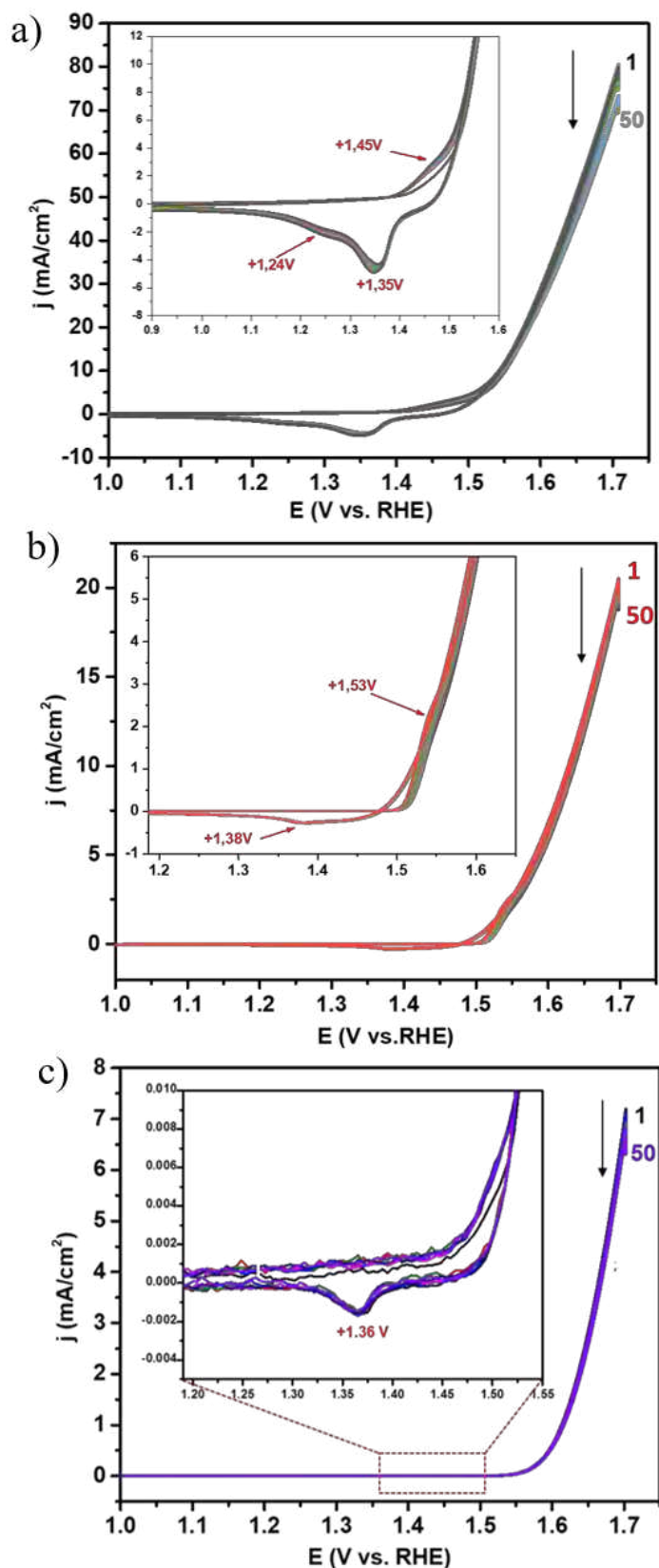


Figure 51. 50 first CVs of a) 2Ni/1Fe oxide-APA, b) 1Ni/1Fe oxide-APA, c) 1Ni/9Fe oxide-HMDS in KOH 1M, scan rate 5mV/s after activation by LSV

Chapter IV – NiFeO_x NPs as an OER catalyst

To conclude on the assesement of the EC activity of the new NiFe systems developed in this chapter: from the literature review, we know that i) introducing an iron oxide component in NiO_x systems increases their conductivity thus favoring electron transfers; ii) amorphous systems which present more defects, in comparison with crystalline phases, are beneficial to the kinetics of the reaction. The nanocatalysts developed herein thus combine interesting features: the Ni metallic component in the core with the amorphous Ni(OH)₂ and iron oxide on the shell that can create junctions suitable to enhance the electrocatalytic activity towards OER. This observation is in line with the work of Manso *et al.*, [18].

4. Conclusions

In this chapter we successfully developed bimetallic NiFe oxide NPs with different Ni/Fe ratios based on the thermal decomposition of organometallic complexes, with well controlled size and morphology. The as-synthesized NiFe NPs are relatively uniform with an overall diameter of 3.1 nm and 3.6 nm for 1Ni/1Fe NPs and 2Ni/1Fe NPs, respectively. After oxidation, highly uniform 1Ni/1Fe oxide NPs and 2Ni/1Fe oxide NPs of core-shell structure were transferred from the organic phase to the aqueous phase through a ligand exchange process using 3-aminopropyl phosphonic acid. Careful characterization of these samples has shown that they could be best described as Ni cores surrounded by a mixed Ni(OH)₂/Fe(III)Oxide layer. For comparison purposes, samples with an Fe rich content namely 1Ni/9Fe oxide-HMDS NPs, pure Ni namely NiOx-PVP NPs and pure Fe namely FeOx-HMDS NPs were also synthesized. The mixed FeNi oxides NPs (2Ni/1Fe oxide-APA, 1Ni/1Fe oxide-APA, 1Ni/9Fe oxide-HMDS NPs) along with the control samples (*i.e.* NiOx-PVP NPs and FeOx-HMDS NPs) were evaluated in OER catalysis. It is noteworthy that among the NiFe based OER catalysts reported so far, only a few consist in NPs. The OER activity of the NPs was assayed using LSV, CV in KOH 1M. The results showed that the sample 2Ni/1Fe oxide-APA NPs exhibited the best performance with the lowest overpotential (10 mA/cm² at 320 mV) and smallest Tafel slope (62 mV/decade). Furthermore, this sample showed a good stability as it could generate 10 mA/cm² in KOH 1M during 16 h. without any sign of degradation. In this respect, the OER activity of 2Ni/1Fe oxide-APA NPs is comparable to, or even better than, the activity reported in the literature for other NiFe based OER nanocatalysts (see Table 6). The present study thus broadens the scope of available nanocatalysts for OER.

Table 6: Summary of the main characteristics of representative NiFe oxide –based electrocatalysts for OER

No.	Catalyst	Ni:Fe ratio	Synthetic method	Morphology	Substrate	Electrolyte	Overpotential (mV) J=10mA/cm ²	Tafel slope (mV.dec ⁻¹)	TOF	Ref	Pub. year
1	Ni _{0.9} Fe _{0.1} Ox	9:1	Solution synthesis, spin coating	Thin film 2-3 nm	Au/Ti QCM or ITO	KOH 1M	336	30	0,21 s ⁻¹ ($\eta=0.3V$)	[2]	2012
2	Fe:NiOx	–	Sputtering	film	–	KOH 1N	80 mA/cm ² at $\eta=362$ mV	40	–	[6]	1997
3	NiO/NiFe ₂ O ₄	1:2	E ISA	powder	Carbon paper	KOH 1M	–	–	–	[7]	2012
4	NiFeOx	0.1% Fe in NiOx electrode	Electrodeposition	Thin film	–	25 w/o KOH	233	25	–	[8]	1987
5	[Ni _{1-x} Fe _x (OH) ₂](NO ₃) _y (OH) _{x-y} .nH ₂ O	22% Fe	Pulsed laser ablation in liquids	NPs 12 nm	Graphite electrode	KOH 1M	260	47	–	[9]	2014
6	NiFeOx	–	Electrodeposited	–	GCE	NaOH 1M	360	–	–	[10]	2013
7	NiFe-LDH	–	Exfoliation	nanosheet	GCE	KOH 1M	302	40	0.05.s ⁻¹ ($\eta=0.3V$)	[11]	2014
8	NiFe-LDH bulk	–	Hydrothermal	Submicrometre	GCE	KOH 1M	347	–	–	[11]	2014
9	NiFe-LDH	–	–	–	GCE	KOH 1M	315	40	–	[12]	2015
10	NiFe-LDH	–	Solvothermal	nanoplates ~50nm	CNTs	KOH 1M	–	31	0.56 s ⁻¹ ($\eta=0.3V$)	[5]	2013

Chapter IV – NiFeOx NPs as an OER catalyst

11	Mesoporous NiFe hydroxide	–	electrodeposition	Thickness ~10nm Lateral extension 50-several hundred nm	Nickel foam	KOH 1M	215	28	0.075 s ⁻¹ ($\eta=0.4V$)	[13]	2015
12	Ni ₄₅ Fe ₅₅	45:55	solvothermal	–	GCE	NaOH 0.1M	180	35	0.1 s ⁻¹ ($\eta=0.3V$)	[14]	2017
13	NiFe ₂ O ₄	1:2	Commercial vendors	30nm	–	NaOH 1M	510	–	–	[15]	2016
14	Ni _{2/3} -Fe _{1/3} LDH	2:1	Homogeneous precipitation, exfoliated method	- Lateral size (NS) ~few hundred nm -Thickness ~0.8 nm	rGO	KOH 1M	210	40	0.2 s ⁻¹ ($\eta=0.3V$)	[16]	2015
15	Ni _{0.69} Fe _{0.31} Ox	7:3	Solution phase nanocapsule	Amorphous Ni- Fe oxide NP ~4 nm	Carbon vulcan	KOH 1M	280	30	0.2 s ⁻¹ ($\eta=0.3V$)	[17]	2014
16	NiOx-NiOx/FeOx	–	Thermal decomposition organometallic	NPs ~19.8 nm	Au electrode	KOH 1M	320	–	1.175 s ⁻¹ ($\eta= ? V$)	[18]	2018
17	NiFeO	3:2	Direct pyrolysis	Nano cube ~60 nm	GCE	KOH 1M	240	41	0.093 s ⁻¹ at ($\eta=0.25V$)	[19]	2019
18	FeNi ₃ @Ni	1:3	Co-decomposition organometallic	NPs ~18.6 nm	GCE	KOH 1M	330	–	–	[20]	2020
19	2Ni/1Fe oxide – APA NPs	2 : 3	Co-decomposition organometallic	NPs	FTO	KOH 1M	320	62	–	This work	2021

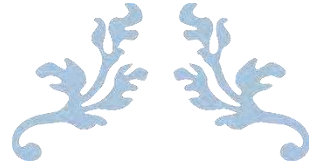
5. References

1. Rodriguez, J., *Physical and chemical properties of bimetallic surfaces*. Surface Science Reports, 1996. **24**(7): p. 223-287.
2. Trotochaud, L., et al., *Solution-Cast Metal Oxide Thin Film Electrocatalysts for Oxygen Evolution*. Journal of the American Chemical Society, 2012. **134**(41): p. 17253-17261.
3. Trotochaud, L., et al., *Nickel–Iron Oxyhydroxide Oxygen-Evolution Electrocatalysts: The Role of Intentional and Incidental Iron Incorporation*. Journal of the American Chemical Society, 2014. **136**(18): p. 6744-6753.
4. Friebel, D., et al., *Identification of Highly Active Fe Sites in (Ni,Fe)OOH for Electrocatalytic Water Splitting*. Journal of the American Chemical Society, 2015. **137**(3): p. 1305-1313.
5. Gong, M., et al., *An Advanced Ni–Fe Layered Double Hydroxide Electrocatalyst for Water Oxidation*. Journal of the American Chemical Society, 2013. **135**(23): p. 8452-8455.
6. Miller, E.L. and R.E. Rocheleau, *Electrochemical Behavior of Reactively Sputtered Iron-Doped Nickel Oxide*. Journal of The Electrochemical Society, 1997. **144**(9): p. 3072-3077.
7. Landon, J., et al., *Spectroscopic Characterization of Mixed Fe–Ni Oxide Electrocatalysts for the Oxygen Evolution Reaction in Alkaline Electrolytes*. ACS Catalysis, 2012. **2**(8): p. 1793-1801.
8. Corrigan, D.A., *The Catalysis of the Oxygen Evolution Reaction by Iron Impurities in Thin Film Nickel Oxide Electrodes*. Journal of The Electrochemical Society, 1987. **134**(2): p. 377-384.
9. Hunter, B.M., et al., *Highly Active Mixed-Metal Nanosheet Water Oxidation Catalysts Made by Pulsed-Laser Ablation in Liquids*. Journal of the American Chemical Society, 2014. **136**(38): p. 13118-13121.
10. McCrory, C.C.L., et al., *Benchmarking Heterogeneous Electrocatalysts for the Oxygen Evolution Reaction*. Journal of the American Chemical Society, 2013. **135**(45): p. 16977-16987.
11. Song, F. and X. Hu, *Exfoliation of layered double hydroxides for enhanced oxygen evolution catalysis*. Nature Communications, 2014. **5**(1): p. 4477.
12. Han, N., F. Zhao, and Y. Li, *Ultrathin nickel–iron layered double hydroxide nanosheets intercalated with molybdate anions for electrocatalytic water oxidation*. Journal of Materials Chemistry A, 2015. **3**(31): p. 16348-16353.
13. Lu, X. and C. Zhao, *Electrodeposition of hierarchically structured three-dimensional nickel–iron electrodes for efficient oxygen evolution at high current densities*. Nature Communications, 2015. **6**(1): p. 6616.
14. Görlin, M., et al., *Oxygen Evolution Reaction Dynamics, Faradaic Charge Efficiency, and the Active Metal Redox States of Ni–Fe Oxide Water Splitting Electrocatalysts*. Journal of the American Chemical Society, 2016. **138**(17): p. 5603-5614.
15. Jung, S., et al., *Benchmarking nanoparticulate metal oxide electrocatalysts for the alkaline water oxidation reaction*. Journal of Materials Chemistry A, 2016. **4**(8): p. 3068-3076.
16. Ma, W., et al., *A Superlattice of Alternately Stacked Ni–Fe Hydroxide Nanosheets and Graphene for Efficient Splitting of Water*. ACS Nano, 2015. **9**(2): p. 1977-1984.

17. Qiu, Y., L. Xin, and W. Li, *Electrocatalytic Oxygen Evolution over Supported Small Amorphous Ni–Fe Nanoparticles in Alkaline Electrolyte*. *Langmuir*, 2014. **30**(26): p. 7893-7901.
18. Manso, R.H., et al., *Controlling the 3-D morphology of Ni–Fe-based nanocatalysts for the oxygen evolution reaction*. *Nanoscale*, 2019. **11**(17): p. 8170-8184.
19. Qiao, J., et al., *Mesoporous spinel NiFe oxide cubes as advanced electrocatalysts for oxygen evolution*. *International Journal of Hydrogen Energy*, 2019. **44**(31): p. 16368-16377.
20. Gatard, V., et al., *FeNi₃ and Ni-Based Nanoparticles as Electrocatalysts for Magnetically Enhanced Alkaline Water Electrolysis*. *Electrocatalysis*, 2020. **11**(5): p. 567-577.
21. Xuan, C., et al., *Heteroatom (P, B, or S) incorporated NiFe-based nanocubes as efficient electrocatalysts for the oxygen evolution reaction*. *Journal of Materials Chemistry A*, 2018. **6**(16): p. 7062-7069.
22. Młynarek, G., M. Paszkiewicz, and A. Radniecka, *The effect of ferric ions on the behaviour of a nickelous hydroxide electrode*. *Journal of Applied Electrochemistry*, 1984. **14**(2): p. 145-149.
23. Natan, M.J., et al., *pH-sensitive nickel(II) hydroxide-based microelectrochemical transistors*. *The Journal of Physical Chemistry*, 1987. **91**(7): p. 1834-1842.
24. Bates, M.K., et al., *Charge-Transfer Effects in Ni–Fe and Ni–Fe–Co Mixed-Metal Oxides for the Alkaline Oxygen Evolution Reaction*. *ACS Catalysis*, 2016. **6**(1): p. 155-161.
25. Gerken, J.B., et al., *Development of an O₂-Sensitive Fluorescence-Quenching Assay for the Combinatorial Discovery of Electrocatalysts for Water Oxidation*. *Angewandte Chemie International Edition*, 2012. **51**(27): p. 6676-6680.
26. Chen, J.Y.C., et al., *Inverse spinel NiFeAlO₄ as a highly active oxygen evolution electrocatalyst: promotion of activity by a redox-inert metal ion*. *Energy & Environmental Science*, 2014. **7**(4): p. 1382-1386.
27. Kanan, M.W. and D.G. Nocera, *In Situ Formation of an Oxygen-Evolving Catalyst in Neutral Water Containing Phosphate and Co²⁺*. *Science*, 2008. **321**(5892): p. 1072.
28. Smith, R.D.L., et al., *Photochemical Route for Accessing Amorphous Metal Oxide Materials for Water Oxidation Catalysis*. *Science*, 2013. **340**(6128): p. 60-63.
29. Smith, R.D.L., et al., *Facile Photochemical Preparation of Amorphous Iridium Oxide Films for Water Oxidation Catalysis*. *Chemistry of Materials*, 2014. **26**(4): p. 1654-1659.
30. Tsuji, E., et al., *Electrocatalytic activity of amorphous RuO₂ electrode for oxygen evolution in an aqueous solution*. *Electrochimica Acta*, 2011. **56**(5): p. 2009-2016.
31. Esswein, A.J., et al., *Highly active cobalt phosphate and borate based oxygen evolving catalysts operating in neutral and natural waters*. *Energy & Environmental Science*, 2011. **4**(2): p. 499-504.
32. Zaharieva, I., et al., *Electrosynthesis, functional, and structural characterization of a water-oxidizing manganese oxide*. *Energy & Environmental Science*, 2012. **5**(5): p. 7081-7089.
33. Indra, A., et al., *Unification of Catalytic Water Oxidation and Oxygen Reduction Reactions: Amorphous Beat Crystalline Cobalt Iron Oxides*. *Journal of the American Chemical Society*, 2014. **136**(50): p. 17530-17536.
34. Esswein, A.J., et al., *Size-Dependent Activity of Co₃O₄ Nanoparticle Anodes for Alkaline Water Electrolysis*. *The Journal of Physical Chemistry C*, 2009. **113**(33): p. 15068-15072.

35. Zaramello, L., et al., *Kinetic investigation into the chemoselective hydrogenation of α,β -unsaturated carbonyl compounds catalyzed by Ni(0) nanoparticles*. Dalton Transactions, 2017. **46**(15): p. 5082-5090.
36. Lacroix, L.-M., et al., *Ultrasmall iron nanoparticles: Effect of size reduction on anisotropy and magnetization*. Journal of Applied Physics, 2008. **103**(7): p. 07D521.
37. Margeat, O., et al., *NiFe nanoparticles: a soft magnetic material?* Small, 2007. **3**(3): p. 451-8.
38. Gharbi, K., et al., *Alkyl phosphonic acid-based ligands as tools for converting hydrophobic iron nanoparticles into water soluble iron-iron oxide core-shell nanoparticles*. New Journal of Chemistry, 2017. **41**(20): p. 11898-11905.
39. Parikh, S.J. and J. Chorover, *ATR-FTIR Spectroscopy Reveals Bond Formation During Bacterial Adhesion to Iron Oxide*. Langmuir, 2006. **22**(20): p. 8492-8500.
40. Basly, B., et al., *Effect of the nanoparticle synthesis method on dendronized iron oxides as MRI contrast agents*. Dalton Transactions, 2013. **42**(6): p. 2146-2157.
41. Mohapatra, S. and P. Pramanik, *Synthesis and stability of functionalized iron oxide nanoparticles using organophosphorus coupling agents*. Colloids and Surfaces A: Physicochemical and Engineering Aspects, 2009. **339**(1): p. 35-42.
42. Ramsier, R.D., P.N. Henriksen, and A.N. Gent, *Adsorption of phosphorus acids on alumina*. Surface Science, 1988. **203**(1): p. 72-88.
43. Daou, T.J., et al., *Phosphate Adsorption Properties of Magnetite-Based Nanoparticles*. Chemistry of Materials, 2007. **19**(18): p. 4494-4505.
44. Radu, T., et al., *X-Ray Photoelectron Spectroscopic Characterization of Iron Oxide Nanoparticles*. Applied Surface Science, 2017. **405**: p. 337-343.
45. Yamashita, T. and P. Hayes, *Analysis of XPS spectra of Fe²⁺ and Fe³⁺ ions in oxide materials*. Applied Surface Science, 2008. **254**(8): p. 2441-2449.
46. Burke, M.S., et al., *Oxygen Evolution Reaction Electrocatalysis on Transition Metal Oxides and (Oxy)hydroxides: Activity Trends and Design Principles*. Chemistry of Materials, 2015. **27**(22): p. 7549-7558.
47. Doyle, R.L., et al., *Redox and electrochemical water splitting catalytic properties of hydrated metal oxide modified electrodes*. Physical Chemistry Chemical Physics, 2013. **15**(33): p. 13737-13783.
48. Corrigan, D.A. and R.M. Bendert, *Effect of Coprecipitated Metal Ions on the Electrochemistry of Nickel Hydroxide Thin Films: Cyclic Voltammetry in 1M KOH*. Journal of The Electrochemical Society, 1989. **136**(3): p. 723-728.
49. Wehrens-Dijksma, M. and P.H.L. Notten, *Electrochemical Quartz Microbalance characterization of Ni(OH)₂-based thin film electrodes*. Electrochimica Acta, 2006. **51**(18): p. 3609-3621.

Chapter IV – NiFeO_x NPs as an OER catalyst



Chapter V – General conclusions and perspectives



Garonne river – Toulouse – France 2019

Chapter V - General conclusions and perspectives

The objective of this PhD was two-fold: investigating new cheap nanocatalysts for the water oxidation reaction, and designing a method to efficiently combine them with a photosensitizer to enable solar driven water splitting.

Fe nanoparticles of average size of *circa* 10 nm were synthesized using an organometallic approach to insure a narrow size distribution. A crystalline iron oxide layer has been engineered at their surface using an oxygen transferring agent $(\text{CH}_3)_3\text{NO}$, followed by a mild annealing process to obtain Fe@FeOx NPs of core-shell structure with an average diameter of *ca.* 11.5 ± 2.3 nm and a $\gamma\text{-Fe}_2\text{O}_3$ oxide shell thickness of *ca.* 2.6 nm. These nanoparticles showed a better O_2 -evolution electrocatalytic activity in alkaline than in a neutral pH electrolyte. They operated with an onset overpotential of 1.75 V and a Tafel slope value of 142 mV/decade at pH 13. Thanks to the $\gamma\text{-Fe}_2\text{O}_3$ oxide shell, these Fe@FeOx NPs (*r*-Fe@FeOx NPs) could be successfully grafted with different aminophosphonic acids and transferred into water. Preliminary assessment of their catalytic activity in OER showed an improved activity for the NPs functionalized by 3-aminopropylphosphonic acid (*r*-Fe@FeOx@APA NPs) as they displayed both lower overpotential (1.62 V *vs.* RHE) and Tafel slope (30 mV/decade) values compared with the pristine *r*-Fe@FeOx NPs (overpotential at 1.75 V *vs.* RHE and Tafel slope 142 mV/decade). These results open promising prospects in the development of Fe-based water oxidation catalysts.

It would be interesting to perform more complete cyclic voltammetry, linear sweep voltammetry, and chronoamperometry measurements on the series of Fe@FeOx NPs grafted with different aminophosphonic acids reported in this work and compare their behavior to that of the non-functionalized *r*-Fe@FeOx NPs. Determination of the electrochemical surface active area and TOF values for these samples would help ascertain their interest in water oxidation catalysis. By doing so, we might be able to correlate the catalytic activity of the nanocatalysts to the number of phosphonic acid or amine groups present at their surface. It is noteworthy that few studies aim at understanding the effect of the surface ligands on the electrocatalytic activity of OER nanocatalysts.

Then, incorporating these nanocatalysts with a conducting material, such as *e.g.* carbon black, could be a mean to improve the electron transfer and efficiency in OER catalysis.

Chapter V - General conclusions and perspectives

Furthermore, a novel hybrid photoanode for solar-driven water splitting was achieved by covalently grafting a Ru-phenanthroline light-harvester onto the Fe@FeOx core/shell nanoparticles through a phosphonate linker. A successful synthetic strategy was developed first to prepare the phosphonate-derivative 1,10-phenanthroline ligand and the corresponding *bis*-heteroleptic ruthenium(II) complex *from* the [Ru(phen)₂Cl₂] precursor. The resulting [Ru-PO(OH)₂]²⁺ complex was fully characterized and qualified to be used as a light harvester to build a hybrid photocatalyst for visible-light driven solar water splitting. Two synthetic pathways were investigated to graft the Ru-complex at the surface of the nanoparticles, namely *via* mono- and biphasic processes in THF/H₂O or CH₂Cl₂/H₂O solvent mixtures, respectively. The monophasic process was found to be more efficient as it provided a higher grafting density at the surface of the nanoparticles, namely 7-folds higher than that obtained by the biphasic process (respectively 56 and 9 Ru per nanoparticles for the mono and biphasic processes). Nevertheless, a maximum grafting density of 56 Ru complexes per nanoparticle indicated the difficulty of exchanging carboxylate ligands by phosphonate ones on a γ -Fe₂O₃ surface. The photoelectrochemical activity of the hybrid photoanode prepared in monophasic conditions was studied under AM 1.5M, 100 mWcm⁻² Xe lamp in 1M KOH showing that the photocurrent density of this hybrid photoanode reached 20 μ A/cm² at an applied potential of +1.0 V *vs.* RHE. It corresponds to a TOF (calculated per mol of Ru complex) of 0.02 s⁻¹. This performance represents *ca.* 9-fold, and 40-fold enhancements in comparison to that achieved for a simple mixture of the ruthenium polypyridyl photosensitizer with the Fe@FeOx nanoparticles without any linker, and for the pristine *r*-Fe@FeOx photoanodes, respectively. The electron transfer between the ruthenium polypyridyl photosensitizer and the Fe@FeOx water oxidation catalyst was identified to be the key step in the operation of this photoanode. The performance enhancement could be attributed to a more efficient electron transfer between the ruthenium polypyridyl photosensitizer and the Fe@FeOx water oxidation catalyst occurring thanks to the covalent bonding between these two components. The covalent grafting was found to not only improve the photocatalytic activity but also to significantly improve the stability of the system. These results offer an inspiration for the design of covalently linked nano-hybrid photoanodes in the light-driven water splitting context.

Yet, in order to have further understanding on this system it would be interesting to perform complementary experiments. For example, as charge recombination is suspected to happen between the (luminescent) ³MLCT excited state of the Ru light-harvester and the O₂ molecules

Chapter V - General conclusions and perspectives

which are generated locally at the surface of the Fe@FeO_x nanoparticles, quickly removing O₂ from the catalyst surface would thus represent a good strategy to increase the performance of the hybrid photocatalyst.

In the last part of this PhD manuscript, we describe the study of bimetallic NiFe-oxide NPs, a group of promising electrocatalysts for water oxidation reaction. NiFe NPs (≈ 4 nm) with two different compositions (Ni_{0.5}Fe_{0.5} NPs and Ni_{0.68}Fe_{0.32} NPs) were synthesized *via* an organometallic route, oxidized in air and 3-aminopropyl phosphonic acid (APA) was grafted at their surface to afford water-soluble NiFe oxide-APA NPs. Their catalytic activity in the water oxidation reaction was studied in an alkaline 1M KOH solution, and compared to the catalytic activity of NiO_x-PVP NPs, FeO_x-HDMS NPs in identical conditions. It was found that the NiFe oxide-APA NPs displayed a significantly higher catalytic activity than the NiO_x and FeO_x counterparts, suggesting a synergetic effect. The NiFe oxide-APA NPs catalyst containing 32 % of Fe (Ni_{0.68}Fe_{0.32}O_x) showed the highest activity, exhibiting a 320 mV overpotential at 10 mA/cm² (equivalent to 10% efficiency of solar-to-fuel conversion) and a Tafel slope of 62 mV/decade in 1 M KOH solution. These NiFe oxide-APA NPs catalysts also exhibited a good stability in the alkaline solution, *e.g.* maintaining an almost constant activity over 16 hours of experiment. Their high efficiency and durability make these NiFeO_x-APA NPs potentially applicable in photoelectrochemical cells for water splitting.

To better compare the intrinsic properties of the bimetallic NiFe oxide – APA NPs, determination of the TOF values based on the metal content in each sample, is now necessary. *In situ* spectroscopic measurements such as, EXAFS, FT-IR, or XPS would help understand the evolution of the catalyst in operation conditions, and especially follow the change in coordination number or oxidation state of the metal oxide.

Finally, all the conditions are now gathered to envisage the successful grafting a Ru photosensitizer on these promising NiFe oxide catalysts, which should provide an efficient catalyst for solar driven water oxidation. Especially as their small size (in comparison to the Fe@FeO_x NPs) suggest that a higher number of PS/NP could be reach.

Chapter V - General conclusions and perspectives

Table of contents – Experimental section

1. Materials	197
2. Synthesis.....	197
2.1. Synthesis of the [Ru(phen) ₂ (phen-PO(OH) ₂](Cl) ₂ complex.....	197
2.2. Synthesis of Fe nanoparticles	198
2.2.1. <i>n</i> -Fe@FeOx NPs.	198
2.2.2. <i>a</i> -Fe@FeOx NPs.....	199
2.2.3. <i>r</i> -Fe@FeOx NPs.....	199
2.2.4. Grafting of aminophosphonic acids	199
2.2.5. PS-Fe@FeOx@Ru hybrid nanomaterial.....	200
2.2.6. NiOx-PVP NPs reference sample	201
2.2.7. FeOx, 2Ni/1Fe oxide, 1Ni/1Fe oxide and 1Ni/9Fe oxide NPs	201
2.2.8. 2Ni/1Fe oxide-APA, 1Ni/1Fe oxide-APA NPs	201
3. Electrochemical measurement of <i>r</i> -Fe@FeOx NPs and <i>r</i> -Fe@FeOx@APAs NPs.....	201
4. Photoelectrochemical measurements	202
4.1 Preparation of photoanodes	202
4.2 Photocatalytic activity of as-prepared photoanodes	202
5. Electrochemical measurements for sample 2Ni/1Fe oxide-APA, 1Ni/1Fe oxide-APA, 1Ni/9Fe oxide-HMDS, FeOx-HMDS, and NiOx-PVP NPs.....	203
6. Characterization techniques	204
6.1. TEM and HR-TEM.....	204
6.2. XPS	204
6.3. ICP-OES.....	205
6.4. WAXS.....	205
6.5. EXAFS.....	205
6.6. Mössbauer spectroscopy	205
6.7. ATR-FTIR.....	206
7. General calculations.....	206
7.1. Estimation of the atomic % of Fe metal in a NP from sample <i>r</i> -Fe@FeOx NPs based on HR-TEM results	206

Experimental section

7.2. Determination of the average shell thickness of the oxide layer in a NP from <i>r</i> -Fe@FeO _x NPs based on Mossbauer data.	207
7.3 Estimation of the number of Ru complexes grafted per Fe@FeO _x NP	208
7.4. Calculation of Turnover number (TON) and Turnover frequency (TOF) of the catalyst:	211
7.4.1 Calculation the TON per PS and TOF per PS on sample <i>m</i> -Fe@FeO _x @Ru NP:	211
7.4.2. Calculation the TON per PS and TOF per PS on sample <i>b</i> -Fe@FeO _x @Ru NP:	212
8. References	213

Experimental Section

1. Materials

All chemicals used in the synthesis of the ligand and ruthenium(II) complex were purchased from commercial suppliers and used without further purification. 5-bromo-1,10-phenanthroline[1-3] and *cis*-[Ru(phen)₂Cl₂][4, 5] were synthesized as previously reported.

Concerning the NPs synthesis, [Fe[N(SiMe₃)₂]₂]₂ was purchased from Nanomeps. Hexadecylamine (HDA) (98%), oleic acid (99%), hydrogen chloride solution, 2 N in diethylether, Trimethylamine *N*-oxide (TMAO) (99%), *tert*-Butyl nitrite (90%), Tetrabutylammonium hexafluorophosphate (98%), Nafion (5% in a mixture of lower aliphatic alcohols and water), 3-aminopropyl phosphonic acid (APA), Iminodi (methylphosphonic acid) (IMPA), Aminotris(methylenephosphonic acid) (ATMPA), and Ethylenediamine tetra(methylene phosphonic acid) (EDTMPA) were purchased from Sigma-Aldrich. Hexadecylammonium chloride (HDA.HCl) was prepared according to Ref [6]. Mesitylene (99.7%, Sigma-Aldrich) was distilled over sodium under Ar prior use. Octadecene ODE (90%, Sigma-Aldrich) was dried over activated molecular sieve 0.4 nm under Ar prior use. Toluene, CH₂Cl₂ and diethyl ether were collected from a MBraun solvent purification system. Ethanol absolute grade was purchased from Sigma-Aldrich and distilled over magnesium under Ar. All the solvents were used after degassing by the freeze–pump–thaw technique. MilliQ water with conductivity at 28.2 Ω was taken directly from the machine without any treatment. FTO slides were cleaned by sonication for 30 minutes each in Acetone and EtOH then let dry at ambient temperature for at least 1 h. before use.

2. Synthesis

2.1. Synthesis of the [Ru(phen)₂(phen-PO(OH)₂](Cl)₂ complex

5-P(O)(OH)₂-1,10-phenanthroline (phen-PO(OH)₂). Under Ar atmosphere, 200 mg of the already described 5-Br-1,10-phenanthroline[2] (0.77 mmol) in toluene, 120 μL of commercially available HP(O)(OEt)₂ (0.93 mmol), 130 μL triethylamine (0.93 mmol), 13 mg Pd(OAc)₂ (0.058 mmol, 7%) and 65 mg ligand 1,1'-Bis(diphenylphosphino)ferrocene (dppf) as co-catalyst (0.12

Experimental section

mmol), were stirred at reflux overnight. The starting brownish suspension turned as an orange solution. The solvent was evaporated to yield the crude material which was purified by column chromatography on silica with a CH₂Cl₂/MeOH/NH₃,H₂O (96/2/2) mixture as eluent. The 55 mg of the desired compound (around 0.17 mmol, Yield = 22%) was obtained already partially deprotected and used as was.

[Ru(phen)₂(phen-PO(OH)₂)](Cl)₂. 20 mg of the ligand **phen-PO(OH)₂** (0.057 mmol) and 1 eq. of the precursor complex **Ru(Phen)₂Cl₂** (31.5 mg) were dissolved, under Ar, in 3 mL of degassed EtOH. The mixture was heated at reflux overnight. After evaporation of the solvent to dryness, 45 mg of an orange/red powder was obtained (Y = 10%). ¹H NMR (250.13 MHz, D₂O) δ(ppm): 9.04 (1H, d, *J* = 5 Hz), 8.48 (6H, d, *J* = 5 Hz), 8.10 (4H, s), 8.08 – 7.95 (6H, m), 7.58 – 7.45 (6H, m); ³¹P NMR (250.13 MHz, D₂O) δ(ppm): 7.13 (d, ²*J* = 40 Hz, P-OH). Anal. calcd for [Ru(Phen)₂(PhenP(O)(OH)₂)]2Cl⁻,7H₂O (Mw = 918.7g/mol) C: 47.1%, H: 4.3%, N: 9.2%; exp: C: 46.9%, H: 3.8%, N: 9.2%; ESI-HRMS, calcd for RuC₃₆H₂₄N₆O₃PRu: 721.0691 MH⁺, exp. 721.0702.

2.2. Synthesis of Fe nanoparticles

2.2.1. *n*-Fe@FeOx NPs.

Iron nanoparticles were synthesized following to a procedure reported by Gharbi, K., *et al* [7] with minor modification. [Fe[N(SiMe₃)₂]₂]₂ (1.9 g, 2.5 mmol), HDA (2.4 g, 10 mmol) and HDA·HCl (2.1 g, 7.5 mmol) were dissolved in 100 mL mesitylene in a Fisher–Porter bottle in a glove box. The dark-brown solution was then immersed in an oil bath pre-heated at 150°C and the heating was continued for 65 h. The reaction was then allowed to return to r. t. and the mesitylene was removed by evaporation under reduced pressure. The iron nanoparticles were then precipitated by the addition of 8 ml oleic acid in 100 mL of toluene. The quantity of oleic acid was added in stoichiometric proportion versus the amine groups present in the crude mixture at the end of the reaction. The particles were then collected by magnetic separation and washed with toluene (4x50 mL) then with ethanol (3x50 mL) and afterward dried under vacuum. The nanoparticles were kept inside glove-box before use (recovered mass: 304 mg, ICP-OES: Fe= 82 wt %).

2.2.2. a-Fe@FeOx NPs

Inside the glove box, *n*-Fe@FeOx NPs were spread on a Petri dish then this dish was taken out of the glove box and exposed to air. After 2 h. the powder (*a*-Fe@FeOx NPs) was collected, characterized by HR-TEM and WAXS to see the change in the morphology and crystallinity of the amorphous oxide layer.

2.2.3. r-Fe@FeOx NPs.

The Fe oxide layer was reconstructed according to Ref[8] with some minor modifications. In brief, 0.18 mmol of (CH₃)₃NO (14 mg) was dispersed in 20 mL ODE, flushed with Ar for 30 min in a Fisher-Porter bottle and heated up to 130°C for 30 min. In another Fisher-Porter bottle, 160 mg Fe nanoparticles were dispersed in 4mL ODE then this mixture was transferred onto the (CH₃)₃NO dispersion by Teflon canula avoiding air exposure and heated for 2 h. at 130°C. Then the mixture was heated up to 250°C for 30 min under Ar, cooled to r.t. and opened in air. Then 25 mL of 1-propanol was added to this mixture and the black powder was collected by using a magnet. The powder was washed with diethyl ether (1x30 mL) then dried in air. (Recovered mass: 147mg, ICP-OES: Fe= 86.95 wt.%).

2.2.4. Grafting of aminophosphonic acids

r-Fe@FeOx@APA NPs

The surface modification process followed the bi-phasic ligand exchange method which was already published by Gharbi *et al.*, [7] with minor modification. In brief, 30 mg of *r*-Fe@FeOx NPs were dispersed in 15 ml CH₂Cl₂ by sonication for 30 min. Then, to the dispersed *r*-Fe@FeOx NPs were added 10 mL of a 7×10^{-3} M solution of 3-aminopropyl phosphonic acid (pH ~7-8). The bi-phasic reaction mixture was left under mechanical stirring for 12 h. After this time, the *r*-Fe@FeOx NPs were almost fully transferred to the aqueous phase as the color of this phase was black, and the CH₂Cl₂ phase had become colorless. The NPs in the aqueous phase were then magnetically collected and washed with Milli Q water (at least 5x30 mL) in order to remove the un-grafted 3-aminopropyl phosphonic acid. Afterwards, the grafted NPs were further washed with ethanol (1x 30 mL) and diethyl ether (1x30 mL), affording the *r*-Fe@FeOx@APA NPs. Recovered mass ≈15 mg.

a-Fe@FeO_x@APANPs

The grafting of 3-aminopropyl phosphonic acid on sample *a*-Fe@FeO_x NPs was performed in an identical procedure as for synthesis of *r*-Fe@FeO_x@APA NPs. The resulting NPs are referred to as *a*-Fe@FeO_x@APA NPs.

r-Fe@FeO_x@IMPA NPs, *r*-Fe@FeO_x@ATMP NPs, and *r*-Fe@FeO_x@EDTMPA NPs

The grafting of IMPA, ATMP, and EDTMPA on *r*-Fe@FeO_x NPs followed the same protocol as describe for sample *r*-Fe@FeO_x@APA NPs. The only difference is the pH value of IMPA, ATMP, and EDTMPA solutions that was adjusted to ~9.5 by addition of NaOH 0.1 M. After mechanical stirring for 12 h, the aqueous phase was black indicating an efficient transfer of the NPs, which were then purified following the procedure described for *r*-Fe@FeO_x@APA NPs.

2.2.5. PS-Fe@FeO_x@Ru hybrid nanomaterial.

a) Biphasic method 1 (*b*-Fe@FeO_x@Ru NPs):

50 mg of Fe@FeO_x NPs were added to 15 mL of CH₂Cl₂ in a closed glass tube and sonicated for 5 min. After that the tube was opened to add 10 mL of a 2.96×10^{-4} M solution of [Ru(phen)₂(phen-PO(OH)₂)](Cl)₂·7H₂O in MilliQ water. The mixture was mechanically stirred for 3 days till the aqueous phase became completely black indicating that the transfer was efficient. The aqueous phase was then collected and purified by repeated magnetic precipitation–solvent removing–redispersion steps and washed with MilliQ water (5x30 ml) then with ethanol (1x30 mL) and diethyl ether (1x30 mL). The particles were dried in air before characterization. (Recovered mass: 39.2 mg)

b) Monophasic method 2 (*m*-Fe@FeO_x@Ru NPs):

A miscible 3:2 (v/v) mixture of THF/H₂O was used as a solvent to improve the interaction between PS and *r*-Fe@FeO_x NPs. First, 21 mg of *r*-Fe@FeO_x NPs was dispersed in 15 mL THF by using sonication for 20 min. Then 10 mL of a 2.28×10^{-4} M solution of [Ru(phen)₂(phen-PO(OH)₂)](Cl)₂·7H₂O in MilliQ water were added to the dispersion of *r*-Fe@FeO_x NPs. The reaction mixture was mechanical stirred at r. t. for 3 days. Then the *m*-Fe@FeO_x@Ru NPs were purified as described for method 1 (§ 2.2.5.a above). (Recovered mass: 17.5mg)

2.2.6. NiO_x-PVP NPs reference sample

Ni-PVP NPs prepared according to ref[9]. The Ni-PVP NPs after synthesis and purification process were obtained in the form of a fine powder which was stored in glove box. Later on, the Ni-PVP NPs were exposed to air in the solid state for 4 days in order to study their electrocatalytic activity for water oxidation reaction.

2.2.7. FeO_x, 2Ni/1Fe oxide, 1Ni/1Fe oxide and 1Ni/9Fe oxide NPs

Fe, 2Ni/1Fe, 1Ni/1Fe and 1Ni/9Fe NPs prepared by F. Robert were exposed to air in the solid state for 4 days.

2.2.8. 2Ni/1Fe oxide-APA, 1Ni/1Fe oxide-APA NPs

In a typical procedure, a dispersion of NiFe-oxide NPs (30 mg) in dichloromethane (15 mL) was added to 10 mL of a 7×10^{-3} M solution of 3-aminopropyl phosphonic acid (pH ~7-8) in a 30 mL closed glass tube. The reacting medium was mechanically stirred for 7 days. Then the aqueous phase was recovered and the NPs collected by magnet separation. The NPs were washed with MilliQ water (5x30 ml) then with ethanol (1x30 mL) and diethyl ether (1x30 mL). The particles were dried in air before characterization. (Recovered mass: ~15.5 mg).

3. Electrochemical measurement of *r*-Fe@FeO_x NPs and *r*-Fe@FeO_x@APAs NPs

The electrochemical measurements were carried out using a three-electrode cell. All the test was performed at room temperature using 0.1 M NaOH and phosphate buffer KPi 0.1M as electrolyte. A FTO electrode, Saturated calomel electrode (SCE) and Pt wire electrode, were used as the working electrode, reference electrode and counter electrode, respectively. Deposition of catalyst materials (*r*-Fe@FeO_x NPs, *r*-Fe@FeO_x@APAs NPs) on the working electrode was then accomplished by drop casting 17 μ l of catalyst ink obtained by dispersing 3 mg of catalyst in 1 mL of a 1/4 (v/v) EtOH/H₂O solvent mixture together with 1 μ l Nafion 5 wt% on FTO electrode (loading catalyst = 1.8×10^{-4} g/cm²).

4. Photoelectrochemical measurements

4.1 Preparation of photoanodes

First, catalyst inks were prepared by sonicating 3 mg of each catalyst in 1 mL of a 1/4 (v/v) EtOH/H₂O solvent mixture together with 1 μl Nafion 5 w% as a linker.

The *m*-Fe@FeOx@Ru NPs, *b*-Fe@FeOx@Ru NPs and *r*-Fe@FeOx NPs photoanodes were prepared by depositing 17 μL of the catalyst ink onto a FTO electrode (S=0.283 cm², loading density of 1.8×10^{-4} g/cm²) followed by a mild annealing process at 100 °C in an oven for 5 h. before testing their photocatalytic activity.

Preparation of non-bonded PS-r-Fe@FeOx (Fe@FeOx//Ru) photoanode for control experiment:

A 1/4 (v/v) EtOH/H₂O solvent mixture together with 1 μL Nafion 5% (w %) was used to prepare a stock solution of [Ru(phen)₃]Cl₂ with concentration 3.8×10^{-5} M. A catalyst ink was prepared by dispersion of *r*-Fe@FeOx NPs (3 mg) in 1 mL of this stock solution. Then this ink was deposited on a FTO electrode with a loading amount of 1.8×10^{-4} g/cm² followed by a mild annealing process at 100 °C for 5 h.

4.2 Photocatalytic activity of as-prepared photoanodes

The photocatalytic activity of the photoanodes was assayed by conducting photoelectrochemical measurements. A conventional three-electrode configuration with the **photoanode** (as-prepared above) as a working electrode, an Ag/AgCl/1M KCl reference electrode and a Pt wire electrode was employed. A Xe arc lamp (LOT, Germany) with the incident intensity set to 100 mW/cm² (being equivalent to the standard 1 Sun illumination) was used to simulate solar illumination. We employed the back illumination mode in which the incident light went through the transparent FTO electrode to the deposited catalyst on the photoanode. The electrolyte was 0.1 M NaOH for pH 13, and a phosphate buffer for pH 7 (KPi 7). I-V curve was recorded with potential scan rate 10 mV/s.

Experimental section

The potential values with reference to Ag/AgCl/KCl 1M were converted with reference to RHE using the following equation:

$$E_{\text{RHE}} = E_{\text{Ag/AgCl/KCl 3M}} + 0.059 \times \text{pH} + E^0_{\text{Ag/AgCl}}$$

where pH = 13 when the measurements were performed in 0.1M NaOH, or pH = 7 when the measurements were performed in phosphate buffer (KPi 7) and $E^0_{\text{Ag/AgCl}} = 0.21 \text{ V vs. RHE}$.

The current density (j , mA/cm²) was calculated by normalization to the geometric surface area of the FTO electrode ($S=0.283 \text{ cm}^2$).

5. Electrochemical measurements for sample 2Ni/1Fe oxide-APA, 1Ni/1Fe oxide-APA, 1Ni/9Fe oxide-HMDS, FeOx-HMDS, and NiOx-PVP NPs

First catalyst inks were prepared by sonicating 3 mg of each catalyst in 1 mL of a 1/4 (v/v) EtOH/H₂O solvent mixture together with 1 μl Nafion 5w% as a linker.

The **2Ni/1Fe oxide-APA**, **1Ni/1Fe oxide-APA**, **1Ni/9Fe oxide-HMDS**, **FeOx-HMDS**, and **NiOx-PVP** WOCs were prepared by depositing 17 μL of the catalyst ink onto a FTO electrode ($S = 0.196 \text{ cm}^2$, loading density of $2.6 \times 10^{-4} \text{ g/cm}^2$) followed by a mild annealing process at 100 °C in an oven for 5 h. before testing their catalytic activity for OER.

The LSV, CV, and CA experiments were performed using a PG300- potentiostat using a 3-electrode configuration. In this setup, the catalyst modified FTO electrode was used as the working electrode while a Pt rod was used as the counter electrode and a saturated calomel electrode (SCE) Hg/Hg₂Cl₂/KCl 3M was used as the reference electrode. In all experiments, 1 M KOH was used as the electrolyte solution. Argon gas was bubbled through the electrolyte at least 5 min before starting the experiment to remove oxygen from the solution.

LSV was run at a scan rate of 5 mV/s from open circuit voltage to 1.7 V vs. RHE. CV was run at a scan rate of 5 mV/s between 1.0 V and 1.7 V vs. RHE. CA was conducted for 16 h at a current density of $j = 10 \text{ mA/cm}^2$.

The potential with reference to SCE was converted into RHE using the following equation:

$E_{\text{RHE}} = E_{\text{SCE}} + 0.059 \times \text{pH} + E^{\circ}_{\text{SCE}}$, where pH was 14 as the measurements were performed in 1M KOH. E°_{SCE} was 0.24 V for the reference electrode. Calculation of the overpotential value was done by subtracting the theoretical potential for the OER 1.23 V from the measured potential vs. RHE. To calculate the current density (j , mA/cm²), the intensity of the current was normalized to the geometric surface area of the FTO electrode ($s=0.196$ cm²).

6. Characterization techniques

The nanoparticles obtained were characterized by different techniques like Fourier transform infrared spectroscopy (FT-IR) in Attenuated Total Reflection (ATR) mode, Transmission electron microscopy in conventional (TEM) or high resolution (HR-TEM) modes, Wide Angle X-Ray Scattering (WAXS), Extended X-ray absorption fine structure (EXAFS), X-ray photoelectron spectroscopy (XPS), Induced coupled plasma - Optical emission spectroscopy (ICP-OES) and Mossbauer spectroscopy.

6.1. TEM and HR-TEM

TEM and HR-TEM analysis were performed at the “Centre de Microcaractérisation Raymond Castaing”, Toulouse. The shape, size and crystallinity of the nanoparticles were examined in conventional TEM (JEOL, JEM-1011 microscope, operating at 100 kV, point resolution of 0.45 nm) and high resolution HAADF-STEM (JEM, ARM200F microscope, operating at 200 kV, point resolution of 0.19 nm). TEM grids were prepared by placing a drop of the Fe@FeO_x NPs solution onto a copper grid (400 hexagonal mesh, carbon coated). Then the TEM grids were further dried under vacuum at least one night before introduction into the microscope chamber. Size distributions were acquired by measuring a minimum 150 objects using the open source Image J software. Sizes are given as mean \pm standard deviation according to a Gaussian fit of the corresponding size distribution. FFT analysis was carried out by Digital micrograph software.

6.2. XPS

X-ray Photoelectron Spectroscopy measurement were performed at CIRIMAT, on a ThermoScientific K-Alpha with a monochromatised Al Kalpha ($h\nu = 1486.6$ eV) source. The X-

ray Spot size was 400 μm . The Pass energy was fixed at 30 eV with a step of 0.1 eV for core levels and 160 eV for surveys (step 1 eV). The spectrometer energy calibration was done using the Au $4f_{7/2}$ (83.9 ± 0.1 eV) and Ag $3d_{5/2}$ (368.2 ± 0.1 eV) photoelectron lines. XPS spectra were recorded in direct mode N (Ec) and the background signal was removed using the Shirley method. XPS High Resolution spectra were recorded in order to extract the chemical environments of the studied species.

6.3. ICP-OES

Metal contents were determined by ICP-OES performed on PerkinElmer, Optima 2100 DV. The samples first were digested into a mixture of HCl: HNO₃ (3:1 v/v) then diluted with MilliQ water.

6.4. WAXS

Wide-Angle X-ray Scattering measurements were carried out at CEMES- CNRS in Toulouse. The samples were sealed in 1.0 mm diameter Lindemann glass capillaries under Argon atmosphere. The X-ray scattering intensity measurements were performed using a dedicated two-axis diffractometer equipped with a high energy resolution solid-state detector allowing for removal of the fluorescence from iron at the measurement step by electronic filtering, using the molybdenum $K\alpha$ (0.071069 nm) radiation monochromatized by a flat graphite crystal. Time for data collection was typical 20 hours for a set of 475 measurements collected at room temperature in the range $0^\circ < \theta < 65^\circ$ for equidistant value [$s=4\pi(\sin\theta/\lambda)$]. Radial distribution functions (RDF) were obtained after Fourier transformation of the corrected and reduced data.

6.5. EXAFS

Extended X-ray Absorption Fine Structure (EXAFS) spectra were recorded at Fe K -edge (7112 eV) at r. t. in transmission mode on BL8 beamline at Synchrotron Light Research Institute (SLRI, Nakhon Ratchasima, Thailand) using a Ge (220) double-crystal monochromator. All data analysis were performed using the ATHENA and ARTEMIS softwares[10].

6.6. Mössbauer spectroscopy

The Mössbauer spectrum was obtained using a spectrometer running in the triangular symmetric mode for the velocity and a radioactive source of 1.85GBq (50mCi) Co⁵⁷ diffused into a Rh matrix.

Experimental section

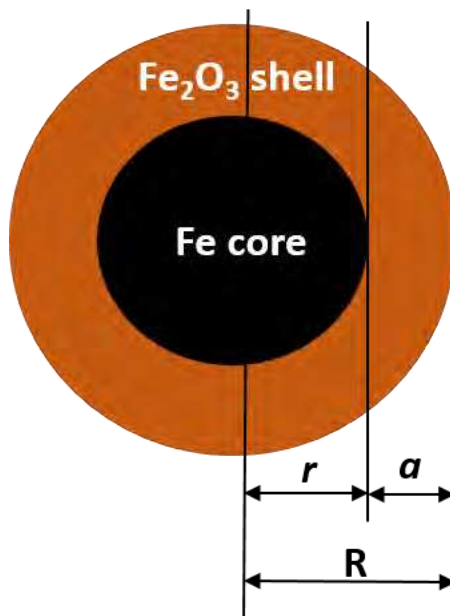
The temperature was regulated at 80K in an OXFORD Cryostat. In the figures, points represent the experimental data and continuous lines represent the curves corresponding to the 4 contributions used to fit the experimental data. The global fitting curve is also displayed as a solid line. Each contribution is defined by its isomer shift with respect to metallic iron (δ_0), quadrupolar splitting ($\Delta = \epsilon_0$), and distribution of hyperfine fields ($\mu_0 H_{hyp}$). We have considered the same width (Γ) of the Lorentzian lines for all the contributions, $\Gamma = 0.4$ mm/s. The height ratios of line -1 to line -3 h_1/h_3 and line -2 to line -3 h_2/h_3 have been fixed for the elemental sextet to the theoretical values expected for randomly oriented systems, i.e. $h_1/h_3 \approx 3$ and $h_2/h_3 \approx 2$.

6.7. ATR-FTIR

IR spectra of samples were recorded in powder form inside the glove-box by using a Bruker ALPHA spectrometer in ATR mode on a diamond crystal.

7. General calculations

7.1. Estimation of the atomic % of Fe metal in a NP from sample r -Fe@FeOx NPs based on HR-TEM results



Scheme E1. Schematic representation of an average NP from r -Fe@FeOx NPs, highlighting its characteristic dimensions

Experimental section

Supposing that a NP from sample *r*-Fe@FeOx NPs has a spherical Fe core with radius *r* and a maghemite shell thickness *a* as described in Scheme E1, the atomic percentage of Fe metal was calculated as follows:

$$\% \text{ Fe metal} = \frac{\text{number of Fe atoms in the core}}{(\text{number of Fe atoms in the core} + \text{number of Fe ions in the Fe}_2\text{O}_3 \text{ shell})} \times 100$$

Number of Fe atoms in the core:

$$N_{\text{Fe}} = \frac{d(\text{Fe}) \times V(\text{Fe core})}{M_{\text{Fe}}} \times N_A$$

Number of Fe ions in the oxide shell, considering there are two Fe(III) ions per Fe₂O₃ unit:

$$N_{\text{Fe(III)}} = \frac{2 \times d(\text{Fe}_2\text{O}_3) \times [V(\text{Fe@Fe}_2\text{O}_3 \text{ NPs}) - V(\text{Fe core})]}{M_{\text{Fe}_2\text{O}_3}} \times N_A$$

$V_{(\text{Fe core})}$: The volume of Fe metal in a core of radius *r* in cm³ = $\frac{4}{3} \times \pi \times (r)^3$ cm³

V_{NP} : The volume of the NP with radius *R* (*R* = *r* + *a*) in cm³ = $\left[\frac{4}{3} \times \pi \times (R)^3 \right]$ cm³

With *d*(Fe), the bcc-Fe density: 7.87 g.cm⁻³; *M*_{Fe}, the atomic mass of Fe : 55.845 g.mol⁻¹; *d*(Fe₂O₃): the maghemite density: 4.88 g.cm⁻³; *M*_{Fe₂O₃}, molar mass of the maghemite unit : 159.69 g.cm⁻³; *N*_A, the Avogadro number: 6.02 × 10²³ mol⁻¹.

e.g. for the nanoparticle highlighted in Figure 29d - Section 2.1.2 - Chapter II, with a core diameter of 7.4 nm (*r* = 3.7 nm) and a FeOx shell thickness *a* = 3.9 nm, the above equations lead to: % Fe metal = 23.

Note that this atomic % is underestimated as the calculation takes into account the maximum oxide shell thickness found in the NP observed in Figure 29d- Section 2.1.2- Chapter II.

7.2. Determination of the average shell thickness of the oxide layer in a NP from *r*-Fe@FeOx NPs based on Mossbauer data.

Experimental section

Mössbauer spectroscopy gives the atomic percentage of Fe in its reduced (metallic) form and oxidized forms (Fe(II) and Fe(III)). For this calculation, we will neglect the contribution of Fe(II) in the sample and consider that the ferromagnetic (FM) and superparamagnetic (SPM) oxide contributions correspond to Fe(III) ions from maghemite grains in the shell of the NPs.

$$\% \text{ Fe} = 28.9 \pm 0.5\%$$

$$\% \text{ Fe(III) shell} = 69.1 \pm 0.5\%$$

which corresponds to the respective weight percentages: 22.6 w% for Fe and 77.4 w% for maghemite

$$V \text{ Fe core: volume of the Fe metal core in nm}^3 = \frac{4}{3} \times \pi \times (R - a)^3 \text{ nm}^3$$

$$V \text{ NP: volume of the NP in nm}^3 = \left[\frac{4}{3} \times \pi \times R^3 \right] \text{ nm}^3$$

$$V \text{ Fe}_2\text{O}_3 \text{ shell} = V \text{ (NP)} - V \text{ (Fe core)} = \left[\frac{4}{3} \times \pi \times (R)^3 - \frac{4}{3} \times \pi \times (R - a)^3 \right] \text{ nm}^3$$

w% Fe metal core =

$$\frac{\text{mass of Fe core}}{(\text{mass of Fe core} + \text{mass of Fe}_2\text{O}_3 \text{ shell})} \times 100 = \frac{d(\text{Fe}) \times V(\text{Fe core})}{d(\text{Fe}) \times V(\text{Fe core}) + d(\text{Fe}_2\text{O}_3) \times V(\text{Fe}_2\text{O}_3 \text{ shell})} \times 100$$

$$= \frac{d(\text{Fe}) \times \frac{4}{3} \times \pi \times (R - a)^3}{d(\text{Fe}) \times \frac{4}{3} \times \pi \times (R - a)^3 + d(\text{Fe}_2\text{O}_3) \times \left[\frac{4}{3} \times \pi \times (R)^3 - \frac{4}{3} \times \pi \times (R - a)^3 \right]} \times 100 = 22.6\%$$

Taking into account the average size of the NP determined by TEM as in Figure 26 - Section 2.1.2 - Chapter II) (diameter 11.5 nm, i.e. R = 5.75 nm), and the values given above for the density of bcc-Fe and maghemite (§7.1), solving the third degree equation leads to an average shell thickness of 2.6 nm.

7.3 Estimation of the number of Ru complexes grafted per Fe@FeOx NP

The number of Ru complexes per NP was determined based on ICP-OES analysis which gives access to the Ru:Fe ratio and supposing that the number of Fe per NP doesn't change during the grafting process *i.e.* it is identical for *m*-Fe@FeOx@Ru, *b*-Fe@FeOx@Ru and *r*-Fe@FeOx NPs.

Experimental section

It was thus calculated taking into account the average size and shell thickness determined for the ***r*-Fe@FeO_x NPs**.

Supposing that a NP from sample ***r*-Fe@FeO_x NPs** has a spherical Fe core with radius *r* and a maghemite shell thickness *a* as described in Scheme E1,

Total number of Fe atoms in one ***r*-Fe@FeO_x NP** = Number of Fe atoms in the core + Number of Fe atoms in the shell

Number of Fe atoms in the core:

$$N_{Fe} = \frac{d(Fe) \times V(Fe \text{ core})}{M_{Fe}} \times N_A = \frac{d(Fe) \times \frac{4}{3} \times \pi \times (r)^3}{M_{Fe}}$$

Number of Fe ions in the oxide shell, considering there are two Fe(III) ions per Fe₂O₃ unit:

$$N_{Fe(III)} = \frac{2 \times d(Fe_2O_3) \times [V(Fe@Fe_2O_3 \text{ NPs}) - V(Fe \text{ core})]}{M_{Fe_2O_3}} \times N_A$$

$V_{(Fe \text{ core})}$: The volume of Fe metal in a core of radius *r* in cm³ = $\frac{4}{3} \times \pi \times (r)^3$ cm³

V_{NP} : The volume of the NP with radius *R* (*R* = *r* + *a*) in cm³ = $\left[\frac{4}{3} \times \pi \times (R)^3 \right]$ cm³

With *d*(Fe), the bcc-Fe density: 7.87 g.cm⁻³; *M*_{Fe}, the atomic mass of Fe : 55.845 g.mol⁻¹; *d*(Fe₂O₃): the maghemite density: 4.88 g.cm⁻³; *M*_{Fe₂O₃}, molar mass of the maghemite unit : 159.69 g.cm⁻³; *N*_A, the Avogadro number: 6.02 × 10²³ mol⁻¹.

Thus for ***r*-Fe@FeO_x NPs** with an average size 11.5 nm (*R*_{NPs}=5.75 nm, *r*_{core}=3.15 nm) and a FeO_x shell thickness *a* = 2.6 nm, the above equations lead to a **total number of Fe atoms in one NPs = 58x10³ atoms**

***e.g.*, case of the monophasic process:**

Estimation of the number of Ru complexes grafted per *m*-Fe@FeO_x@Ru NP:

Table E1. ICP-OES results for *m-Fe@FeOx@Ru* NPs

Sample	Mass (mg)	Fe percentage (wt. %)	Ru percentage (wt. %)
<i>m-Fe@FeOx@Ru</i> NPs	8.3	73.76	0.13

The number of Fe atoms in 8.3 mg m-Fe@FeOx@Ru NP:

$$\frac{m(\text{Fe}) \text{ in sample}}{M(\text{Fe})} \times N_A = \frac{(8.3 \times 10^{-3} \times 73.76)}{100} \times \frac{1}{55.8} \times (6.02 \times 10^{23}) = 6.60 \times 10^{19} \text{ atoms}$$

Number of NPs in 8.3 mg m-Fe@FeOx@Ru NP:

$$\text{Number of NPs} = \frac{\text{Number of Fe atoms in } m\text{-Fe@FeOx@Ru NPs}}{\text{Number of Fe atoms in one NP}} = \frac{6.60 \times 10^{19}}{58 \times 10^3} = 1.14 \times 10^{15} \text{ NPs}$$

The number of Ru complex in 8.3 mg m-Fe@FeOx@Ru NP, supposing Ru is only present as a complex in the nanomaterial:

$$\text{Number of Ru complexes} = \text{Number of mole of Ru complex} \times N_A = \frac{m(\text{Ru}) \text{ in sample}}{M(\text{Ru})} \times N_A$$

molecules

$$\text{Number of Ru complexes} = \frac{(8.3 \times 10^{-3} \times 0.13)}{100} \times \frac{1}{101.0} \times (6.02 \times 10^{23}) = 6.43 \times 10^{16} \text{ molecules}$$

Where: N_A : The Avogadro number $6.02 \times 10^{23} \text{ mol}^{-1}$

$M(\text{Ru})$: The atomic weight of Ruthenium 101.0 g.mol^{-1}

The number of Ru complexes per *m*-Fe@FeO_x@Ru NP:

$$\text{Number of Ru complexes per NP} = \frac{\text{Number of Ru complexes in sample}}{\text{Number of NPs in sample}} = \frac{6.43 \times 10^{16}}{1.14 \times 10^{15}} \approx 56$$

There are **56 Ru complexes** grafted per nanoparticle by the **monophasic method** (method 2).

A similar calculation leads to a value of **9 Ru complexes** grafted per nanoparticle according to the **biphasic method** (method 1).

7.4. Calculation of Turnover number (TON) and Turnover frequency (TOF) of the catalyst:

The turnover number (TON) per photosensitizer PS (number of O₂ molecules obtained per PS) was obtained by dividing the number of moles of O₂ obtained during the photocatalytic experiments by the total number of moles of PS anchored.

$$\text{TON} = \frac{\text{Number of mole of Oxygen obtained}}{\text{Number of mole of PS anchored}}$$

Calculation of turnover frequency of the catalyst (TOF):

The turnover frequency per PS is obtained by dividing the TON per PS by the time (in seconds) at which the catalysis has reached a plateau.

$$\text{TOF} = \frac{\text{TON}}{\text{Time (s)}}$$

7.4.1 Calculation the TON per PS and TOF per PS on sample *m*-Fe@FeO_x@Ru NP:

Calculate the number of mole of Oxygen obtained:

$$\begin{aligned} \text{Number of mole of Oxygen obtained} &= \frac{\text{Number of coulombs of electricity flowed}}{4 \times F} = \frac{J \times A \times \text{time (s)}}{4 \times F} \\ &= \frac{20 \times 10^{-6} \times 0.283 \times 30}{4 \times 9.65 \times 10^4} = 4.39 \times 10^{-10} \text{ mole Oxygen} \end{aligned}$$

Where J is a current density at a given potential (1.0 V vs. RHE), A is the surface area of the catalyst deposited on the FTO electrode, F is Faraday constant (a value of 9.65×10^4 C.mol⁻¹)

The number of mole of PS anchored:

Experimental section

Calculate for 1.8×10^{-4} g/cm² catalyst loading density on FTO electrode

$$\text{Number of mole of PS anchored} = \frac{\text{Catalyst loading density} \times A \times \text{ICP}(\% \text{wt. Ru})}{100 \times M(\text{Ru})}$$

$$= \frac{1.8 \times 10^{-4} \times 0.283 \times 0.13}{100 \times 101.0} = 6.55 \times 10^{-10} \text{ mole PS}$$

$$\text{TON of catalyst per PS} = \frac{4.39 \times 10^{-10}}{6.55 \times 10^{-10}} = 0.67$$

$$\text{TOF of the catalyst per PS} = \frac{\text{TON}}{\text{Time (s)}} = \frac{0.67}{30} = 0.02. \text{s}^{-1}$$

7.4.2. Calculation the TON per PS and TOF per PS on sample *b*-Fe@FeO_x@Ru NP:

Calculate the number of mole of Oxygen obtained:

$$\text{Number of mole of Oxygen obtained} = \frac{\text{Number of coulombs of electricity flowed}}{4 \times F} = \frac{J \times A \times \text{time (s)}}{4 \times F}$$

$$= \frac{3 \times 10^{-6} \times 0.283 \times 30}{4 \times 9.65 \times 10^4} = 6.59 \times 10^{-11} \text{ mole Oxygen}$$

Where J is a current density at a given potential (1.0 V vs. RHE), A is the surface area of the catalyst deposited on the FTO electrode, F is Faraday constant (a value of 9.65×10^4 C.mol⁻¹)

The number of mole of PS anchored:

Calculate for 1.8×10^{-4} g/cm² catalyst loading density on FTO electrode

$$\text{Number of mole of PS anchored} = \frac{\text{Catalyst loading density} \times A \times \text{ICP}(\% \text{wt. Ru})}{100 \times M(\text{Ru})}$$

$$= \frac{1.8 \times 10^{-4} \times 0.283 \times 0.03}{100 \times 101.0} = 1.51 \times 10^{-10} \text{ mole PS}$$

$$\text{TON of catalyst per PS} = \frac{6.59 \times 10^{-11}}{1.51 \times 10^{-10}} = 0.44$$

$$\text{TOF of the catalyst per PS} = \frac{\text{TON}}{\text{Time (s)}} = \frac{0.44}{30} = 0.015. \text{s}^{-1}$$

8. References

1. Hissler, M., et al., *Platinum Diimine Bis(acetylide) Complexes: Synthesis, Characterization, and Luminescence Properties*. Inorganic Chemistry, 2000. 39(3): p. 447-457.
2. Girardot, C., et al., *Novel ruthenium(ii) and zinc(ii) complexes for two-photon absorption related applications*. Dalton Transactions, 2007(31): p. 3421-3426.
3. Girardot, C., et al., *Novel 5-(oligofluorenyl)-1,10-phenanthroline type ligands: synthesis, linear and two-photon absorption properties*. Tetrahedron Letters, 2008. 49(11): p. 1753-1758.
4. Giordano, P.J., C.R. Bock, and M.S. Wrighton, *Excited state proton transfer of ruthenium(II) complexes of 4,7-dihydroxy-1,10-phenanthroline. Increased acidity in the excited state*. Journal of the American Chemical Society, 1978. 100(22): p. 6960-6965.
5. Hackett, J.W. and C. Turro, *Luminescent Ru(phen)_n(bps)_{3-n} Complexes (n = 0–3) as Probes of Electrostatic and Hydrophobic Interactions with Micellar Media*. Inorganic Chemistry, 1998. 37(8): p. 2039-2046.
6. Meffre, A., et al., *Use of long chain amine as a reducing agent for the synthesis of high quality monodisperse iron(0) nanoparticles*. Journal of Materials Chemistry, 2011. 21(35): p. 13464-13469.
7. Gharbi, K., et al., *Alkyl phosphonic acid-based ligands as tools for converting hydrophobic iron nanoparticles into water soluble iron–iron oxide core–shell nanoparticles*. New Journal of Chemistry, 2017. 41(20): p. 11898-11905.
8. Peng, S., et al., *Synthesis and Stabilization of Monodisperse Fe Nanoparticles*. Journal of the American Chemical Society, 2006. 128(33): p. 10676-10677.
9. Zaramello, L., et al., *Kinetic investigation into the chemoselective hydrogenation of α,β -unsaturated carbonyl compounds catalyzed by Ni(0) nanoparticles*. Dalton Transactions, 2017. 46(15): p. 5082-5090.
10. Ravel, B. and M. Newville, *ATHENA, ARTEMIS, HEPHAESTUS: data analysis for X-ray absorption spectroscopy using IFEFFIT*. Journal of Synchrotron Radiation, 2005. 12(4): p. 537-541.

Experimental section

Introduction générale

Cette thèse de doctorat a été soutenue par une bourse d'excellence délivrée par le gouvernement français. Elle a été co-supervisée par le Professeur Dr Catherine Amiens du Laboratoire de Chimie de Coordination (LCC-CNRS, Toulouse, France) et le Professeur Dr Phong Tran Dinh de l'Université des Sciences et Technologies de Hanoi (USTH, Hanoi, Viet Nam). Le travail expérimental a été mené dans trois laboratoires : au LCC où les nanocatalyseurs métal/oxyde métallique ont été développés, au CECS (Laboratory of Chemistry for Energy Conversion and Storage, à Hanoi) pour l'évaluation de l'activité électro et photocatalytique des nanomatériaux, et à l'ICMR (Institut de Chimie Moléculaire de Reims) pour la synthèse des photosensibilisateurs à base de Ru en collaboration avec le Pr. Gilles Lemercier et le Dr Elodie Rousset. Ce travail a également bénéficié de collaborations avec le Dr. Pierre Lecante et le Pr. Marc Respaud (CEMES, Toulouse) pour l'étude des propriétés structurales et magnétiques des nanomatériaux, respectivement, et du Dr. Jérôme Esvan (CIRIMAT, Toulouse) pour l'étude de leurs propriétés électroniques.

L'objectif était d'étudier le potentiel de nanomatériaux abondants et bon marché pour le développement de nouvelles photoélectrodes qui pourraient être utilisées dans les cellules photoélectrochimiques, en se concentrant sur la demi-réaction d'oxydation de l'eau, plus difficile à réaliser. Pour ce faire, nous avons envisagé le greffage covalent d'un absorbeur moléculaire, à base de complexe de Ru, sur des catalyseurs nanostructurés métal/oxyde métallique de métaux bon marché et abondants tels que des nanoparticules cœur@coquille, Fe@FeOx, ou des nanoparticules d'oxyde mixte NiFeOx.

En effet, de nos jours et comme décrit au **chapitre I**, avec l'augmentation de la population, de l'urbanisation et du niveau de vie, la demande en énergie augmente rapidement. Cependant, en raison de cette croissance de la consommation d'énergie, et comme 85 % de l'énergie consommée provient de combustibles fossiles, nous sommes maintenant confrontés à des problèmes

environnementaux et sanitaires de plus en plus graves. Par conséquent, le remplacement des combustibles fossiles par une source d'énergie propre et renouvelable est aujourd'hui l'un des défis les plus urgents pour l'humanité. Dans ce contexte, il est prévu que l'hydrogène joue un rôle important dans le développement d'une énergie durable et d'un environnement préservé. La dissociation de l'eau étant l'une des méthodes les plus connues pour la production massive d'hydrogène, ceux des procédés faisant appel à l'énergie solaire représentent des solutions technologiques prometteuses aux problèmes de consommation d'énergie, et d'environnement, auxquels nous sommes actuellement confrontés. Cependant, le processus de dissociation de l'eau est non seulement énergétiquement défavorable, mais également lent; il nécessite donc à la fois de l'énergie et un catalyseur pour être efficace. Ce processus peut être réalisé dans une cellule photoélectrochimique qui imite le procédé de la photosynthèse naturelle. Cependant, le coût des catalyseurs développés jusqu'à présent est trop élevé pour permettre la mise en œuvre à grande échelle de cette technologie. Il est donc nécessaire de développer des catalyseurs à bas coût constitués de matériaux abondants et peu toxiques.

Au **chapitre II**, nous avons étudié la synthèse et la fonctionnalisation de nanoparticules cœur-coquille Fe-oxide de fer (Fe@FeOx NPs) avec différents acides aminophosphoniques et évalué ces nouveaux nanomatériaux pour la catalyse de l'oxydation de l'eau. Ainsi :

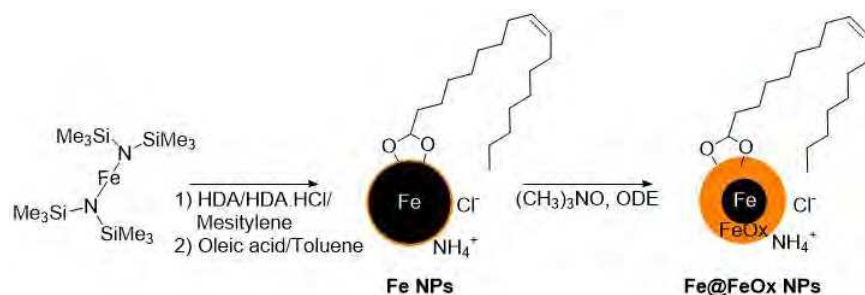


Schéma 1. Voie de synthèse des nanoparticules cœur-coquille de Fe@FeOx (r-Fe@FeOx NPs).

1) les nanoparticules cœur-coquille Fe@FeOx ont été synthétisées en utilisant une procédure en deux étapes (Schéma 1). La première étape a consisté en la préparation de nanoparticules de fer bcc (Fe NPs) comme rapporté par K. Gharbi *et al.* [1]. Ensuite, suite à une étude précédente de notre groupe où il a été démontré que l'efficacité du greffage d'un groupe phosphonique augmentait avec la cristallinité de la couche d'oxyde de fer de surface [1, 2], une oxydation contrôlée de ces

nanoparticules natives a été réalisée afin de générer une coquille d'oxyde de fer adaptée au greffage ultérieur des différents acides aminophosphoniques via le groupement phosphonate. La méthode rapportée par Peng *et al.* [3] a permis d'obtenir une couche d'oxyde de fer cristalline conduisant à un échantillon ci-après dénommé *r*-Fe@FeOx NPs (*r* signifiant reconstruit). L'analyse par TEM (microscopie électronique à transmission) a montré que les nanoparticules présentaient une taille moyenne de $11,5 \pm 2,3$ nm. Les principales caractéristiques observées par TEM haute résolution (HR-TEM) étaient (i) une coquille discontinue de contraste plus clair (Figure 2a), (ii) des nanoparticules avec une morphologie "en fleur" et une coquille d'épaisseur irrégulière (Figures 2b et c), et (iii) des grains cristallins d'oxyde de fer bien définis dont l'épaisseur maximale a été estimée à 3,9 nm (Figure 2d).

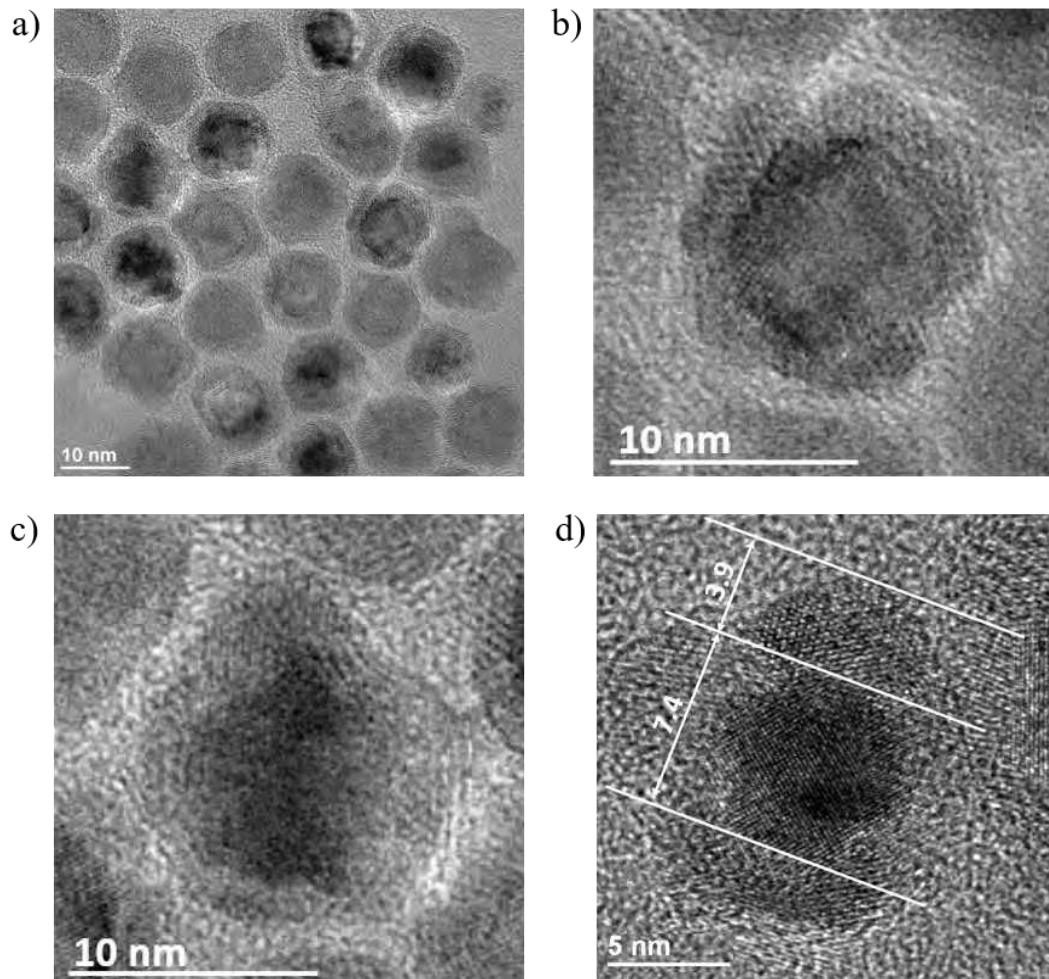


Figure 2. Images HR-TEM typiques des nanoparticules de *r*-Fe@FeOx NPs.

Des mesures XPS (X-Ray photoelectron spectroscopy) et WAXS (Wide-Angle X-ray Scattering) effectuées sur un échantillon de poudre, et ont confirmé la persistance d'un cœur de Fe cc, la cristallinité de la couche d'oxyde de fer et indiqué que celle-ci était très probablement constituée de α - ou γ -Fe₂O₃, même si la présence d'espèces FeOOH sur la surface ne pouvait être exclue. Une évaluation quantitative du rapport Fe/FeOx dans les nanoparticules et l'identification de l'oxyde formé ont été obtenues par spectroscopie Mössbauer (Figure 2, Tableau 1). La mesure a été effectuée à 80 K avec une source de ⁵⁷Co dans une matrice de Rh et a été calibrée par rapport au Fe massif (cc). À cette température, et compte tenu de la taille des nanoparticules, les phénomènes de relaxation à l'échelle de temps de la spectroscopie Mössbauer (10⁻¹¹ - 10⁻⁹ s) devaient initialement être négligeables. Compte tenu de la morphologie des nanoparticules, les lignes définies observées sur le spectre pouvaient être attribuées aux contributions des phases ferromagnétiques du Fe cc (FM Fe, 28,9 ± 0,5%) et de l'oxyde de fer (FM Fe oxyde, 42,9 ± 0,5%). Cependant, pour ajuster précisément la courbe expérimentale, deux autres contributions ont dû être introduites : une première correspondant à l'oxyde de fer en régime superparamagnétique (SPM Fe oxide, 26,2 ± 0,5%), et une seconde correspondant à une trace de fer paramagnétique (PM Fe, 2,0 ± 0,2%).

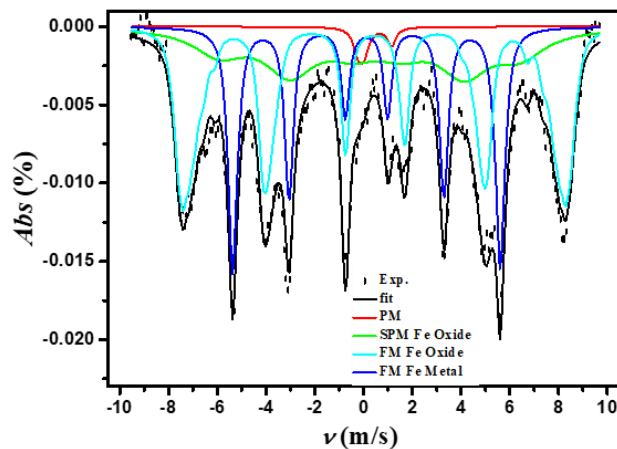


Figure 2. Spectre Mössbauer de *r*-Fe@FeOx NPs enregistré à 80K (données expérimentales en diamants), et meilleur ajustement obtenu (ligne continue) à partir d'une combinaison des contributions du fer et de l'oxyde de fer (voir la légende de la figure)

Tableau 1. Distributions des déplacements isomériques et des champs hyperfins utilisés pour ajuster le spectre Mössbauer expérimental mesuré à 80 K.

Contribution	Déplacement isomérique (mm.s ⁻¹)	Eclatement quadrupolaire (mm.s ⁻¹)	Champ hyperfin (T)	Poids de la contribution au fit
FM Fe	0.11	-	33	28.9±0.5
FM Fe oxide	0.46	-0.03	Distribution centre autour de (Figure. 3)	42.9±0.5
SPM Fe oxide	0.40	-0.3	38.5	26.2±0.5
PM Fe ²⁺	0.45	1.4	-	2.0±0.2

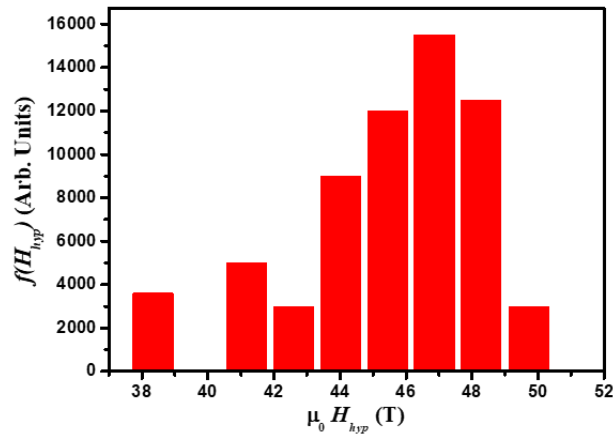


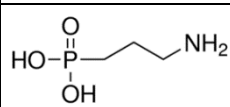
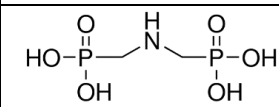
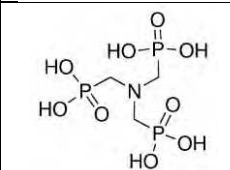
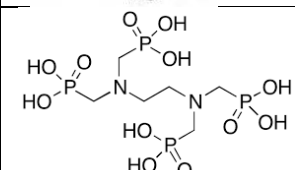
Figure 3. Distribution des champs hyperfins utilisée pour ajuster la contribution de l'oxyde de Fe FM au spectre Mössbauer des *r*-Fe@FeOx NPs.

Le tableau 1 et la Figure 3 présentent les champs hyperfins, l'éclatement quadrupolaire et les déplacements isomériques utilisés pour ajuster le spectre. Les paramètres utilisés pour ajuster les contributions de l'oxyde de fer sont en bon accord avec ceux attendus pour γ -Fe₂O₃ à l'échelle nanométrique [4]. Les deux contributions observées (l'une FM et l'autre SPM) pourraient refléter l'hétérogénéité de l'épaisseur de l'enveloppe d'oxyde de fer et sa polycristallinité.

Le rapport atomique Fe(0)/Fe(III) extrait de l'ajustement du spectre Mössbauer a indiqué une épaisseur de coquille moyenne de 2,6 nm. Ainsi, les *r*-Fe@FeOx NPs peuvent être décrites comme des nanoparticules de Fe@ γ -Fe₂O₃ cœur/coquille avec une taille moyenne de $11,5 \pm 2,3$ nm et une épaisseur moyenne de coquille de 2,6 nm.

2) Ces nanoparticules ont été exposées à différents acides amino-phosphoniques présentant différents nombres de groupes phosphoniques dans leur structure chimique (Tableau 2) afin d'obtenir des catalyseurs d'oxydation solubles dans l'eau.

Tableau 2. Acides aminophosphoniques utilisés dans cette étude

No.	Nom chimique	Acronyme	Structure chimique	pKa
1	3-aminopropyl phosphonic acids	APA		pKa ₁ = 2.1, pKa ₂ = 6.4, pKa ₃ = 10.5
2	Iminodi (methylphosphonic acid)	IMPA		valeurs non répertoriées
3	Aminotris(methylenephosphonic acid)	ATMPA		pKa ₁ <2, pKa ₂ <2, pKa ₃ = 4.30, pKa ₄ = 5.4, pKa ₅ = 6.6, pKa ₆ = 12.3
4	Ethylenediamine tetra (methylene phosphonic acid)	EDTMPA		pKa ₄ = 1.16, pKa ₅ = 2.80, pKa ₆ = 5.00, pKa ₇ = 6.24, pKa ₈ = 7.72, pKa ₉ =9.64

Pour EDTMPA : les pKa₁, pKa₂ et pKa₃ n'ont pas pu être mesurés dans l'eau car ils sont trop faibles et le pKa₁₀ n'a pas pu être mesuré car il est trop élevé [5].

Un procédé biphasique a été utilisé suivant les travaux antérieurs réalisés par K. Gharbi *et al.* dans notre groupe [1]. En bref, il consiste à mélanger une phase organique contenant les NPs (ici le dichlorométhane a été utilisé comme solvant) et une phase aqueuse contenant l'APA à un pH compris entre 7 et 8. Les Figure 4 et 5 montrent le succès du transfert des *r*-Fe@FeOx NPs de la phase CH₂Cl₂ à la phase aqueuse par ce procédé, conduisant à des dispersions aqueuses stables pendant une très longue période. Les NPs, après le processus de greffage, sont appelées ci-après *r*-Fe@FeOx@APA NPs, *r*-Fe@FeOx@IMPA NPs, *r*-Fe@FeOx@ATMPA NPs et *r*-Fe@FeOx@EDTMPA NPs.

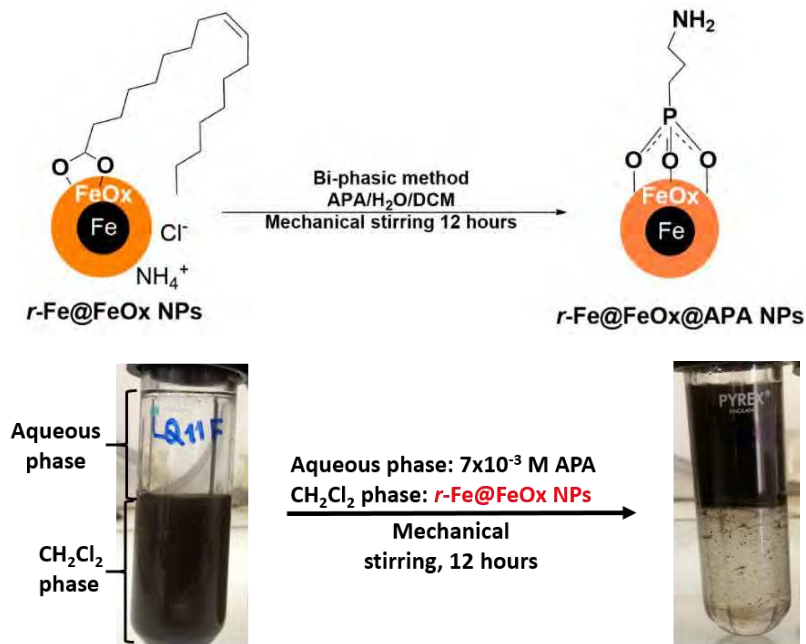


Figure 4. Voie de synthèse (en haut) et photographie du milieu réactionnel lors du greffage de l'APA aux $r\text{-Fe@FeOx}$ NPs par une méthode biphasique ($\text{CH}_2\text{Cl}_2/\text{eau MilliQ}$) (en bas).

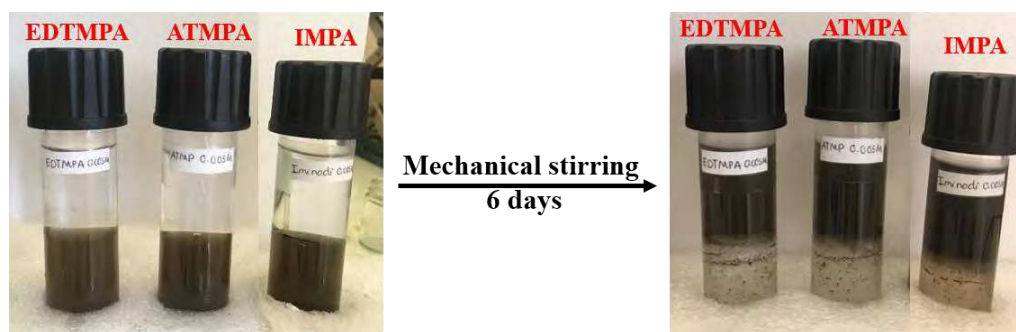


Figure 5. Photographie du milieu réactionnel lors du greffage de l'EDTMPA, de l'ATMPA, de l'IMPA sur les $r\text{-Fe@FeOx}$ NPs par une méthode biphasique ($\text{CH}_2\text{Cl}_2/\text{eau MilliQ}$).

La performance électrocatalytique des $r\text{-Fe@FeOx}$ NPs pour la réaction d'oxydation de l'eau (OER) a été étudiée à pH 7 (tampon phosphate 0,1M KPi) et dans un électrolyte alcalin à pH 13 (0,1 M NaOH). Une encre catalytique composée de $r\text{-Fe@FeOx}$ NPs dispersées dans un mélange de solvant EtOH/eau avec 1 μl de Nafion 5% (w%) comme liant a été déposée sur une électrode d'oxyde d'étain dopé au fluor (FTO) à une densité de chargement en masse de 1.8×10^{-4} g/cm² (Figure 6). Le comportement de l'électrode catalytique résultante a ensuite été analysée par

voltampérométrie à balayage linéaire à une vitesse de balayage du potentiel de 5mV/s à pH 7 et pH 13. À pH 13, l'amorçage de la réaction a été observé à $\sim 1,75$ V par rapport à l'ENH et une pente de Tafel de 142 mV/décade a pu être déduite des données (Figure 7, trace noire). À pH 7, l'amorçage de la réaction a été observé à un potentiel beaucoup plus élevé de $\sim 1,95$ V et la pente de Tafel était également plus élevée: 207 mV/décade (Figure 7, trace rouge). Ce test a démontré que l'échantillon $r\text{-Fe@FeOx}$ NPs est un catalyseur actif pour le OER, et qu'il est significativement plus actif en solution alcaline.



Figure 6. Dépôt de $r\text{-Fe@FeOx}$ NPs sur une électrode FTO pour tester son activité catalytique en oxydation de l'eau à pH 7 et pH 13.

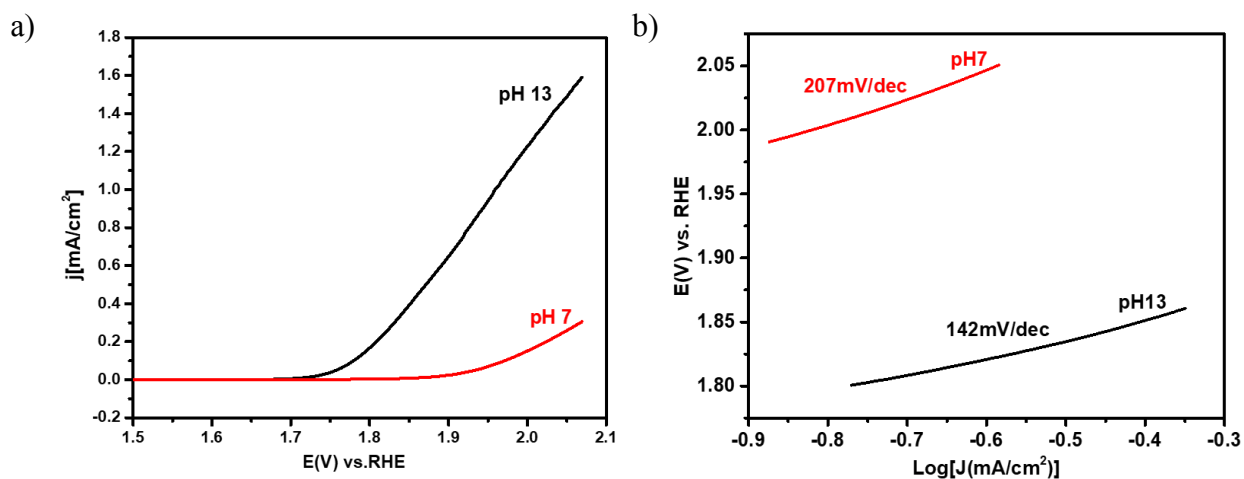


Figure 7. a) Courbes de polarisation d'une électrode $r\text{-Fe@FeOx}$ NPs enregistrées dans des solutions électrolytiques de pH 7 (ligne rouge) et pH 13 (ligne noire), à une vitesse de balayage du potentiel de 5 mV/s. b) Droites de Tafel de l'électrode $r\text{-Fe@FeOx}$ NPs à pH 7 (ligne rouge) et pH 13 (ligne noire).

Par manque de temps, nous n'avons pas pu étudier l'activité électrocatalytique de tous les échantillons préparés, et seules les NPs fonctionnalisées par APA et EDTMPA ont été étudiées. L'activité électrocatalytique des $r\text{-Fe@FeOx@APA}$ NPs et $r\text{-Fe@FeOx@EDTMPA}$ NPs est comparée à celle des $r\text{-Fe@FeOx}$ NPs natives Figure 8. Le greffage de l'APA a manifestement

amélioré l'activité catalytique des $r\text{-Fe@FeOx}$ NPs, car le potentiel d'amorçage de la réaction est passé de 1,75 V à 1,62 V par rapport à l'ENH. La pente de la droite de Tafel est fortement diminuée de 142 mV/décade pour les $r\text{-Fe@FeOx}$ NPs natives à 30 mV/décade pour les $r\text{-Fe@FeOx@APA}$ NPs. Parallèlement, le greffage d'EDTMPA sur les NPs de $r\text{-Fe@FeOx}$ n'a pas montré de changement significatif en termes de courant catalytique et de pente de Tafel.

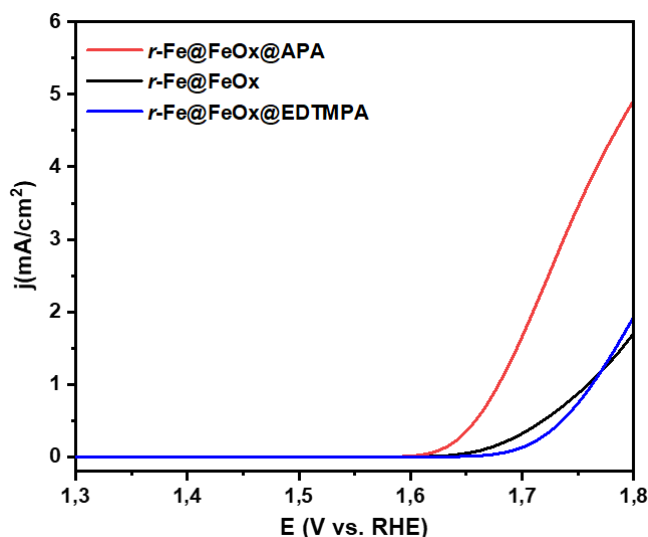


Figure 8. Courbes de polarisation des électrodes $r\text{-Fe@FeOx}$ NPs (trace noire), $r\text{-Fe@FeOx@APA}$ NPs (trace rouge) et $r\text{-Fe@FeOx@EDTMPA}$ NPs (trace bleue) enregistrées dans des solutions électrolytiques de pH 13, à une vitesse de balayage du potentiel de 5 mV/s.

Forts de ces résultats, nous avons envisagé de coupler ce catalyseur à un photosensibilisateur par une liaison covalente pour obtenir un nanocatalyseur hybride qui pourrait être intégré comme photoanode dans une cellule photoélectrochimique, comme décrit au **chapitre III**.

Premièrement, une stratégie de synthèse a été développée pour préparer le ligand 1,10-phénanthroline phosphonate et le complexe de ruthénium(II) bis-hétéroleptique correspondant appelé $[\text{Ru-PO}(\text{OH})_2]\text{Cl}_2 \cdot 7\text{H}_2\text{O}$ à partir du précurseur $[\text{Ru}(\text{phen})_2\text{Cl}_2]$ comme le montre le schéma 2.

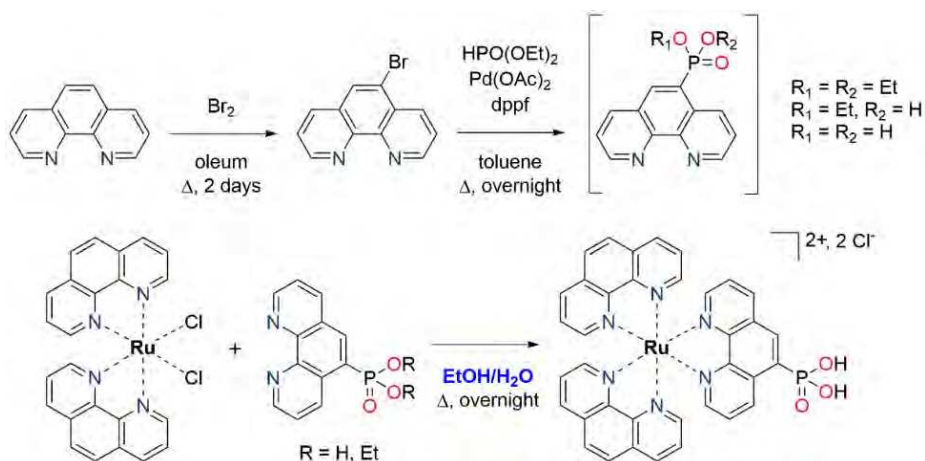


Schéma 2. Voies de synthèse du ligand 1,10-phen-PO(OH)₂ (procédure en 2 étapes) et de son complexe [Ru-PO(OH)₂]Cl₂.7H₂O.

L'étude des propriétés photophysiques de ce composé a montré que le complexe [Ru-PO(OH)₂]²⁺ présente les caractéristiques requises pour être utilisé comme photosensibilisateur approprié car il absorbe dans le domaine visible et est émissif par son état excité ³MLCT. En d'autres termes, la présence du groupe acide phosphonique ne semble pas affecter les propriétés photophysiques de l'archétype [Ru(phen)₃]²⁺ qui peut donc être utilisé comme référence dans les études de photo-électrocatalyse présentées ici, et le complexe [Ru-PO(OH)₂]²⁺ est pleinement qualifié pour être utilisé comme capteur de lumière afin de construire un photocatalyseur hybride pour la séparation solaire de l'eau en lumière visible.

Les deux voies de greffage décrites au chapitre II, ont été testées pour greffer le complexe [Ru-PO(OH)₂]Cl₂ sur les Fe@FeOx NPs (Schéma 3). Dans un premier temps, la méthode biphasique a été suivie. Cependant, elle n'a permis d'obtenir qu'une faible densité de greffage du complexe Ru sur la surface de l'oxyde de fer (9 complexes Ru par nanoparticule, échantillon appelé ci-après *b*-Fe@FeOx@Ru NPs, *b* signifiant biphasique). Ensuite, la méthode monophasique a été mise en œuvre dans laquelle les Fe@FeOx NPs et le [Ru-PO(OH)₂]Cl₂ ont été ajoutés à une phase homogène THF-eau. L'échantillon résultant présente une bien meilleure densité de greffage du complexe Ru sur la surface de l'oxyde de fer (56 complexes Ru par NP, échantillon ci-après dénommé *m*-Fe@FeOx@Ru NPs, *m* signifiant monophasique).

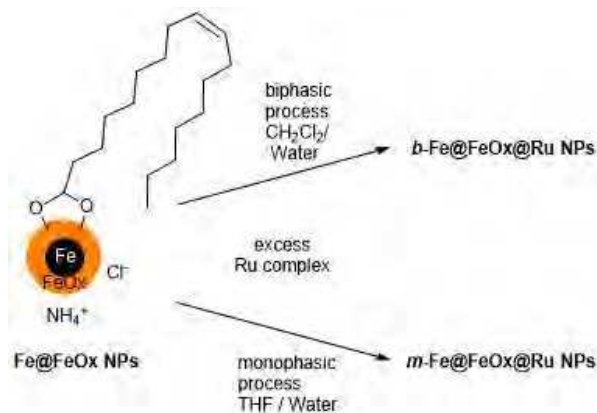


Schéma 3. Voies de synthèse pour les photocatalyseurs hybrides préparés dans un milieu biphasique (*b-Fe@FeOx@Ru* NPs) ou dans un milieu monophasique (*m-Fe@FeOx@Ru* NPs).

Nous avons ensuite étudié l'activité photocatalytique des nanomatériaux hybrides (*m/b*)-*Fe@FeOx@Ru* NPs pour comprendre dans quelle mesure un lien covalent entre le capteur de lumière moléculaire et le nanocatalyseur peut être bénéfique à son fonctionnement global, en solution alcaline. À cette fin, une encre a été préparée à partir des échantillons de (*m/b*)-*Fe@FeOx@Ru* NPs et déposée sur une électrode FTO comme décrit pour les *r-Fe@FeOx* NPs (chapitre II). La source de lumière était fournie par une lampe à arc Xe équipée d'un filtre UV. Nous avons utilisé le mode rétro-éclairage dans lequel la lumière incidente traversait l'électrode FTO transparente pour atteindre le catalyseur. L'intensité de la lumière incidente atteignant l'électrode FTO a été fixée à 100 mW/cm². Afin de souligner l'avantage d'un greffage covalent entre le capteur de lumière et le catalyseur, nous avons également enregistré l'activité photocatalytique d'un simple mélange de NPs de *r-Fe@FeOx* et de chlorure de ruthénium tris-phénanthroline, [Ru(phen)₃]Cl₂, dans le même rapport Ru par NP (c'est-à-dire 56) que dans l'échantillon de NPs de *m-Fe@FeOx@Ru*, appelé ci-après *r-Fe@FeOx//Ru*. Le [Ru(phen)₃]Cl₂ a été choisi comme photosensibilisateur de référence en raison de ses propriétés photophysiques comparables à celles du [Ru-PO(OH)₂]Cl₂. Une électrode de contrôle a également été fabriquée en chargeant uniquement des nanoparticules *r-Fe@FeOx* à une densité de chargement identique, sans ajouter de complexe Ru. La figure 9a montre les courbes I-t enregistrées à 1,0 V/ENH avec des électrodes composées de *m-Fe@FeOx@Ru* NPs (trace rouge), *r-Fe@FeOx//Ru* (trace bleue)

et $r\text{-Fe@FeOx}$ NPs (trace noire). La photoanode $r\text{-Fe@FeOx}$ NPs a généré une densité de photocourant négligeable d'environ $0,5 \mu\text{A}/\text{cm}^2$.

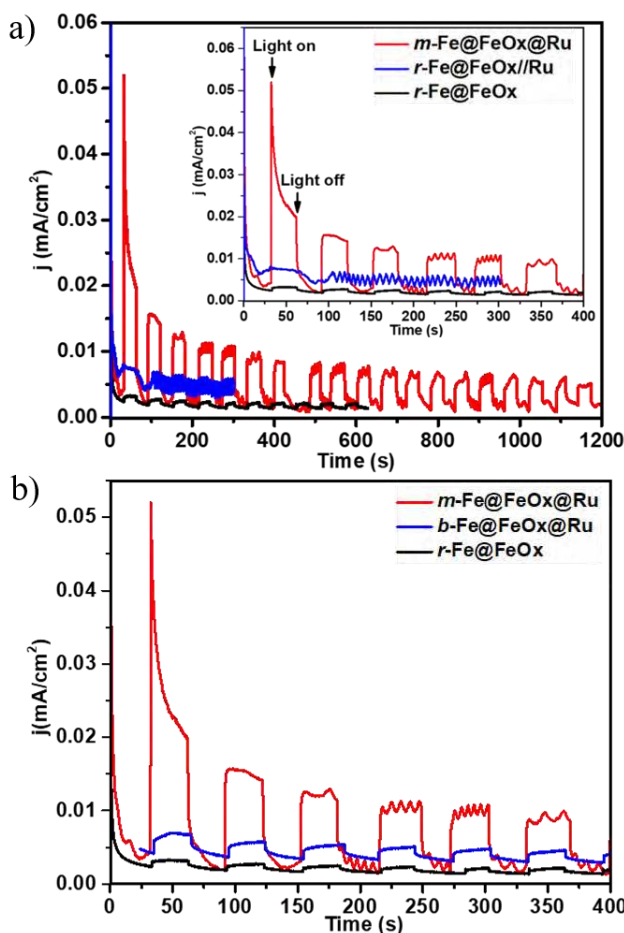


Figure 9. (a) Courbes I - t enregistrées sur des photoanodes $m\text{-Fe@FeOx@Ru}$ NPs (trace rouge), $r\text{-Fe@FeOx//Ru}$ (trace bleue) et $r\text{-Fe@FeOx}$ NPs (trace noire) ; (b) Courbes I - t enregistrées sur des photoanodes $m\text{-Fe@FeOx@Ru}$ NPs (trace rouge), $b\text{-Fe@FeOx@Ru}$ NPs (trace bleue) et $r\text{-Fe@FeOx}$ (trace noire). Potentiel appliqué : $1.0 \text{ V}/\text{ENH}$. Electrolyte : solution NaOH à $\text{pH } 13$. Puissance lumineuse incidente : $100 \text{ mW}/\text{cm}^2$.

Le mélange $r\text{-Fe@FeOx//Ru}$ a montré une densité de photocourant plus élevée ($2,3 \mu\text{A}/\text{cm}^2$), ce qui démontre l'amélioration de la collecte de la lumière apportée par le complexe Ru. De manière intéressante, une densité de photocourant significativement plus élevée d'environ $20 \mu\text{A}/\text{cm}^2$ a été obtenue pour l'électrode $m\text{-Fe@FeOx@Ru}$ NPs (où le complexe Ru est greffé de manière covalente sur le nanocatalyseur $r\text{-Fe@FeOx}$). Cette valeur correspond à des activités environ 9

fois et 40 fois plus élevées que celles obtenues avec les électrodes $r\text{-Fe@FeOx//Ru}$ et $r\text{-Fe@FeOx}$, respectivement. Ce résultat a clairement démontré l'utilité d'un greffage covalent entre l'absorbant de lumière Ru et le catalyseur Fe@FeOx pour promouvoir le transfert de charge et donc augmenter l'activité photocatalytique globale. Ce résultat est en parfaite adéquation avec les quelques études précédentes où un greffage covalent entre les photo-récupérateurs et les catalyseurs d'oxydation de l'eau s'est avéré plus efficace en comparaison avec un simple mélange des deux [6, 7].

En répétant les cycles d'illumination on-off, la photoanode $m\text{-Fe@FeOx@Ru}$ NPs s'est avérée produire encore 50% de la densité de photocourant initiale (déterminée dans le premier cycle on-off) après 20 minutes de test, tandis que le mélange $r\text{-Fe@FeOx//Ru}$ (non lié) n'a plus généré de photocourant notable à partir du deuxième cycle on-off. Cette dégradation peut être attribuée à un détachement rapide du complexe $[\text{Ru}(\text{phen})_3]\text{Cl}_2$ de la surface de l'électrode en raison de l'absence de liaison covalente et de la grande solubilité de ce complexe dans l'eau. Ainsi, le greffage covalent améliore également la stabilité du système hybride $m\text{-Fe@FeOx@Ru}$ NPs.

Comme décrit ci-dessus, les NPs de $b\text{-Fe@FeOx@Ru}$ avaient une densité de greffage de complexes de Ru beaucoup plus faible que les NPs de $m\text{-Fe@FeOx@Ru}$, soit 9 complexes de Ru contre 56 complexes de Ru par nanoparticule. À densité de chargement identique, la photoanode $b\text{-Fe@FeOx@Ru}$ NPs a montré une densité de photocourant 7 fois plus faible que la photoanode $m\text{-Fe@FeOx@Ru}$ NPs (Figure 9b, traces rouges et bleues). Cependant, des performances photocatalytiques comparables ont été déduites pour ces deux photoanodes en normalisant l'activité catalytique par nombre de photosensibilisateur (PS), c'est-à-dire par nombre de complexe de Ru greffé, confirmant ainsi que l'étape limitante implique le complexe de Ru. Des fréquences de rotation par complexe de Ru (TOF_{Ru}) de $0,015 \text{ s}^{-1}$ et $0,02 \text{ s}^{-1}$ ont été calculées pour les photoanodes préparées avec $b\text{-Fe@FeOx@Ru}$ NPs et $m\text{-Fe@FeOx@Ru}$ NPs, respectivement, ce qui représente la meilleure valeur de TOF rapportée jusqu'à présent en comparaison avec les données de la littérature publiées pour des systèmes comparables (voir Tableau 3). Une densité plus élevée d'absorbant de lumière de Ru augmenterait la performance globale du système.

Table 3. Summary of the representative photocatalytic activity toward OER using hybrid photoanodes based on a molecular dye covalently grafted on a MOx catalyst.

No.	Substrate /PS/ WOC	PS:WOC ratio	Electrolyte	V _{onset} (V vs. RHE)	Photocurrent/testing conditions	TON	TOF	Ref
1	[Ru(bipy) ₂ (bipy(COO) ₂)]/ [Mn ₄ O ₄ ((MeOPh) ₂ PO ₂) ₆]	4.5:1	Na ₂ SO ₄ 0.1M, pH 6.5	-	-	-	0.013 O ₂ .cluster ⁻¹ .s ⁻¹	[8]
2	[Ru(bpy)(4,4'-(PO ₃ H ₂) ₂ bpy) ₂](Cl) ₂ / Co ₃ O ₄	0.15:1	Na ₂ SiF ₆ -NaHCO ₃ (0.02-0.04 M, pH 5.6)	-	-	2.53	0.001 O ₂ .PS ⁻¹ .s ⁻¹	[7]
3	TiO ₂ /[Ru(bpy) ₃] ²⁺ modified malonate ligand/IrO ₂ .nH ₂ O	-	Na ₂ SiF ₆ -NaHCO ₃ 0.02M pH 5.75	-	12.7 μA/cm ² , at 0 V vs. Ag/AgCl/KCl, Under 450 nm light (7.8mW/cm ²)	-	-	[9]
4	ITO/PMPDI/CoOx	-	0.1 M pH 7 KPi	-	150 μA/cm ² , at 1 V vs. Ag/AgCl, simulated sunlight (100 mW/cm ²)	-	-	[10]
5	FTO/[Ru(phen)₂(phen-PO(OH)₂)](Cl)₂/ r-Fe@FeOx = m-Fe@FeOx@Ru NP	85:1	0.1M NaOH pH13	0.75	20 μA/cm² At 1 V vs. RHE 1 Sun illumination (100 mW/cm²)	0.67	0.02 O₂.PS⁻¹.s⁻¹	This work

conséquent, afin d'étudier l'activité catalytique de ces NPs d'oxyde de NiFe pour la réaction d'oxydation de l'eau, un échange de ligand a été nécessaire afin de conférer un revêtement hydrophile aux NPs. Leur transfert de la phase organique à la phase aqueuse a été réalisé en échangeant l'HDA et le HMDS contre de l'acide 3-aminopropyl phosphonique (APA) en adaptant un procédé déjà publié par notre groupe [1] et appliqué aux NPs de Fe@FeOx (Figure 10). Les NPs obtenues seront appelées ci-après NPs d'oxyde de 1Ni/1Fe-APA et NPs d'oxyde de 2Ni/1Fe-APA. L'étude par spectroscopie IR et XPS a montré que ces NPs étaient bien décrites par un noyau de Ni entouré d'une couche de surface mixte Ni(OH)₂/Fe₂O₃, dans laquelle le rapport Ni/Fe varie en fonction de la composition des NPs NiFe initiales, et portant des ligands APA à la surface, comme le montre le schéma 6.

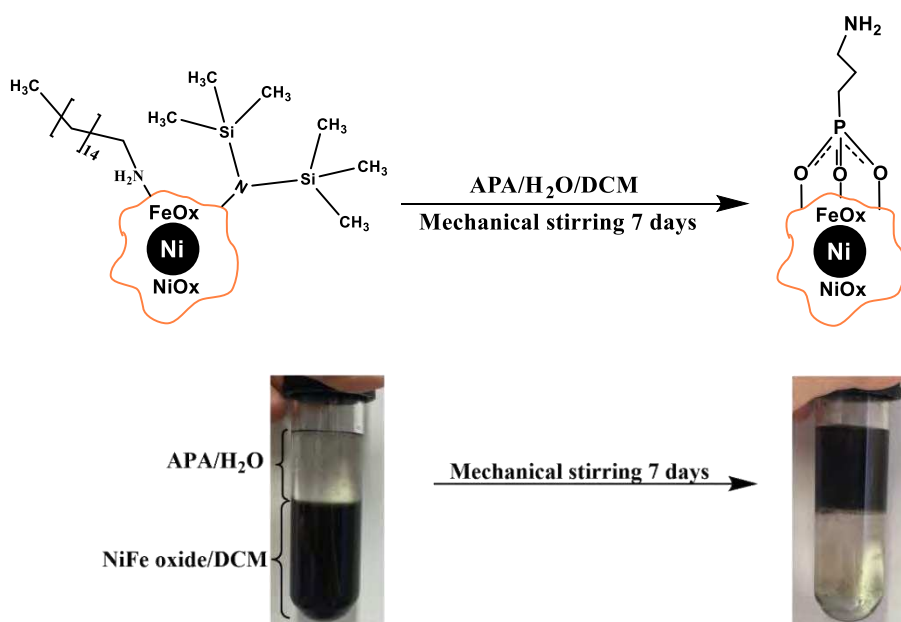


Figure 10. Voie de synthèse (en haut) et photographie du processus d'échange de ligands (en bas).

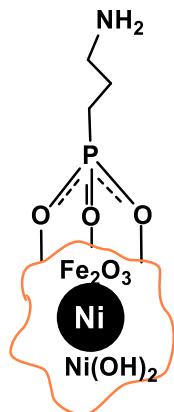


Schéma 6. Représentation provisoire des échantillons de NPs 1Ni1Fe-APA et 2Ni1Fe-APA.

2) A des fins de comparaison, des échantillons de référence de NiOx-PVP NPs, FeOx-HMDS et 1Ni/9Fe oxide-HMDS NPs ont été préparés en suivant les voies de synthèse décrites dans le schéma 7.

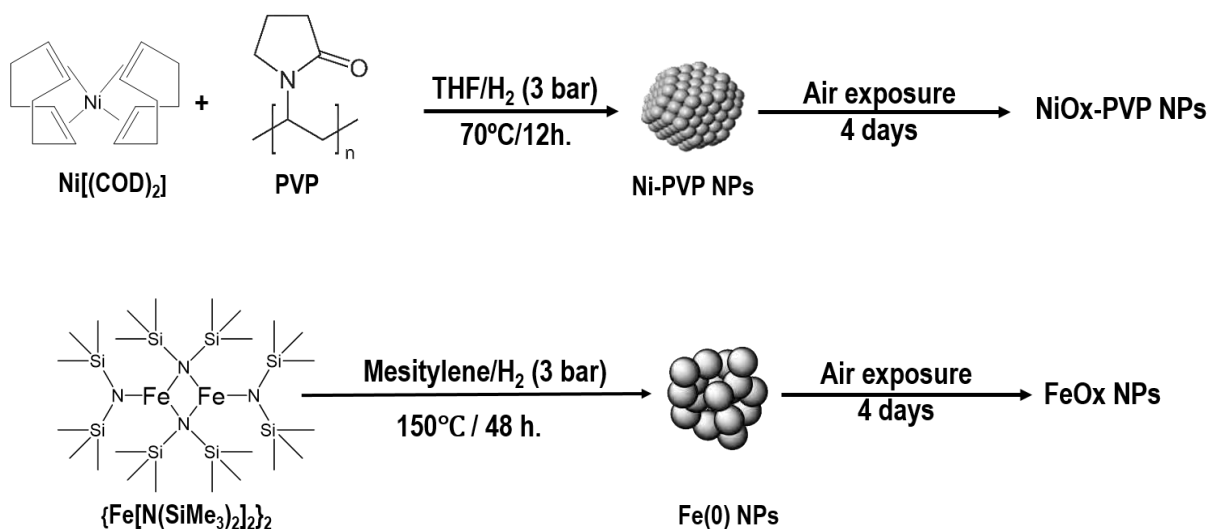


Schéma 7. Voie de synthèse des échantillons de référence d'oxyde de Ni (en haut) et de Fe (en bas).

Tout d'abord, les NPs de Ni[11] et de Fe[12] ont été synthétisées selon les procédures décrites dans les publications précédentes de notre groupe. Brièvement, les NPs de Ni ont été obtenues par hydrogénation du complexe organométallique de biscyclooctadiène nickel(0) dans du THF à 70°C pendant 12 h. en présence de polyvinylpyrrolidone (PVP) comme stabilisateur conduisant à un

nanomatériau avec une charge de Ni de 9,0 % en poids selon les données ICP-OES. Les NP de Fe ont été synthétisées par hydrogénation du complexe de di-bis(bis(triméthylsilylamido)fer (II), $[\text{Fe}(\text{N}(\text{SiMe}_3)_2)_2]_2$, dans du mésitylène à 150°C pendant 48h. Les NPs de Fe ainsi obtenues sont stabilisées par l'hexaméthylidisilazane (HMDS) qui se forme *in situ*. L'introduction de 10 at.%Ni dans les NPs de Fe décrites ci-dessus a été réalisée en utilisant le ratio correspondant des précurseurs Ni et Fe, et la voie de synthèse utilisée pour préparer les FeNPs de référence (schéma 6, bas). Comme pour les NPs de Fe, le nanomatériau final était constitué de NPs stabilisées par l'HMDS formé *in situ*. Grâce à leur enrobage de PVP, les NPs NiOx-PVP de référence ont été facilement dispersées dans l'eau. De même, une dispersion satisfaisante a pu être obtenue avec les NPs d'oxyde de FeOx et de 1Ni/9Fe enrobées de HMDS, très probablement en raison de la grande quantité de ligand formant des multicouches exposant finalement la fonction amine de l'HMDS.

3) les propriétés catalytiques de ces NPS pour la réaction d'oxydation de l'eau ont été testées dans une solution électrolytique alcaline en utilisant une configuration standard à trois électrodes. Le catalyseur a été dispersé dans l'eau en présence de nafion et déposé sur une électrode de FTO avec une charge de $2,6 \times 10^{-4}$ g/cm². L'activité electrocatalytique a été évaluée par voltampérométrie à balayage linéaire (LSV) à 5 mV/s. L'activité de 2Ni/1Fe oxyde-APA NPs a été comparée avec celles de 1Ni/1Fe oxyde-APA NPs, 1Ni/9Fe oxyde-HMDS NPs, NiOx-PVP NPs et FeOx-HMDS NPs étudiées dans des conditions similaires (Figure 11a). Parmi tous les échantillons, les NPs d'oxyde de 2Ni/1Fe-APA ont montré la meilleure activité catalytique. Pour atteindre une densité de courant catalytique (*j*) de 10 mA/cm², ces 2Ni/1Fe NPs ont nécessité 320 mV, soit respectivement 40, 130 et 250 mV de moins que les échantillons 1Ni/1Fe oxide-APA NPs, 1Ni/9Fe oxide-HMDS et FeOx-HMDS NPs. La surtension à *j* = 10 mA/cm² pour l'échantillon NiOx-PVP NPs n'a pas pu être enregistrée en raison du détachement rapide des NPs pendant les mesures LSV. Ces résultats montrent que les NPs NiFeOx ont une activité catalytique plus élevée que les FeOx et NiOx purs, indiquant une synergie entre le Ni et le Fe. L'activité catalytique des NiFOx NPs ayant un noyau de Ni et une enveloppe de Ni(OH)₂/Fe₂O₃ varie en fonction de leur composition chimique : le système avec la plus haute teneur en Ni montre le plus haut courant catalytique (vitesse) à un potentiel appliqué donné.

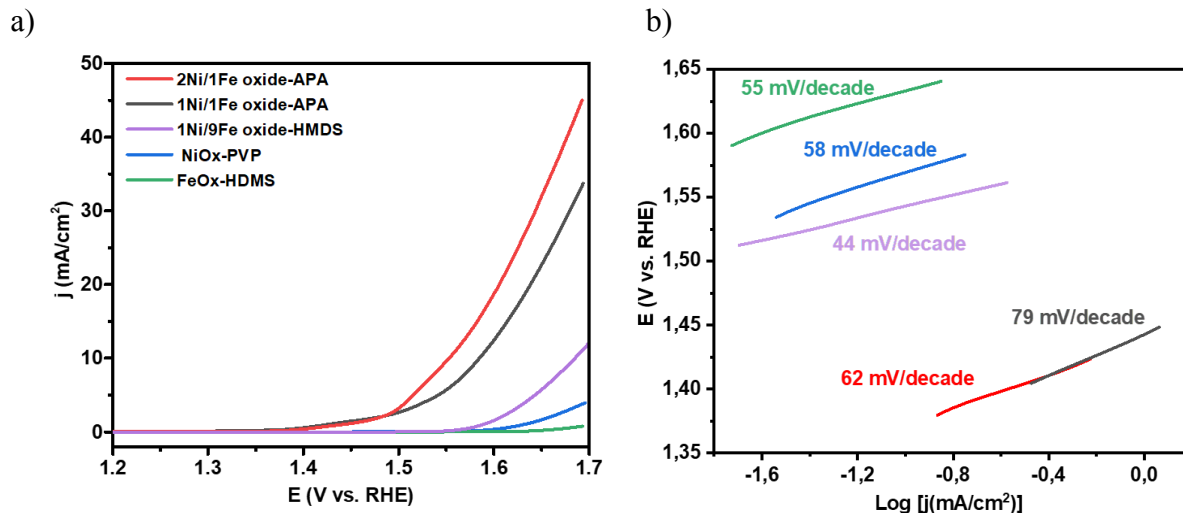


Figure 11. a) Courbes LSV et b) tracés de Tafel correspondants pour 2Ni/1Fe oxyde-APA NPs (ligne rouge), 1Ni/1Fe oxyde-APA NPs (ligne noire), 1Ni/9Fe oxyde-HMDS NPs (ligne violette), NiOx-PVP NPs (ligne bleue) et FeOx-HMDS NPs (ligne verte) dans KOH 1M, vitesse de balayage 5mV/s.

Pour obtenir plus d'informations sur la cinétique de réaction, les courbes de Tafel ont été tracées et analysées (Figure 11b). Les pentes de Tafel des NPs d'oxyde de 2Ni/1Fe-APA, des NPs d'oxyde de 1Ni/1Fe-APA, des NPs d'oxyde de 1Ni/9Fe-HMDS, des NPs de NiOx-PVP et des NPs de FeOx-HMDS étaient respectivement de 62, 79, 44, 58 et 55 mV/décade. Le tableau 4 présente les valeurs des surtensions à $j=10 \text{ mA/cm}^2$ et les pentes de Tafel pour tous les échantillons étudiés à des fins de comparaison.

Tableau 4. Valeurs de surtension à 10 mA/cm^2 , pentes de Tafel correspondantes et positions des pics redox observés en voltamétrie cyclique pour tous les échantillons étudiés.

	2Ni/1Fe oxyde - APA NPs	1Ni/1Fe oxyde - APA NPs	1Ni/9Fe oxyde - APA NPs	FeOx NPs	NiOx NPs
η_{10} (mA/cm ²)	320	360	450	570	—
Pente de Tafel (mV/décade)	62	79	44	55	58
Pic de réduction (V/ENH)	+1.35 + 1.24	+1.38	+1.37	—	+1.38
Pic d'oxydation (V/ENH)	+1.45	+1.45	—	—	+1.48

Ces résultats sont en accord avec ceux publiés par Ma *et al.* qui ont étudié l'influence du ratio Ni:Fe dans l'hydroxyde double lamellaire (LDH) Ni-Fe sur son activité catalytique en solution alcaline et ont également observé que les nano-feuillets de composition $\text{Ni}_{2/3}\text{Fe}_{1/3}$ étaient les catalyseurs d'oxydation de l'eau les plus efficaces dans KOH 1M que ceux de composition $\text{Ni}_{3/4}\text{Fe}_{1/4}$ et $\text{Ni}_{4/5}\text{Fe}_{1/5}$ [13].

Pour mieux évaluer l'activité électrocatalytique des NPs d'oxyde de NiFe-APA, la détermination de la valeur du TOF aurait été intéressante. Cependant, en raison de la quantité limitée de matériau préparé, nous n'avons pas pu déterminer la teneur réelle en métal dans chaque échantillon.

La stabilité et la durabilité des catalyseurs 2Ni/1Fe oxyde-APA, 1Ni/1Fe oxyde-APA, 1Ni/9Fe oxyde-HMDS et FeOx-HMDS NPs ont été évaluées en effectuant des mesures chronoampérométriques (CA) à une densité de courant de $j=10 \text{ mA/cm}^2$ dans KOH 1M. L'échantillon NiOx-PVP s'est avéré être le moins stable, et de loin, puisqu'il s'est facilement détaché de l'électrode pendant la réaction. Comme le montre la Figure 12a, l'activité électrocatalytique des NPs d'oxyde de 2Ni/1Fe-APA, d'oxyde de 1Ni/1Fe-APA, et d'oxyde de 1Ni/9Fe-HMDS est stable sur 16 h de mesure. Ceci est donc indépendant du revêtement de surface (APA ou HMDS). Au contraire, l'échantillon de NPs FeOx-HMDS a d'abord montré une dégradation rapide de son activité qui est ensuite restée stable à $\sim 5 \text{ mA/cm}^2$. Ce résultat exprime à nouveau la synergie entre le Ni et le Fe dans les NPs bimétalliques. Les mesures de LSV enregistrées pour les NPs d'oxyde 2Ni/1Fe - APA après les expériences chronoampérométriques ont montré que l'échantillon présentait presque la même activité qu'auparavant (Figure 12b). La même observation a été faite pour les échantillons 1Ni/1Fe oxyde-APA, et 1Ni/9Fe oxyde-HMDS NPs. La seule différence notable était une augmentation de l'intensité du pic de pré-oxydation après les expériences chronoampérométriques.

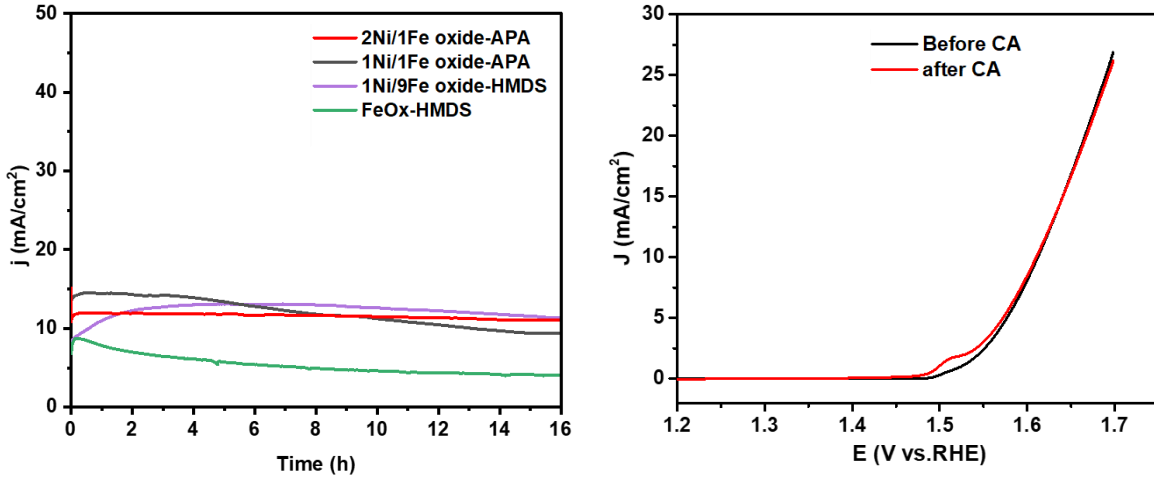


Figure 12. a) Évaluation de l'AC de 2Ni/1Fe oxide-APA NPs (ligne rouge), 1Ni/1Fe oxide-APA NPs (ligne noire), 1Ni/9Fe oxide-HMDS NPs (ligne violette), et FeOx-HMDS NPs (ligne verte) à $j=10$ mA/cm² dans KOH 1M; b) Courbes LSV de l'échantillon 2Ni/1Fe oxide-APA NPs avant et après l'essai AC.

Les NPs d'oxyde de 2Ni/1Fe-APA sont beaucoup plus stables que les NPs d'oxyde de NiFe amorphes de taille similaire (~ 4nm) incorporées dans du noir de carbone (stabilité à $j=10$ mA/cm² pendant 16h. pour nos systèmes par rapport à seulement 6h. [14], dans des conditions identiques). La stabilité des NPs d'oxyde de 2Ni/1Fe-APA peut également être comparée à celle de nanocatalyseurs de taille plus importante (~19.8 nm) mais d'état de surface comparable de Manso *et al.* [15] ; ces NPs avec un coeur NiOx et une enveloppe mixte NiOx/FeOx ont montré une stabilité pendant 2 h. à $j=10$ mA/cm² dans du KOH 1M (conditions identiques aux nôtres). La comparaison avec les données de la littérature souligne donc la bonne stabilité des nouveaux nanocatalyseurs NiFe rapportés ici, et l'intérêt de combiner à la fois une taille réduite et une surface mixte Ni(OH)₂/Fe₂O₃.

Les voltamogrammes cycliques (CV) ont été enregistrés dès que les échantillons ont atteint l'état d'équilibre pendant les mesures LSV (c'est-à-dire que des courbes I-V stables ont été obtenues). Des CV représentatifs pour les NiOx-PVP NPs et les FeOx-HMDS NPs sont présentés Figure 13 et 14, respectivement. La Figure 13 montre une série de 50 CV collectés pour les NiOx NPs. Avant l'apparition de O₂ (à un potentiel de départ de 1,53 V/ENH), un événement redox quasi-réversible a été observé (pic de potentiel d'oxydation à 1,48 V et pic de réduction à 1,38 V/ENH) qui a été attribué au couple Ni³⁺/Ni²⁺. Aucun changement évident dans le comportement électrochimique

de l'électrode n'est apparu lors de la répétition du balayage du potentiel, à l'exception d'une légère diminution du courant catalytique, qui peut être due au détachement des NiOx-PVP NPs en solution alcaline car la matrice PVP est très soluble dans l'eau. Une transition de phase des oxydes vers les phases hydroxydes et oxyhydroxydes est souvent observée dans les catalyseurs lors de l'oxydation électrocatalytique de l'eau [16, 17]. La modification des catalyseurs NiOx lors des études CV a donc été attribuée à la formation *in situ* d'espèces d'hydroxydes/oxyhydroxydes Ni(OH)₂/NiOOH pendant le processus de conditionnement électrochimique (schéma 8) en conditions alcalines. L'observation de la vague d'oxydation de Ni²⁺ à 1,48 V/ENH est donc attribuée à la réaction d'oxydoréduction réversible Ni(OH)₂/NiOOH, comme cela a déjà été signalé dans la littérature [18-21].



Schéma 8. Oxydation de Ni(OH)₂ en NiOOH en solution alcaline.

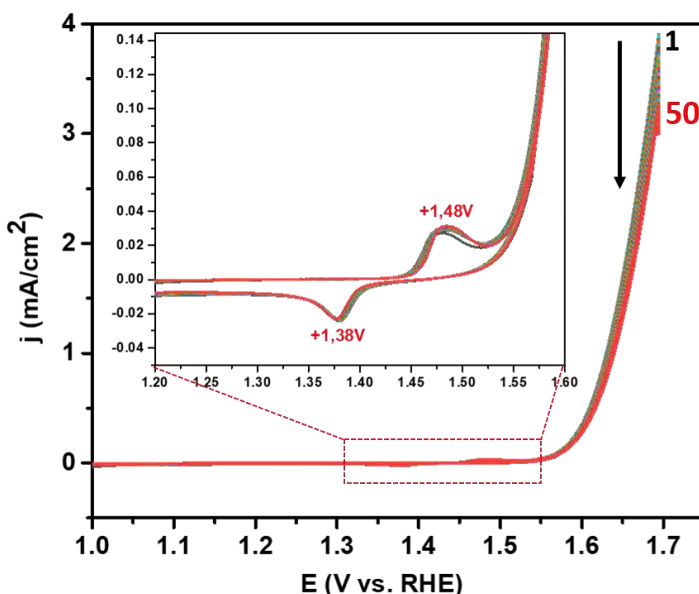


Figure 13. Voltammogrammes cycliques (CVs) pour les NiOx-PVP NPs dans un électrolyte KOH 1M.

Flèche noire soulignant la diminution de l'activité catalytique lors de balayages consécutifs.

Dans un essai parallèle utilisant le catalyseur FeOx-HMDS, aucun événement redox précatalytique n'a été observé. L'activité catalytique a été significativement dégradée lors de la

répétition du cycle de potentiel (Figure 14). Cela indique un détachement rapide du catalyseur FeOx-HMDS NP de la surface de l'électrode.

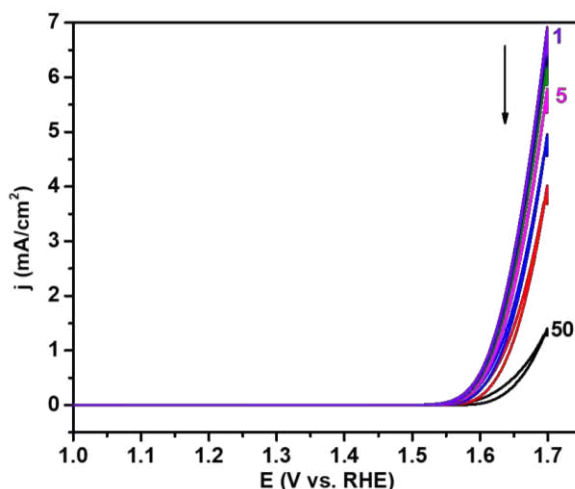


Figure 14. Superposition de 50 voltammogrammes cycliques (CV) pour des NPs FeOx-HMDS dans un électrolyte KOH 1M. Flèche noire soulignant la diminution de l'activité catalytique lors de balayages successifs.

Une étude similaire a été réalisée pour les électrocatalyseurs à oxyde mixte de NiFe. Une superposition des 50 premiers CV est présentée dans la Figure 15a, b, c, pour les NPs 2Ni/1Fe oxide-APA, 1Ni/1Fe oxide-APA, et 1Ni/9Fe oxide-HMDS respectivement. Les CV sont caractérisés par: le OER (déjà étudié par LSV) et le couple redox Ni(OH)₂/NiOOH. Concernant ce dernier, un pic de pré-oxydation à environ + 1,45 V (2Ni/1Fe oxyde-APA), et +1,53 V (1Ni/1Fe oxyde-APA) est observé, mais un tel pic est presque négligeable pour l'échantillon 1Ni/9Fe oxyde-APA NPs. Néanmoins, les CV des trois échantillons montrent clairement un pic de réduction à +1,35 V (2Ni/1Fe oxide-APA), +1,38 V (1Ni/1Fe oxide-APA), et + 1,36 V (1Ni/9Fe oxide-APA) qui pourrait correspondre au pic de réduction de Ni³⁺ (dans NiOOH) en Ni²⁺ (dans Ni(OH)₂). Ce pic de réduction est plus évident pour l'échantillon avec la plus haute teneur en Ni, 2Ni/1Fe oxide-APA NPs.

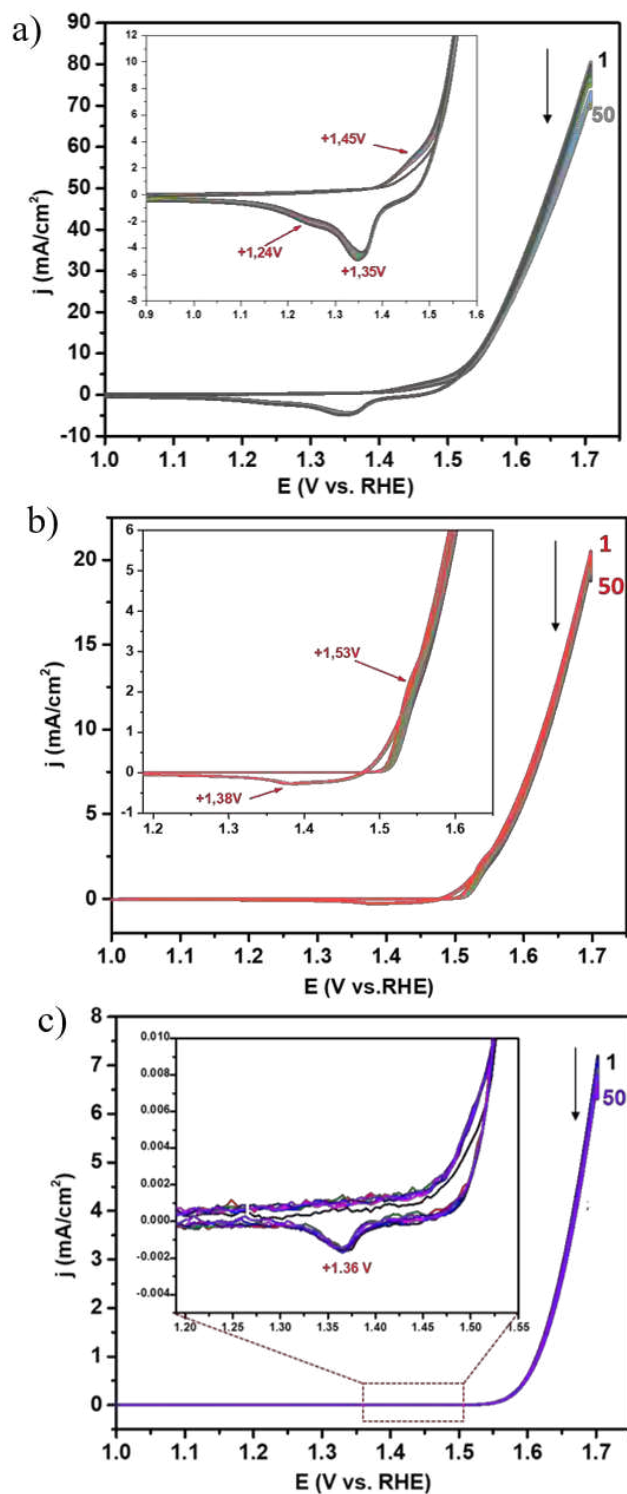


Figure 29. 50 premiers CV de a) 2Ni/1Fe oxide-APA, b) 1Ni/1Fe oxide-APA, c) 1Ni/9Fe oxide-HMDS dans KOH 1M, taux de balayage 5mV/s après activation par LSV.

Pour conclure sur l'évaluation de l'activité électrocatalytique des nouveaux systèmes NiFe développés dans ce chapitre : d'après la revue de la littérature, nous savons que i) l'introduction d'un composant oxyde de fer dans les systèmes NiOx augmente leur conductivité favorisant ainsi les transferts d'électrons ; ii) les systèmes amorphes qui présentent plus de défauts, par rapport aux phases cristallines, sont bénéfiques à la cinétique de la réaction. Les nanocatalyseurs développés ici combinent donc des caractéristiques intéressantes : Le composant métallique Ni dans le noyau avec le Ni(OH)₂ amorphe et l'oxyde de fer sur l'enveloppe qui peuvent créer des jonctions appropriées pour améliorer l'activité électrocatalytique pour la réaction d'oxydation de l'eau. Cette observation est en accord avec les travaux de Manso *et al.* [15].

En conclusion, l'objectif de cette thèse était double : étudier de nouveaux nanocatalyseurs bon marché pour la réaction d'oxydation de l'eau, et concevoir une méthode pour les combiner efficacement avec un photosensibilisateur afin de permettre la séparation de l'eau par voie solaire. Des nanoparticules de Fe d'une taille moyenne d'environ 10 nm ont été synthétisées en utilisant une approche organométallique pour assurer une distribution de taille étroite. Une couche d'oxyde de fer cristallin a été créée à leur surface à l'aide d'un agent de transfert d'oxygène (CH₃)₃NO, suivi d'un processus de recuit doux pour obtenir des NPs Fe@FeOx de structure cœur-coquille avec un diamètre moyen d'environ 11,5 ± 2,3 nm et une épaisseur de coquille d'oxyde γ-Fe₂O₃ d'environ 2,6 nm. Ces nanoparticules ont montré une meilleure activité électrocatalytique pour la production d'O₂ dans des conditions alcalines que neutres, montrant une surtension de départ de 1,75 V et une valeur de pente de Tafel de 142 mV/décade à pH 13. Grâce à la couche d'oxyde γ-Fe₂O₃, ces NPs Fe@FeOx (*r*-Fe@FeOx NPs) ont pu être greffées avec succès avec différents acides aminophosphoniques et transférées dans l'eau. L'évaluation préliminaire de leur activité catalytique pour l'oxydation de l'eau a montré une amélioration pour les NPs fonctionnalisées par l'acide 3-aminopropylphosphonique (NPs *r*-Fe@FeOx@APA) car elles ont affiché à la fois une surtension (1,62 V/ENH) et une pente de Tafel (30 mV/décade) plus faibles que les NPs *r*-Fe@FeOx vierges (surtension à 1,75 V/ENH et pente de Tafel 142 mV/décade). Ces résultats ouvrent des perspectives prometteuses dans le développement de catalyseurs d'oxydation de l'eau à base de Fe.

En outre, une nouvelle photoanode hybride pour la séparation de l'eau par voie solaire a été réalisée en greffant de manière covalente un photosensibilisateur de type Ru-phénanthroline sur les nanoparticules de type coeur/coquille $r\text{-Fe@FeOx}$ par le biais d'un lien phosphonate. Une stratégie a été développée pour préparer le ligand 1,10-phénanthroline phosphonate et le complexe bis-hétéroleptique de ruthénium(II) correspondant à partir du précurseur $[\text{Ru}(\text{phen})_2\text{Cl}_2]$. Le complexe $[\text{Ru-PO}(\text{OH})_2]^{2+}$ qui en résulte a été entièrement caractérisé et qualifié pour être utilisé comme absorbeur de lumière afin de construire un photocatalyseur hybride pour la dissociation de l'eau à l'aide de la lumière visible. Deux voies de synthèse ont été étudiées pour greffer le complexe de Ru à la surface des nanoparticules, à savoir via des processus monophasiques et biphasiques dans des mélanges de solvants THF/H₂O ou CH₂Cl₂/H₂O, respectivement. Le processus monophasique s'est avéré plus efficace car il a fourni une densité de greffage 7 fois plus élevée que celle obtenue par le processus biphasique (respectivement 56 et 9 Ru par nanoparticule pour les processus mono et biphasique). L'activité photoélectrochimique de la photoanode hybride préparée dans des conditions monophasiques a été étudiée sous une lampe Xe AM 1.5M, 100 mWcm⁻² dans du KOH 1M. La densité de photocourant de cette photoanode hybride a atteint 20 μA/cm² à un potentiel appliqué de +1.0 V/ENH. Cela correspond à un TOF (calculé par mole de complexe de Ru) de 0,02 s⁻¹. Cette performance est 9 fois et 40 fois supérieure à celle obtenue pour un simple mélange du photosensibilisateur ruthénium polypyridyle avec les nanoparticules Fe@FeOx et les photoanodes $r\text{-Fe@FeOx}$ natives, respectivement. Le transfert d'électrons entre le photosensibilisateur ruthénium polypyridyle et le catalyseur d'oxydation de l'eau Fe@FeOx a été identifié comme l'étape clé dans le fonctionnement de cette photoanode. L'amélioration des performances pourrait être attribuée à un transfert d'électrons plus efficace entre le photosensibilisateur ruthénium polypyridyle et le catalyseur d'oxydation de l'eau Fe@FeOx, grâce à la liaison covalente entre ces deux composants. Le greffage covalent s'est avéré non seulement améliorer l'activité photocatalytique mais aussi améliorer significativement la stabilité du système. Ces résultats offrent une inspiration pour la conception de photoanodes nano-hybrides liées de manière covalente dans le contexte de la séparation de l'eau induite par la lumière.

Nous avons ensuite étudié des NPs bimétalliques NiFe-oxyde, un groupe d'électrocatalyseurs prometteurs pour la réaction d'oxydation de l'eau. Des NPs de NiFe (≈ 4 nm) de deux compositions

différentes ($\text{Ni}_{0,5}\text{Fe}_{0,5}$ NPs et $\text{Ni}_{0,68}\text{Fe}_{0,32}$ NPs) ont été synthétisées par une voie organométallique, oxydées à l'air et l'acide 3-aminopropyl phosphonique (APA) a été greffé à leur surface pour donner des NPs d'oxyde de NiFe-APA hydrosolubles. Leur activité catalytique dans la réaction d'oxydation de l'eau a été étudiée dans une solution alcaline de KOH 1M, et comparée à l'activité catalytique des NPs NiOx-PVP, des NPs FeOx-HDMS, et des NPs $\text{Ni}_{0,1}\text{Fe}_{0,9}\text{Ox}$ dans des conditions identiques. Il a été constaté que les NPs d'oxyde de NiFe-APA présentaient une activité catalytique nettement supérieure à celle de leurs homologues NiOx et FeOx, ce qui suggère un effet synergique. Le catalyseur NiFe-APA NPs contenant 32 % de Fe ($\text{Ni}_{0,68}\text{Fe}_{0,32}\text{Ox}$) a montré l'activité la plus élevée, présentant une surtension de 320 mV à 10 mA/cm² (équivalent à 10 % d'efficacité de conversion solaire-carburant) et une pente de Tafel de 62 mV/décade dans une solution de KOH 1M. Ces catalyseurs à base de NPs d'oxyde de NiFe- APA ont également montré une bonne durabilité dans la solution alcaline en maintenant une activité presque constante pendant 16 heures à $j=10\text{mA/cm}^2$. Leur efficacité et leur durabilité élevées rendent ces NPs NiFeOx-APA potentiellement applicables dans les cellules photoélectrochimiques pour la séparation de l'eau. Ainsi, toutes les conditions sont maintenant réunies pour envisager le greffage réussi d'un photosensibilisateur Ru sur ces catalyseurs prometteurs à base d'oxyde de NiFe, ce qui devrait fournir un catalyseur efficace pour l'oxydation solaire de l'eau.

References

1. Gharbi, K., et al., *Alkyl phosphonic acid-based ligands as tools for converting hydrophobic iron nanoparticles into water soluble iron-iron oxide core-shell nanoparticles*. New Journal of Chemistry, 2017. **41**(20): p. 11898-11905.
2. Sahoo, Y., et al., *Alkyl Phosphonate/Phosphate Coating on Magnetite Nanoparticles: A Comparison with Fatty Acids*. Langmuir, 2001. **17**(25): p. 7907-7911.
3. Peng, S., et al., *Synthesis and Stabilization of Monodisperse Fe Nanoparticles*. Journal of the American Chemical Society, 2006. **128**(33): p. 10676-10677.
4. da Costa, G.M., E. De Grave, and R.E. Vandenberghe, *Mössbauer studies of magnetite and Al-substituted maghemites*. Hyperfine Interactions, 1998. **117**(1): p. 207-243.
5. Di Marco, V., et al., *Complexation Properties of Ethylenediaminetetramethylenephosphonic Acid (EDTMP) with AlIII and VIVO*. European Journal of Inorganic Chemistry, 2004. **2004**(12): p. 2524-2532.
6. Youngblood, W.J., et al., *Visible Light Water Splitting Using Dye-Sensitized Oxide Semiconductors*. Accounts of Chemical Research, 2009. **42**(12): p. 1966-1973.
7. De Tovar, J., et al., *Light-driven water oxidation using hybrid photosensitizer-decorated Co₃O₄ nanoparticles*. Materials Today Energy, 2018. **9**: p. 506-515.
8. Brimblecombe, R., et al., *Solar Driven Water Oxidation by a Bioinspired Manganese Molecular Catalyst*. Journal of the American Chemical Society, 2010. **132**(9): p. 2892-2894.
9. Youngblood, W.J., et al., *Photoassisted Overall Water Splitting in a Visible Light-Absorbing Dye-Sensitized Photoelectrochemical Cell*. Journal of the American Chemical Society, 2009. **131**(3): p. 926-927.
10. Kirner, J.T., et al., *Visible-Light-Assisted Photoelectrochemical Water Oxidation by Thin Films of a Phosphonate-Functionalized Perylene Diimide Plus CoOx Cocatalyst*. ACS Applied Materials & Interfaces, 2014. **6**(16): p. 13367-13377.
11. Zaramello, L., et al., *Kinetic investigation into the chemoselective hydrogenation of α,β -unsaturated carbonyl compounds catalyzed by Ni(0) nanoparticles*. Dalton Transactions, 2017. **46**(15): p. 5082-5090.
12. Lacroix, L.-M., et al., *Ultrasmall iron nanoparticles: Effect of size reduction on anisotropy and magnetization*. Journal of Applied Physics, 2008. **103**(7): p. 07D521.
13. Ma, W., et al., *A Superlattice of Alternately Stacked Ni-Fe Hydroxide Nanosheets and Graphene for Efficient Splitting of Water*. ACS Nano, 2015. **9**(2): p. 1977-1984.
14. Qiu, Y., L. Xin, and W. Li, *Electrocatalytic Oxygen Evolution over Supported Small Amorphous Ni-Fe Nanoparticles in Alkaline Electrolyte*. Langmuir, 2014. **30**(26): p. 7893-7901.
15. Manso, R.H., et al., *Controlling the 3-D morphology of Ni-Fe-based nanocatalysts for the oxygen evolution reaction*. Nanoscale, 2019. **11**(17): p. 8170-8184.
16. Burke, M.S., et al., *Oxygen Evolution Reaction Electrocatalysis on Transition Metal Oxides and (Oxy)hydroxides: Activity Trends and Design Principles*. Chemistry of Materials, 2015. **27**(22): p. 7549-7558.
17. Doyle, R.L., et al., *Redox and electrochemical water splitting catalytic properties of hydrated metal oxide modified electrodes*. Physical Chemistry Chemical Physics, 2013. **15**(33): p. 13737-13783.
18. Corrigan, D.A., *The Catalysis of the Oxygen Evolution Reaction by Iron Impurities in Thin Film Nickel Oxide Electrodes*. Journal of The Electrochemical Society, 1987. **134**(2): p. 377-384.
19. Corrigan, D.A. and R.M. Bendert, *Effect of Coprecipitated Metal Ions on the Electrochemistry of Nickel Hydroxide Thin Films: Cyclic Voltammetry in 1M KOH*. Journal of The Electrochemical Society, 1989. **136**(3): p. 723-728.

20. Wehrens-Dijksma, M. and P.H.L. Notten, *Electrochemical Quartz Microbalance characterization of Ni(OH)₂-based thin film electrodes*. *Electrochimica Acta*, 2006. **51**(18): p. 3609-3621.
21. Trotochaud, L., et al., *Solution-Cast Metal Oxide Thin Film Electrocatalysts for Oxygen Evolution*. *Journal of the American Chemical Society*, 2012. **134**(41): p. 17253-17261.

Résumé de thèse en Français

Dans ce travail, différents systèmes catalytiques nanostructurés ont été synthétisés par une approche organométallique pour obtenir des nanoparticules de petite taille et de distribution de taille étroite, et leur activité catalytique dans la réaction d'oxydation de l'eau a été évaluée.

Premièrement, des NPs de fer stabilisées par l'acide oléique ont été synthétisées qui présentaient une taille moyenne d'env. $10 \text{ nm} \pm 1,1 \text{ nm}$. Une couche d'oxyde, $\gamma\text{-Fe}_2\text{O}_3$, d'env. $2,6 \text{ nm}$ d'épaisseur a été formée à leur surface pour obtenir des structures cœur-coquille $\text{Fe}@/\text{FeOx}$ d'env. $11,5 \pm 2,3 \text{ nm}$ de diamètre. Malgré leur hydrophobicité, ces nanoparticules ont montré une bonne activité électrocatalytique en conditions alcalines. La coquille d'oxyde $\gamma\text{-Fe}_2\text{O}_3$ étant bien adaptée au greffage de groupements phosphoniques, ces NPs $\text{Fe}@/\text{FeOx}$ ont été greffées avec différents acides aminophosphoniques afin de les transférer dans l'eau. Une évaluation préliminaire de leur activité catalytique montre une amélioration lorsque les NPs sont greffées avec l'acide 3-aminopropylphosphonique, ce qui ouvre des perspectives prometteuses.

En outre, un photosensibilisateur, un complexe Ru-phénanthroline avec un groupe phosphonate pendant, a été synthétisé et greffé sur les NPs $\text{Fe}@/\text{FeOx}$ pour former une photoanode hybride et catalyser la photoélectrodecomposition de l'eau. Des processus mono et biphasiques ont été étudiés pour greffer le complexe à la surface des nanoparticules. Le processus monophasique s'est avéré plus efficace car il a fourni une densité de greffage plus élevée (respectivement 56 et 9 Ru par NP pour les processus mono et biphasiques). Des mesures photoélectrochimiques ont montré que le nanocatalyseur hybride comprenant la teneur en Ru la plus élevée était env. 9 fois plus actif qu'un simple mélange entre un photosensibilisateur au ruthénium sans fonction de greffage et les nanoparticules $\text{Fe}@/\text{FeOx}$, et env. 40 fois plus actif que les NPs $\text{Fe}@/\text{FeOx}$. L'amélioration des performances pourrait être attribuée à un transfert d'électrons plus efficace entre le photosensibilisateur et le catalyseur $\text{Fe}@/\text{FeOx}$ grâce à la liaison covalente entre ces deux composants. Le greffage covalent s'est avéré améliorer non seulement l'activité photocatalytique mais également la stabilité du système.

Enfin, des NPs NiFe amorphes (diamètre env. 4 nm) avec deux compositions différentes ($\text{Ni}_{0,5}\text{Fe}_{0,5}$ NPs et $\text{Ni}_{0,68}\text{Fe}_{0,32}$ NPs) ont été synthétisées, oxydées à l'air et fonctionnalisées avec de l'acide 3-aminopropyl phosphonique. L'activité électrocatalytique de ces NP hydrosolubles a été étudiée en milieu alcalin, en comparaison avec des NPs NiOx, FeOx et $\text{Ni}_{0,1}\text{Fe}_{0,9}\text{Ox}$. Les NPs hydrosolubles contenant 32% de Fe ($\text{Ni}_{0,68}\text{Fe}_{0,32}\text{Ox}$) ont montré l'activité la plus élevée et une bonne durabilité en solution alcaline. Ces caractéristiques rendent ces NP amorphes potentiellement applicables dans les cellules photoélectrochimiques pour la photodécomposition de l'eau.

Résumé de thèse en Anglais

In this work, different nanostructured catalytic systems have been synthesized by an organometallic approach to produce nanoparticles (NPs) of small size and narrow size distribution, and their catalytic activity in the water oxidation reaction has been evaluated.

First Fe NPs stabilized by oleic acid were synthesized that displayed an average size of *ca.* 10 nm \pm 1.1 nm. A γ -Fe₂O₃ oxide layer *ca.* 2.6 nm thick has been formed at their surface to obtain Fe@FeOx core-shell structure of *ca.* 11.5 \pm 2.3 nm in diameter. Despite their hydrophobicity, these nanoparticles showed good electrocatalytic activity in alkaline conditions. As the γ -Fe₂O₃ oxide shell is well adapted to the grafting of phosphonic groups, these Fe@FeOx NPs were grafted with different aminophosphonic acids in order to transfer them into water. Preliminary assessment of their catalytic activity showed improved activity for the NPs functionalized by 3-aminopropylphosphonic acid which opens promising prospects.

Subsequently, a Ru-phenanthroline light-harvester with a pendant phosphonate group was synthesized and grafted onto the Fe@FeOx core/shell NPs to afford a novel hybrid photoanode for solar-driven water splitting. Mono- and biphasic processes were investigated to graft the Ru-complex at the surface of the NPs. The monophasic process was found to be more efficient as it provided a higher grafting density at the surface of the NPs (respectively 56 and 9 Ru per nanoparticles for the mono and biphasic processes). Photoelectrochemical measurements showed that the hybrid nanocatalyst comprising the highest Ru content was *ca.* 9-fold more catalytically active than a simple mixture between a ruthenium polypyridyl photosensitizer bearing no grafting group and the Fe@FeOx nanoparticles, and 40-fold more active than the pristine Fe@FeOx NPs. The performance enhancement could be attributed to a more efficient electron transfer between the ruthenium polypyridyl photosensitizer and the Fe@FeOx water oxidation catalyst thanks to the covalent bonding between these two components. The covalent grafting was found to improve not only the photocatalytic activity but also the stability of the system.

Finally, amorphous NiFe NPs (diameter *ca.* 4 nm) with two different ratios between Ni and Fe (Ni_{0.5}Fe_{0.5} NPs and Ni_{0.68}Fe_{0.32} NPs) were synthesized, oxidized in air and grafted with 3-aminopropyl phosphonic acid in order to obtain hydrophilic systems. The electrocatalytic activity of these water-soluble NPs was studied in alkaline solution, in comparison with that of crude NiOx NPs, FeOx NPs, and Ni_{0.1}Fe_{0.9}Ox NPs. The water soluble NPs containing 32 % of Fe (Ni_{0.68}Fe_{0.32}Ox) showed the highest activity and a good durability in alkaline solution. These characteristics make these amorphous NPs potentially applicable in photoelectrochemical cells for water splitting.